Integrated Micromechanical-Structural Framework for the Nonlinear Viscoelastic Behavior of Laminated and Pultruded Composite Materials and Structures

A Thesis
Presented to
The Academic Faculty

by

Anastasia Hanifah Muliana

In Partial Fulfillment
of the Requirements for the Degree
Doctor of Philosophy in Civil and Environmental Engineering

Georgia Institute of Technology

November 2003

Integrated Micromechanical-Structural Framework for the Nonlinear Viscoelastic Behavior of Laminated and Pultruded Composite Materials and Structures

Approved by:

Dr. Rami Haj-Ali, Advisor
Civil and Environmental Engineering

Dr. Donald White
Civil and Environmental Engineering

Dr. Kenneth Will
Civil and Environmental Engineering

Dr. Erian Armanios
Aerospace Engineering

Dr. Karl Jacob
Polymer, Textile, and Fiber Engineering

Date Approved: November 26, 2003

ACKNOWLEDGEMENT

This dissertation is based on my doctoral study which was conducted at Georgia Institute of Technology. This research was supported by NSF, through the Civil and Mechanical Systems (CMS) Division, and under grant number 9876080.

I wish to gratefully acknowledge Dr. Rami Haj-Ali who first introduced me to the micromechanics of composite materials. Furthermore, I want to thank Dr. Haj-Ali for his academic guidance, fruitful ideas, countless encouragements and support to complete this thesis. I would also like to thank Dr. Donald White, Dr. Kenneth Will, Dr. Erian Armanios, and Dr. Karl Jacobs to be on my thesis committee and for providing valuable feedback on several aspects of my research. I thank Dr. Lisa Rosenstein for her assistance in improving my technical writing skills.

Moreover, I would like to thank my office mates Dr. Hakan Kilic, Ahmet Citipitioglu, Rani El-Hajjar, and all my other colleagues for sharing their valuable time and for the many discussions we had. I would also like to thank Rani El-Hajjar for helping me with the experimental part of my work. I also want to take this opportunity to acknowledge my best friends Sarah, Nanny, Katia, Aank, and all my other friends for their support and friendship. Finally, I thank my parents, my family and Maikel for the love they give me.

I hope this work can be useful and can serve as a starting point for further research to extend and improve this work.

TABLE OF CONTENTS

LIST OF TABLES

LIST OF FIGURES

SUMMARY

This study introduces a new three-dimensional (3D) multi-scale constitutive framework for the nonlinear viscoelastic analysis of laminated and pultruded composites. Two previously developed nonlinear micromechanical models for unidirectional and in-plane random composite layers are modified to include time-dependent and nonlinear behavior. A new recursive-iterative numerical integration method is introduced for the Schapery nonlinear viscoelastic model and is used to model the isotropic matrix subcells in the two micromodels. In addition, a sublaminate model is used to provide for a through-thickness 3D nonlinear equivalent continuum of a layered medium. The fiber medium is considered as transversely isotropic and linear elastic. Incremental micromechanical formulations of the above three micromodels are geared towards the time integration scheme in the matrix phase. New iterative numerical algorithms with predictor-corrector type steps are derived and implemented for each micromodel to satisfy both the constitutive and homogenization equations. Experimental creep tests are performed for off-axis pultruded specimens in order to calibrate and examine the predictions of the constitutive framework for the multi-axial nonlinear viscoelastic response. Experimental creep data, available in the literature, is also used to validate the micromodel formulation for laminated composite materials. Nonlinear viscoelastic effects at the matrix level, such as aging, temperature, and moisture effects can be easily incorporated in the constitutive framework. The multi-scale constitutive framework is implemented in a displacement-based finite element (FE) code for the analysis of laminated and pultruded structures. Several examples are presented to demonstrate the coupled multi-scale material and structural analysis. The overall structural modeling framework is numerically efficient and accurate when compared with experimental creep response of structural components.

CHAPTER I

INTRODUCTION

Fiber reinforced composites are heterogeneous material systems that consist of fiber reinforcements with high strength and stiffness, and a matrix system that is used to bind the fibers. Different reinforcements are used such as unidirectional fibers, woven fabrics, and braided preforms, which are made of glass, carbon, kevlar, aramid, or alumina. Polymeric, metal, or ceramic materials are usually used for the matrix. Fiber reinforced composites offer unique advantage over metallic structures, in addition to their high strength and high stiffness properties, such as light weight, resistance to harsh corrosive environment, better absorption of energy, electrical or magnetic insulation, and flexibility in designs. Currently, fiber reinforced composite plastic (FRP) materials are widely used in structural components of aircraft, automotive, marine, building, and sporting goods.

Pultruded FRP systems are another type of composite materials that combine different forms of reinforcement layers, such as roving, continuous filament mats (CFM), woven fabrics, and braided preforms. The reinforcement combination is usually repeated through the wall thickness of the cross-section of a pultruded member. The thickness of the pultruded systems varies from 1/16 to 1 in. Fibers can be made of carbon or glass. Matrix materials are commonly made of polyester or vinylester resin that includes additives such as glass microspheres and clay particles. During the pultrusion process, the reinforcement systems are stacked and pulled from one end through the resin system and heated die to produce a long prismatic structural component with constant cross section geometry. Thin and thick-walled composite members can be made having similar shapes to the standard steel beam shapes, such as wide-flange, channels, and angle sections. The relatively fast production of pul-

truded structural components allows for mass manufacturing and cost competitive composite materials. Recently, FRP pultruded composite materials have been widely applied for civil and infrastructural engineering applications, such as bridges, transmission towers, and structural components of buildings.

FRP composites experience a time-dependent (viscoelastic) behavior mainly due to their polymeric matrix. Viscoelastic materials respond to a mechanical load with both instantaneous (elastic) and delayed (viscous) parts. The delayed response in polymers is usually accompanied by energy dissipation due to the evolving microstructure, such as the relative movement of polymeric chains and bond breaking. The viscoelastic behavior of a material depends on its previous thermo-mechanical states and environmental conditions. In most amorphous polymers, environmental effects such as increasing temperature and moisture content enhance the nonlinear deformation and deterioration of the internal microstructure, especially when coupled with mechanical loading. The moisture content can greatly decrease the energy required to produce deformation at a constant temperature due to the reversible change of the microstructure. Under isothermal and constant environmental conditions, both the instantaneous and the transient responses increase with increasing applied loading.

Manufacturing and curing methods such as hand lay up, compression molding, pultrusion, and filament winding can lead to different time-dependent characteristics. The viscosity of FRP composites increases with increasing cure time and temperatures, and decreases with increasing cure pressures. The addition of fillers into a resin system can also increase its viscosity. The presence of voids in the composites is considered to be major defect during the manufacturing process, which can significantly reduce the strength and stiffness of the composites and also increase the viscosity and rate of moisture absorption in a humid environment condition. The axial stiffness and strength of unidirectional FRP materials having

high fiber volume fraction (FVF) are not usually affected by time-dependent effects, due to the dominant presence of the linear elastic fiber.

Linear viscoelastic response is considered whenever stress or strain response satisfies proportionality condition and superposition principle. Therefore, the time-dependent linear creep (constant stress) and relaxation (constant strain) functions are interrelated and permit the construction of one from the other. Boltzmann convolution integral, which is represented by a single time integral, has been widely used to express the history (memory) dependency of linear viscoelastic materials. In a nonlinear viscoelastic material proportionality and superposition conditions are violated. This is the case when large stress levels are applied, especially when combined with elevated temperatures or high moisture. In addition, existence of imperfections and discontinuities in the material can enhance the nonlinear viscoelastic behavior.

This chapter presents a literature review of analytical, numerical, and experimental studies carried out to characterize the time-dependent behavior in FRP laminated and pultruded composites. Micromechanical models, time-dependent behavior of laminated and pultruded composites, homogeneous and anisotropic viscoelastic constitutive models, and long-term behaviors of FRP materials and structures are reviewed.

1.1 Micromechanical Models for Composite Materials

The overall effective mechanical properties and response of a composite material can be characterized from its microstructures: fiber and matrix constituents. Refined models include fiber coating and interphase (or interface) between the fiber and matrix constituents. Several micromodels have been proposed in order to characterize the effective properties of fiber reinforced composites. Hill (1964) defined average stress and strain over the fiber and matrix volumes in order to determine overall elastic properties of the composite. Concentration matrices are formulated for each phase, which relate the phase's average stress or strain to the overall response. The composite effective stiffness and compliance are determined

from the stress or strain concentration matrices. Hashin and Rosen (1964) proposed a concentric cylinder assemblage (CCA) model to analyze a unidirectional and continuous fiber composite with isotropic phases. The CCA model consists of an assembly of fiber and matrix concentric cylinders with different radii used to fill the entire medium. The FVF in each two cylinders is fixed. Hashin (1990) extended the CCA model to include orthotropic phases. Christensen and Lo (1979) used a three-phase cylinder model in order to determine the effective transverse shear modulus of a unidirectional composite. In this model a cylindrical fiber surrounded by a concentric cylindrical matrix is embedded in an effective homogeneous medium. Both fiber and matrix phases are considered isotropic. The solution of this model is determined using an averaged formulation of all constituents and satisfying all boundary conditions and continuity conditions. Benveniste (1987) generalized the Mori-Tanaka (1973) relations and provided a general method for determining the effective properties. Two phase composites with anisotropic elastic constituents can be considered. Linear micromechanical models have been extensively investigated and covered in several books on advanced mechanics of composites, such as Christensen (1979), Gibson (1994), Herakovich (1998), Jones (1999), and Nemat-Nasser and Hori (1999).

A class of 3D nonlinear micromechanical models capable of predicting the overall nonlinear response has been proposed. The method of cells (MOC) was developed, e.g. Aboudi (1991), for a periodical medium with rectangular fibers embedded in the matrix. A quarter micromodel , which has finite number of rectangular subcells can be modeled due to the symmetric condition. Polynomial expansions in term of local coordinate system located at the center of each subcells are used to express the displacement. Displacement and traction continuity between the fiber-matrix subcells and adjacent cells are reinforced in an average manner. Haj-Ali and Pecknold (1996) used the MOC four-cell micromodel and presented an incremental formulation in terms of the average strains and stresses in the subcells. Numerical stress update and correction schemes were also developed. The new incremental

formulation and the numerical methods are suitable for integration into finite element (FE) structural analysis.

1.2 Mechanical Behavior of Pultruded FRP Composites

Experimental and analytical studies have been performed to characterize the material properties and behavior of pultruded FRP composites. Herakovich and Mirzadeh (1991) studied the effects of fiber spacing and fiber volume content in the effective properties of pultruded graphite/epoxy composite. The fiber spacing and resin rich area were distributed non-uniformly. Fiber waviness, which reduces the stiffness and strength of the pultruded composites, was also found due to a compression loading. Binshan et al. (1995) performed a series of tests in order to determine FVF and mass density in pultruded specimens cut from standard profiles, plates, gratings, and rebars. The pultruded specimens consisted of vinylester and polyester matrix systems reinforced with alternating layers of glass roving, CFM, and woven. They found that the grating and rebar specimens had the highest FVF and the lowest amount of added fillers, while standard profile specimens had a relatively low FVF and high filler content. The addition of fillers reduced the void content and mechanical properties and significantly increased the mass of the pultruded composites. Wang and Zureick (1994) characterized the tensile behavior of coupon specimens cut from different locations of a pultruded I-shape beam. A significant number of voids were found in these coupons. Furthermore, the roving reinforcement was distributed unevenly. The specimen size effects on the effective properties were also examined.

Barbero (1991) and Sonti and Barbero (1996) proposed a linear micromechanical modeling approach to generate the overall effective stiffness of pultruded composite material systems. The micromodel, which employed the periodic microstructure formulae of Luciano and Barbero (1994), was combined with the classical lamination theory and mechanics of laminated beams approach in order to determine the overall effective stiffness of pultruded composite beams. The in-plane stiffness for the CFM layers was modeled using approxi-

mate models proposed by Tsai and Pagano (1968). The predicted effective stiffness matched well with their experimental results. A 3D micromechanical and structural modeling framework for the nonlinear analysis of pultruded composite materials and structures has been proposed (Haj-Ali et al., 2001, Haj-Ali and Kilic 2002, 2003). Multi-scale micromodels were proposed to model the roving and CFM layers. A sublaminate model was used to generate the through-thickness 3D effective behavior of the material. Kilic and Haj-Ali (2003a, 2003b) coupled the nonlinear micromechanical formulation along with different failure models to perform progressive failure analysis of pultruded components. Haj-Ali and El-Hajjar (2003) studied mode-I fracture of pultruded composite components using singe-edge-notched-tension ESE(T) specimens. The nonlinear micromodels along with cohesive FE were used to simulate and predict the crack growth.

The long and slender nature of pultruded structural members makes buckling an important aspect of compression response. Zureick and Scott (1997) presented design guidelines for FRP slender pultruded structural members under axial compression based on global buckling limit states. Axially compression tests on box and I-shape cross sections of E-glass/vinylester pultruded specimens were performed. The modified Euler buckling load, which is a function of the longitudinal elastic modulus and moment of inertia about the minor axis, was used to determine a critical buckling load. Barbero and Tomblin (1993) investigated global buckling loads for pultruded I-shape long columns. Southwell's (1932) method was used to determine the critical load from experimental tests assuming no interaction between the buckling modes. In the Southwell method, the experimental load (P) and lateral displacement (δ) are used to plot a (δ/P) vs (δ) curve and regress linearly in the postbuckling range close to the initial buckling. The critical load is determined from the linear relation when the lateral displacement at the center of the beam approaches the critical magnitude of L/100 (L is the column length). As expected, the results for the long columns were well predicted by the Euler buckling. Barbero et al. (2000) studied the interaction between local

and global buckling modes for intermediate length pultruded wide-flange (WF) columns. Twelve WF specimens with two different dimensions were tested with pin-pin support. Initial imperfection was induced to all columns by applying lateral loads with a slow loading rate (2.5 mm/min) until an initial pattern was achieved, which measured using a shadow moire optical technique. After the initial imperfection was achieved, the compression test continued until the column collapsed. Axial and lateral displacements were measured during the test. It was concluded that the interaction between the local and global buckling modes created an unstable postbuckling path that can lead to early failure.

FE models have been used to analyze pultruded composite structures. Most of these studies consider the material to be linear orthotropic and homogeneous. Bank and Yin (1999) studied the separation between the compression flange and web of an I shape pultruded beam in postbuckling regime. A FE analysis was generated using a node separation technique in order to simulate the progressive failure of flange-web junction following a local buckling of the flange. Vakanier et al. (1991) performed linearized buckling analysis of pultruded columns with stocky WF cross-sections using FE models. Most of geometries studied had relatively small slenderness ratio and allow for local flange buckling. Smith et al. (1998, 1999) performed experimental tests and FE analyses using shell elements for connections in FRP pultruded members. Both I-beam and box-beam with standard and bolted connections were implemented. The strength and stiffness in box-beam were higher than the one in I-beam. Two FE models were considered: simplified beam model and "condensed" FE model. In simplified model, the connections were replaced by elastic members and torsional spring. While detailed connections were constructed in the "condensed" FE model.

1.3 Viscoelastic Constitutive Models for Isotropic and Anisotropic Material

The linear viscoelastic response of a material subjected to complex loading histories can be obtained using either an integral or differential constitutive forms. The Boltzmann convolution integral is commonly used to represent the superposition principle for the linear vis-

coelastic behavior. In this case, infinitesimal deformations are usually considered. Two common methods are often used to represent the uniaxial transient part of a viscoelastic response. Findley et al. (1976) applied a power law function to express the transient creep strain. Nonlinear and temperature effects can be included by having the power-law coefficients as functions of stress or temperature. Stress and temperature dependence is often expressed in a hyperbolic form; and can be expanded to a polynomial series for curve-fitting purposes. A Prony series (exponentials) mathematical form is also used to represent the transient compliance or modulus. The Prony series can be linked to the solution of a mechanical analogy of springs and dashpots (Kelvin and Maxwell arrangements) used to represent the instantaneous and transient responses of the material. The Prony series form is very convenient in numerical formulation using recursive integration methods. Lai and Findley (1973) conducted creep and recovery tests for polyurethane material under several temperature levels. The time-dependent response was adequately described by a power law model and its exponent was independent of stress and temperature. They showed that this material was nonlinear with increasing temperature and load levels.

Viscoelastic formulations have also been coupled with finite deformations, e.g. Coleman and Noll (1961). Stress was given by a functional of deformation gradient history at instant time. In a linear viscoelastic solid, stress or strain can be represented by a single time integral that expresses the history (memory) dependence. In general, the viscoelastic constitutive model can be functions of both position and time. However, if the homogeneity (proportionality) condition is assumed, the position dependent is withheld in the constitutive models. Haddad (1988) discussed linear viscoelastic material modeling with an arbitrary degree of anisotropy using the symmetric fourth order tensorial creep and relaxation functions. These tensorial functions and their derivatives were continuous functions of time during the applied loading. Each component of the viscoelastic stress-strain relation should satisfy a fad-

ing memory type behavior. The concept and definition of fading memory can be found in Coleman and Noll (1961).

A nonlinear viscoelastic material is considered whenever proportionality and superposition conditions are violated. The existence of imperfections and discontinuities in the material can enhance its nonlinear response. Green and Rivlin (1957) presented a three-dimensional nonlinear viscoelastic model based on a multiple integral formulation. The viscoelastic response was expressed as a third order polynomial expansion having time-dependent material properties. This theory can be applied to a wide range of materials because it permits higher orders of nonlinearity. However, the experimental requirements to determine material properties for this theory become impractical when the material has strong nonlinearities. Coleman and Noll (1961) derived a nonlinear theory, which is restricted to a slow process of deformation. The stress was determined by linearly integrating the deformation history with reference to the current configuration. Coleman (1964) proposed a thermomechanical theory of nonlinear viscoelastic model under non-isothermal condition. The theory is based on assumption that the specific internal energy and stress in the material are functions of the histories of the deformation gradient tensor and the absolute temperature. Christensen (1971) used and simplified Coleman theory to formulate a general nonlinear viscoelastic model under isothermal condition. Stress-based constitutive equation was derived from the combination of the local energy balance and local entropy production. Both stress and stored energy per unit mass were functional of past history deformation. The deformation function and its derivatives were assumed to be continuous. In this model, the nonlinear deformation function is history dependent.

The thermodynamics of irreversible processes (TIP) with the use of internal state variables (ISVs) is very helpful in developing material models that relate histories of stress tensor, strain tensor, temperature and other deformation parameters. The concept of ISVs has been applied to continuum mechanics by Biot (1954), Coleman and Gurtin (1967), Schapery

(1964, 1997), Lubliner (1972), and many other researchers. Biot (1954) formulation permits the system to have a non-uniform temperature distribution. The temperature at the geometric boundary of the system is maintained at a constant reference temperature, assuming excess temperature, which is the actual temperature minus the reference temperature, is small. The temperature variation at the boundary is an important factor to determine the generalized force. Another assumption made by Biot is that the viscous properties of the system are temperature independent. The above assumptions are valid within the linear viscoelastic range. Coleman and Gurtin (1967) showed that thermodynamics with ISVs yields similar results to those derived from thermodynamics with fading memory (Coleman and Noll, 1961). Lubliner (1969) showed that material with ISVs, in fact, possess fading memory if the constitutive model for the ISVs satisfies stability of equilibrium states. Lubliner (1972) explored a non-equilibrium thermodynamics with ISVs governed by rate equations in order to develop a nonlinear time-dependent constitutive model. The number of ISVs is small for non-amorphous polymers. Finite number of ISV's was proposed to represent the average nonlinear behavior of amorphous polymers over a certain range of time-scale. Schapery (1964) developed the constitutive model for viscoelastic media under uniform temperature. The equation of motion was expressed in term of generalized coordinates, forces, temperatures and heat flow. His work represents a modification of Biot's theory. The temperature-dependent properties can be carried through the time-scale (reduced time). This simplification yields to a time-temperature superposition principal. Schapery (1967) used the thermodynamics based constitutive model to analyze the linear viscoelastic moduli of anisotropic composites, including the temperature effects.

Schapery (1964, 1969) developed a uniaxial single integral equation for the nonlinear viscoelastic model based on TIP. Four nonlinear material coefficients were introduced. The use of stresses, rather than strains, as independent variables was made for polymeric materials in a glassy phase. The linear and nonlinear viscoelastic material parameters were func-

tions of ISVs and can be easily characterized from creep and recovery uniaxial tests. Moreover, Schapery's nonlinear viscoelastic equations can be expanded to account for the effects of temperature, moisture, or aging in the viscoelastic material properties. Schapery (1997) extended the formulation to include the nonlinear viscoplastic and damage modeling in the material. Lou and Schapery (1971) calibrated and used this nonlinear integral constitutive form to describe the viscoelastic behavior of glass FRP composites under multiaxial in-plane loading. The matrix octahedral shear stress was used as the stress variable in the nonlinear viscoelastic parameters or functions.

1.4 Experimental Work on Viscoelastic Behavior in Composites

Several experimental studies have been performed to test and characterize the nonlinear viscoelastic behavior of polymeric materials and FRP composites. Martirosyan (1965) conducted creep tests on glass-fiber and phenolic resin composites with cross-ply and angle-ply fiber orientations. Linear viscoelastic behavior was evident for the cross-ply tests, while nonlinear behavior was apparent for the angle-ply tests at high stress levels. Lou and Schapery (1971) performed experimental tests on glass and graphite epoxy composites with different off-axis fiber orientations. Mechanical conditioning for 10 cycles of 1 hour creep followed by 24 hours recovery were carried out prior testing in order to maintain the same strain response under the same load for repeated tests on the same specimen. Creep response was negligible in the axial (fiber) direction. Pronounced nonlinear viscoelastic behavior was shown in the creep tests for 30^{o} (and higher) off-axis specimens at moderate levels of applied stress. The four nonlinear viscoelastic functions in the Schapery single integral creep equations were assumed to be variables of the average octahedral shear stress in the matrix. A simplified relation for the matrix octahedral stress was derived as a function of the applied in-plane stresses and the off-axis angle.

Yeow et al. (1979) used time-temperature superposition principle (TTSP) to determine the long-term compliances of unidirectional T300/934 graphite/epoxy materials. Short-

term (15 minutes) tension creep tests were conducted for various laminates: $[10^o]_{8s}$, $[30^o]_{8s}$, $[60^o]_{8s}$, and $[90^o]_{8s}$ under large temperature ranges: 20°C-210°C. The mechanical conditioning of the specimens prior testing was not necessary since the stress-strain curve obtained after the last cycle of mechanically conditioning was the same as the stress-strain curve obtained after the first thermally conditioning. It is also established that the same specimen could be used repeatedly. The linear response was shown at all temperature levels when loading was applied along the fiber direction. While, more pronounced viscoelastic behavior was shown for transverse and shear responses with increasing temperature. The transverse and shear creep master curves, which were produced from the creep short-term tests, were able to predict the long-term (25 hours) creep data. In addition, the 25 hours creep tests were performed in order to verify the prediction of analytical model for the long-term period. Hiel et al. (1983) used Schapery's nonlinear viscoelastic integral to characterize the long-term viscoelastic behaviors of a T300/934 graphite/epoxy unidirectional composite calibrated from short-term test results. The nonlinear integral relations were calibrated separately for the uniaxial transverse and axial-shear modes. Time shift methods for generating a master curve were applied for the axial shear response, in both stress and temperature scales. This allows for accelerated testing and long-term predictions. A linear viscoelastic response was shown in the transverse mode. Mohan and Adams (1985) conducted one-hour creep test and one-hour recovery test under tensile and compression loading for neat epoxy resin, graphite/epoxy and glass/epoxy materials. Prior testing, mechanically conditioning was done with 3 short-time loading-unloading cycles followed by 30 minutes creep and 2 hours recovery tests. The tests were also carried out at various temperatures and at several relative humidity. They mentioned that temperature and moisture content affected the nonlinear viscoelastic parameters in the Schapery equation. Tuttle and Brinson (1986) used Schapery's nonlinear viscoelastic model with the Classical Laminate Theory (CLT) to analyze the nonlinear viscoelastic response of graphite-epoxy laminates under in-plane load-

ing. Short-term creep-recovery (480/120 minutes) tests for off-axis T300/5208 graphite/epoxy composites with 0^o, 10^o, and 90^o angles were conducted. The viscoelastic parameters in the Schapery model were taken as functions of matrix octahedral stress. Accelerated method based on time-temperature-stress-superposition principle (TTSSP) was used in order to predict the long-term material properties based on short-term data. Two different laminates $[-80/-50/40/-80]_s$ and $[20/50/-40/20]_s$ layups were also tested for 69.4 days. They mentioned that the long-term compliance predictions were compared well with the experimental response for both layups. Tuttle et al. (1995) and Pasricha et al. (1995) used the CLT with combined nonlinear viscoelastic, viscoplastic, and thermal effects to analyze laminated plates subjected to a repeated number of creep/recovery intervals at different temperature levels. Each testing cycle included a four hours creep test, followed by a three hours of recovery. This model was integrated with the CLT to predict the response of different laminates with various stacking sequences.

Howard and Holloway (1987) performed 300 to 700 hour tensile creep tests, followed by 1000 hour recovery, on randomly oriented glass/polyester laminates under several load levels: 0.1-0.4 of the composite ultimate strength. The stress-dependent nonlinear viscoelastic parameters in Schapery equation were adequately calibrated from the creep and recovery tests. Katouzian et al. (1995) performed 10 hours creep tests on neat epoxy resin (thermoset), PEEK polymer (thermoplastic), carbon/PEEK and carbon/epoxy composites under several stress levels at different temperatures: 23^oC, 100^oC and 140^oC. Schapery's single integral constitutive equation was used to characterize the nonlinear parameters. They mentioned that the nonlinear viscoelastic responses were more pronounced by increasing the temperature for both polymers and $[\pm 45_4]_s$ laminated systems. While for $[90_4]_s$ laminates, the linear viscoelastic responses were exhibited. An extensive review of other studies on linear and nonlinear viscoelastic modeling and behavior of composite materials and structures can be found in Scott et al. (1995).

1.5 Numerical Integration Methods for Viscoelastic Material Response

Numerical integration methods for the nonlinear viscoelastic constitutive models within a finite element (FE) formulation have been explored for both isotropic and anisotropic materials. A recurrence numerical algorithm for linear viscoelastic integral has been proposed by Taylor et al. (1970). The convolution integral is divided into recursive parts. This allows the incremental formulation and integration for the current stress-state from the history variables stored at the previous time step, and the current time and strain increments. The recursive approach tremendously minimizes the computational storage required to perform the constitutive integration. Henriksen (1984) used Schapery's nonlinear formulation and developed a recursive numerical integration algorithm. A Prony exponential series is required to express the transient compliance in order to allow for a recursive form of the hereditary integral. The computer storage requirement for using this method is proportional to the number of terms in the Prony series at each integration point. The nonlinear viscoelastic behavior considered was mainly due to higher stress magnitudes. FE analysis was performed for FM-73 adhesive systems under creep and recovery tests. Their results compared very well with the experimental data performed by Perez and Weitsman (1983). Roy and Reddy (1988) used a similar integration approach to Henriksen's and formulated a numerical integration method for the Schapery nonlinear viscoelastic model coupled with moisture sorption used for 2D FE modeling of adhesively bonded joints. The nonlinear viscoelastic parameters depended on stress and temperature. A coupled nonlinear Fickean diffusion model was also used where its diffusion coefficient was a function of temperature, dilatational strain and stress, and moisture concentration. Lai and Bakker (1996) modified Henriksen recursive algorithm in order to include nonlinear effects due to temperature and physical aging effects that accounted for by using a reduced time function. Isotropic material was considered which allows decoupling deviatoric and volumetric parts. The constitutive formulation was used to model experimental tests with PMMA polymer. Li (1997) developed a FE

procedure to analyze nonlinear viscoelastic response for anisotropic solid materials subjected to mechanical and hygrothermal loads. A recursive algorithm was used to evaluate the hereditary integral. The time increment was assumed to be small and the stress varied linearly over the short time period. The nonlinear viscoelastic parameters were function of current stresses. Therefore, the stiffness, which is inverted from the compliance, was dependent on current stress. Thus, hereditary stresses can be obtained from material properties, time increment, strains and stresses of the previous step. Touati and Cederbaum (1997) presented a numerical scheme to obtain nonlinear stress relaxation response from the nonlinear creep experimental data. An exponential (Prony) series was used for the transient creep compliance. Their method transforms the nonlinear convolution integral into a system of first order differential equations. Nonlinear stress relaxation was predicted by solving these equations. Touati and Cederbaum (1998a) extended this numerical procedure for the nonlinear viscoelastic characterization and analysis of orthotropic laminated plates.

Poon and Ahmad (1998) proposed an integration scheme for Schapery's integral expressed with strain state variables and applied independently for each of the anisotropic moduli. Therefore, the nonlinear viscoelastic parameters were strain dependent. Tangent stiffness was formulated by the consistent tangent operator concept that included the time integration algorithm in the constitutive update. In the case of temperature effect the derivative of consistent tangent operator with respect to temperature is also needed. This constitutive form is more suited for FE constitutive environment (a given strain and unknown stress). However, it is not clear how this model can be calibrated for general anisotropic behavior. Yi et al. (1996, 1997, and 1998) developed a FE integration procedure to analyze nonlinear viscoelastic response in laminated composites subjected to mechanical and hygrothermal loading. A lamina was modeled under generalized plane strain. A virtual work with small strain theory was used to derive the equilibrium equations. A recursive viscoelastic exponential series is generated from the time-domain integration of the virtual work with the non-

linear constitutive model. The terms of the integration can be expressed as residual nodal vectors that are stored only for the previous increment. Different nonlinear viscoelastic problems in laminated composites were solved using this FE method, such as interlaminar stress, bending and twisting of laminated composites. Klasztorny and Wilczynski (2000) formulated an iterative procedure in order to characterize linear viscoelastic material properties for a unidirectional fibrous composite. The unidirectional fibrous composite, which consisted of linear viscoelastic isotropic matrix and elastic fiber, were modeled as a homogeneous monotropic material. The elastic and viscoelastic properties in the polymeric matrix were coupled together to form the elasticity and viscoelasticity constitutive equation. Total of 5 elastic and 27 viscoelastic parameters in the composites were characterized.

1.6 Micromechanical Viscoelastic Models of FRP Composite Materials

Micromechanical models with linear and nonlinear viscoelastic behavior for the matrix phase have been proposed. Schaffer and Adams (1981) presented a unit cell FE model. Nonlinear viscoelastic parameters for the matrix were determined by creep and recovery tests. Effective creep results of the unit-cell were presented for 50 hours creep and compared with a test of glass/epoxy unidirectional composite loaded in transverse compression. Aboudi (1990) used his method of cells (MOC) with a four-cell micromechanical model to analyze nonlinear viscoelastic behavior of unidirectional composites. Fibers were assumed linear elastic and transversely isotropic. The Schapery 3D constitutive model for nonlinear viscoelastic behavior was used for the isotropic matrix. Predictions of the MOC were compared with FE unit-cell results found in the study of Schaffer and Adams for longitudinal and transverse creep responses of glass/epoxy and graphite/epoxy composites. The micromechanical predictions showed good agreement with the FE analysis. Sadkin and Aboudi (1989) used the MOC with four-cell micromodel to analyze thermal effects on the viscoelastic response of unidirectional fiber reinforced composites. The viscoelastic matrix was modeled as a thermorheologically-complex material, in which the nonlinear parameters are temperature-

dependent and not function of stress levels. Thus, the stress-strain relation involves two different time scales. Predictions were compared with FE results of a unit-cell for longitudinal and transverse creep responses of graphite/epoxy composites. Cederbaum and Aboudi (1989a, 1989b) determined the time-dependent properties of laminated composite plates by using the MOC with the different lamination theories. Coupled micromechanics and CLT analyses of viscoelastic laminates were performed for quasi-static bending, quasi-static buckling, dynamic, and vibration loading. Results from classical lamination theory and first-order shear deformation theory were compared. Yancey and Pindera (1990) used Aboudi's four-cell micromechanical model to predict the linear creep response for T300/934 graphite/epoxy at room temperature and at 250°F. The linear effective creep compliance was obtained by inverting the effective relaxation modulus.

Horoschenkoff (1990) used Schapery's constitutive equation to formulate the nonlinear viscoelastic compliances of orthotropic composites under plane stress condition. The nonlinear parameters in the matrix phase depended on the octahedral shear stress. Predictions of 100 hour transverse and shear creep responses on carbon/PEEK and carbon/epoxy composites were in good agreement with the experimental data. Gosz et al. (1990) used a unit cell model with a linear viscoelastic interface in order to characterize transverse properties of fiber reinforced composites. Both fiber and matrix phases exhibited linear elastic responses. The fiber reinforced composites were modeled with a periodic array of hexagonally packed fibers. Traction continuity and displacement discontinuity across the interface were assumed in order to simulate matrix phase separation. The effective transverse properties derived from analytical formulation were compared well with the results from FE analysis. Barbero and Luciano (1995) formulated an analytical model of creep and relaxation responses using the Laplace transformation for composite materials having transversely isotropic fibers and linear viscoelastic matrix. Power law model was used for the matrix phase. A unit cell of a cylindrical fibers embedded in the matrix medium was modeled and periodi-

cally distributed in the entire composite. Predictions were compared with experimental data obtained by Yancey and Pindera (1990). Fisher and Brinson (2001) derived the effective viscoelastic moduli of a three phase (fiber, matrix, and interphase) composite using the original and the modified Mori-Tanaka micromechanical models. The two micromechanical models were also used to study the aging effect of a viscoelastic composite. The results showed that the interphase was important in determining overall aging factor, but it was not responsible for the difference in aging factor of the transverse shear and axial shear moduli.

1.7 Aging Effects on Viscoelastic Behavior

The physical aging effects of polymers and polymeric composites have been considered. Struik (1978) defined physical aging as the process that a polymeric material undergoes by a gradual continuation of the glass formation below its glass transition temperature (T_g). The aging material is not under thermodynamic equilibrium (stable state) and its mechanical (elastic and viscoelastic) properties change with time. This is indicated by the molecular mobility and a slow process to establish equilibrium over time. The long-term mechanical behavior of FRP composites in a state below T_g is important for accurate analysis and design of structures.

Struik (1978) studied physical aging of various polymers and developed a model to predict long-term viscoelastic behavior based on short-term test data. The momentary master curves (MMC) were created from the short-term test data at various aging times. The effective time was developed to shift the short-term test data using the aging shift factor in order to predict the long-term response. Brinson and Gates (1995) used Struik physical aging theory to model the long-term response of unidirectional lamina with different off-axis angles. Their model was then combined with the CLT to predict the long-term response of laminated composites. Momentary creep compliance was created by shifting a series of short-term creep test and effective time theory was incorporated through the aging shift factor. Experimental test on IM7-8320 lamina with various fiber orientations were performed

and were predicted up to 10^6 seconds. This study indicates a different rate of change in the shear and transverse modes of viscoelastic response due to aging. Gates et al. (1997) studied the effects of physical aging on creep compliance of IM7/K3B composite under tension and compression. Short-term creep tests (96 hours) at various temperatures and aging times were performed for laminates with $[90]_{12}$ and $[+-45]_{2s}$ layups to determine the transverse and shear responses. Time-temperature superposition was used to create the tension and compression momentary master curves for both transverse and shear compliances. The long-term prediction (1500 hours) compared well with the experimental data. Pasricha et al. (1997) used the Schapery model with reduced effective time and recursive formulation for the physical aging effect on creep in laminated composites. The Schapery integral was separately applied for shear and transverse modes. This constitutive model was combined with CLT theory in order to predict the multi-angle laminate response. Bradshaw and Brinson (1999a) presented a method to determine the physical aging properties from repeated creep relaxation tests under different isothermal conditions. The effective time theory was employed in the Schapery's hereditary integral equation. Compliance curves were modeled using Prony series. The iterative optimization method was used to find the optimal shift rate and all parameters in the compliance function. The analytical results showed good comparison with the experimental data for polyamide resin and carbon/polyamide composite. Bradshaw and Brinson (1999b) predicted the mechanical response of laminated composites due to physical aging by incorporating their model with the CLT. Each lamina was considered as thermorheologically simple material; therefore, the physical aging effect was carried through the time shift factor. The long-term compliance was performed by mapping the time into the effective time through aging shift factor. Different aging parameters were calibrated for the shear and transverse directions. Laminates with various layups consisted of carbon fiber and thermoplastic polyamide resin were tested and predicted. Skrypnyk et al. (2000) presented a numerical method in order to predict long-term behaviors of polymers based on

short-term tests by incorporating a physical aging effect. The Schapery single integral model was combined with the Struik physical aging theory. The stress-strain relationships were represented in incremental form, which requires storing the internal parameters from previous step. A creep master curve from different aging times was created by horizontally shifting the creep response to the one at the reference aging time. The creep master curve can be used to predict the long-term creep response. Hu and Sun (2000) studied the physical aging effect within a linear viscoelastic range of IM7/977-3 carbon/epoxy composites. Several off-axis coupons were tested under different aging time. Experimental data showed different physical aging effects on the elastic and creep compliances. The transient creep compliance was expressed separately for each aging time and off-axis angle. Shift factors and time shift rates were introduced to create reference master curves in term of the effective compliances.

1.8 Viscoelastic Behavior of Pultruded Composites

A relatively limited number of studies have been conducted on the viscoelastic behavior of pultruded composites. To the best knowledge of the authors, there is no multi-axial nonlinear viscoelastic constitutive model used for predicting the effective response of pultruded composites. Most of the current work on pultruded composites has been limited to testing and/or calibrating the uniaxial nonlinear viscoelastic response. Spence (1990) performed test for unidirectional glass/epoxy pultruded specimen under compression creep for 840 hours. It was mentioned that long-term creep response was negligible under applied load below 30% of the material compressive strength. Bank and Mossalam (1990) conducted long-term creep and short-term failure tests for E-glass/vinylester pultruded structures with continuous strand mat and roving layers. A 6 feet high and 9 feet wide plane portal frames were tested under four point bending load. The bottom support was a pin-type support and a bolted connection was used between the girder and column. The 10,000 hours creep test was conducted with applied load 3400 lbs (25% of the ultimate failure strength). They found

that the bulk of the axial and shear creep response occurred during the first 2000 hours. A number of short-term loading and unloading was performed at various load levels. The short-term tests with applied loads less than 10 kips showed a linear viscoelastic response. Beyond this load level, the frame showed nonlinear behavior and the progressive damage increased and the frame ultimate failure reached at 25,000 lbs. Scott and Zureick (1998) conducted compression creep tests on pultruded E-glass/vinylester coupons cut from I-shape pultruded sections in their longitudinal direction. The samples were subjected to three different stress levels for the duration of 10,000 hours. Findley's power law with a constant exponent was used to model the uniaxial time-dependent behavior. The stress-dependent coefficients were calibrated from the short duration tests (1000 hours). Good comparisons between the model and the experimental data were shown for the reminder of the creep results. Barpanda and Raju (1998) evaluated creep and stress relaxation characteristics of pultruded glass-graphite/epoxy hybrid composites. Coupon specimens were subjected to a combination of static and dynamic flexure loading conditions at wide temperature ranges (140°F-284°F) and over 30 minutes creep and 15 minutes recovery. Time-temperature superposition was used to predict the long-term response from the short-term test data. It was shown that flexural creep compliance and flexural relaxation modulus were dependent on the fiber type and configuration in the hybrid composites.

1.9 Present Study

The soft polymeric matrix in FRP composites makes consideration of time-dependent behavior or integral part of any reliable structural analysis. Nonlinear viscoelastic responses are pronounced when the applied mechanical loads are large enough and when coupled with elevated temperature and moisture. A general 3D integrated micromechanical-structural analysis framework is attractive because the overall behavior can be predicted by determining the fiber and matrix constituents.

The present study introduces analytical and numerical formulations in order to derive the effective nonlinear viscoelastic response of laminated and pultruded composites. Simplified 3D micromechanical models are proposed for the effective response of the different layers used in the pultruded cross section and in laminated composite structures. These micromodels recognize the in-situ response of the fiber and matrix constituents. A sublaminate model is also proposed for the nonlinear effective continuum response of a periodic layered medium. The second chapter includes a recursive-iterative numerical integration method for the Schapery nonlinear viscoelastic 3D model that is used for the isotropic matrix in the micromodels. The third chapter describes a micromechanical model needed to generate the effective viscoelastic response of laminated composite materials and structures. Temperature and physical aging effects are also investigated. Experimental creep data for laminated composites from the literature is used to calibrate the in-situ properties and verify the prediction ability of the constitutive framework. The fourth chapter is concerned with developing a nested micromechanical and structural modeling framework for the viscoelastic behavior of pultruded composites. Short-term experimental creep tests with off-axis pultruded coupons are used to examine the ability of the proposed models in their prediction of multi-axial deformation states. The fifth chapter deals with implementation of the constitutive models with a FE code. Both 3D and shell based finite elements are employed in this study. Notched off-axis specimens are tested under compression and tension loads and the creep strain is compared with the FE results measured at different locations. In addition, creep responses on eccentrically-loaded-single-edge (tensile) ESE(T) pultruded specimens are aslo predicted. Applications of FE modeling approaches for the long-term behavior of laminated composite structures are performed. The next chapter deals with viscoelastic buckling and collapse of FRP composite structures. Conclusions and recommendations for future research are given in the last chapter.

CHAPTER II

A RECURSIVE-ITERATIVE NUMERICAL INTEGRATION FOR A CLASS OF NONLINEAR VISCOELASTIC MATERIAL MODELS

This chapter presents a numerical integration method for the 3D Schapery nonlinear viscoelastic constitutive material model based on the work of Haj-Ali and Muliana (2004). In the first section, the Schapery's viscoelastic material model, derived using the thermodynamics of irreversible processes (TIP), is described. A new recursive-iterative method is introduced next to integrate the Schapery single-integral constitutive model. The numerical formulation is well suited for a displacement-based nonlinear constitutive framework. The new numerical formulation is implemented within the ABAQUS general purpose FE code. The proposed recursive-iterative numerical integration was examined in terms of computational efficiency and accuracy. Finally, available experimental data with nonlinear response of PMMA polymeric material is used to examine the prediction of the proposed constitutive formulation.

2.1 Thermodynamics-Based Constitutive Formulation

An irreversible process of a continuum system is usually characterized by a change in they microstructure as a result of thermomechanical loading. The entropy always increases in an irreversible process (Clausius, 1850) and the energy dissipation is manifested by a change in temperature or heat rate. In thermodynamics, internal energy is measured by thermodynamic potentials, such as the Helmholtz free energy, enthalpy, and Gibbs free energy. Thermodynamics potentials can be expressed as functions of state variables, such as temperature, microstrcuture and damage parameter. The Helmholtz free energy is a portion of the

total internal energy produced by doing work at constant temperature and volume, while enthalpy is a portion of the internal energy that is released with heat or temperature for a volume change, and Gibbs free energy is the net energy in the system at certain temperature and pressure.

In order to characterize the state of a system, thermodynamic parameters, called state variables, are needed. The choice of a state variable depends on the physical phenomena of the system. Under isothermal conditions, the free energy of a continuum can be expressed as a function of the total strains or stresses and other possible internal state variables (ISVs). The Helmholtz free energy, ψ, is generally expressed in term of the total strain and ISVs, η_m:

$$\psi = \psi(\varepsilon, \eta_m) \quad , m = 1, 2, ...N \tag{2.1}$$

The rate of entropy production expressed in the Clausius-Duhem inequality is given by:

$$\sigma : \dot{\varepsilon} - \dot{\psi}(\varepsilon, \eta_m) \geq 0 \tag{2.2}$$

where σ is the second order stress tensor. The time derivation of the free energy is expressed by:

$$\dot{\psi} = \frac{\partial \psi}{\partial \varepsilon} : \dot{\varepsilon} + \frac{\partial \psi}{\partial \eta_m} \dot{\eta}_m \tag{2.3}$$

Substitute Eq. (2.3) into Eq. (2.2) gives:

$$\left(\sigma - \frac{\partial \psi}{\partial \varepsilon} \right) : \dot{\varepsilon} - \frac{\partial \psi}{\partial \eta_m} : \dot{\eta}_m \geq 0 \tag{2.4}$$

The local state law (Lemaitre and Chaboche, 1990) states that the behavior of a material at a given point is completely defined by the knowledge of its state variables at the current time. Therefore, $\dot{\varepsilon}$ can be taken as an arbitrarily variable and $\dot{\eta}_m$ is not dependent on the rate of entropy production, $\dot{S}$. Thus, the inequality in Eq. (2.4) leads to the following equations:

$$\sigma = \frac{\partial \psi}{\partial \varepsilon} = \sigma(\varepsilon, \eta_m) \tag{2.5}$$

$$\frac{\partial \psi}{\partial \eta_m} \dot{\eta}_m \leq 0 \tag{2.6}$$

The thermodynamic forces, f_m, are associated with the internal variables, η_m, and defined as:

$$f_m = \frac{\partial \psi}{\partial \eta_m} \tag{2.7}$$

The inverse of Helmholtz free energy is defined as Gibbs free energy (complementary energy) and is expressed in term of the stress tensor and other ISVs, ξ_m, as:

$$G \equiv \sigma : \varepsilon - \psi = G(\sigma, \xi_m) \tag{2.8}$$

The inequality similar to the one in Eq. (2.4) will lead to:

$$\varepsilon = \frac{\partial G}{\partial \sigma} = \varepsilon(\sigma, \xi_m) \tag{2.9}$$

$$\frac{\partial G}{\partial \xi_m} \dot{\xi}_m \geq 0 \tag{2.10}$$

$$f_m = \frac{\partial G}{\partial \xi_m} \tag{2.11}$$

A material, whose free energy (ψ or G) is independent of the ISVs, ξ_m, is elastic. For such material, with the energy balance equations, the inequalities in Eqs. (2.6) and (2.10) are trivially satisfied. The evolution of ISVs is defined by prescribing the rate $\dot{\xi}_m$ as a potential function of the stress. This can be generally expressed as:

$$\dot{\xi}_m = g_m(\sigma, \xi_n) \quad , n = 1, 2, ...N \tag{2.12}$$

The above equation determines the dissipative irreversible process. The potential functions g_m are usually smooth in terms of their dependent variables in the case of a viscoelastic material, Lubliner (1972).

The Schapery nonlinear viscoelastic model for an isotropic material is derived from the above TIP formulation with evolving ISVs (Schapery 1964, 1969, 1997). The constitutive model assumes small deformations. Isothermal conditions are assumed such that strains are the only observable state variables and temperature effects can be carried through the material properties. Moreover, the material is considered to be thermo-rheologically simple, in which time can be scaled with temperature and humidity functional. Thus, the mechanical behavior can be characterized through this reduced time. It is assumed that ISVs are associated with small energy changes, which allows expressing Gibbs free energy as a second order function in terms of its ISVs (Schapery 1997). This is generally expressed as:

$$G = G_0 - A_m \xi_m + \frac{1}{2} B_{mn} \xi_m \xi_n \tag{2.13}$$

where G_0, A_m, and B_{mn} are functions of the stresses (σ), temperatures (T), moistures (M) and possibly time (t) if aging effects are considered. The strain tensor is obtained by neglecting the second order terms of ξ_m in Eq. (2.13):

$$\varepsilon = -\frac{\partial G}{\partial \sigma} = -\frac{\partial G_0}{\partial \sigma} + \frac{\partial A_m}{\partial \sigma} \xi_m \tag{2.14}$$

In order to describe the changes in the ISVs, evolution equations are needed to define the relationship between the ISVs and the thermodynamic forces (stability conditions). These are the well-known Kuhn-Tucker conditions:

$$f_m \equiv -\frac{\partial G}{\partial \xi_m} = A_m - B_{mn} \xi_n \quad , \quad f_m \dot{\xi}_m \geq 0 \tag{2.15}$$

Following Schapery (1997), the strains in Eq. (2.14) may be represented schematically by a mechanical analogy consisting of springs and dashpots, as seen in Figure 2.1. Each ξ_m is proportional to the strain of a one cell (a spring with modulus E_m and a dasphot with viscosity η_m connected in parallel). The elastic strain of the spring with modulus E_0 is the term $-\frac{\partial G_0}{\partial \sigma}$ in Eq. (2.14). The second term $\frac{\partial A_m}{\partial \sigma} \xi_m$ represents the transient part.

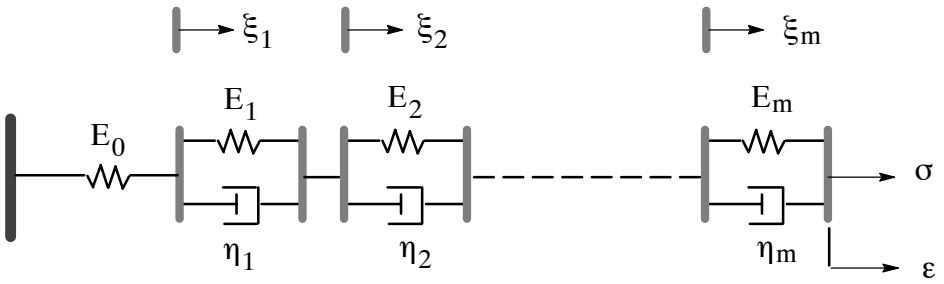

Figure 2.1 Schematic spring analogy (Generalized Voigt Model, Schapery 1997).

Next, an associate potential formulation is used, in Eq. (2.12), to relate the rate of ISVs to the thermodynamics forces:

$$\dot{\xi}_m \equiv g_m(\sigma, \xi_n) = -\frac{1}{a_1} C_{mn} \frac{\partial G}{\partial \xi_n} = \frac{1}{a_1} C_{mn} f_n \tag{2.16}$$

where C_{mn} is a constant, positive definite and symmetric matrix; a_1 is a positive scalar, which may be a function of σ, T, M, and other ISVs. At the reference state, a_1=1. The positive definite characteristic of C_{mn} insures that the free energy is minimum at equilibrium. The symmetry of C_{mn} comes from Onsager's principle (Lemaitre and Chaboche, 1990). Time dependence of a_1 is introduced explicitly in the case where physical aging is considered. Next, Eq. (2.16) can be rewritten as:

$$\dot{\xi}_m = \frac{1}{a_1} \frac{\partial F_v}{\partial f_m} \quad , \quad F_v \equiv \frac{1}{2} C_{mn} f_m f_n \tag{2.17}$$

The thermodynamic forces in Eq. (2.15) are combined with the inverse of Eq. (2.16), yields:

$$a_1 C_{mn}^{-1} \dot{\xi}_n = -\frac{\partial G}{\partial \xi_m} = f_m = A_m - B_{mn} \xi_n \tag{2.18}$$

Therefore,

$$a_1 C_{mn}^{-1} \dot{\xi}_n + B_{mn} \xi_n = A_m \tag{2.19}$$

and assuming:

$$B_{mn} = a_2 D_{mn} \tag{2.20}$$

where D_{mn} is a constant, positive definite, and symmetric matrix; a_2 is a positive scalar, which may be a function of σ, T, M, and other ISVs and a_2=1 at the reference state. Similar to C_{mn}, a positive definite charateristic of D_{mn} insures that free energy is minimum at equilibrium. Dividing Eq. (2.18) by a_2 and introducing a reduced time ψ and its rate $d\psi$, yield to:

$$\begin{gathered} C_{mn}^{-1} \frac{\partial \xi_m}{\partial \psi} + D_{mn}\xi_n = \frac{A_m}{a_2} \\ \text{where} \qquad d\psi \equiv \frac{a_2}{a_1} dt \qquad \psi \equiv \int_0^t \frac{a_2}{a_1} d\tau \end{gathered} \tag{2.21}$$

Since C_{mn} and D_{mn} are symmetric and positive definite matrices, it is always possible to diagonalize the above relations. Thus, another set of principal ISVs can be used to write uncoupled set of equations in terms of the new principal ISVs:

$$\frac{\partial \xi_m}{\partial \psi} + C_m D_m \xi_m = \frac{C_m A_m}{a_2} \tag{2.22}$$

The general solution of Eq. (2.22) is:

$$\begin{gathered} \xi_m = \frac{1}{D_m} \int_0^{\psi} \left[1 - \exp\left(\frac{-(\psi - \psi')}{\tau_m} \right) \right] \frac{d}{d\psi'} \left(\frac{A_m}{a_2} \right) d\psi' \\ \tau_m \equiv (C_m D_m)^{-1} \end{gathered} \tag{2.23}$$

where τ_m is a positive retardation time. The term ψ' is a function of time t', time at which the input function is applied.

Next, another simplification is introduced to allow the characterization of master creep functions and account for environmental and aging effects through a reduced time. The parameter A_m is assumed as:

$$A_m = E_m \hat{\sigma} + \alpha_m \phi \tag{2.24}$$

where E_m and α_m are constants. Stress dependent $\hat{\sigma}$ may be a function of σ, T, M, t, and possibly other variables that relate it to structural changes. In the linear viscoelastic range $\hat{\sigma}$ is a linear function of σ through coefficients that may depend on T, M, and t. The term ϕ accounts for thermal and moisture expansion effects. Thus, ϕ is equal to 0 at the reference state. Substituting Eqs. (2.24) and (2.23) into Eq. (2.14) yields:

$$\begin{aligned}\frac{\partial A_m}{\partial \sigma}\,\xi_m &= \frac{\partial}{\partial \sigma}\left(E_m\,\hat{\sigma} + \alpha_m\,\phi\right)\frac{1}{D_m}\int_0^{\psi}\left[1 - \exp\left(\frac{-(\psi-\psi')}{\tau_m}\right)\right]\frac{d}{d\psi'}\left(\frac{\left(E_m\,\hat{\sigma} + \alpha_m\,\phi\right)}{a_2}\right)d\psi' \\ &= \frac{\partial \hat{\sigma}}{\partial \sigma}\left(\Delta\hat{\varepsilon} + \Delta\hat{\alpha}\right) + \frac{\partial \phi}{\partial \sigma}\left(\Delta\hat{\hat{\varepsilon}} + \Delta\hat{\hat{\alpha}}\right)\end{aligned} \tag{2.25}$$

For simplicity, the dependence of ϕ on σ is excluded. If it is necessary to account for stress-dependent expansion in A_m, this can be done by modifying $\hat{\sigma}$. Thus, the terms $\Delta\hat{\varepsilon}$ and $\Delta\hat{\alpha}$ are:

$$\begin{aligned}\Delta\hat{\varepsilon} &\equiv \int_0^{\psi}\Delta S(\psi-\psi')\frac{d}{d\psi'}\left(\frac{\hat{\sigma}}{a_2}\right)d\psi' \\ \Delta S(\psi) &\equiv \sum_m \frac{E_m\,E_m}{D_m}\left(1 - \exp\left(-\frac{\psi}{\tau_m}\right)\right)\end{aligned} \tag{2.26}$$

$$\begin{aligned}\Delta\hat{\alpha} &\equiv \int_0^{\psi}\Delta\alpha(\psi-\psi')\frac{d}{d\psi'}\left(\frac{\phi}{a_2}\right)d\psi' \\ \Delta\alpha(\psi) &\equiv \sum_m \frac{E_m\,\alpha_m}{D_m}\left(1 - \exp\left(-\frac{\psi}{\tau_m}\right)\right)\end{aligned} \tag{2.27}$$

The terms ΔS and $\Delta\alpha$ are transient components of the mechanical and creep expansion compliances, respectively. The compliances in Eqs. (2.26) and (2.27) are dependent on the reduced time and lead the strain response to a unit value of $\frac{\hat{\sigma}}{a_2}$ and $\frac{\phi}{a_2}$. Therefore, it is appropriate to call them as master creep compliances. The total strains are then obtained by

substituting simplification of Eq. (2.25) into Eq. (2.14) and uses the definition of reduced time as in Eq. (2.21).

Consider a strain response due to a mechanical loading ($\hat{\sigma} = \sigma$) and introduce nonlinear parameters that reflect higher orders of the Gibb's free energy in terms of the applied stresses (Schapery 1969). The strain in Eq. (2.14) can be rewritten in order to incorporate nonlinear effects as:

$$\varepsilon^t \equiv \varepsilon(t) = g_0^{\sigma^t} D_0 \sigma^t + g_1^{\sigma^t} \int_0^t \Delta D^{(\psi^t - \psi^\tau)} \frac{d(g_2^{\sigma^\tau}\sigma^\tau)}{d\tau} d\tau \tag{2.28}$$

where D_0 is the instantaneous uniaxial elastic compliance, ΔD is the uniaxial transient compliance, g_0, g_1, g_2, and a_σ are the nonlinear parameters, and ψ is the reduced-time (effective time) given by:

$$\psi^t \equiv \psi(t) = \int_0^t \frac{d\xi}{a_\sigma^{\sigma^\xi} a_T a_e} \tag{2.29}$$

The upper right superscript of a given term is used to denote an explicit variable of this term or function. In general, the nonlinear material parameters: g_0, g_1, g_2, and a_σ can be dependent on the stress, temperature, moisture and possible other variables. With fixed environmental conditions the parameters: g_0, g_1, g_2, and a_σ are stress dependent only. These functions are always positive and equal to one for relatively small values of stress magnitudes (Boltzmann Integral in linear viscoelasticity). The parameter g_0 is the nonlinear instantaneous elastic compliance and measures the reduction or increase in stiffness. The transient creep parameter g_1 measures the nonlinearity effect in the transient compliance. The parameter g_2 accounts for the load rate effect on the creep response. The parameter a_σ acts as a stress dependent time-scaling factor. The function a_T is a temperature dependent that is used to define a time scale shift factor for thermorheologically simple material. The parameter

a_e is a time shift factor due to aging effects. The stress functions can also be temperature dependent which makes Eq. (2.28) represent the viscoelastic behavior of a thermorheologically complex material.

2.2 A Recursive-iterative Integration Method for Nonlinear Viscoelastic Response

A multi-axial nonlinear viscoelastic constitutive model for the isotropic matrix is formulated in this section. The Schapery (1969) single integral constitutive model is used for this purpose. A numerical integration, suitable for a displacement based FE material modeling environment (constant strain rate increment), is developed. Recurrence numerical algorithm for linear viscoelastic integral has been proposed by Taylor et al. (1970). The convolution integral is divided into recursive parts. This allows the incremental formulation and integration of the current stress state from the history variables stored at the previous time step with current variables, time and strain increments. Other similar recursive approaches were also applied to integrate the Schapery nonlinear viscoelastic model. Henriksen (1984), and Lai and Bakker (1996) used a similar recursive algorithm for the nonlinear constitutive integral. However, there are additional assumptions that are needed in order to use the same recurrence integration approach and apply it to the viscoelastic relations. These include the assumption that the term ($g_2^\tau \sigma^\tau$) has a constant derivative within the time increment and nonlinear parameters are constant over time increment. In general, this is not the case. Therefore, an iterative scheme should be employed in order to minimize this error, especially when the nonlinear viscoelastic integral is used to express the strains in terms of stress-based variables.

The current constitutive modeling approach modifies that of Lai and Bakker (1996). Additional nonlinear and iterative formulation is needed to complete the integration of the nonlinear viscoelastic model of Schapery. Furthermore, a consistent algorithmic tangent stiffness matrix is developed to enhance equilibrium and to help avoid misleading conver-

gent states. A suggested general polynomial form for the nonlinear parameters is proposed. Iterative correction algorithm is implemented and executed simultaneously at the constitutive level.

2.2.1 Uniaxial Stress-Strain Formulation

The uniaxial transient compliance ΔD, in Eq. (2.28), is expressed using a Prony series as:

$$\Delta D^{\psi^t} = \sum_{n=1}^{N} D_n \left(1 - \exp\left[-\lambda_n \psi^t\right]\right) \tag{2.30}$$

where D_n is the n^{th} coefficient of Prony series and λ_n is the n^{th} reciprocal of retardation time. An attempt will be made in the next equations to list the nonlinear functions and other terms with only dependent variable in the upper right superscript. Substitute Eq. (2.30) into Eq. (2.28) will give:

$$\varepsilon^t = g_0^t D_0 \sigma^t + g_1^t g_2^t \sigma^t \sum_{n=1}^{N} D_n - g_1^t \sum_{n=1}^{N} D_n q_n^t \tag{2.31}$$

$$q_n^t = \int_0^t \exp\left[-\lambda_n (\psi^t - \psi^\tau)\right] \frac{d(g_2^\tau \sigma^\tau)}{d\tau} d\tau \tag{2.32}$$

A recursive integration form can be obtained from Eq. (2.32) by dividing the integration into two parts. The first part includes the integral with limits (0, t-Δt), i.e. up to the previous time step. The limits of the second part are taken as (t-Δt, t), where t is the current time.

$$q_n^t = \int_0^{t-\Delta t} \exp\left[-\lambda_n(\psi^t - \psi^\tau)\right] \frac{d(g_2^\tau \sigma^\tau)}{d\tau} d\tau + \int_{t-\Delta t}^{t} \exp\left[-\lambda_n(\psi^t - \psi^\tau)\right] \frac{d(g_2^\tau \sigma^\tau)}{d\tau} d\tau \tag{2.33}$$

The reduced time increment is defined by:

$$\Delta\psi^t \equiv \psi^t - \psi^{t-\Delta t} \tag{2.34}$$

The first term of integral in Eq. (2.33) can be expressed by:

$$\int_0^{t-\Delta t} \exp[-\lambda_n(\psi^t - \psi^\tau)] \frac{d(g_2^\tau \sigma^\tau)}{d\tau} d\tau = \exp[-\lambda_n \Delta\psi^t] q_n^{t-\Delta t} \tag{2.35}$$

The second integral of Eq. (2.33) is carried out by parts while assuming that the term $(g_2^\tau \sigma^\tau)$ is linear over the current time step increment, Δt. Also, the shift function, a_σ, is not directly a function of time. The final result is written as:

$$\int_{t-\Delta t}^{t} \exp[-\lambda_n(\psi^t - \psi^\tau)] \frac{d(g_2^\tau \sigma^\tau)}{d\tau} d\tau = \frac{1 - \exp[-\lambda_n \Delta\psi^t]}{\lambda_n \Delta\psi^t} (g_2^t \sigma^t - g_2^{t-\Delta t} \sigma^{t-\Delta t}) \tag{2.36}$$

The $q_n^{t-\Delta t}$ term in Eq. (2.35) is the hereditary integral for every Prony series term at the end of previous time, t-Δt. These can be considered as history variables that need to be updated and stored at the end of each time increment. Substitute Eq. (2.35) and Eq. (2.36) into Eq. (2.33), the hereditary integral in Eq. (2.32) at the end of current time t can be obtained from:

$$q_n^t = \exp[-\lambda_n \Delta\psi^t] q_n^{t-\Delta t} + (g_2^t \sigma^t - g_2^{t-\Delta t} \sigma^{t-\Delta t}) \frac{1 - \exp[-\lambda_n \Delta\psi^t]}{\lambda_n \Delta\psi^t} \tag{2.37}$$

The current total strain is obtained by substituting Eq. (2.37) into Eq. (2.31):

$$\begin{aligned} \varepsilon^t = & \left[g_0^t D_0 + g_1^t g_2^t \sum_{n=1}^{N} D_n - g_1^t g_2^t \sum_{n=1}^{N} D_n \frac{1 - \exp[-\lambda_n \Delta\psi^t]}{\lambda_n \Delta\psi^t} \right] \sigma^t - \\ & g_1^t \sum_{n=1}^{N} D_n \left(\exp[-\lambda_n \Delta\psi^t] q_n^{t-\Delta t} - g_2^{t-\Delta t} (1 - \exp[-\lambda_n \Delta\psi^t]) \frac{\sigma^{t-\Delta t}}{\lambda_n \Delta\psi^t} \right) \\ \equiv & \overline{D}^t \sigma^t - f^t \end{aligned} \tag{2.38}$$

Substituting Eq. (2.37) into the second term in Eq. (2.38), allows term f^t to be rewritten as:

$$f^t = g_1^t \sum_{n=1}^{N} D_n \left[q_n^t - g_2^t \, \sigma^t \, \frac{1 - \exp[-\lambda_n \Delta\psi^t]}{\lambda_n \Delta\psi^t} \right] \tag{2.39}$$

The above equation allows for the incremental stress-strain calculation for a time increment Δt, which is then added to the total stress or strain from the previous time step, $t-\Delta t$. The incremental form of Eq. (2.39) is expressed as the following:

$$\begin{aligned} f^t - f^{t-\Delta t} &= g_1^t \sum_{n=1}^{N} D_n \left[q_n^t - g_2^t \, \sigma^t \, \frac{1 - \exp[-\lambda_n \Delta\psi^t]}{\lambda_n \Delta\psi^t} \right] - \\ &\quad g_1^{t-\Delta t} \sum_{n=1}^{N} D_n \left[q_n^{t-\Delta t} - g_2^{t-\Delta t} \, \sigma^{t-\Delta t} \, \frac{1 - \exp[-\lambda_n \Delta\psi^{t-\Delta t}]}{\lambda_n \Delta\psi^{t-\Delta t}} \right] \\ &= \sum_{n=1}^{N} D_n \left\{ \left(g_1^t \exp[-\lambda_n \Delta\psi^t] - g_1^{t-\Delta t} \right) q_n^{t-\Delta t} + \right. \\ &\quad \left. g_2^{t-\Delta t} \, \sigma^{t-\Delta t} \left(g_1^{t-\Delta t} \, \frac{1 - \exp[-\lambda_n \Delta\psi^{t-\Delta t}]}{\lambda_n \Delta\psi^{t-\Delta t}} - g_1^t \, \frac{1 - \exp[-\lambda_n \Delta\psi^t]}{\lambda_n \Delta\psi^t} \right) \right\} \end{aligned} \tag{2.40}$$

The current incremental strain is obtained by:

$$\begin{aligned} \Delta\varepsilon^t &= \varepsilon^t - \varepsilon^{t-\Delta t} = \left(\overline{D}^t \, \sigma^t - \overline{D}^{t-\Delta t} \, \sigma^{t-\Delta t} \right) - (f^t - f^{t-\Delta t}) \\ &= \overline{D}^t \, \sigma^t - \overline{D}^{t-\Delta t} \, \sigma^{t-\Delta t} - \sum_{n=1}^{N} D_n \left(g_1^t \exp[-\lambda_n \Delta\psi^t] - g_1^{t-\Delta t} \right) q_n^{t-\Delta t} - \\ &\quad g_2^{t-\Delta t} \sum_{n=1}^{N} D_n \left[g_1^{t-\Delta t} \left(\frac{1 - \exp[-\lambda_n \Delta\psi^{t-\Delta t}]}{\lambda_n \Delta\psi^{t-\Delta t}} \right) - g_1^t \left(\frac{1 - \exp[-\lambda_n \Delta\psi^t]}{\lambda_n \Delta\psi^t} \right) \right] \sigma^{t-\Delta t} \end{aligned} \tag{2.41}$$

2.2.2 Multiaxial Stress-Strain Formulation

The previous numerical formulations for uniaxial viscoelastic behavior are now used and generalized in the multiaxial 3D constitutive relations for the isotropic matrix medium. To that end, the deviatoric and volumetric strain-stress relations are decoupled. Stress compo-

nents are chosen as the independent state variables. The formulation further assumes that the incremental total strain is known. Hence the numerical formulation is carried out with a constant strain rate. This is consistent with many nonlinear constitutive models implemented within a displacement-based finite element.

The strain responses for the isotropic materials are decoupled into deviatoric and volumetric parts and are expressed as:

$$\varepsilon_{ij} = \frac{1}{2G} S_{ij} + \frac{1}{3} \frac{\sigma_{kk}}{3K} \delta_{ij} = \frac{1}{2} J\, S_{ij} + \frac{1}{3} B\, \sigma_{kk} \delta_{ij} \tag{2.42}$$

Where G and K are shear modulus and bulk modulus, respectively, which can be converted into shear compliance J and bulk compliance B. S_{ij} is the deviatoric stress and σ_{kk} is the volumetric stress.

The Schapery integral constitutive model is applied twice for the deviatoric and volumetric strains in the general forms:

$$e_{ij}^{t} = \frac{1}{2}\, g_0^t\, J_0\, S_{ij}^t + \frac{1}{2}\, g_1^t \int_0^t \Delta J^{(\psi^t - \psi^\tau)} \frac{d(g_2^\tau\, S_{ij}^\tau)}{d\tau}\, d\tau \tag{2.43}$$

$$\varepsilon_{kk}^{t} = \frac{1}{3}\, g_0^t\, B_0\, \sigma_{kk}^t + \frac{1}{3}\, g_1^t \int_0^t \Delta B^{(\psi^t - \psi^\tau)} \frac{d(g_2^\tau\, \sigma_{kk}^\tau)}{d\tau}\, d\tau \tag{2.44}$$

The nonlinear parameters are assumed to be general polynomial functions of the effective octahedral stress, and expressed as:

$$g_j = 1 + \sum_{i=1}^{ng_j} \alpha_j^i \left\langle \frac{\bar{\sigma}}{\bar{\sigma}_o} - 1 \right\rangle^i \qquad a_\sigma = 1 + \sum_{i=1}^{na_\sigma} \delta_i \left\langle \frac{\bar{\sigma}}{\bar{\sigma}_o} - 1 \right\rangle^i$$

$$j = 0, 1, 2 \tag{2.45}$$

$$\psi^t = \frac{t}{a_\sigma} \qquad \text{where} \qquad < x > = \begin{cases} x\ , & x > 0 \\ 0\ , & x \le 0 \end{cases}$$

where $(\alpha_j^i\,,\ \delta_i)$ are the calibrated coefficients, $\bar{\sigma}_o$ is the effective stress limit that determines the end of the linear viscoelastic range. A constant value can be assumed to determine the nonlinear parameters for the effective stress beyond the calibration range. The constant nonlinear parameters will help the convergence at the out of range calibration, although it may not provide the correct nonlinear parameters for a given effective stress. J_0 and B_0 are the instantaneous elastic shear and bulk compliances, respectively. The terms ΔJ and ΔB are the transient shear and bulk compliances, respectively. Next, we further assume that the matrix Poisson's ratio, ν, is time independent. This allows expressing the two integrals in Eqs. (2.43) and (2.44) as a function of one hereditary integral:

$$\begin{aligned}\varepsilon_{ij}^t = e_{ij}^t + \frac{1}{3}\,\varepsilon_{kk}^t\,\delta_{ij} = \\ (1+\nu)\,D_0\,g_0^t\,S_{ij}^t + (1+\nu)\,g_1^t \int_0^t \Delta D^{(\psi^t-\psi^\tau)}\,\frac{d(g_2^\tau\,S_{ij}^\tau)}{d\tau}\,d\tau\ + \\ \frac{(1-2\nu)}{3}\delta_{ij}\left[D_0\,g_0^t\,\sigma_{kk}^t + g_1^t\int_0^t \Delta D^{(\psi^t-\psi^\tau)}\,\frac{d(g_2^\tau\,\sigma_{kk}^\tau)}{d\tau}\,d\tau\right]\end{aligned} \tag{2.46}$$

Comparing the terms in Eqs. (2.43) and (2.44) with those in Eq. (2.46) yields:

$$\begin{aligned} J_0 &= 2(1+\nu)D_0 & B_0 &= 3(1-2\nu)D_0 \\ \Delta J(\psi) &= 2(1+\nu)\,\Delta D(\psi) & \Delta B(\psi) &= 3(1-2\nu)\,\Delta D(\psi)\end{aligned} \tag{2.47}$$

Equations (2.43) and (2.44) are rewritten in term of hereditary integral formulation as of Eq. (2.38):

$$\begin{aligned} e_{ij}^t = \frac{1}{2}\left[g_0^t J_0 + g_1^t g_2^t \sum_{n=1}^N J_n - g_1^t g_2^t \sum_{n=1}^N J_n\,\frac{1-\exp[-\lambda_n\,\Delta\psi^t]}{\lambda_n\,\Delta\psi^t}\right] S_{ij}^t - \\ \frac{1}{2}\,g_1^t \sum_{n=1}^N J_n\left[\exp[-\lambda_n\,\Delta\psi^t]\,q_{ij,n}^{t-\Delta t} - g_2^{t-\Delta t}\,\frac{(1-\exp[-\lambda_n\,\Delta\psi^t])}{\lambda_n\,\Delta\psi^t}\,S_{ij}^{t-\Delta t}\right] \\ \equiv \bar{J}^t\,S_{ij}^t - d_{ij}^t\end{aligned} \tag{2.48}$$

$$\varepsilon_{kk}^{t} = \frac{1}{3}\left[g_0^t B_0 + g_1^t g_2^t \sum_{n=1}^{N} B_n - g_1^t g_2^t \sum_{n=1}^{N} B_n \frac{1 - \exp[-\lambda_n \Delta\psi^t]}{\lambda_n \Delta\psi^t} \right] \sigma_{kk}^{t} - \frac{1}{3} g_1^t \sum_{n=1}^{N} B_n \left[\exp[-\lambda_n \Delta\psi^t] q_{kk,n}^{t-\Delta t} - g_2^{t-\Delta t} \frac{(1 - \exp[-\lambda_n \Delta\psi^t])}{\lambda_n \Delta\psi^t} \sigma_{kk}^{t-\Delta t} \right] \equiv \overline{B}^t \sigma_{kk}^t - v_{kk}^t \quad (2.49)$$

Equations (2.48) and (2.49) are used with some algebraic manipulations as in Eq. (2.41) to derive the equations for the incremental deviatoric and volumetric strains. These are written as:

$$\Delta e_{ij}^t = e_{ij}^t - e_{ij}^{t-\Delta t} = \overline{J}^t S_{ij}^t - \overline{J}^{t-\Delta t} S_{ij}^{t-\Delta t} - \frac{1}{2} \sum_{n=1}^{N} J_n (g_1^t \exp[-\lambda_n \Delta\psi^t] - g_1^{t-\Delta t}) q_{ij,n}^{t-\Delta t} - \frac{1}{2} g_2^{t-\Delta t} \sum_{n=1}^{N} J_n \left[g_1^{t-\Delta t} \left(\frac{1 - \exp[-\lambda_n \Delta\psi^{t-\Delta t}]}{\lambda_n \Delta\psi^{t-\Delta t}} \right) - g_1^t \left(\frac{1 - \exp[-\lambda_n \Delta\psi^t]}{\lambda_n \Delta\psi^t} \right) \right] S_{ij}^{t-\Delta t} \quad (2.50)$$

$$\Delta\varepsilon_{kk}^t = \varepsilon_{kk}^t - \varepsilon_{kk}^{t-\Delta t} = \overline{B}^t \sigma_{kk}^t - \overline{B}^{t-\Delta t} \sigma_{kk}^{t-\Delta t} - \frac{1}{3} \sum_{n=1}^{N} B_n (g_1^t \exp[-\lambda_n \Delta\psi^t] - g_1^{t-\Delta t}) q_{kk,n}^{t-\Delta t} - \frac{1}{3} g_2^{t-\Delta t} \sum_{n=1}^{N} B_n \left[g_1^{t-\Delta t} \left(\frac{1 - \exp[-\lambda_n \Delta\psi^{t-\Delta t}]}{\lambda_n \Delta\psi^{t-\Delta t}} \right) - g_1^t \left(\frac{1 - \exp[-\lambda_n \Delta\psi^t]}{\lambda_n \Delta\psi^t} \right) \right] \sigma_{kk}^{t-\Delta t} \quad (2.51)$$

$q_{ij,n}^{t-\Delta t}$ and $q_{kk,n}^{t-\Delta t}$ are the shear and volumetric hereditary integral for every Prony series term at the end of previous time, t-Δt. At the end of each time integration, the hereditary integrals in each Prony series are updated and stored in order to be used in the next time integration step. These are:

$$q_{ij,n}^t = \exp[-\lambda_n \Delta\psi^t] q_{ij,n}^{t-\Delta t} + (g_2^t S_{ij}^t - g_2^{t-\Delta t} S_{ij}^{t-\Delta t}) \frac{1 - \exp[-\lambda_n \Delta\psi^t]}{\lambda_n \Delta\psi^t} \quad (2.52)$$

$$q^{t}_{kk,n} = \exp\left[-\lambda_n \Delta\psi^t\right] q^{t-\Delta t}_{kk,n} + \left(g^{t}_{2}\,\sigma^{t}_{kk} - g^{t-\Delta t}_{2}\,\sigma^{t-\Delta t}_{kk}\right) \frac{1-\exp\left[-\lambda_n \Delta\psi^t\right]}{\lambda_n \Delta\psi^t} \tag{2.53}$$

Equations (2.50) and (2.51) are used to determine the unknown stress increment for a given strain increment and the previous history state, i.e. $q^{t-\Delta t}_{ij,n}$ and $q^{t-\Delta t}_{kk,n}$, n=1..N. The problem is that the nonlinear stress functions at the current time t are not known. Therefore, an iterative method is needed in order to find the correct stress. To that end, Eqs. (2.50) and (2.51) are further linearized and expression for approximate or trial incremental stresses is generated using the following approximations:

$$\begin{aligned} g^{t}_{\alpha} &= g^{t-\Delta t}_{\alpha} \quad ; \; \alpha = 0, 1, 2 \\ \Delta\psi^{t} &= \Delta\psi^{t-\Delta t} \end{aligned} \tag{2.54}$$

The iterative scheme for determining the stress increment starts with a trial stress-based on Eqs. (2.50) and (2.51), and is expressed by:

$$\Delta S^{t,tr}_{ij} = \frac{1}{\bar{J}^{t,tr}} \left[\Delta e^{t}_{ij} + \frac{1}{2}\, g^{t,tr}_{1} \sum_{n=1}^{N} J_n \left(\exp\left[-\lambda_n \Delta\psi^t\right] - 1\right) q^{t-\Delta t}_{ij,n} \right] \tag{2.55}$$

$$\Delta\sigma^{t,tr}_{kk} = \frac{1}{\bar{B}^{t,tr}} \left[\Delta\varepsilon^{t}_{kk} + \frac{1}{3}\, g^{t,tr}_{1} \sum_{n=1}^{N} B_n \left(\exp\left[-\lambda_n \Delta\psi^t\right] - 1\right) q^{t-\Delta t}_{kk,n} \right] \tag{2.56}$$

The terms $\bar{J}^{t,tr}$ and $\bar{B}^{t,tr}$ are the same as in Eqs. (2.48) and (2.49), respectively, but with the nonlinear parameters: g_0, g_1, g_2, and a_σ are functions of the current trial effective stress. Equations (2.55) and (2.56) are identical to the linearized relations developed by Lai and Bakker (1996).

In this study an iterative scheme is developed in order to arrive at the correct stress state for a given strain increment. Otherwise, the strain and time increments may have to be very small in order to maintain accurate stress updates and minimize the errors due to the approxi-

mations in Eq. (2.54). The residual equations can be defined by using either the incremental strains, Eqs. (2.50) and (2.51), or total strains, Eqs. (2.48) and (2.49), respectively. These equations can be combined to form the residual strain errors from the deviatoric and volumetric residuals. This is expressed by:

$$
\begin{aligned}
R_{ij}^{t} &= \Delta e_{ij}^{t} + \frac{1}{3}\Delta\varepsilon_{kk}^{t}\,\delta_{ij} - \Delta\varepsilon_{ij}^{t} \\
&= \bar{J}^{t}\,\sigma_{ij}^{t} + \frac{1}{3}\left(\bar{B}^{t} - \bar{J}^{t}\right)\sigma_{kk}^{t}\,\delta_{ij} - \bar{J}^{t-\Delta t}\,\sigma_{ij}^{t-\Delta t} - \frac{1}{3}\left(\bar{B}^{t-\Delta t} - \bar{J}^{t-\Delta t}\right)\sigma_{kk}^{t-\Delta t}\,\delta_{ij} - \\
&\quad \left\{ \frac{1}{2}\sum_{n=1}^{N} J_n\left(g_1^{t}\,\exp\left[-\lambda_n\,\Delta\psi^{t}\right] - g_1^{t-\Delta t}\right) q_{ij,n}^{t-\Delta t} + \right. \\
&\quad \frac{1}{9}\left[\sum_{n=1}^{N} B_n\left(g_1^{t}\,\exp\left[-\lambda_n\,\Delta\psi^{t}\right] - g_1^{t-\Delta t}\right) q_{kk}^{t-\Delta t}\right]\delta_{ij} + \\
&\quad \frac{1}{2}\,g_2^{t-\Delta t}\sum_{n=1}^{N} J_n\left[g_1^{t-\Delta t}\left(\frac{1-\exp\left[-\lambda_n\,\Delta\psi^{t-\Delta t}\right]}{\lambda_n\,\Delta\psi^{t-\Delta t}}\right) - g_1^{t}\left(\frac{1-\exp\left[-\lambda_n\,\Delta\psi^{t}\right]}{\lambda_n\,\Delta\psi^{t}}\right)\right] S_{ij}^{t-\Delta t} + \\
&\quad \left.\frac{1}{9}\,g_2^{t-\Delta t}\sum_{n=1}^{N} B_n\left[g_1^{t-\Delta t}\left(\frac{1-\exp\left[-\lambda_n\,\Delta\psi^{t-\Delta t}\right]}{\lambda_n\,\Delta\psi^{t-\Delta t}}\right) - g_1^{t}\left(\frac{1-\exp\left[-\lambda_n\,\Delta\psi^{t}\right]}{\lambda_n\,\Delta\psi^{t}}\right)\right]\delta_{ij}\,\sigma_{kk}^{t-\Delta t}\right\} \\
&\quad - \Delta\varepsilon_{ij}^{t}
\end{aligned}
\tag{2.57}
$$

A jacobian matrix is formed by taking the derivative of the residual vector with respect to the incremental stress vector as:

$$
\begin{aligned}
\frac{\partial R_{ij}^{t}}{\partial \Delta\sigma_{kl}^{t}} &= \bar{J}^{t}\,\delta_{ik}\,\delta_{jl} + \frac{1}{3}\left(\bar{B}^{t} - \bar{J}^{t}\right)\delta_{ij}\,\delta_{kl} + \\
&\frac{\partial \Delta\bar{\sigma}^{t}}{\partial \Delta\sigma_{kl}^{t}}\left\{ \frac{\partial \bar{J}^{t}}{\partial \Delta\bar{\sigma}^{t}}\,\sigma_{ij}^{t} + \frac{1}{3}\left(\frac{\partial \bar{B}^{t}}{\partial \Delta\bar{\sigma}^{t}} - \frac{\partial \bar{J}^{t}}{\partial \Delta\bar{\sigma}^{t}}\right)\sigma_{kk}^{t}\,\delta_{ij} - \right. \\
&\frac{1}{2}\,\frac{\partial g_{1}^{t}}{\partial \Delta\bar{\sigma}^{t}}\sum_{n=1}^{N} J_{n}\left[\exp\left[-\lambda_{n}\,\Delta\psi^{t}\right] q_{ij,n}^{t-\Delta t} - g_{2}^{t-\Delta t}\left(\frac{1-\exp\left[-\lambda_{n}\,\Delta\psi^{t}\right]}{\lambda_{n}\,\Delta\psi^{t}}\right) S_{ij}^{t-\Delta t}\right] - \\
&\frac{1}{2}\,\frac{\partial a_{\sigma}^{t}}{\partial \Delta\bar{\sigma}^{t}}\,g_{1}^{t}\sum_{n=1}^{N} J_{n}\left[\exp\left[-\lambda_{n}\,\Delta\psi^{t}\right]\left(\frac{\lambda_{n}\,\Delta t\, q_{ij,n}^{t-\Delta t}}{a_{\sigma}^{t\,2}} + \frac{S_{ij}^{t-\Delta t}}{a_{\sigma}^{t}}\right) - \right. \\
&\qquad\left. g_{2}^{t-\Delta t}\left(\frac{1-\exp\left[-\lambda_{n}\,\Delta\psi^{t}\right]}{\lambda_{n}\,\Delta\psi^{t}}\right) S_{ij}^{t-\Delta t}\right] - \\
&\frac{1}{9}\,\frac{\partial g_{1}^{t}}{\partial \Delta\bar{\sigma}^{t}}\sum_{n=1}^{N} B_{n}\left[\exp\left[-\lambda_{n}\,\Delta\psi^{t}\right] q_{kk,n}^{t-\Delta t} - g_{2}^{t-\Delta t}\left(\frac{1-\exp\left[-\lambda_{n}\,\Delta\psi^{t}\right]}{\lambda_{n}\,\Delta\psi^{t}}\right)\sigma_{kk}^{t-\Delta t}\right]\delta_{ij} - \\
&\frac{1}{9}\,\frac{\partial a_{\sigma}^{t}}{\partial \Delta\bar{\sigma}^{t}}\,g_{1}^{t}\sum_{n=1}^{N} B_{n}\left[\exp\left[-\lambda_{n}\,\Delta\psi^{t}\right]\left(\frac{\lambda_{n}\,\Delta t\, q_{kk,n}^{t-\Delta t}}{a_{\sigma}^{t\,2}} + \frac{\sigma_{kk}^{t-\Delta t}}{a_{\sigma}^{t}}\right) - \right. \\
&\qquad\left.\left. g_{2}^{t-\Delta t}\left(\frac{1-\exp\left[-\lambda_{n}\,\Delta\psi^{t}\right]}{\lambda_{n}\,\Delta\psi^{t}}\right)\sigma_{kk}^{t-\Delta t}\right]\delta_{ij}\right\} \\
\text{where}\quad &\frac{\partial \Delta\bar{\sigma}^{t}}{\partial \Delta\sigma_{kl}^{t}} = \frac{3}{2}\,\frac{S_{ij}^{t}}{\Delta\bar{\sigma}^{t}}\left(\delta_{ik}\,\delta_{jl} - \frac{1}{3}\,\delta_{ij}\,\delta_{kl}\right)
\end{aligned}
\tag{2.58}
$$

Linearization of the residual allows forming a system of linear equation that can be solved to obtain an updated trial stress that is used iteratively until a satisfied level of residual norm can be tolerated. Once convergence has been achieved, the stress and the hereditary integrals for each Prony series are calculated and stored for next time step integration. Next, we can define a consistent tangent compliance by taking the partial derivative of the incremental strain with respect to the incremental stress at the end of the current time step. Using Eq. (2.58), the consistent tangent compliance matrix, $\dot{S}_{ijkl}^{t}$, at the converged state, is:

$$
\dot{S}_{ijkl}^{t} \equiv \frac{\partial \Delta\varepsilon_{ij}^{t}}{\partial \Delta\sigma_{kl}^{t}} = \frac{\partial R_{ij}^{t}}{\partial \Delta\sigma_{kl}^{t}} \quad ; \quad \left\| R_{ij}^{t} \right\| \to 0 \tag{2.59}
$$

The complete numerical algorithm, which is used to provide the correct stress and its corresponding nonlinear parameters for a given strain increment, is presented in Figure 2.2. This numerical method is suitable for displacement based FE environment.

1. Input variables

$\Delta\varepsilon_{ij}^{t}$, Δt History : $\sigma_{ij}^{t-\Delta t}$, $q_{ij,n}^{t-\Delta t}$, $q_{kk,n}^{t-\Delta t}$

2. Initialize linear elastic state

$$g_{\beta}^{t} = g_{\beta}^{t-\Delta t} \;;\; \beta = 0, 1, 2 \qquad \Delta\psi^{t} = \Delta\psi^{t-\Delta t}$$

$$\bar{J}^{t,tr} = \bar{J}^{t}\left(g_{\beta}^{t}, \Delta\psi^{t}\right) \qquad \bar{B}^{t,tr} = \bar{B}^{t}\left(g_{\beta}^{t}, \Delta\psi^{t}\right)$$

$$\Delta\sigma_{ij}^{t,tr} = \Delta\sigma_{ij}^{t,tr}\left(\Delta S_{ij}^{t,tr}, \Delta\sigma_{kk}^{t,tr}\right)$$

$$\sigma_{ij}^{t,(0)} = \sigma_{ij}^{t-\Delta t} + \Delta\sigma_{ij}^{t,tr}$$

3. Iterate for k=1, 2, 3 ....

3.1 Compute nonlinear parameters

$$g_{\beta}^{t,(k)} = 1 + \sum_{i=1}^{ng_{\beta}} \alpha_{\beta}^{i} \left\langle \frac{\bar{\sigma}^{(k)}}{\sigma_{o}} - 1 \right\rangle^{i} \;;\; \beta = 0, 1, 2$$

$$a_{\sigma}^{t,(k)} = 1 + \sum_{i=1}^{na_{\sigma}} \delta_{i} \left\langle \frac{\bar{\sigma}^{(k)}}{\sigma_{o}} - 1 \right\rangle^{i}$$

3.2 Compute stress correction

$$\Delta\sigma_{ij}^{t,(k+1)} = \Delta\sigma_{ij}^{t,(k)} + \left[\frac{\partial R_{ij}^{t,(k)}}{\partial\Delta\sigma_{kl}}\right]^{-1} R_{kl}^{t,(k)}$$

$$\sigma_{ij}^{t,(k+1)} = \sigma_{ij}^{t,(k)} + \Delta\sigma_{ij}^{t,(k+1)}$$

3.1 Evaluate residual strain

$$R_{ij}^{t,(k)} = \Delta e_{ij}^{t,(k)} + \frac{1}{3}\,\delta_{ij}\,\Delta\varepsilon_{kk}^{t,(k)} - \Delta\varepsilon_{ij}^{t}$$

IF $\| R^{t,(k)} \| \leq$ Tol THEN GOTO 4 and EXIT

ENDIF GOTO 3

4. Update stress, consistent tangent stiffness, and history variables

$$\sigma_{ij}^{t} \leftarrow \sigma_{ij}^{t,(k+1)} \qquad C_{ij}^{t} \leftarrow \left[\frac{\partial R_{ij}^{t,(k)}}{\partial\Delta\sigma_{kl}}\right]^{-1} \qquad q_{ij,n}^{t} \leftarrow q_{ij,n}^{t,(k+1)} \qquad q_{kk,n}^{t} \leftarrow q_{kk,n}^{t,(k+1)}$$

Figure 2.2 Recursive-iterative algorithm for the nonlinear isotropic viscoelastic model.

2.3 A Numerical Integration Method that Includes Aging Effects

In this section, the previous viscoelastic nonlinear model is generalized to include physical aging which can have different effects on both the elastic and transient creep compliances. Therefore, the elastic and transient creep responses due to aging are characterized independently. The material becomes stiffer during the aging process, (Struik, 1978), and an exponential function in term of aging time can be chosen to model the changes in the material stiffness. It is assumed in this study that there is no physical aging effect on the Poisson's ratio. The transient creep strain that carries the aging effect is computed in the effective time-scale domain, λ, as proposed by Struik (1978). The strains can be mapped back to the real time scale, t, to predict the long-term creep response due to physical aging.

The time interval, dt, is related to the effective time interval, $d\lambda$, by the acceleration factor, a_{te}, which can be expressed, at any time as:

$$d\lambda = a_{t_e}(t)\, dt \tag{2.60}$$

$$a_{t_e}(t) = \left(\frac{t_e}{t_e + t}\right)^{\mu} \tag{2.61}$$

where t_e is the aging time at the start of the test, measured from the time when the material is rapidly cooled down below its glass transition temperature, T_g. The momentary creep compliance curve can be constructed through horizontal shifting in the logarithmic scale of creep compliance curves at different aging times. The logarithmic shift rate, μ, is defined as:

$$\mu = -\frac{d \log a_{t_e}}{d \log t_e} \tag{2.62}$$

The total effective time is then reduced to:

$$\lambda = \int_0^t a_{t_e}(\xi)\, d\xi \qquad \lambda = \begin{cases} t_e \ln\left(1 + \dfrac{t}{t_e}\right), & \mu = 1 \\ \dfrac{t_e}{1-\mu}\left[\left(1 + \dfrac{t}{t_e}\right)^{\mu} - 1\right], & \mu \neq 1 \end{cases} \tag{2.63}$$

where ξ is an integration variable for the time scale.

Following the work by Pasricha et al. (1997), the effect of physical aging is incorporated into the Schapery constitutive model by calculating creep response in the effective time scale, λ. Thus, the integrations in Eqs. (2.43) and (2.44) are carried over the λ domain. The terms, which are involving the current incremental time, Δt, are mapped to the incremental effective time, $\Delta\lambda$. Thus, the hereditary integrals in Eqs. (2.52) and (2.53) are expressed at the end of the current effective time λ by:

$$q_{ij,n}^{\lambda} = \exp[-\lambda_n \Delta\psi^{\lambda}]\, q_{ij,n}^{\lambda-\Delta\lambda} + (g_2^t S_{ij}^t - g_2^{t-\Delta t} S_{ij}^{t-\Delta t}) \frac{1 - \exp[-\lambda_n \Delta\psi^{\lambda}]}{\lambda_n \Delta\psi^{\lambda}} \tag{2.64}$$

$$q_{kk,n}^{\lambda} = \exp[-\lambda_n \Delta\psi^{\lambda}]\, q_{kk,n}^{\lambda-\Delta\lambda} + (g_2^t \sigma_{kk}^t - g_2^{t-\Delta t} \sigma_{kk}^{t-\Delta t}) \frac{1 - \exp[-\lambda_n \Delta\psi^{\lambda}]}{\lambda_n \Delta\psi^{\lambda}} \tag{2.65}$$

where the reduced effective time increment is:

$$\Delta\psi^{\lambda} \equiv \psi^{\lambda} - \psi^{\lambda-\Delta\lambda}$$
$$\psi^{\lambda} = \int_0^{\lambda} \frac{d\xi}{a_\sigma a_T} \tag{2.66}$$

The deviatoric and volumetric creep strains in Eqs. (2.48) and (2.49) are rewritten to incorporate the physical aging effect as:

$$e_{ij}^{t} = \frac{1}{2}\left[g_0^t J_0 + g_1^t g_2^t \sum_{n=1}^{N} J_n - g_1^t g_2^t \sum_{n=1}^{N} J_n \frac{1 - \exp[-\lambda_n \Delta\psi^{\lambda}]}{\lambda_n \Delta\psi^{\lambda}} \right] S_{ij}^{t} - \frac{1}{2} g_1^t \sum_{n=1}^{N} J_n \left[\exp[-\lambda_n \Delta\psi^{\lambda}] q_{ij,n}^{\lambda-\Delta\lambda} - g_2^{t-\Delta t} \frac{(1 - \exp[-\lambda_n \Delta\psi^{\lambda}])}{\lambda_n \Delta\psi^{\lambda}} S_{ij}^{t-\Delta t} \right] \tag{2.67}$$

$$\varepsilon_{kk}^{t} = \frac{1}{3}\left[g_0^t B_0 + g_1^t g_2^t \sum_{n=1}^{N} B_n - g_1^t g_2^t \sum_{n=1}^{N} B_n \frac{1 - \exp[-\lambda_n \Delta\psi^{\lambda}]}{\lambda_n \Delta\psi^{\lambda}} \right] \sigma_{kk}^{t} - \frac{1}{3} g_1^t \sum_{n=1}^{N} B_n \left[\exp[-\lambda_n \Delta\psi^{\lambda}] q_{kk,n}^{\lambda-\Delta\lambda} - g_2^{t-\Delta t} \frac{(1 - \exp[-\lambda_n \Delta\psi^{\lambda}])}{\lambda_n \Delta\psi^{\lambda}} \sigma_{kk}^{t-\Delta t} \right] \tag{2.68}$$

2.4 Implementation of the Recursive-iterative Algorithm for the Viscoelastic Response of a Glassy Amorphous Polymer PMMA

The proposed numerical constitutive model is implemented within a displacement-based FE code. The material subroutine (UMAT) of the ABAQUS (2002) FE code is used for this purpose. The 3D viscoelastic response is generated at each material point (Gaussian integration point). Calibration and verification of the proposed numerical model are performed with test results on glassy amorphous polymer material (PMMA) reported by Lai and Bakker (1996). The calibrated elastic compliance and Prony parameters are given in Table 2.1. The polynomial stress-dependent nonlinear functions in the Schapery equation are determined from the experimental test, as shown in Figure 2.3. The effective stress that determines the limit of the linear response, $\bar{\sigma}_o$, is 20 MPa. The polynomial coefficients are calibrated from the experimental data where the range of the effective stress is 0-40 MPa. Fourth-order polynomials, Eq. (2.45), are sufficient in calibrating the nonlinear stress-dependent parameters. The accuracy of these polynomial functions is within this range; beyond this stress level the polynomial functions may not represent the actual behavior of the material. The calibrated polynomial coefficients for all nonlinear parameters are shown in Table 2.2.

Table 2.1 Prony series coefficients for the PMMA polymer (Lai and Bakker, 1996).

n	λ_n (sec^{-1})	D_n x 10^{-6}(MPa^{-1})
1	1	23.6358
2	10^{-1}	5.6602
3	10^{-2}	14.8405
4	10^{-3}	18.8848
5	10^{-4}	28.5848
6	10^{-5}	40.0569
7	10^{-6}	60.4235
8	10^{-7}	79.6477
9	10^{-8}	162.1790
D_o	270.9 x 10^{-6}(MPa^{-1})	

Table 2.2 Calibrated nonlinear viscoelastic coefficients for the PMMA polymer.

g_j \ α_j^i	α_j^1	α_j^2	α_j^3	α_j^4
g_0	0.183	0.567	-1.067	0.533
g_1	0.067	0.133	2.133	-2.133
g_2	-0.773	9.707	-15.787	8.533

a_σ	δ_1	δ_2	δ_3	δ_4
	-0.373	2.580	-5.227	3.520

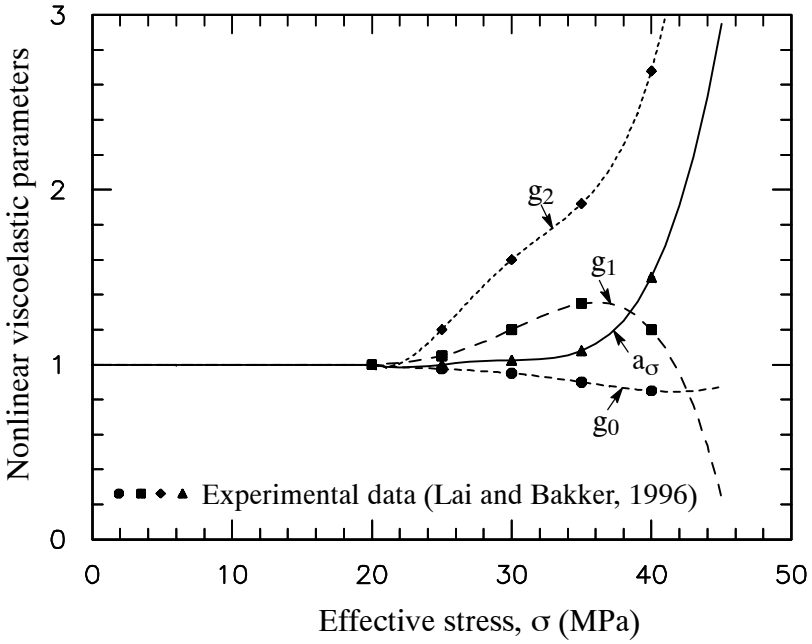

Figure 2.3 Nonlinear stress-dependent parameters in the Schapery's equations for PMMA polymer.

Parametric studies

The first parametric study is carried in order to determine the range of initial time increment that can be used to simulate a Heaviside step function and to examine the effect of using different initial time increments on the instantaneous material response with varying stress levels. The recursive-iterative viscoelastic material model is used. Total uniaxial strain values are reported for different time-increment sizes and are compared with the analytical solution for several load levels: 10 MPa - 40 MPa, as shown in Figure 2.4. The initial time-increment size can affect the accuracy of the results and a large time-increment may lead to a diverged solution. The divergence from the elastic response occurs either with increasing applied stress levels or with large initial time increments. As a results, it is concluded that an initial time increment can be chosen in the range: 10^{-5} to 10^{-2} seconds in order to represent an instantaneous response for this material.

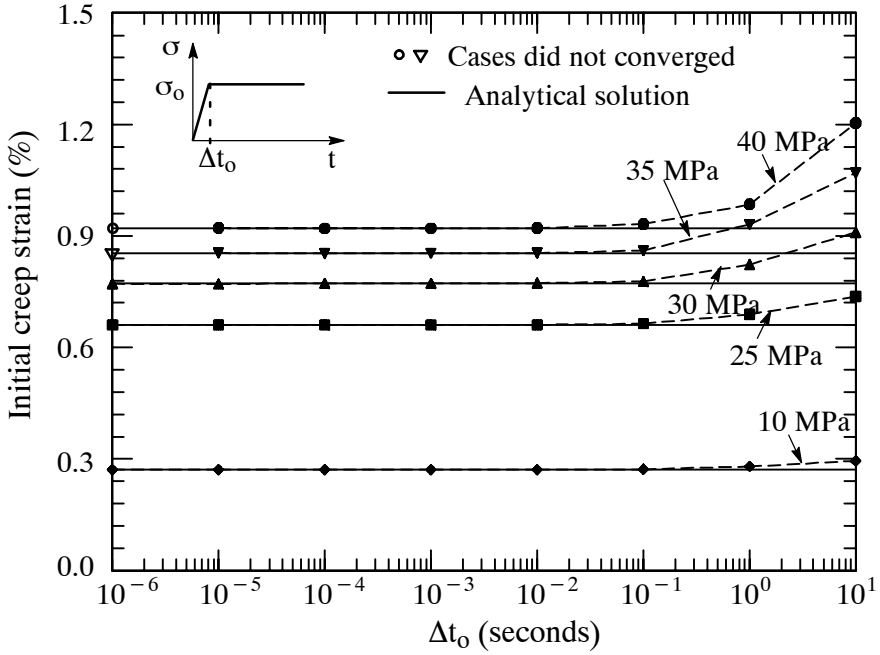

Figure 2.4 Effect of the time-increment size in the instantaneous static analysis for PMMA polymer.

The second parametric study is performed to examine the constitutive-level strain residuals generated during the iterations of a given time increment. Loading is simulated with two steps. The first step simulates the instantaneous loading. In this step, loading is applied with the duration of 10^{-4}. The second step simulates the viscoelastic analysis, in which constant load is held for 1800 seconds. Figures 2.5 and 2.6 show the strain residuals during the iteration process for creep analyses under two applied stresses of 35 MPa and 40 MPa, respectively. It is seen from the initial residuals that using a linearized stress-update alone usually leads to a large residual strain, an error of more than 5% in this case. The proposed recursive-iterative procedure is needed in order to minimize this error. Similar convergence behavior is shown in Figure 2.6 for the analysis with applied stress of 40 MPa. Convergence problems occurred during or at the beginning of the cases where applied stresses are equal or exceed the 40 MPa. This is because the nonlinear functions were calibrated up to the 40 MPa stress magnitude, as shown in Figure 2.3. Convergence is also not guaranteed beyond this stress level because some of the nonlinear functions have rapidly changing values and approach asymptotic levels. This will slow convergence and often lead to divergence.

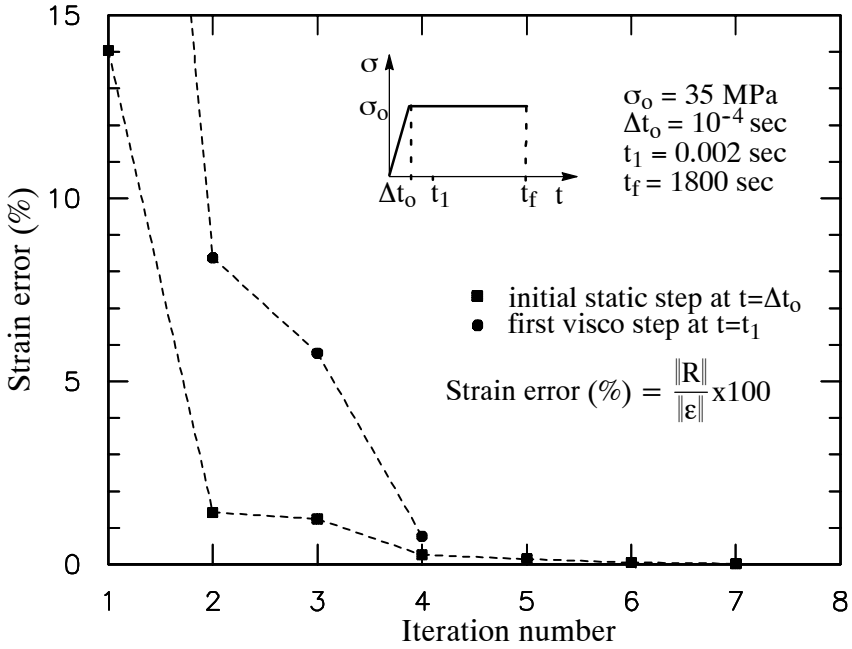

Figure 2.5 Residual strain for different time increments in the material level under constant stress of 35 MPa.

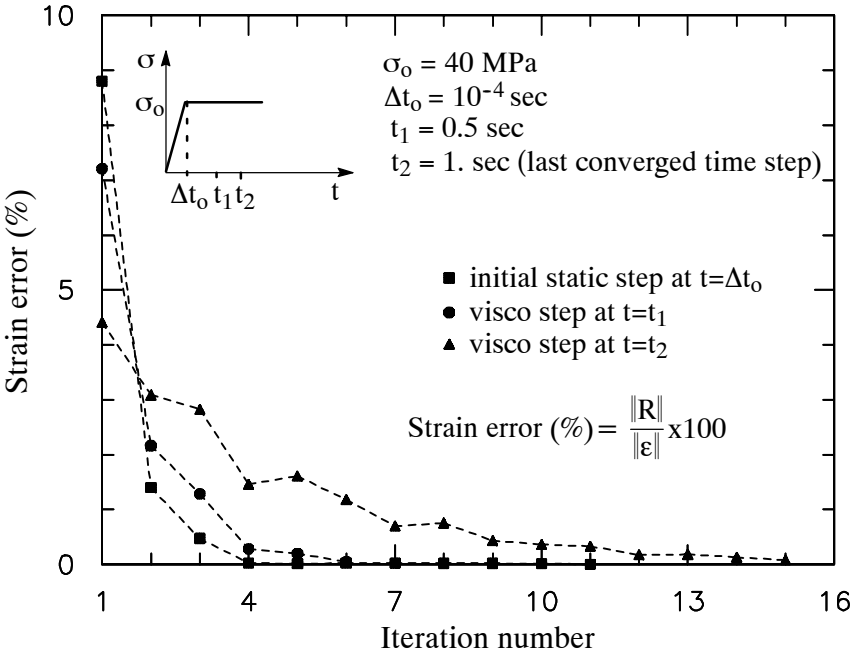

Figure 2.6 Residual strain for different time increments in the material level under constant stress of 40 MPa.

The global residual corrections at the element level have been monitored. Table 2.3 shows the force residual during the instantaneous loading step at various applied creep loads. As expected, for a relatively small load levels, both recursive-iterative and predictor-only schemes lead to the same iteration procedure at the element level. The recursive-iterative algorithm has accelerated convergence and decreased residual at the element level, especially in the case of highly nonlinear viscoelastic response. It is interesting to note that the automatic step marching scheme in ABAQUS has divided the step into two with the P=35 MPa applied load mainly due to lack of convergence and nonlinear excessive behavior when the entire load is applied. The efficiency of the proposed numerical method is evident by examining the convergence of the second step in P=35 MPa loading. Table 2.4 is the same as Table 2.3 but with residuals for the viscoelastic analysis. Results are shown for the first 35 seconds during viscoelastic analysis because the error is the largest during this time interval. The efficiency of the proposed method is also demonstrated in Table 2.4 by examining the number of iterations needed for convergence with their decreasing residuals.

Table 2.3 Iteration process at element and material levels for recursive-iterative and predictor-only schemes during instantaneous "static" creep step loading ($\Delta t_o = 10^{-4}$).

Load (MPa)	Recursive-iterative					Predictor-only		
	Time step (sec)	Element level		Material level		Time step (sec)	Element level	
		Iteration	Residual (N) **	# Iteration	Residual *		Iteration	Residual (N)**
10	$1.x10^{-4}$	1	$8.1x10^{-8}$	1	$4.9x10^{-11}$	$1.x10^{-4}$	1	$8.0x10^{-8}$
15	$1.x10^{-4}$	1	$8.0x10^{-8}$	1	$7.3x10^{-11}$	$1.x10^{-4}$	1	$8.0x10^{-8}$
20	$1.x10^{-4}$	1	$9.0x10^{-8}$	1	$9.9x10^{-11}$	$1.x10^{-4}$	1	$9.0x10^{-8}$
25		1	$6.4x10^{-2}$	4	$5.1x10^{-7}$		1	$6.4x10^{-2}$
		2	$6.4x10^{-3}$	3	$4.0x10^{-7}$		2	$6.4x10^{-3}$
	$1.x10^{-4}$	3	$6.8x10^{-4}$	3	$4.2x10^{-7}$	$1.x10^{-4}$	3	$6.8x10^{-4}$
30		1	$1.7x10^{-1}$	5	$3.7x10^{-7}$		1	$1.7x10^{-1}$
		⋮	⋮	⋮	⋮		⋮	⋮
	$1.x10^{-4}$	5	$1.8x10^{-3}$	4	$4.8x10^{-7}$	$1.x10^{-4}$	5	$1.8x10^{-3}$
35	$5.x10^{-5}$	1	$8.0x10^{-8}$	1	$8.6x10^{-11}$	$2.x10^{-5}$	1	$8.0x10^{-8}$
		1	$2.0x10^{-1}$	5	$5.6x10^{-7}$		1	$1.0x10^{-2}$
		2	$9.6x10^{-3}$	6	$9.7x10^{-7}$	$4.x10^{-5}$	2	$1.2x10^{-3}$
	$1.x10^{-4}$	3	$2.7x10^{-3}$	7	$7.7x10^{-7}$			
						⋮		
							1	$2.0x10^{-2}$
							⋮	⋮
						$1.x10^{-4}$	8	$4.6x10^{-3}$

* Residual at converged step in the material level. Convergence at material level was set for $\|R\| \leq 10^{-6}$

** Convergence at element level was set for residual force $\|R\| \leq 5x10^{-3}$

Table 2.4 Iteration process at element and material level for recursive-iterative and predictor-only schemes during creep analysis.

Load (MPa)	Recursive-iterative					Predictor-only		
	Time step (sec)	Element level		Material level		Time step (sec)	Element level	
		Iteration	Residual (N)**	# Iteration	Residual*		Iteration	Residual(N)**
10	1.0	1	$8.0\text{x}10^{-10}$	1	$3.1\text{x}10^{-13}$	1.0	1	$8.0\text{x}10^{-12}$
	30.0	1	$6.9\text{x}10^{-11}$	1	$4.8\text{x}10^{-14}$	30.0	1	$7.0\text{x}10^{-11}$
15	1.0	1	$7.6\text{x}10^{-10}$	1	$4.6\text{x}10^{-13}$	1.0	1	$7.5\text{x}10^{-10}$
	30.0	1	$6.9\text{x}10^{-11}$	1	$7.2\text{x}10^{-14}$	30.0	1	$1.0\text{x}10^{-10}$
20		1	$1.1\text{x}10^{-3}$	1	$1.5\text{x}10^{-7}$		1	$5.5\text{x}10^{-3}$
	2.9	2	$7.3\text{x}10^{-5}$	1	$6.3\text{x}10^{-7}$	2.8	2	$2.0\text{x}10^{-10}$
		1	$8.1\text{x}10^{-5}$	1	$6.1\text{x}10^{-9}$		1	$1.0\text{x}10^{-3}$
	30.0	2	$5.5\text{x}10^{-6}$	1	$1.6\text{x}10^{-9}$	30.0	2	$4.0\text{x}10^{-11}$
25		1	$1.2\text{x}10^{-3}$	1	$3.8\text{x}10^{-9}$		1	$3.0\text{x}10^{-3}$
	4.7	2	$1.2\text{x}10^{-5}$	1	$3.2\text{x}10^{-9}$	4.8	2	$2.3\text{x}10^{-4}$
		1	$8.3\text{x}10^{-4}$	1	$4.8\text{x}10^{-7}$		1	$1.0\text{x}10^{-3}$
		2	$1.1\text{x}10^{-4}$	1	$6.2\text{x}10^{-8}$		2	$1.1\text{x}10^{-4}$
	35.0	3	$1.4\text{x}10^{-5}$	1	$7.9\text{x}10^{-9}$	35.0	3	$1.4\text{x}10^{-5}$
30		1	$4.0\text{x}10^{-4}$	2	$1.3\text{x}10^{-7}$		1	$3.9\text{x}10^{-4}$
		⋮	⋮				⋮	⋮
	0.1	4	$1.2\text{x}10^{-5}$	2	$1.1\text{x}10^{-7}$	0.1	4	$1.2\text{x}10^{-5}$
		1	$1.4\text{x}10^{-3}$	1	$1.5\text{x}10^{-7}$		1	$1.4\text{x}10^{-3}$
		⋮	⋮				⋮	⋮
	35.0	3	$2.9\text{x}10^{-5}$	1	$2.4\text{x}10^{-8}$	35.0	3	$2.8\text{x}10^{-5}$
35	0.5	1	$2.6\text{x}10^{-4}$	3	$5.1\text{x}10^{-7}$		1	$1.2\text{x}10^{-2}$
							⋮	⋮
						0.5	6	$4.4\text{x}10^{-3}$
		1	$2.0\text{x}10^{-2}$	3	$9.9\text{x}10^{-7}$		1	$3.0\text{x}10^{-2}$
	3.6	2	$2.3\text{x}10^{-4}$	1	$2.4\text{x}10^{-8}$		⋮	⋮
						3.0	3	$2.9\text{x}10^{-4}$
	35.0	1	$4.0\text{x}10^{-4}$	4	$7.5\text{x}10^{-7}$	35.0	1	$5.0\text{x}10^{-4}$

* Residual at converged step in the material level. Convergence at material level was set for $\|R\| \leq 10^{-6}$

** Convergence at element level was set for residual force $\|R\| \leq 5\text{x}10^{-3}$

The effect of using different polynomial forms for the nonlinear viscoelastic functions (g_0) on the convergence during the instantaneous loading step is examined. This was done by plotting the element-level norm for the residual force as a function of iterations during a time increment. Two nonlinear elastic stress-dependent functions are considered. The first function is the previously calibrated g_0 parameter with fourth order polynomial coefficients, Table 2.2, and is extended for effective stress up to 50 MPa. The second function is the Ramberg-Osgood (R-O) strain-stress curve. The R-O equation is chosen because it has a smooth, continuous, and monotonic behavior. The two forms used in the convergence study are:

Polynomial function:

$$g_0 = 1 + \sum_{i=1}^{ng_j} \alpha_0^i \left\langle \frac{\bar{\sigma}}{\bar{\sigma}_o} - 1 \right\rangle^i$$

$$\alpha_0^1 = 0.183 \qquad \alpha_0^2 = 0.567 \qquad \bar{\sigma}_o = 20\text{MPa}$$

$$\alpha_0^3 = -1.067 \qquad \alpha_0^4 = 0.533$$

R-O function:

$$\gamma = \frac{\tau}{G} + \frac{\beta \tau_o}{G}\left(\frac{\tau}{\tau_o}\right)^n = \left[1 + \beta\left(\frac{\tau}{\tau_o}\right)^{n-1}\right]\frac{\tau}{G} \tag{2.69}$$

$$\equiv g_0^{R-O} J_0 \tau$$

$$g_0^{R-O} = \left[1 + \beta\left(\frac{\tau}{\tau_o}\right)^{n-1}\right]$$

$$\frac{\beta}{\tau_o^{n-1}} = 10^{-5} \qquad n = 4$$

where β and n are the nonlinear material variables. It should be noted that this is a numerical excersice and the R-O function was not calibrated to match any experimental data. Figure 2.7 shows the curves for the above functions. The norm for the element residual forces at various applied static loads, using the nonlinear polynomial and Ramberg-Osgood equations are shown in Figures 2.8 (a) and (b), respectively. It is clear that the 'elastic' part of the viscoelastic constitutive formulation strongly affects the convergence. A smooth and

monotonic function, in which its slope does not change drastically, will accelerate convergence and decrease the number of numerical iterations.

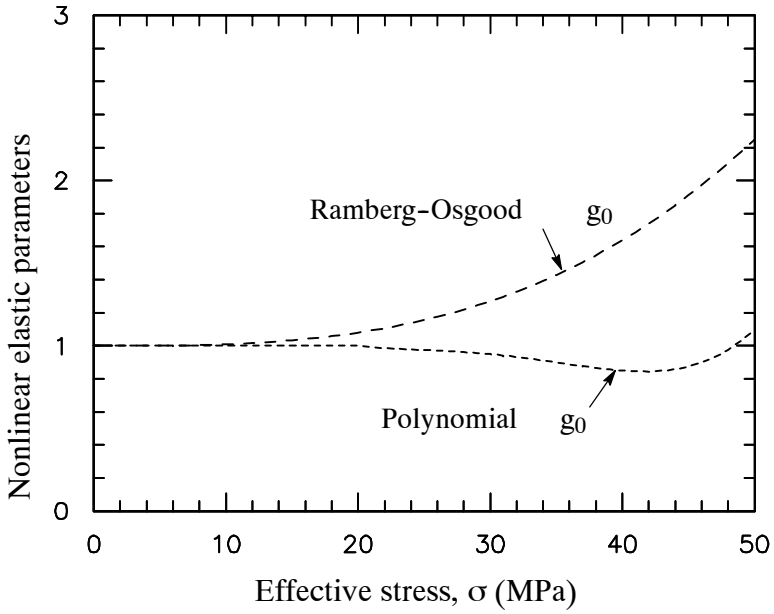

Figure 2.7 Nonlinear stress-dependent functions for the elastic material.

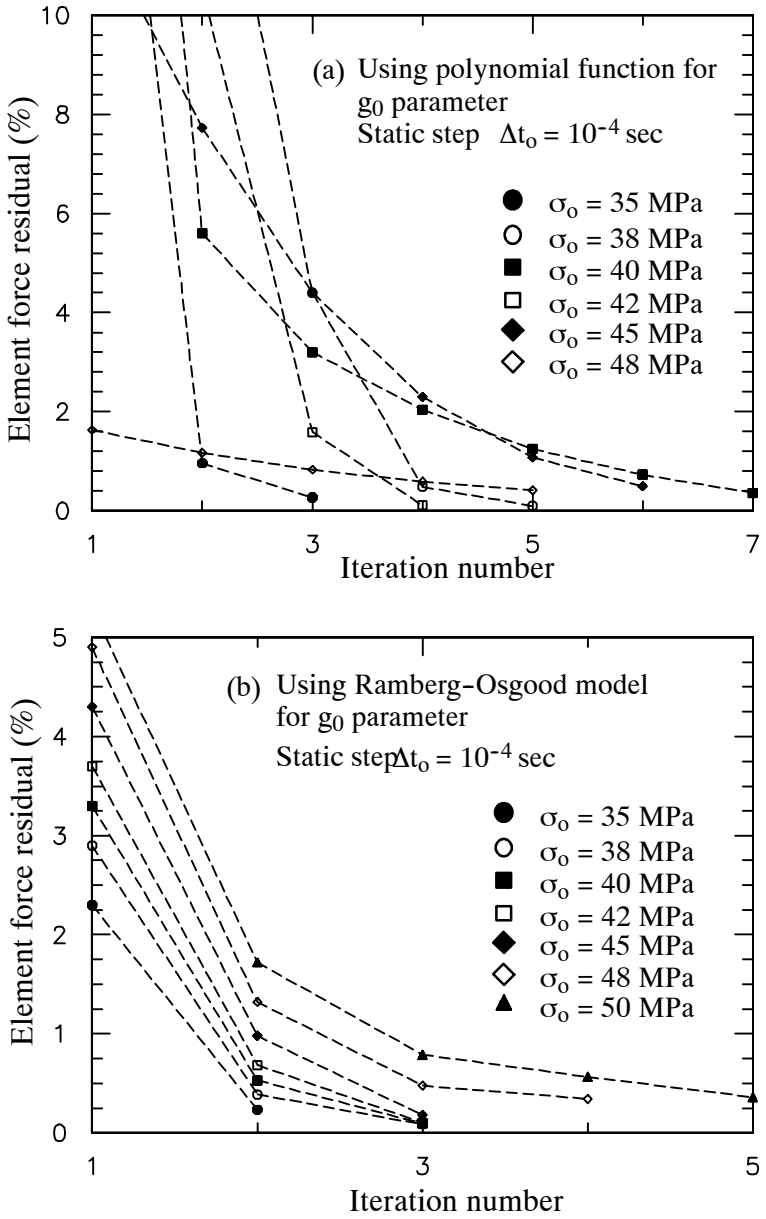

Figure 2.8 Global force residual under various stress (a) polynomial g_0, (b) Ramberg-Osgood g_0.

The experimental data from Lai and Bakker (1996) are used to verify the proposed numerical modeling algorithm. A series of tensile creep test for 30 minutes followed by recovery test for 1 hour were conducted under several stress levels: 15 MPa - 35 MPa, at room temperature. It was shown that the linear response occurs below 20 MPa. Figure 2.9 illus-

trates the creep strain response from creep simulations using recursive-iterative and predictor-only models. This is done to compare the proposed recursive-iterative model with the results using a predictor-only scheme at the material level. Both cases include the same correction scheme at the element-level. It is interesting to note that the "global" iterative residual correction is not sufficient to reduce the error at the element level with increasing applied stress. The FE analyses for creep and recovery are comparable with the experimental data as seen in Figures 2.10 and 2.11, respectively. Another numerical calculation of uniaxial response is performed to verify the proposed algorithm. Two-step creep loading for PMMA polymer is shown in Figure 2.12. The FE prediction is in good agreement with the experimental data.

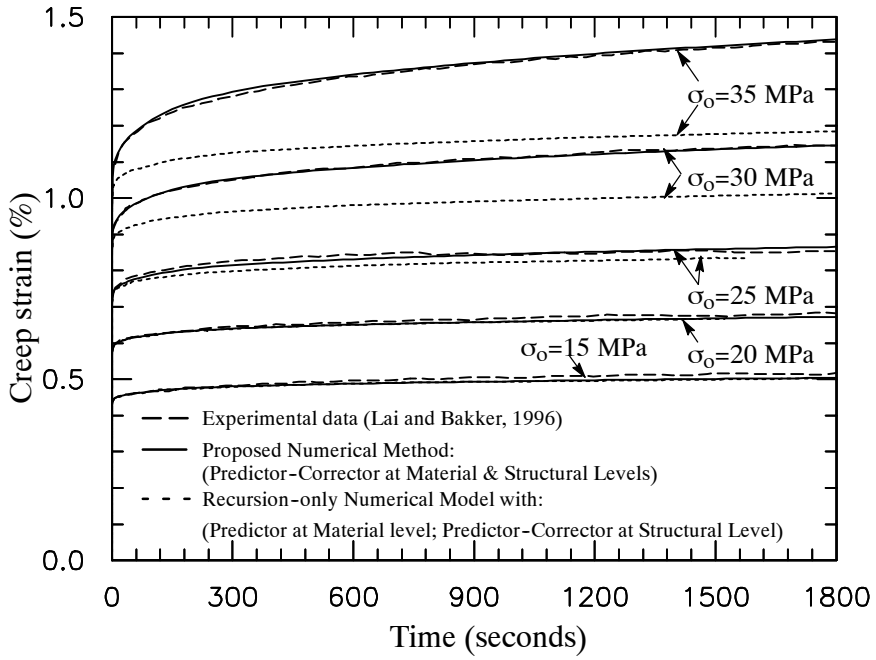

Figure 2.9 Creep strain response of PMMA using recursive-only model compared with the proposed recursive-iterative model (both models include the same correction scheme at the element-level).

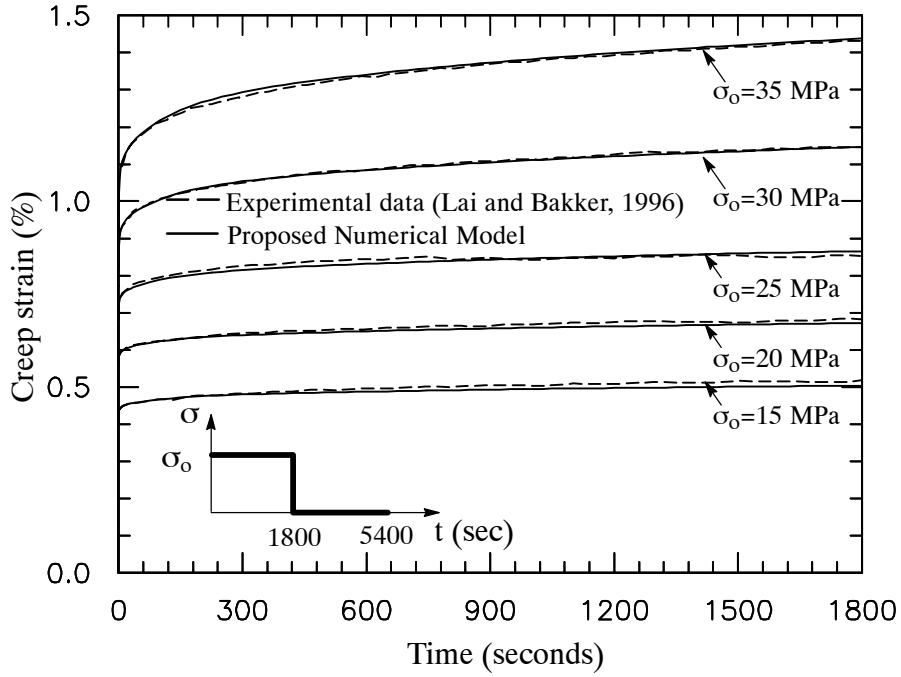

Figure 2.10 Axial creep strain for PMMA polymer.

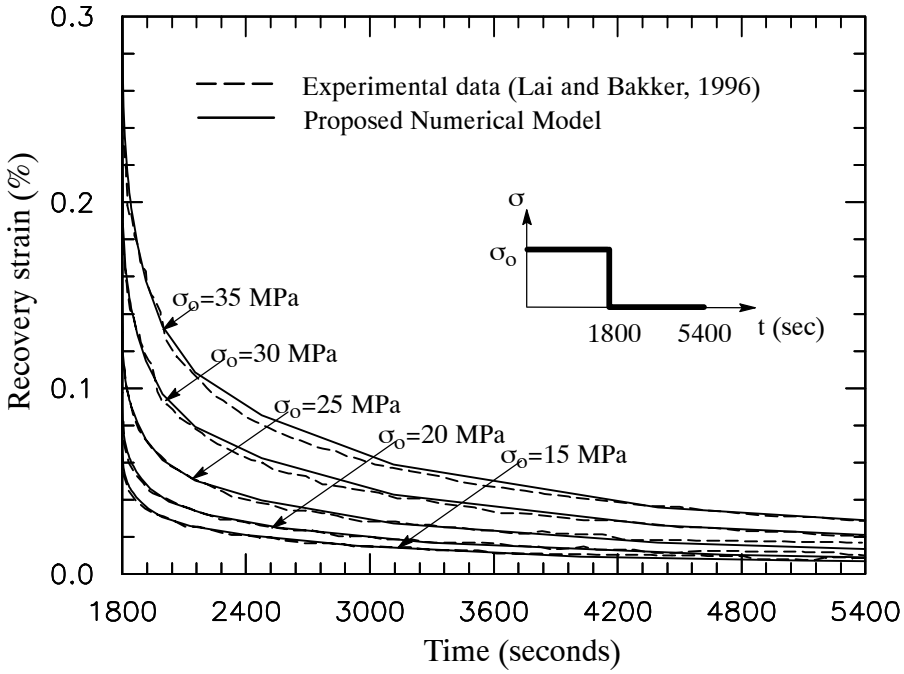

Figure 2.11 Axial recovery strain for PMMA polymer.

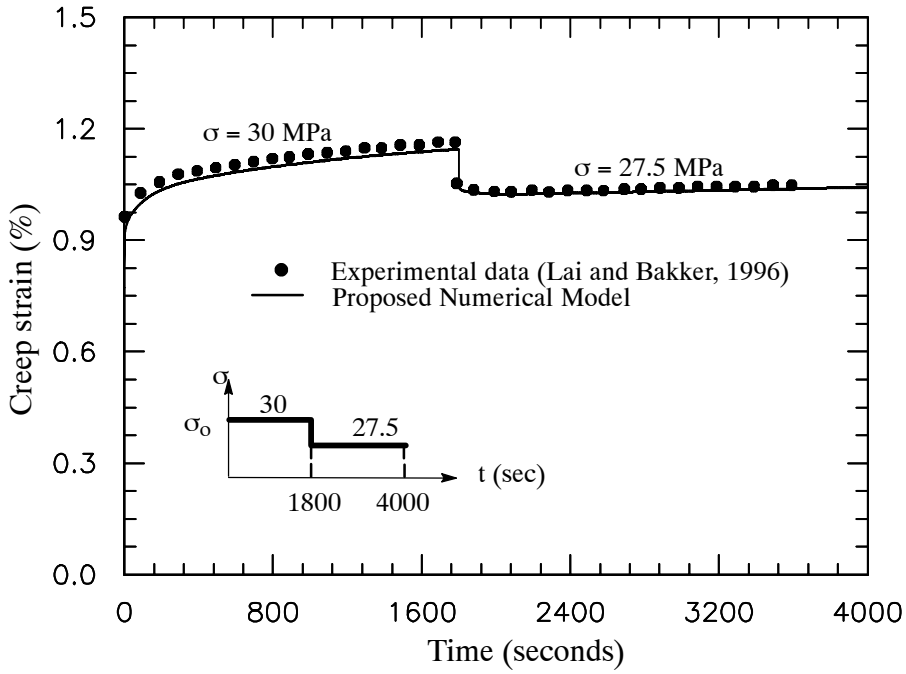

Figure 2.12 Two-step creep response for PMMA polymer.

Application of the multiaxial deformation

The application of the proposed numerical algorithm under multiaxial response is presented using a notched plate specimen under plane stress condition. The configuration of the rectangular plate follows the one of Lai and Bakker (1996) with the dimension of 800 mm x 400 mm and hole radius of 20 mm. Due to the double symmetric condition, only a quarter of the plate is modeled. A 20-node brick continuum element with reduced integration (C3D20R) is used for the analyses. One element is used through the thickness of 1 mm. Total 1814 nodes and 204 elements are generated.

Two analyses are performed for the notched plate. The first analysis is a stress relaxation type subjected to a uniform remote strain of 0.09% for duration 10^6 seconds. Figure 2.13 shows the contours of strain error and number of iteration at various times: 10^{-5}, 20, 1020 and 10^6 seconds. The large initial residual strain at different time has the magnitude of 0.15%

or more, which is caused by the linearized approximation. As time increases, the accumulation or error also increases. The iterative algorithm, which accomplishes the stress correction, is carried out. This correction reduces the magnitude of strain error below 0.1% within number of iteration less than 8. The stress relaxation response at three different locations is performed on Figure 2.14. At the hole edge, the stress magnitude of 37 MPa occurs that shows highly nonlinearity response. While at the distance away from the hole edge, the responses are in linear viscoelastic range. Therefore, the residual strain and number of iteration at this location, as seen in Figure 2.13, are less than the ones at the hole edge. Figure 2.15 shows the spatial distribution of the axial-stress relaxation along the symmetry line, for short, intermediate, and long times.

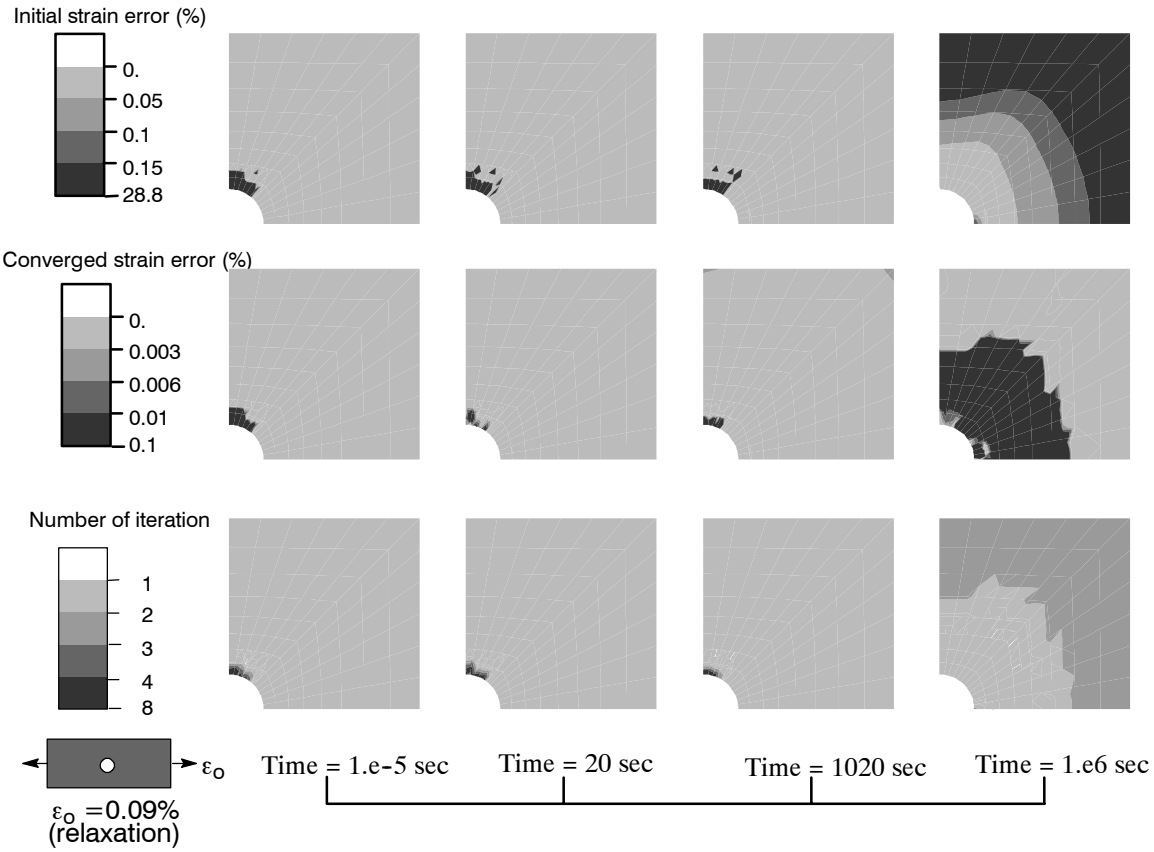

Figure 2.13 Contour of residual strain and number of iteration for notched plate under stress relaxation.

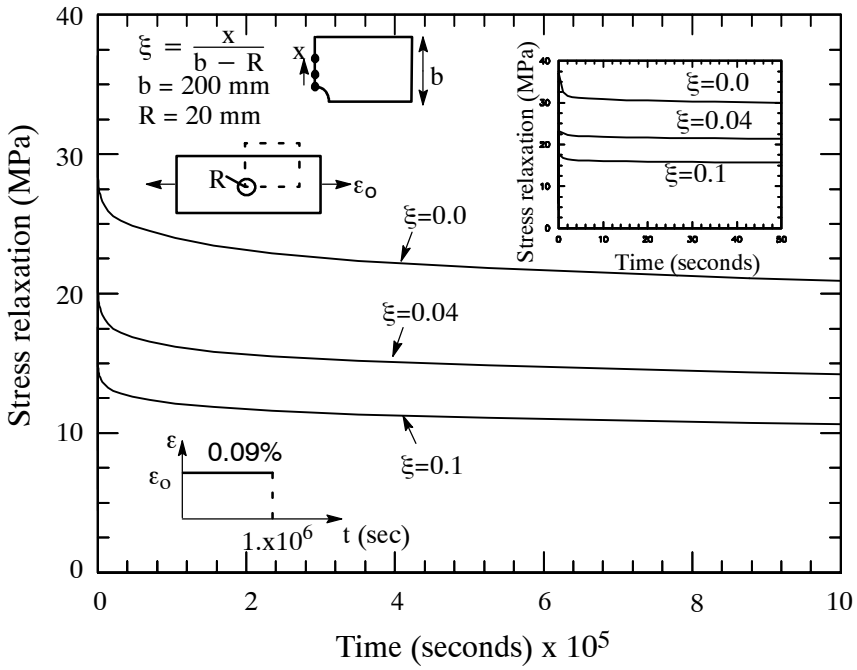

Figure 2.14 Stress relaxation for notched plate under tensile remote strain 0.09%.

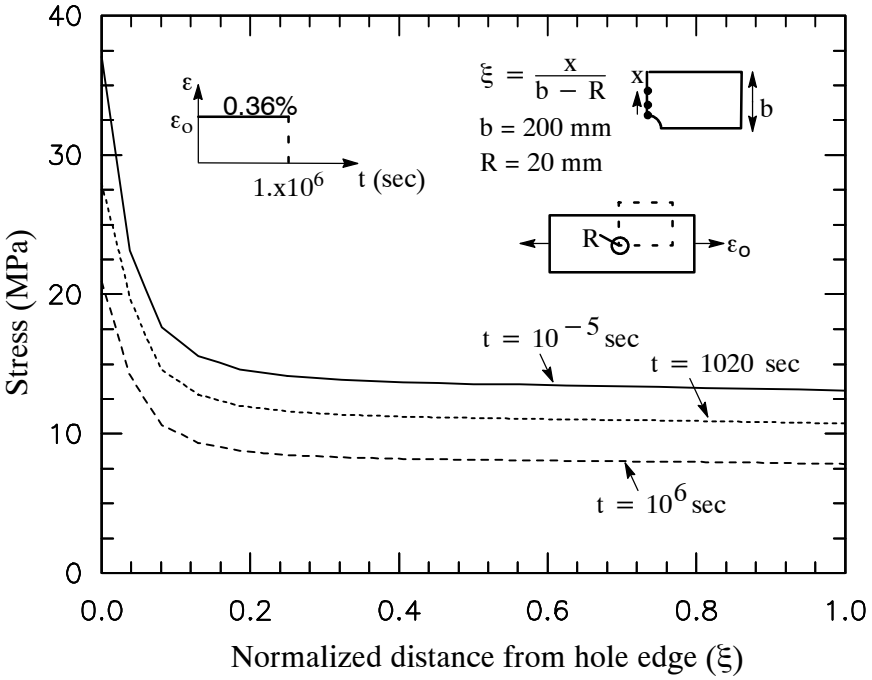

Figure 2.15 Stress distribution at the center of a notched plate under tensile remote strain 0.36%.

The second analysis is a creep strain type subjected to a uniform remote stress of 13.5 MPa for duration 10^6 seconds. The stress distributions along the mid-section of the plate at times 10^{-5}, 1020 and 10^6 seconds are shown in Figure 2.16. It is shown that the stress distribution changes with time when the large nonlinearity occurs. While in the relatively low nonlinear visoelastic range, the stress distribution is independent on time. The contours of strain error and number of iteration at various times: 10^{-5}, 20, 1020 and 10^6 seconds, are shown in Figure 2.17. The linearized approximation causes large residual strain, as indicated by the large initial residual strain (0.15% or more). The iterative procedure helps decreasing the residual strain until the magnitude of less than 0.1%. The creep strain response at three different locations is performed on Figure 2.18. The maximum strain occurs at the hole edge. Figure 2.19 shows the spatial distribution of the axial creep strain along the symmetry line, for short, intermediate, and long times.

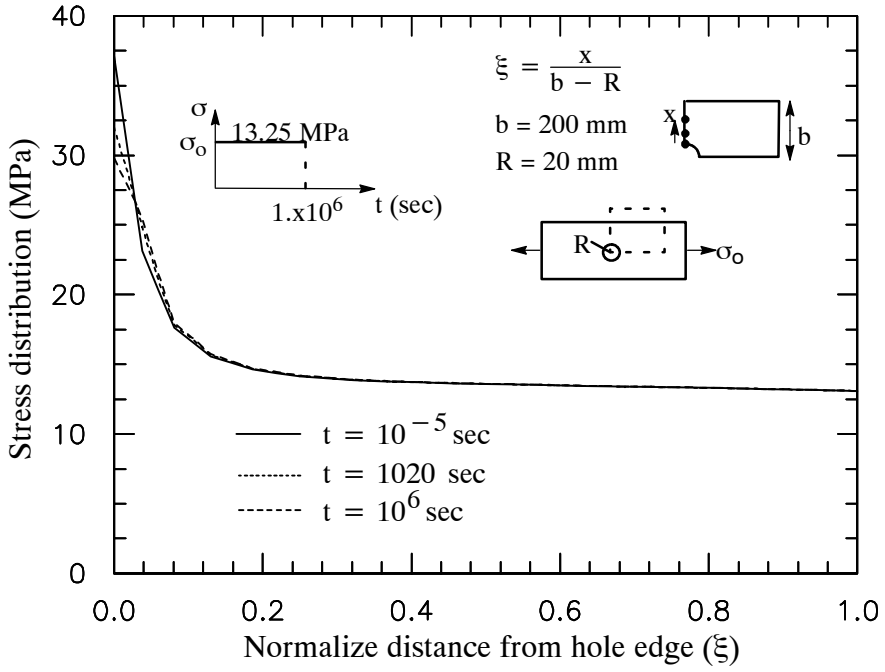

Figure 2.16 Stress distribution for notched plate at different time.

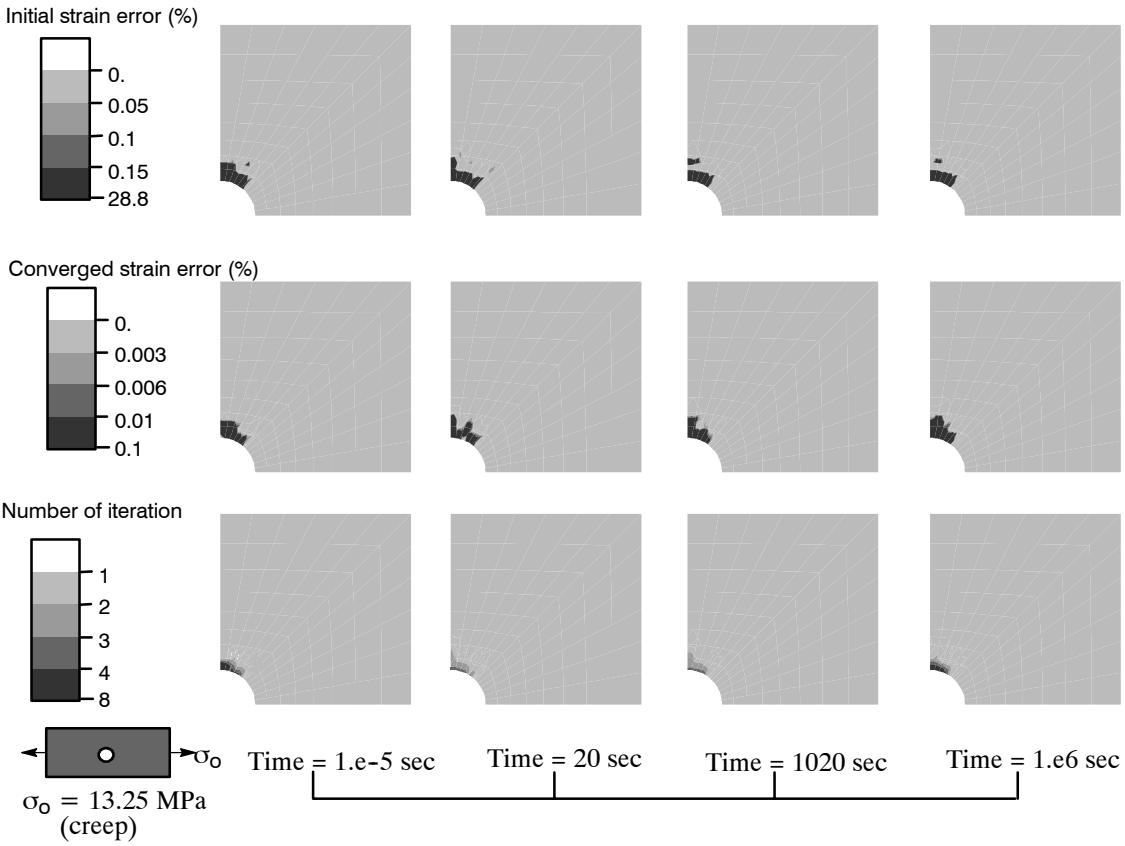

Figure 2.17 Contour of residual strain and number of iteration for notched plate under creep.

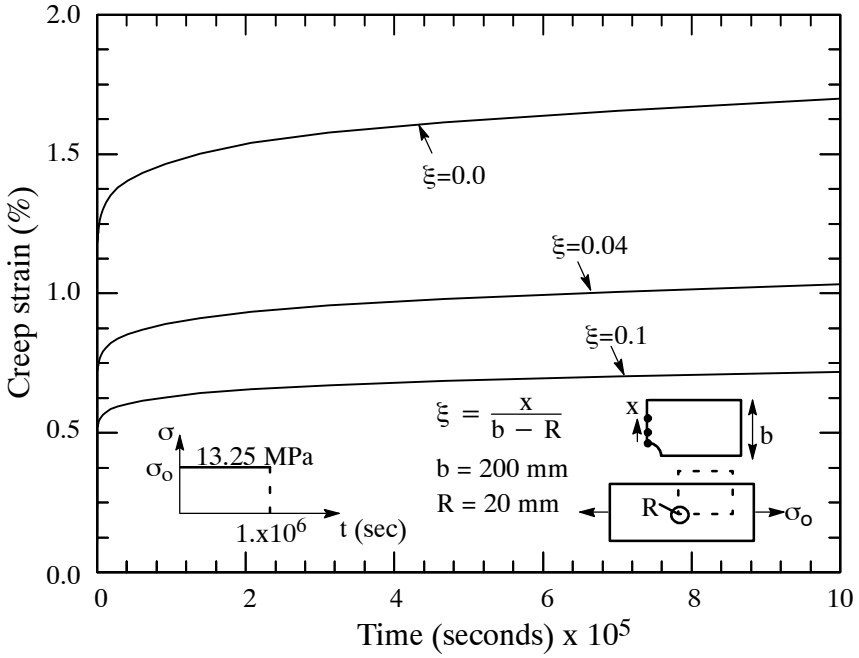

Figure 2.18 Creep strain at three points subjected to tensile remote stress of 13.5 MPa.

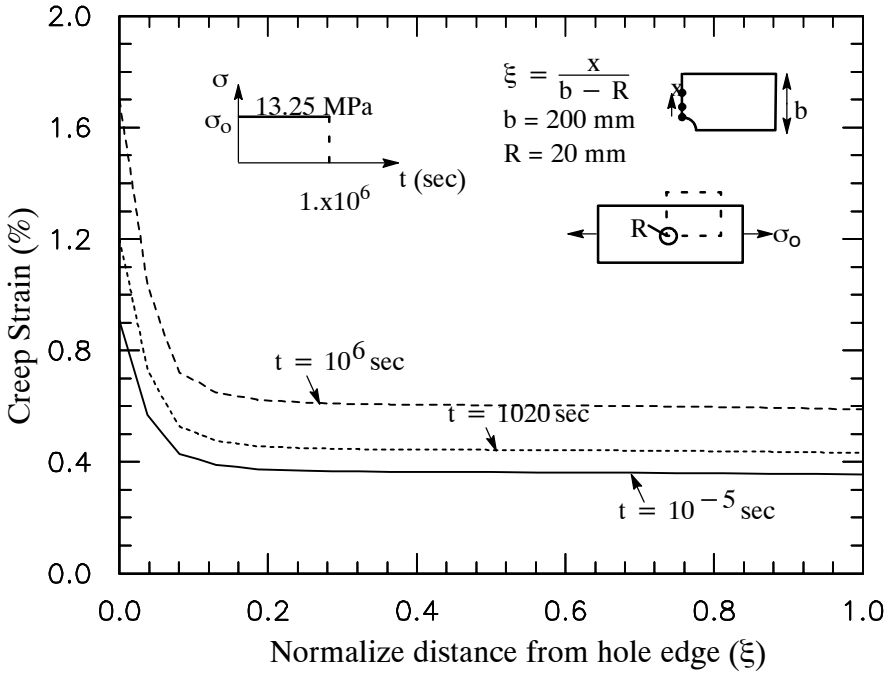

Figure 2.19 Strain distribution at the center of a notched plate under tensile remote stress 13.5 MPa.

CHAPTER III

MICROMECHANICAL MODELS FOR THE NONLINEAR VISCOELASTIC BEHAVIOR OF LAMINATED COMPOSITES

This chapter presents a micromechanical framework for the nonlinear viscoelastic analysis of laminated composite materials and structures. Each unidirectional lamina is idealized using the Aboudi four-cell micromodel with a new incremental formulation in term of the average strains and stresses in the subcells. A new recursive-iterative method is used for the numerical integration of the Schapery model at the matrix levels. This constitutive model is nested within a second numerical stress-update algorithm at the lamina level. The latter is based on a predictor-corrector scheme that satisfies the fiber and matrix viscoelastic constitutive relations along with the micromechanical equations in the form of traction continuity and strain compatibility between the subcells. The micromechanical model can be implemented for the nonlinear analysis of multi-layered composite structures in a displacement-based FE models. Creep test data for off-axis plates, available in the literature, are used to calibrate and validate the prediction of the proposed material model. Physical aging and temperature effects on creep are also examined.

3.1 Micromechanical Formulation

The four-cell micromodel of a unidirectional lamina, Aboudi (1991), is described in this section. A new incremental formulation for this micromodel, in term of the average strains and stresses, was presented by Haj-Ali and Pecknold (1996). The purpose of this section is to generalize the incremental formulation to include an explicit time-scale and to allow modeling time-dependent behavior.

It is assumed that for a given heterogeneous periodic medium, it is possible to define a basic unit-cell that represents its major geometrical and material characteristics. Each unit-cell is divided into a number of subcells. A uniform spatial variation of the stress and strain fields is assumed in each subcell. Traction continuity at an interface between subcells can therefore be satisfied only in an average sense. This class of approximate micromechanical models is referred herein as Constant Deformation Cell (CDC) micromodels. The subcell strain-interaction matrix, $B^{(\alpha)}$, which relates the subcell average strain increment vector, $d\varepsilon^{(\alpha)}$, to the overall unit-cell average strain increment, $d\bar{\varepsilon}$, is defined as:

$$d\varepsilon^{(\alpha)} = B^{(\alpha)}\, d\bar{\varepsilon} \quad , \quad \text{where} \quad d\bar{\varepsilon} = \frac{1}{V}\sum_{\alpha=1}^{Ns} v^{(\alpha)}\, d\varepsilon^{(\alpha)} = \frac{1}{V}\sum_{\alpha=1}^{Ns} V^{(\alpha)}\, B^{(\alpha)}\, d\bar{\varepsilon} \tag{3.1}$$

where α is the subcell number, V is the unit-cell total volume and $v^{(\alpha)}$ is the subcell volume. Since Eq. (3.1) must hold for an arbitrary average strain increment $d\bar{\varepsilon}$, the following relations must be satisfied:

$$\frac{1}{V}\sum_{\alpha=1}^{Ns} V^{(\alpha)}\, B^{(\alpha)} = I \quad \text{and} \quad \sum_{\alpha=1}^{Ns} V^{(\alpha)}\,(B^{(\alpha)} - I) = 0 \tag{3.2}$$

where I is a unit matrix. Next, the incremental constitutive equation is expressed for each subcell:

$$d\sigma^{(\alpha)} = C^{(\alpha)}\, d\varepsilon^{(\alpha)} = C^{(\alpha)}\, B^{(\alpha)}\, d\bar{\varepsilon} \tag{3.3}$$

where $C^{(\alpha)}$ is the current tangent stiffness matrix of the subcell. The strain-interaction matrices can be determined by solving the unit-cell's governing equations, including the traction and compatibility along with the incremental stress-strain relations. The incremental unit-cell average stresses are expressed as:

$$d\bar{\sigma} = \frac{1}{V}\sum_{\alpha=1}^{Ns} v^{(\alpha)}\, d\sigma^{(\alpha)} = \frac{1}{V}\sum_{\alpha=1}^{Ns} v^{(\alpha)}\, C^{(\alpha)}\, B^{(\alpha)}\, d\bar{\varepsilon} = \bar{C}\, d\bar{\varepsilon} \tag{3.4}$$

where $\bar{C}$ is the unit-cell effective tangent stiffness matrix. In order to derive the strain-interaction matrices for a unit-cell, the traction and displacement continuity conditions must be imposed, and stress-strain relations must be invoked. Up to this stage, the properties of the strain-interaction matrices and the expression for the unit-cell effective stiffness matrix have been dealt with. It can be shown that a subcell strain-interaction matrix is a function of subcell tangent stiffness and the relative volumes from all subcells. Using the incremental stress-strain relations in Eq. (3.3), these equations can ultimately be written in a general incremental form as:

$$\mathcal{C}\left(C^{(\alpha)},\ d\varepsilon^{(\alpha)},\ d\bar{\varepsilon},\ V^{(\alpha)},\ \alpha = 1, 2, .., Ns \right) = 0 \tag{3.5}$$

Equation (3.5) forms a set of linear equations in terms of the unknown incremental strain vectors for each subcell. The equations can be arranged in terms of these unknown and known values, the current tangent stiffness matrices and the unit-cell strain vector, $d\bar{\varepsilon}$. Finally, the above equation is represented in a general matrix form as:

$$\underset{6Ns \times 6Ns}{\begin{bmatrix} & A & \end{bmatrix}} \underset{6Ns \times 1}{\begin{Bmatrix} d\varepsilon^{(1)} \\ d\varepsilon^{(2)} \\ \cdots \\ \cdots \\ \cdots \\ d\varepsilon^{(Ns)} \end{Bmatrix}} = \underset{6Ns \times 6}{\begin{bmatrix} & D & \end{bmatrix}} \underset{6 \times 1}{\begin{Bmatrix} d\bar{\varepsilon} \end{Bmatrix}} \tag{3.6}$$

Once Eq. (3.6) is solved, the incremental stress in each of the subcells and the average stress of the unit-cell can be back calculated using the incremental stress-strain relations. The incremental strain-concentration matrices are expressed, using Eqs. (3.1) and (3.6), by:

$$\begin{bmatrix} B^{(1)} \\ \hline B^{(2)} \\ \hline \vdots \\ \hline B^{(Ns)} \end{bmatrix} = \begin{bmatrix} \quad\quad A^{-1} \quad\quad \end{bmatrix} \begin{bmatrix} D \end{bmatrix} \tag{3.7}$$

A four-cell micromodel is derived next using the method of cells (MOC), Aboudi (1991). Aboudi's model has been shown to be well suited for highly nonlinear matrix response, such as that exhibited by metal matrix composites. However, integration of the MOC formulation in general 3D analysis of composite structures has been limited, perhaps because of the large computational effort that is needed. Therefore, it is important to develop efficient stress update and correction algorithms for this model that are suitable for nonlinear structural analysis. Haj-Ali and Pecknold (1996) presented an incremental formulation of Aboudi's model in terms of the average stresses and strains in the subcells. New stress update and correction algorithms are developed. These can significantly reduce the computational effort that is needed when using this micromodel. The new algorithms are formulated given a constant average strain rate for each time step, which make them suitable for integration with FE constitutive framework.

The micromechanical model is shown in Figure 3.1. The unidirectional composite, which consists of long fibers arranged unidirectionally in the matrix system, is idealized as doubly periodic array of fibers with rectangular cross section. A quarter unit-cell that consists of four subcells is modeled due to symmetry. The first subcell is a fiber constituent, while subcells 2, 3, and 4 represent the matrix constituents. The long fibers are aligned in the x_1 direction. The other cross-section directions are referred to as the transverse directions. The total volume of the unit-cell is taken to be equal to one.

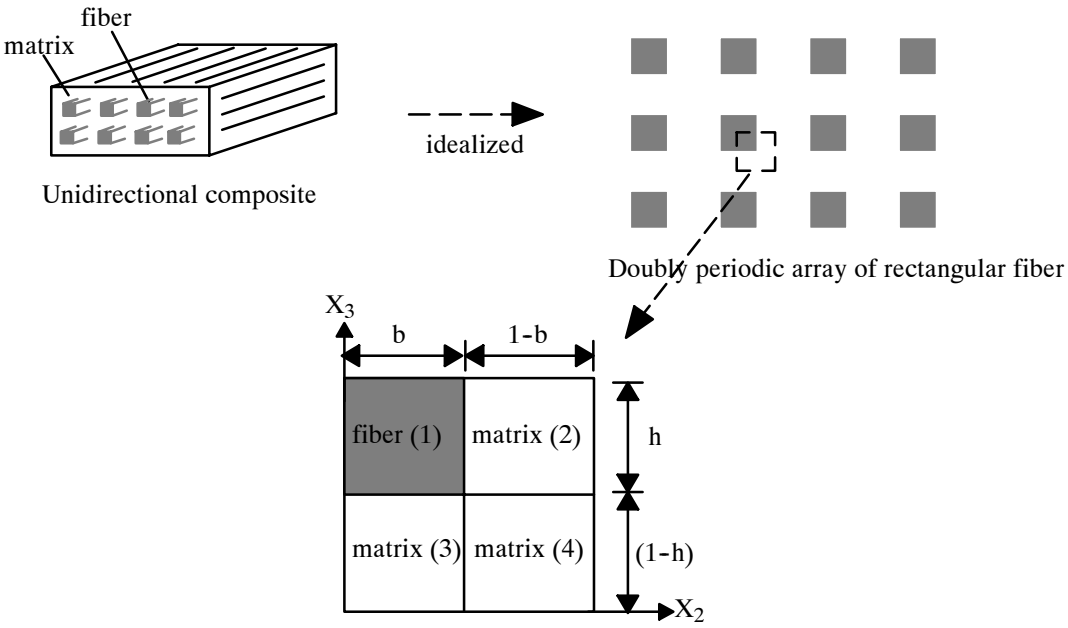

Figure 3.1 Micromodel of unidirectional composites.

The volumes of the four subcells are:

$$V_1 = b\,h \qquad V_2 = h\,(1-b) \qquad V_3 = b\,(1-h) \qquad V_4 = (1-h)\,(1-b) \tag{3.8}$$

where V_1 is the fiber volume fraction (FVF) for unidirectional layer. The effective incremental stress and strain vectors notations are:

$$\begin{aligned} d\sigma_k^{(\alpha)} &= \{d\sigma_{11},\ d\sigma_{22},\ d\sigma_{33},\ d\tau_{12},\ d\tau_{13},\ d\tau_{23}\} && \alpha = 1,..,4 \\ d\varepsilon_k^{(\alpha)} &= \{d\varepsilon_{11},\ d\varepsilon_{22},\ d\varepsilon_{33},\ d\gamma_{12},\ d\gamma_{13},\ d\gamma_{23}\} && k = 1,..,6 \end{aligned} \tag{3.9}$$

The 3D nonlinear constitutive integration for the fiber and matrix constituents is performed separately for each subcell. The fiber is linear elastic and transversely isotropic, while the matrix medium is viscoelastic. The homogenization of the micromodel should satisfy displacement compatibility and traction continuity. Perfect bond is assumed along the interfaces of the subcells. In the fiber direction, the four subcells satisfy the same strain continuity relation. The axial average stress definition is used as a second independent relation

in order to relate the effective axial stress to the stresses in the subcells. The following equations summarize the relations in the axial mode:

$$\begin{gathered} d\varepsilon_{11}^{(1)} = d\varepsilon_{11}^{(2)} = d\varepsilon_{11}^{(3)} = d\varepsilon_{11}^{(4)} = d\bar{\varepsilon}_{11} \\ V_1\, d\sigma_{11}^{(1)} + V_2\, d\sigma_{11}^{(2)} + V_3\, d\sigma_{11}^{(3)} + V_4\, d\sigma_{11}^{(4)} = d\bar{\sigma}_{11} \end{gathered} \tag{3.10}$$

Considering interfaces between the subcells with normal in the x_2 direction, the in-plane stress components σ_{22} and τ_{12} must satisfy traction continuity conditions. The total strain components ε_{22} and γ_{12} from subcells 1 and 2, and subcells 3 and 4, respectively should also satisfy strain compatibility conditions. These relations are written in an incremental form as:

$$\begin{gathered} d\sigma_{22}^{(1)} = d\sigma_{22}^{(2)} \\ d\sigma_{22}^{(3)} = d\sigma_{22}^{(4)} \\ \frac{V_1}{V_1 + V_2}\, d\varepsilon_{22}^{(1)} + \frac{V_2}{V_1 + V_2}\, d\varepsilon_{22}^{(2)} = d\bar{\varepsilon}_{22} \\ \frac{V_3}{V_3 + V_4}\, d\varepsilon_{22}^{(3)} + \frac{V_4}{V_3 + V_4}\, d\varepsilon_{22}^{(4)} = d\bar{\varepsilon}_{22} \end{gathered} \tag{3.11}$$

$$\begin{gathered} d\tau_{12}^{(1)} = d\tau_{12}^{(2)} \\ d\tau_{12}^{(3)} = d\tau_{12}^{(4)} \\ \frac{V_1}{V_1 + V_2}\, d\gamma_{12}^{(1)} + \frac{V_2}{V_1 + V_2}\, d\gamma_{12}^{(2)} = d\bar{\gamma}_{12} \\ \frac{V_3}{V_3 + V_4}\, d\gamma_{12}^{(3)} + \frac{V_4}{V_3 + V_4}\, d\gamma_{12}^{(2)} = d\bar{\gamma}_{12} \end{gathered} \tag{3.12}$$

Considering interfaces between subcells with normal in the x_3 direction, the out-of-plane stress components σ_{33} and τ_{13} must satisfy traction continuity conditions. The total strain components ε_{33} and γ_{13} from subcells 1 and 3, and subcells 2 and 4, respectively should also satisfy strain compatibility conditions. These relations are expressed in incremental form as:

$$
\begin{aligned}
d\sigma_{33}^{(1)} &= d\sigma_{33}^{(3)} \\
d\sigma_{33}^{(2)} &= d\sigma_{33}^{(4)} \\
\frac{V_1}{V_1 + V_3}\, d\varepsilon_{33}^{(1)} &+ \frac{V_3}{V_1 + V_3}\, d\varepsilon_{33}^{(3)} = d\bar{\varepsilon}_{33} \\
\frac{V_2}{V_2 + V_4}\, d\varepsilon_{33}^{(2)} &+ \frac{V_4}{V_2 + V_4}\, d\varepsilon_{33}^{(4)} = d\bar{\varepsilon}_{33}
\end{aligned}
\tag{3.13}
$$

$$
\begin{aligned}
d\tau_{13}^{(1)} &= d\tau_{13}^{(3)} \\
d\tau_{13}^{(2)} &= d\tau_{13}^{(4)} \\
\frac{V_1}{V_1 + V_3} d\gamma_{13}^{(1)} &+ \frac{V_3}{V_1 + V_3}\, d\gamma_{13}^{(3)} = d\bar{\gamma}_{13} \\
\frac{V_2}{V_2 + V_4}\, d\gamma_{13}^{(2)} &+ \frac{V_4}{V_2 + V_4}\, d\gamma_{13}^{(4)} = d\bar{\gamma}_{13}
\end{aligned}
\tag{3.14}
$$

Finally, both types of interfaces should satisfy transverse shear stress continuity. Therefore, the transverse shear stresses in the four subcells are equal to the effective transverse shear stress. The transverse shear strains from the four subcells in the average strain definition are used to express the relations with the effective transverse shear strain of the unit-cell. The transverse shear relations are summarized as:

$$
\begin{aligned}
d\tau_{23}^{(1)} = d\tau_{23}^{(2)} = d\tau_{23}^{(3)} = d\tau_{23}^{(4)} &= d\bar{\tau}_{23} \\
V_1\, d\gamma_{23}^{(1)} + V_2\, d\gamma_{23}^{(2)} + V_3\, d\gamma_{23}^{(3)} + V_4\, d\gamma_{23}^{(4)} &= d\bar{\gamma}_{23}
\end{aligned}
\tag{3.15}
$$

Equations (3.9) to (3.15) along with the stress-strain relations within each fiber and matrix subcells, complete the micromechanical formulation of the unidirectional layer. These relations are used in incremental (rate) form due to the nonlinear constitutive relations in the matrix subcells. Next, the strain components in the subcells are grouped into two parts: (a) and (b). The first part corresponds to the incremental compatibility equations and the second part is the traction continuity relations (homogeneous equations). The two groups of strain vectors are defined by:

$$d\varepsilon_a^T = \left\{ d\varepsilon_1^{(1)},\ d\varepsilon_1^{(2)},\ d\varepsilon_1^{(3)},\ d\varepsilon_1^{(4)},\ d\varepsilon_2^{(1)},\ d\varepsilon_2^{(3)},\ d\varepsilon_4^{(1)},\ d\varepsilon_4^{(3)},\ d\varepsilon_3^{(1)}, d\varepsilon_3^{(2)},\ d\varepsilon_5^{(1)},\ d\varepsilon_5^{(2)},\ d\varepsilon_6^{(1)} \right\} \quad (3.16)$$

(1 x 13)

and

$$d\varepsilon_b^T = \left\{ d\varepsilon_2^{(2)},\ d\varepsilon_2^{(4)},\ d\varepsilon_4^{(2)},\ d\varepsilon_4^{(4)},\ d\varepsilon_3^{(3)},\ d\varepsilon_3^{(4)},\ d\varepsilon_5^{(3)},\ d\varepsilon_5^{(4)},\ d\varepsilon_6^{(2)},\ d\varepsilon_6^{(3)}, d\varepsilon_6^{(4)} \right\} \quad (3.17)$$

(1 x 11)

The set of equations, (3.10) to (3.15), can be expressed in terms of the strain increments in the subcells after substituting the incremental stress-strain relations. The rearrangement of the strain increments in Eq. (3.6) allows this set to be transformed into:

$$\begin{Bmatrix} dR_\varepsilon \\ (13 \times 1) \\ \hline dR_\sigma \\ (11 \times 1) \end{Bmatrix} = \left[\begin{array}{c|c} \mathbf{I} & \overline{A}_{ab} \\ (13 \times 13) & (13 \times 11) \\ \hline \overline{A}_{ba} & \overline{A}_{bb} \\ (11 \times 13) & (11 \times 11) \end{array}\right] \begin{Bmatrix} d\varepsilon_a \\ (13 \times 1) \\ \hline d\varepsilon_b \\ (11 \times 1) \end{Bmatrix} = \left[\begin{array}{c} \overline{D}_a \\ (13 \times 6) \\ \hline 0 \\ (11 \times 6) \end{array}\right] \left\{ \begin{matrix} d\bar{\varepsilon} \\ (6 \times 1) \end{matrix} \right\} \quad (3.18)$$

dR_σ in Eq. (3.18) is the residual form of the stress relations in Eqs. (3.9) to (3.15) expressed incrementally in terms of the strains in the subcells. The matrices that appear in Eq. (3.18) can be identified by examining Eqs. (3.9) to (3.15) and are listed below. The non-zero terms of $\overline{A}_{ab}$ are:

$$\begin{gathered} \overline{A}_{ab}(5,1) = \overline{A}_{ab}(6,2) = \overline{A}_{ab}(7,3) = \overline{A}_{ab}(8,4) = \overline{A}_{ab}(13,9) = \frac{1-h}{h} \\ \overline{A}_{ab}(9,5) = \overline{A}_{ab}(10,6) = \overline{A}_{ab}(11,7) = \overline{A}_{ab}(12,8) = \overline{A}_{ab}(13,10) = \frac{1-b}{b} \\ \overline{A}_{ab}(13,11) = \frac{(1-b)(1-h)}{b\,h} \end{gathered} \quad (3.19)$$

The $\overline{A}_{ba}$ and $\overline{A}_{bb}$ matrices are:

$$\overline{A}_{ba} = \begin{bmatrix} -C_{12}^{(1)} & C_{12}^{(2)} & 0 & 0 & -C_{22}^{(1)} & 0 & 0 & 0 & -C_{23}^{(1)} & C_{23}^{(2)} & 0 & C_{25}^{(2)} & 0 \\ 0 & 0 & -C_{12}^{(3)} & C_{12}^{(4)} & 0 & -C_{22}^{(3)} & 0 & -C_{24}^{(3)} & 0 & 0 & 0 & 0 & 0 \\ 0 & C_{14}^{(2)} & 0 & 0 & 0 & 0 & -C_{44}^{(1)} & 0 & 0 & C_{34}^{(2)} & 0 & C_{45}^{(2)} & 0 \\ 0 & 0 & -C_{14}^{(3)} & C_{14}^{(4)} & 0 & -C_{24}^{(3)} & 0 & -C_{44}^{(3)} & 0 & 0 & 0 & 0 & 0 \\ -C_{12}^{(1)} & 0 & C_{13}^{(3)} & 0 & -C_{23}^{(1)} & C_{23}^{(3)} & 0 & C_{34}^{(3)} & -C_{22}^{(1)} & 0 & 0 & 0 & 0 \\ 0 & -C_{13}^{(2)} & 0 & C_{13}^{(4)} & 0 & 0 & 0 & 0 & 0 & -C_{33}^{(2)} & 0 & -C_{35}^{(2)} & 0 \\ 0 & 0 & C_{15}^{(3)} & 0 & 0 & C_{25}^{(3)} & 0 & C_{45}^{(3)} & 0 & 0 & -C_{44}^{(1)} & 0 & 0 \\ 0 & -C_{15}^{(2)} & 0 & C_{15}^{(4)} & 0 & 0 & 0 & 0 & 0 & -C_{35}^{(2)} & 0 & -C_{55}^{(2)} & 0 \\ 0 & C_{16}^{(2)} & 0 & 0 & 0 & 0 & 0 & 0 & 0 & C_{36}^{(2)} & 0 & C_{56}^{(2)} & -C_{66}^{(1)} \\ 0 & 0 & C_{16}^{(3)} & 0 & 0 & C_{26}^{(3)} & 0 & C_{46}^{(3)} & 0 & 0 & 0 & 0 & -C_{66}^{(1)} \\ 0 & -C_{16}^{(2)} & 0 & C_{16}^{(4)} & 0 & 0 & 0 & 0 & 0 & -C_{36}^{(2)} & 0 & -C_{56}^{(2)} & 0 \end{bmatrix} \quad (3.20)$$

$$\overline{A}_{bb} = \begin{bmatrix}
C_{22}^{(2)} & 0 & C_{24}^{(2)} & 0 & 0 & 0 & 0 & 0 & C_{26}^{(2)} & 0 & 0 \\
0 & C_{22}^{(4)} & 0 & C_{24}^{(4)} & -C_{23}^{(3)} & C_{23}^{(4)} & -C_{25}^{(3)} & C_{25}^{(4)} & 0 & -C_{26}^{(3)} & C_{26}^{(4)} \\
C_{24}^{(2)} & 0 & C_{44}^{(2)} & 0 & 0 & 0 & 0 & 0 & C_{46}^{(2)} & 0 & 0 \\
0 & C_{24}^{(4)} & 0 & C_{44}^{(4)} & -C_{34}^{(3)} & C_{34}^{(4)} & -C_{45}^{(3)} & C_{45}^{(4)} & 0 & -C_{46}^{(3)} & C_{46}^{(4)} \\
0 & 0 & 0 & 0 & C_{33}^{(3)} & 0 & C_{35}^{(3)} & 0 & 0 & C_{36}^{(3)} & 0 \\
-C_{23}^{(2)} & C_{23}^{(4)} & -C_{34}^{(2)} & C_{34}^{(4)} & 0 & C_{33}^{(4)} & 0 & C_{35}^{(4)} & -C_{36}^{(2)} & 0 & C_{36}^{(4)} \\
0 & 0 & 0 & 0 & C_{35}^{(3)} & 0 & C_{55}^{(3)} & 0 & 0 & C_{56}^{(3)} & 0 \\
-C_{25}^{(2)} & C_{25}^{(4)} & -C_{45}^{(2)} & C_{45}^{(4)} & 0 & C_{35}^{(4)} & 0 & C_{55}^{(4)} & -C_{56}^{(2)} & 0 & C_{56}^{(4)} \\
C_{26}^{(2)} & 0 & C_{46}^{(2)} & 0 & 0 & 0 & 0 & 0 & C_{66}^{(2)} & 0 & 0 \\
0 & 0 & 0 & 0 & C_{36}^{(3)} & 0 & C_{56}^{(3)} & 0 & 0 & C_{66}^{(3)} & 0 \\
-C_{26}^{(2)} & C_{26}^{(4)} & -C_{46}^{(2)} & C_{46}^{(4)} & 0 & C_{36}^{(4)} & 0 & C_{56}^{(4)} & -C_{66}^{(2)} & 0 & C_{66}^{(4)}
\end{bmatrix} \tag{3.21}$$

The non-zero terms of $\overline{D}_a$ are:

$$\begin{aligned}
&\overline{D}_a(1,1) = \overline{D}_a(2,1) = \overline{D}_a(3,1) = \overline{D}_a(4,1) = 1 \\
&\overline{D}_a(5,2) = \overline{D}_a(6,2) = \overline{D}_a(7,4) = \overline{D}_a(8,4) = \frac{1}{h} \\
&\overline{D}_a(9,3) = \overline{D}_a(10,3) = \overline{D}_a(11,5) = \overline{D}_a(12,5) = \frac{1}{b} \\
&\overline{D}_a(13,6) = \frac{1}{b\,h}
\end{aligned} \tag{3.22}$$

Only the inverse of the (11x11) sub-matrix in Eqs. (3.18) is needed to solve for $d\varepsilon_a$ and $d\varepsilon_b$.

The strain-concentration matrices are determined by solving $dR_\sigma = 0$ and $dR_\varepsilon = 0$.

Stress Correction Algorithm

The micromechanical relations are derived in incremental formulation, are exact only in the case of linear constitutive model in all of the subcells. Due to the nonlinear and time-dependent response in the matrix subcells, the incremental relations will usually violate the constitutive equations. An iterative correction scheme is needed in order to satisfy both the micromechanical constraints and the constitutive equations. The stress correction algorithm consists of a predictor step, which give a trial elastic stress-strain states, and a corrector step, which corrects the trial elastic stress-strain states. If only the predictor step is performed, two types of errors will result at each trial increment, and will accumulate during the analysis. The first error occurs in the strain increments because the strain-increment matrices are derived using the tangent stiffness of the subcells at the beginning of the increment. The second error occurs as a result of using the tangent stiffness to compute the stress increment. The key general idea is to use the incremental micromechanical relations with tangential material matrices for generating trial incremental stresses and strains for the subcells (trial solution). The total micromechanical relations are then used to define a residual error for all subcells. This residual is then used to correct the trial solution. The tasks for the micromechanical algorithm can be states as: given history variables in the subcells from previous converged solution and incremental effective strain for the unit-cell, update the effective stress, effective stiffness, and history variables at the end of the increment. The complete numerical algorithm, which is used to provide the correct stress and its corresponding nonlinear parameters for a given strain increment, is presented in Figure 3.2.

1. Input variables

$$\Delta\bar{\varepsilon}_{ij}^{t} \quad , \bar{\sigma}_{ij}^{t-\Delta t} \quad , \Delta t \quad , \text{Hist}^{t-\Delta t} : \quad \varepsilon_{ij}^{(\alpha),\,t-\Delta t} \quad , \sigma_{ij}^{(\alpha),\,t-\Delta t} \quad , \alpha = 1, 2, 3, 4$$

$$q_{ij,n}^{(\beta),\,t-\Delta t} \quad , q_{kk,n}^{(\beta),\,t-\Delta t} \quad , \beta = 2, 3, 4$$

2. Initialize linearized state

$$C^{(\alpha),\,t-\Delta t} = C^{(\alpha),\,t-\Delta t}\,(\text{Hist}^{t-\Delta t})$$

$$B^{(\alpha),\,t,tr} = B^{(\alpha),\,t,tr}\,(\,v^{(\alpha)}, C^{(\alpha),\,t-\Delta t}\,)$$

$$\Delta\varepsilon^{(\alpha),\,t,(0)} = \Delta\varepsilon^{(\alpha),\,t,tr} = B^{(\alpha),\,t,tr}\,\Delta\bar{\varepsilon}^{t}$$

3. Iterate for k=1, 2, 3....

3.1 Evaluate stresses at all subcells

CALL Algorithm in Figure 2.2 to get $\sigma_{ij}^{(\alpha),\,t,(k+1)}$, $C^{(\alpha),\,t,(k)}$

3.2 Compute strain correction

$$\delta\Delta\varepsilon^{(\alpha),t,(k+1)} = \begin{Bmatrix} \delta\Delta\varepsilon_a \\ \hline \delta\Delta\varepsilon_b \end{Bmatrix}^{t,\,(k+1)} = -\left[\begin{array}{c|c} \mathbf{I} & \bar{A}_{ab} \\ \hline \bar{A}_{ba} & \bar{A}_{bb} \end{array}\right]^{t,\,(k),\,-1} \begin{Bmatrix} R_\varepsilon \\ \hline R_\sigma \end{Bmatrix}^{t,(k)}$$

$$\Delta\varepsilon^{(\alpha),\,t,\,(k+1)} = \Delta\varepsilon^{(\alpha),\,t,\,(k)} + \delta\Delta\varepsilon^{(\alpha),\,t,\,(k+1)}$$

3.3 Evaluate residual vector $R^{t,(k)} = (\,R_\varepsilon, R_\sigma\,)$ from Eq. (3.18).

IF $\|\,R^{t,(k)}\,\| \le$ Tol THEN GOTO 4 and EXIT

ENDIF GOTO 3

4. Update effective stress, consistent tangent stiffness, and history variables

$$\bar{\sigma}_{ij}^{t} \leftarrow \bar{\sigma}_{ij}^{t,(k+1)} \qquad \bar{C}_{ij}^{t} \leftarrow \bar{C}_{ij}^{t,(k+1)}$$

$$\varepsilon_{ij}^{(\alpha),\,t} \leftarrow \varepsilon_{ij}^{(\alpha),\,t,(k+1)} \quad , \sigma_{ij}^{(\alpha),\,t} \leftarrow \sigma_{ij}^{(\alpha),\,t,(k+1)} \quad , \alpha = 1, 2, 3, 4$$

$$q_{ij,n}^{(\beta),\,t} \leftarrow q_{ij,n}^{(\beta),\,t,(k+1)} \quad , q_{kk,n}^{(\beta),\,t} \leftarrow q_{kk,n}^{(\beta),\,t,(k+1)} \quad , \beta = 2, 3, 4$$

Figure 3.2 A micromechanical recursive-iterative integration algorithm for nonlinear viscoelastic behavior in laminated composite.

3.2 Validation of the Nonlinear Constitutive Framework

The proposed modeling framework is examined in its ability to predict the nonlinear viscoelastic behavior of composite materials and structures. The effective response is generated from calibrated in-situ properties of the matrix and fiber constituents. To that end, different creep tests on laminated composites available in the literature are used. Off-axis test results are available for glass/epoxy (Lou and Schapery, 1971) and T300/5208 graphite/epoxy (Tuttle and Brinson, 1986) composites. Prediction of the calibrated model is examined against test results that are not used in the calibration process. Thermomechanical creep test on T300/934 graphite/epoxy (Hiel et al. 1983) is also examined in order to predict long-term responses. Finally, the aging effect on creep response of IM7/977-3 (Hu and Sun, 2000) is characterized.

Glass/epoxy laminated composites

The creep data for glass/epoxy off-axis coupon tests reported by Lou and Schapery (1971) are used for validation of the current modeling approach. Five sets of specimens with different fiber orientations: 0^o, 30^o, 45^o, 60^o, and 90^o were tested at 164^oF and 21% humidity. The FVF of these specimens is 47.6%. The elastic fiber and the calibrated elastic matrix properties are shown in Table 3.1. The linear elastic effective compliances for all off-axis coupon tests compared with the micromodel predictions are shown in Figure 3.3. One hour creep test data were reproduced from a given fitted equations of linear creep compliance combined with the corresponding nonlinear parameters for each off-axis test. The nonlinear material properties g_0, g_1, g_2, and a_σ are stress dependent, which are expressed as functions of an average octahedral shear stress in the plastic matrix.

Table 3.1 Glass and epoxy elastic material properties, ν_f=0.476.

	E GPa (ksi)	ν
Glass Fiber	72.4 (10500)	0.22
Epoxy Matrix	4.3 (620)	0.31

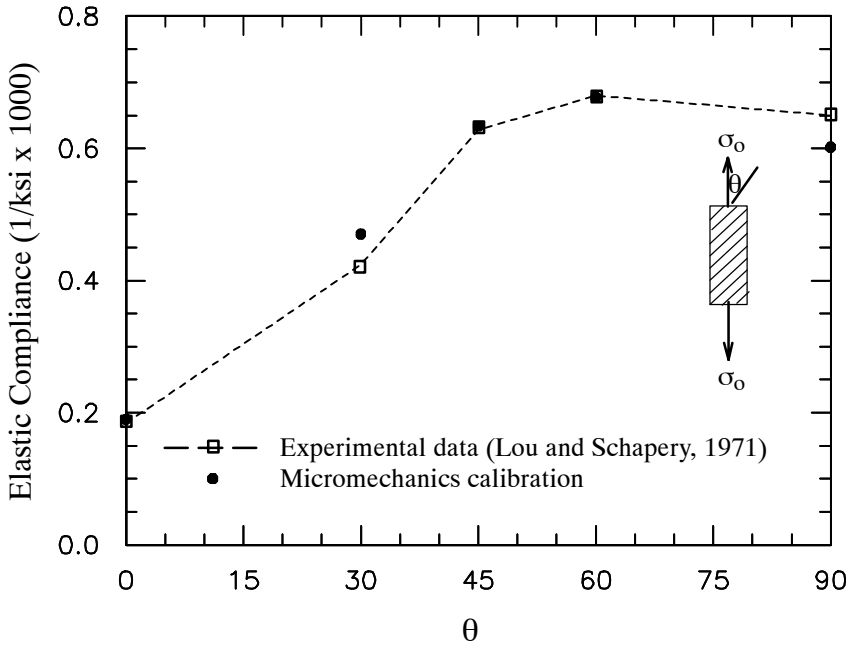

Figure 3.3 Elastic compliance from glass/epoxy off-axis coupon test.

Lou and Schapery (1971) derived a simple micromechanical relation for the average octahedral matrix stress in a lamina subjected to a plane stress state. Fibers are relatively stiff, such that the strain along fiber direction is negligible, $\varepsilon_x \simeq 0$. Thus, the stress components in the matrix are expressed as:

$$\sigma_{yy}^m = \sigma_y \qquad \sigma_{xx}^m = \nu_m \sigma_{yy} \qquad \tau_{xy}^m = \tau_{xy}$$
$$\text{where} \quad \sigma_y = \sigma_o \sin^2\theta \quad \text{and} \quad \tau_{xy} = -\frac{\sigma_o}{2}\sin 2\theta \tag{3.23}$$

where ν_m is the matrix Poisson's ratio and σ_o is the axial applied stress. The octahedral shear stress in the matrix is defined by:

$$\bar{\sigma} = \tau_{oct} = \sqrt{\frac{2}{3\gamma}\left[\sigma_{yy}^{m\,2} + \gamma\,\tau_{xy}^{m\,2}\right]} \qquad \gamma \equiv \frac{3}{1 - \nu_m + \nu_m^2} \tag{3.24}$$

The matrix octahedral shear stress was proposed as the nonlinear stress-variable used in the Schapery viscoelastic integral applied for the overall strain-stress relations of a lamina. Excellent creep and predictions were demonstrated by Lou and Schapery's modeling approach. The current approach is similar but employs a refined 3D micromodel that can ultimately be used in both 2D and 3D structural models. The matrix octahedral shear stresses is plotted as function of the off-axis fiber orientation along with a mean stress from the simplified micromodel of Lou and Schapery (1971) and the current four-cell micromodel, as illustrated in Figure 3.4. It is clear that in the case of plane-stress, the effective stress in subcell-2 is a good matrix that can be used as an equivalent stress measured and represents the nonlinear behavior. The advantage of using four-cell model is that subcell-3 can have the same nonlinear response for a general 3D stress state.

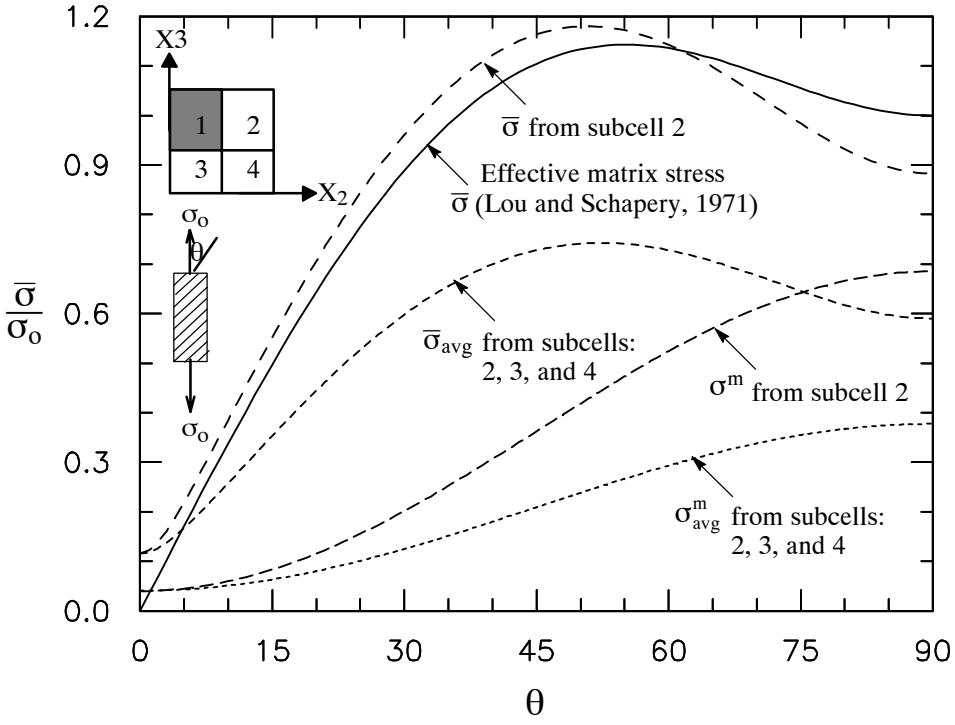

Figure 3.4 Normalized matrix octahedral stress vs off-axis angle.

The linear and nonlinear calibrations of the in-situ viscoelastic parameters of the matrix are carried out. Linear viscoelastic calibration was performed using results from the 45° off-axis specimen under the lowest applied axial stress (1.382 ksi). The Prony series coefficients were calibrated until the overall response matches with the experimental data. The inverse of the retardation times (λ_n) were chosen as $\lambda_n = 10^{1-n}$. The results from Prony series calibration are shown in Tabel 3.2. The limit for the matrix linear viscoelastic response, $\bar{\sigma}_o$ in Eq. (2.45), was determined from the different linear creep responses to be 1.4 ksi. The viscoelastic parameter g_0 was calibrated using second order polynomial function from the 45° off-axis test for applied stress of 3.448 ksi, as shown in Figure 3.5. Other creep responses for the same angle were also monitored during the calibration. The same process was repeated in the calibration of g_2 using the 30° off-axis test results. An effort was made to match the creep in both curves with applied stress levels of 6.897 ksi and 8.058 ksi. Overall the nonlinear calibration strikes a balance between all nonlinear curves as seen in Figure 3.6. The calibrated polynomial coefficients are shown in Figure 3.7. The parameters g_1 and a_σ are fixed to one. The predicted results are close to the experimental data as shown in Figures 3.8 and 3.9 for 60° and 90° off-axis coupons, respectively.

Table 3.2 Calibrated Prony series coefficients for the epoxy matrix.

n	λ_n (sec^{-1})	D_n x 10^{-6} MPa^{-1} (ksi^{-1})
1	1	2.18 (15.0)
2	10^{-1}	4.87 (33.6)
3	10^{-2}	5.08 (35.0)
4	10^{-3}	6.64 (45.8)
5	10^{-4}	1.83 (12.6)
6	10^{-5}	2.90 (20.0)

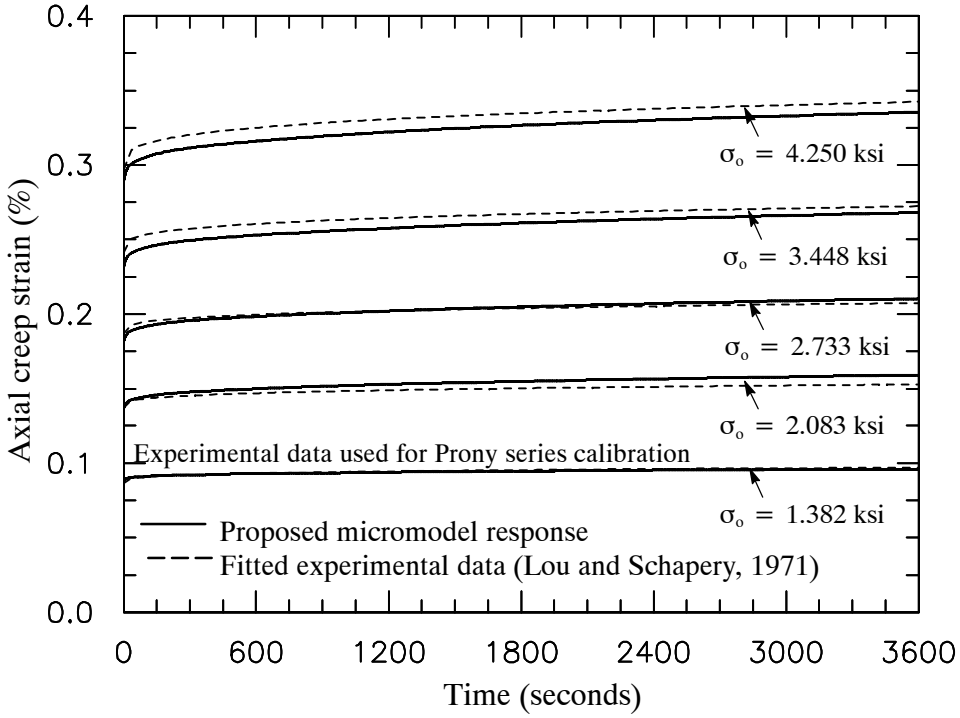

Figure 3.5 Axial creep strain for 45º off axis coupons.

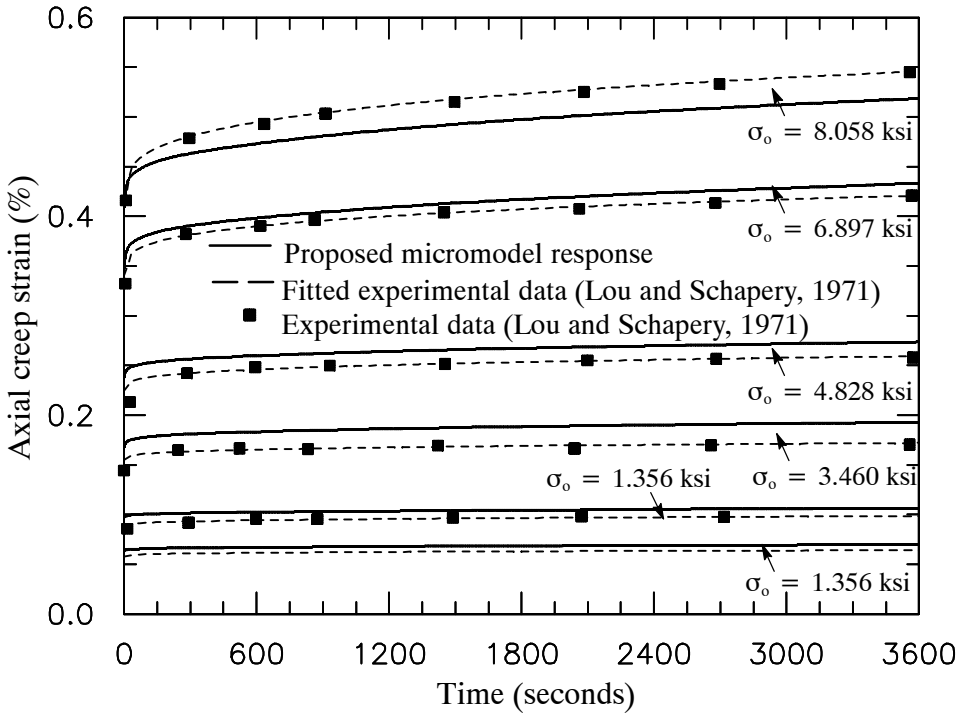

Figure 3.6 Axial creep strain for 30º off axis coupons.

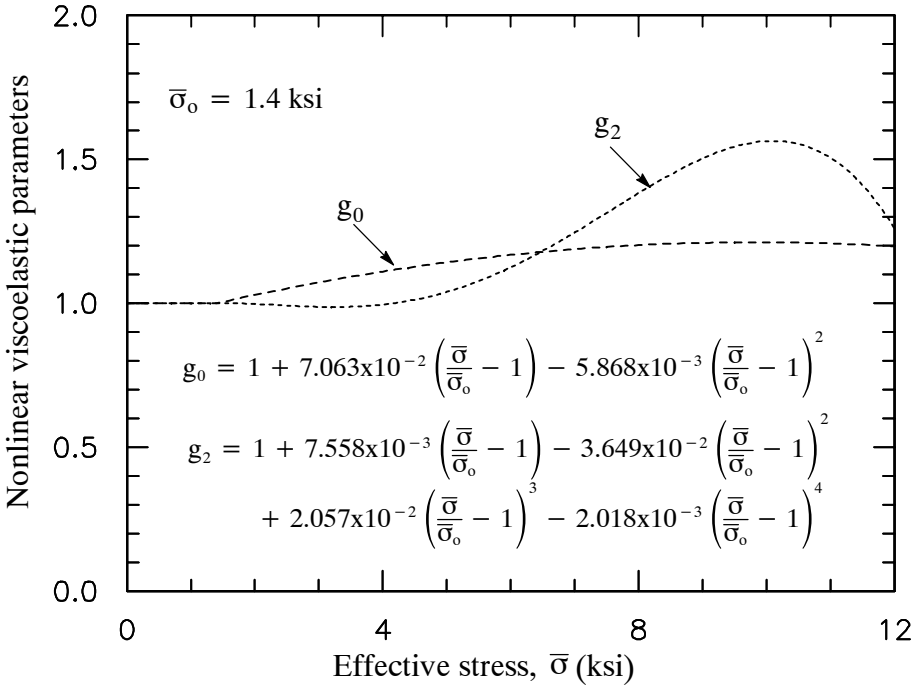

Figure 3.7 Nonlinear viscoelastic parameters in the Schapery's equations.

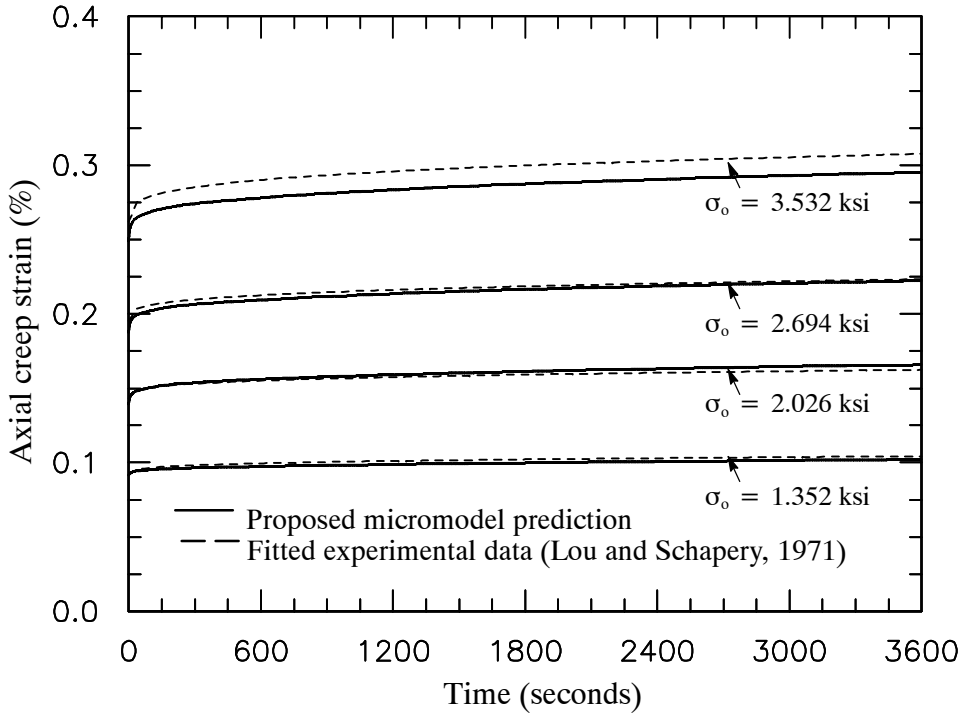

Figure 3.8 Axial creep strain for 60° off axis coupons.

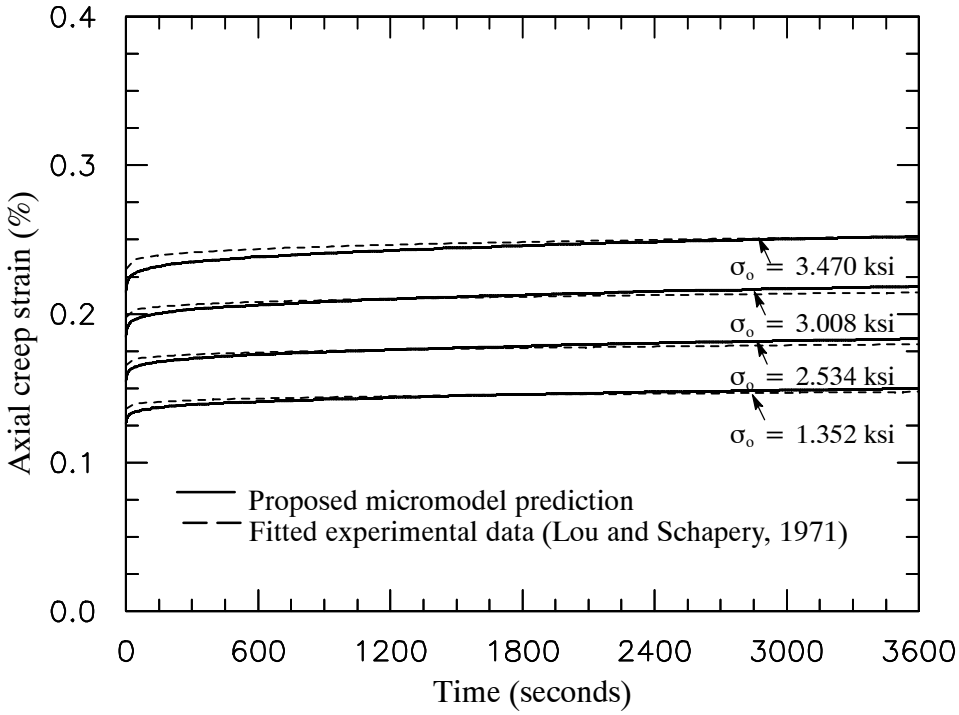

Figure 3.9 Axial creep strain for 90° off axis coupons.

T300/5208 graphite/epoxy laminated composites

Another creep test performed by Tuttle and Brinson (1986) on T300/5208 graphite/epoxy is used to examine the micromodel. Off-axis specimens with 10° and 90° fiber orientations were subjected to 480 minutes creep tests. Transverse creep responses were determined from 90° off-axis specimen under several axial tensile loads (10.5 - 20.7 MPa). Shear creep responses were performed on 10° off-axis coupon under several shear stresses (2.9 - 32.5 MPa). The creep tests were reproduced from the fitted linear creep data combined with the reported nonlinear parameters for each transverse and shear responses. The elastic properties for graphite and epoxy are given in Table 3.3. The effective properties of T300/5208 composites with FVF of 0.65 are shown in Table 3.4.

Table 3.3 Elastic material properties for T300 Graphite and 5208 Epoxy.

	E_{11}	E_{22}	G_{12}	ν_{12}	ν_{23}
	GPa (ksi)				
Fiber (T300 - Graphite)	200 (29000)	13 (1886)	44 (6382)	0.39	0.40
Matrix (5208 Epoxy)	4.6 (667)			0.35	

Table 3.4 Elastic properties for T300/5208 Graphite-Epoxy Lamina, v_f=0.65.

	E_{11}	E_{22}	G_{12}	ν_{12}	ν_{23}
	GPa (ksi)				
Experimental data (Tuttle and Brinson, 1986)	132.2 (19174)	9.434 (1368)	6.410 (930)	0.273	
Micromodel (four-cell model)	131.6 (19087)	9.434 (1368)	6.435 (933)	0.377	0.425

Linear viscoelastic calibration was performed from 10^o off-axis coupon under the lowest applied shear stress (2.9 MPa), as shown in Figure 3.10. Prony series coefficients with four terms were calibrated, as seen in Table 3.5. The viscoelastic parameters, g_0, g_2, and a_σ were also calibrated from the 10^o off-axis creep results. The calibrated results are shown in Figure 3.11. The linear viscoelastic limit of the matrix effective stress, $\bar{\sigma}_o$, was determined as 25 MPa. Good predictions from the proposed micromodel are shown in Figures 3.10 and 3.12 for the shear and transverse creep responses, respectively.

Table 3.5 Calibrated Prony series coefficients for the 5208 epoxy matrix.

n	λ_n $\left(\text{min}^{-1}\right)$	D_n short-term creep (480 min) x 10^{-6} MPa^{-1} (ksi^{-1})
1	1	8.50 (58.61)
2	10^{-1}	8.36 (57.64)
3	10^{-2}	5.50 (37.92)
4	10^{-3}	33.80 (233.04)

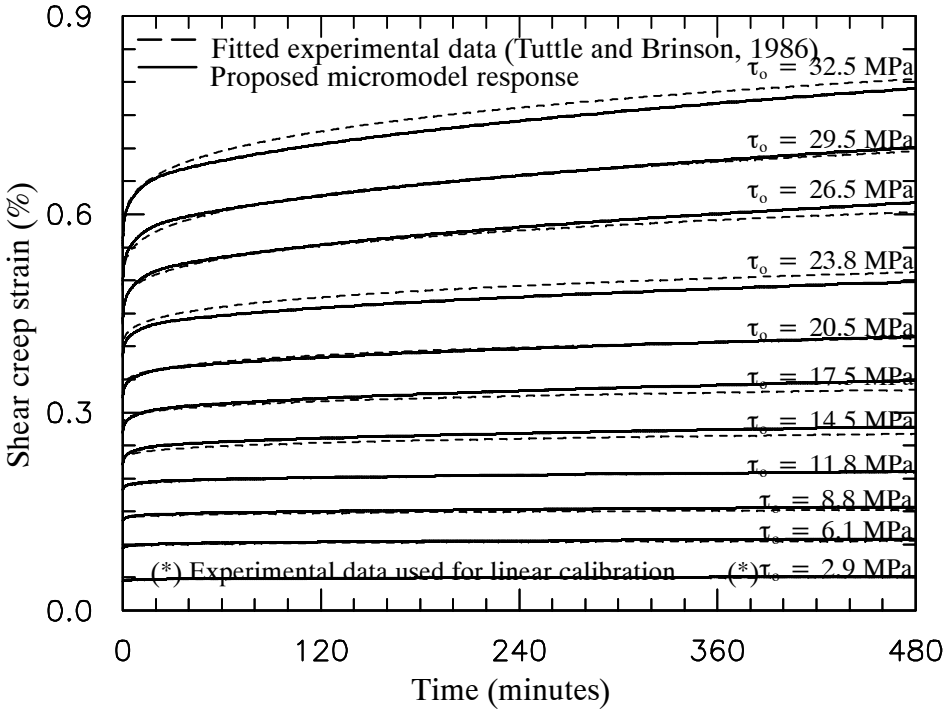

Figure 3.10 Shear creep strain from 10° off-axis specimens.

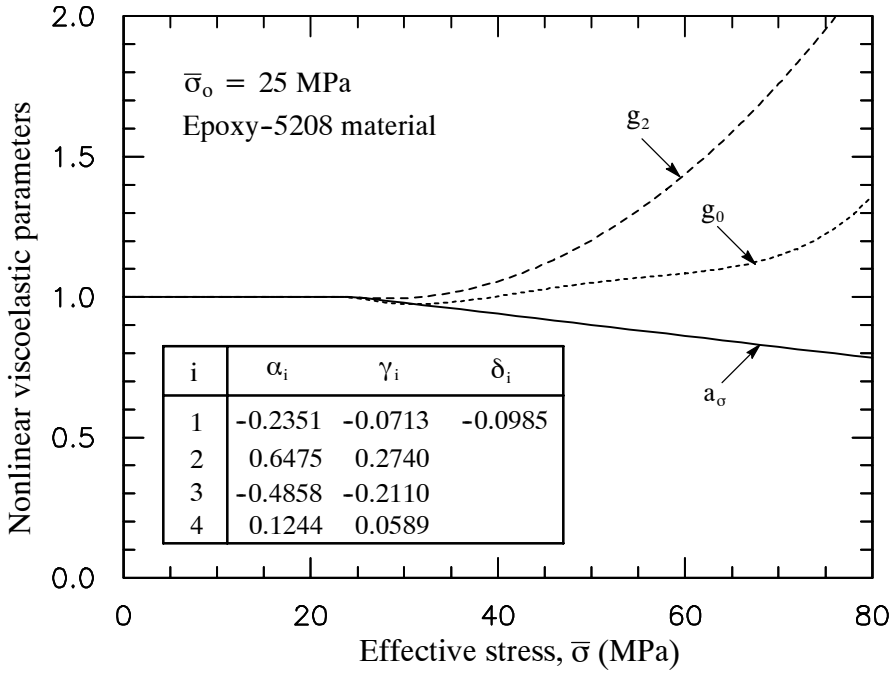

Figure 3.11 In-situ nonlinear viscoelastic parameters as function of the effective stress for epoxy (5208) matrix.

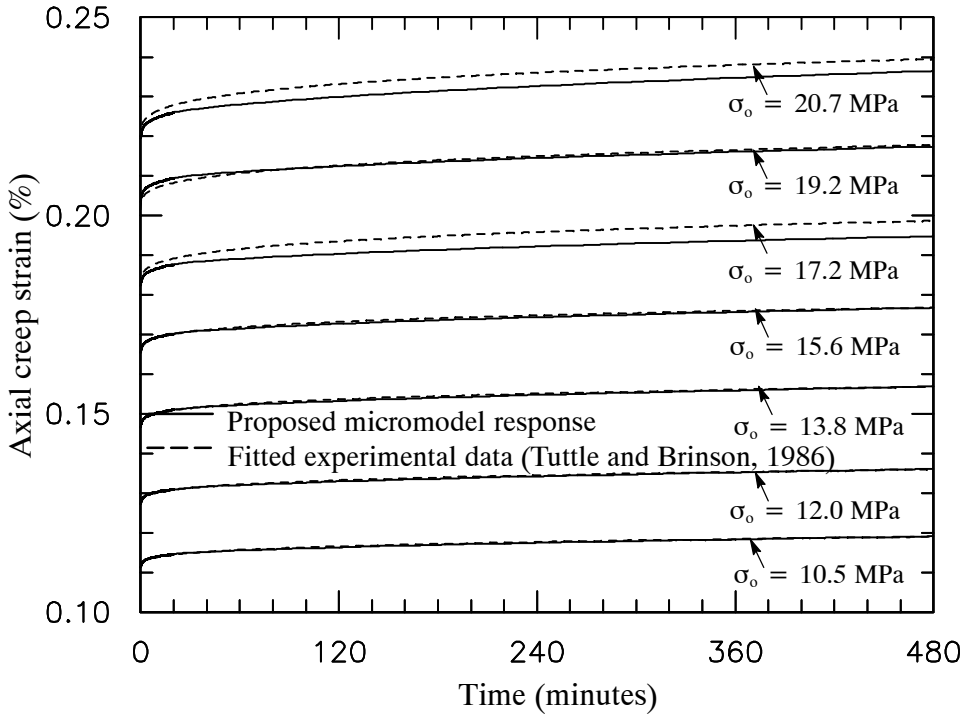

Figure 3.12 Axial creep strain from transverse specimens.

Long-term Creep Behavior of T300/934 Graphite/Epoxy Composites

Long-term experimental creep tests under shear loading reported by Hiel et al. (1983) are used to characterize the time-dependent properties of T300/934 graphite/epoxy composites. Coupon tests have an average FVF of 60%. The elastic properties of fiber and matrix are listed in Table 3.6. Tensile creep tests were conducted at different temperatures: 119°C, 148°C, 160°C, and 168°C. At each temperature, short term creep tests (less than 100 minutes) were performed under several load levels. Shear compliance master curve was created using time-stress-superposition principle (TSSP) with a reference temperature of 119°C. The compliance master curve can be used to predict the long-term creep responses up to 5 days, as illustrated in Figure 3.13.

Next, the calibrated lamina viscoelastic macro-response of Hiel et al. (1983) was used to calibrate the linear and nonlinear viscoelastic in-situ parameters for the matrix constituents. A Prony series at the matrix has been calibrated to match the master curve in Figure 3.13. The inverse of the retardation times (λ_n) were chosen as $\lambda_n = 10^{1-n}$. The parameters used in the Prony series are shown in Table 3.7. Hiel et al. (1983) creep test data, in the form of linear creep compliance (power law) combined with nonlinear parameters (g_1 and g_2) for each stress levels, was then used for the in-situ calibration of nonlinear stress-dependent parameters. The reproduced creep data for various stress levels at temperature 119°C are shown in Figure 3.14. The nonlinear viscoelastic parameters were calibrated from shear creep test by matching the overall creep data at different stress levels as shown in Figure 3.14. The calibrated nonlinear parameters are given in Figure 3.15. The limit for the matrix linear viscoelastic response, $\bar{\sigma}_o$, was determined to be 2.9 ksi.

Table 3.6 Elastic material properties for T300 Graphite and 934 Epoxy.

	E_{11}	E_{22}	G_{12}	ν_{12}	ν_{23}
	GPa (ksi)				
Fiber (T300 - Graphite)	200 (29000)	26 (3772)	44 (6382)	0.39	0.40
Matrix (5208 Epoxy)	5.0 (725)			0.35	

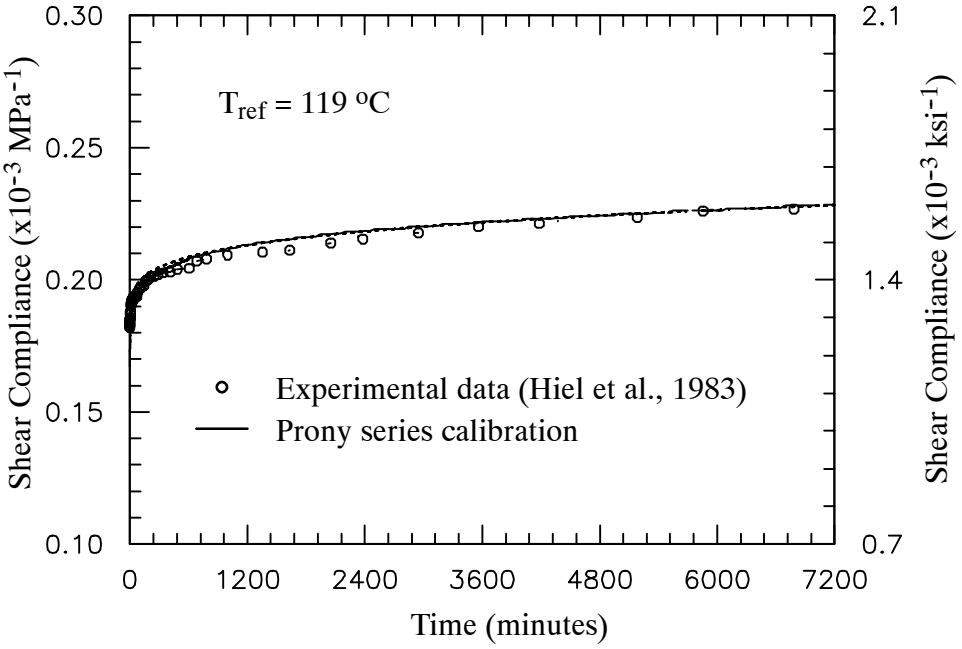

Figure 3.13 Shear compliance master curve at 119°C.

Table 3.7 Calibrated Prony series coefficients for the epoxy-934 matrix.

n	λ_n (min^{-1})	D_n x 10^{-5} MPa^{-1} (ksi^{-1})
1	1	1.00 (6.89)
2	10^{-1}	1.86 (12.82)
3	10^{-2}	1.10 (7.58)
4	10^{-3}	1.88 (12.96)
5	10^{-4}	2.86 (19.72)
6	10^{-5}	3.00 (20.68)

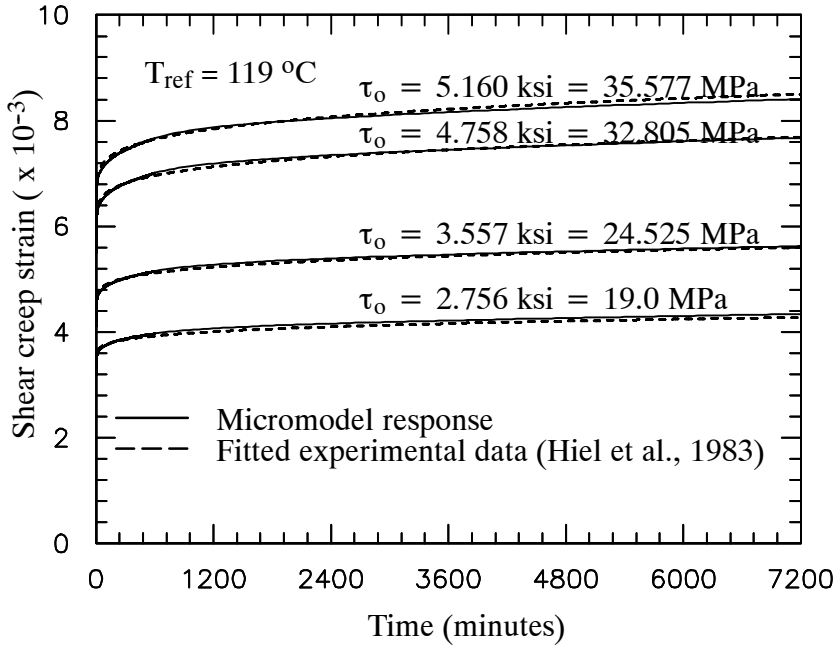

Figure 3.14 Shear creep strain at 119^{o}C.

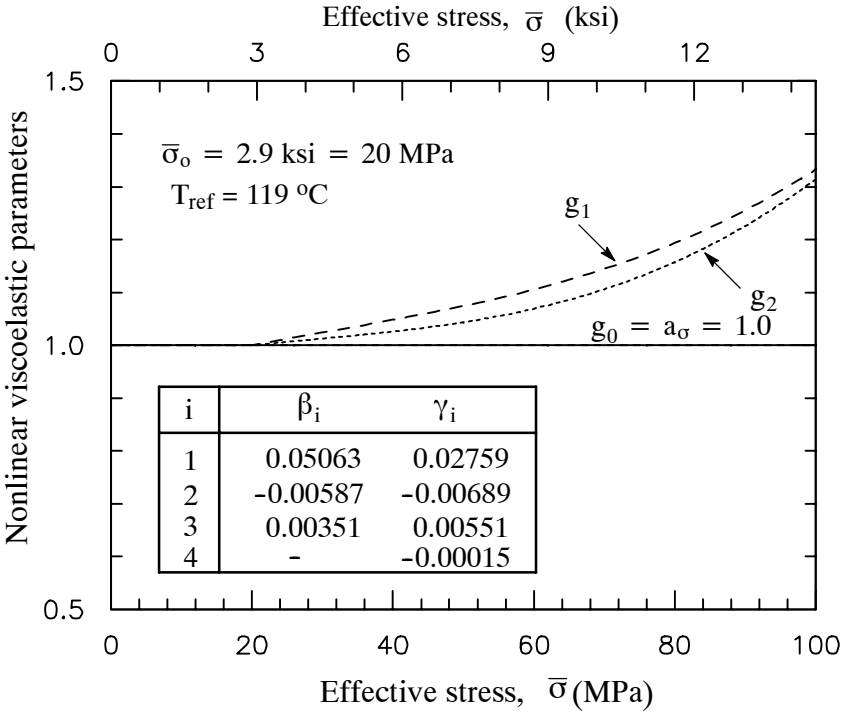

Figure 3.15 Nonlinear parameters for epoxy-934 matrix.

The effect of temperature on the creep responses was also studied by Hiel et al. (1983). Creep tests were performed at several temperatures: 119°C, 148°C, 160°C, and 168°C. At each temperature, experimental creep data are reported for stress levels: 1 to 5 ksi. The in-situ temperature shift factor, a_T, given in Eq. (2.29), was calibrated by matching the creep data at stress level 4.5 ksi for all tests under T=148°C, 160°C, and 168°C. Figure 3.16 shows the calibrated temperature shift factors. The a_T parameter at the reference temperature (T_{ref}=119°C) is equal to one. The creep strain predictions for different stress levels, at all temperatures, are given in Figure 3.17.

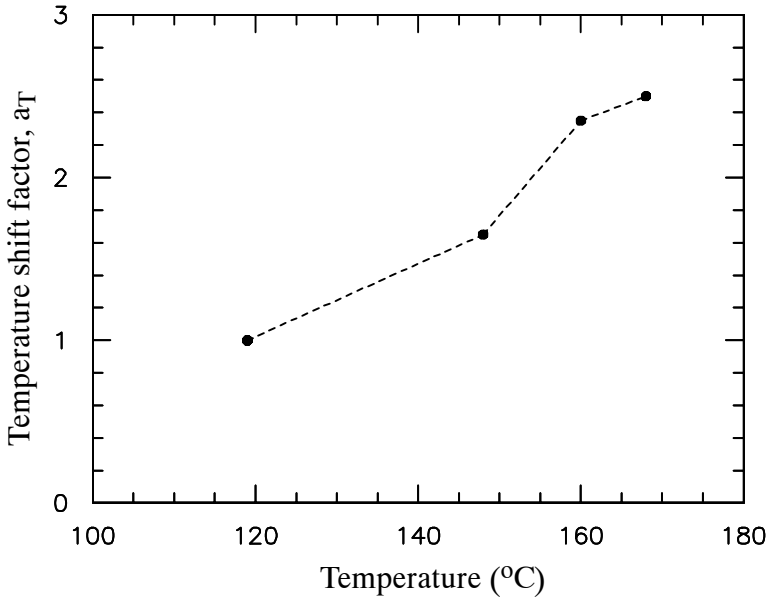

Figure 3.16 Temperature shift factor for epoxy-934 matrix.

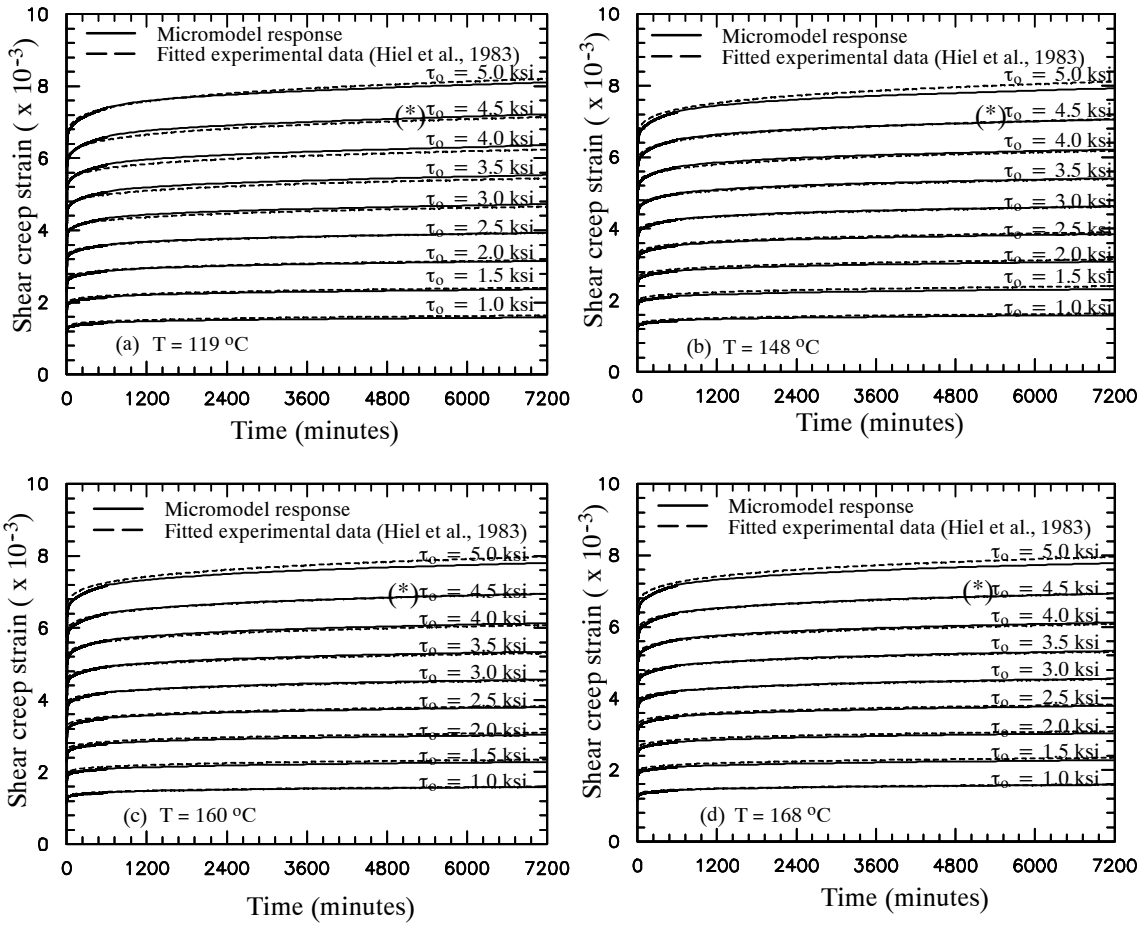

Figure 3.17 Creep shear strain curves (a) T=119°C, (b) T=148°C, (c) T=160°C, and (d) T=168°C. (* experimental data used for temperature shift factor calibration)

Physical Aging Effect on the creep of Off-axis Specimens

Hu and Sun (2000) investigated the effect of physical aging on IM7/977-3 graphite/ epoxy laminated plates. Physical aging affects both the initial elastic and creep compliances. In this study, the physical aging effect on the linear creep responses is considered and implemented in the viscoelastic constitutive framework. The experimental data reported by Hu and Sun (2000) is used to calibrate and validate the prediction of the micromodel with an aging matrix. Four sets of off-axis specimens with different fiber orientations: 15°, 30°, 45°, and 90° were aged for different aging times, t_e: 5, 12, 24, 48, 72, and 96 hours. Creep tests were then conducted for times less than 1/10 of their aging time. Relatively low axial tensile

loads, with magnitudes: 43.4, 23.5, 19.7, and 15.2 MPa, were applied to the 15°, 30°, 45°, and 90° off-axis coupons, respectively. The linear elastic effective compliances for each off-axis test are shown in Figure 3.18. The elastic compliances are defined at aging time t_e=5 hours. The compliances in the axial and transverse specimen were used to calibrate the in-situ elastic properties of the fiber and matrix. Figure 3.18 also shows the predicted effective elastic compliance from the micromodel along with test data for the off-axis specimen. Table 3.8 includes the calibrated elastic properties for the IM7 fiber and 977-3 matrix used in the micromodel.

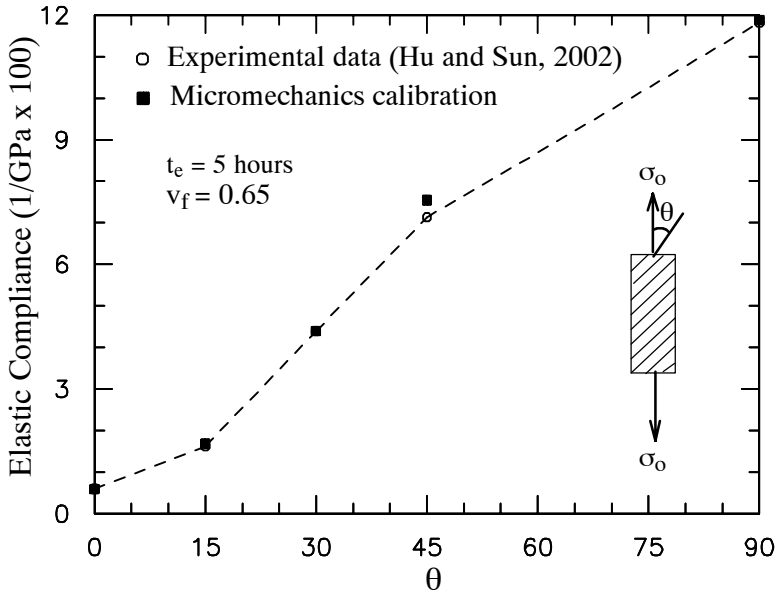

Figure 3.18 Elastic compliance from IM7/977-3 off-axis coupon test at t_e=5 hours.

Table 3.8 Elastic material properties for IM7 Graphite and 977-3 Epoxy.

	E_{11}	E_{22}	G_{12}	ν_{12}	ν_{23}
	GPa (ksi)				
IM7 Fiber	256 (37129)	14.6 (2118)	56.6 (8209)	0.25	0.30
977-3 Matrix	3.5 (508)			0.25	

Next, the matrix viscoelastic parameters are calibrated to model the aging effect on the elastic and transient creep responses. Elastic and transient creep experimental data are reproduced from the fitted experimental equations of Hu and Sun (2000). Their experimental results show that elastic compliances of all off-axis specimens decrease as aging time increases. Therefore, the matrix Young's modulus in the micromodel is modified to account for the effect of aging time. In this study, a Prony series is used to describe the matrix modulus as a function of aging time:

$$E_m^{t_e} = E_m\left[1 + \sum_{k=1}^{K} A_k \exp\left(-\frac{\omega_k}{t_e - t_{e,ref}}\right)\right] \tag{3.25}$$

where E_m is the initial matrix Young's modulus at reference time as shown in Table 3.8. The terms A_k and ω_k were calibrated from the 90^o off-axis coupon tests. Two terms are used in the above equation: $(A_1, \omega_1) = (0.08, 140.5)$ and $(A_2, \omega_2) = (0.01, 10.5)$. The calibrated and predicted elastic compliances as a function of aging time are shown in Figure 3.19 for different off-axis specimens. Good prediction is shown by the micromodel when the aging effect is attributed to the matrix Young's modulus. The transient creep parameters were calibrated from 45^o off-axis coupon at the reference aging time, t_e=5 hours. Prony series coefficients with six terms are used for the in-situ matrix, as seen in Table 3.9.

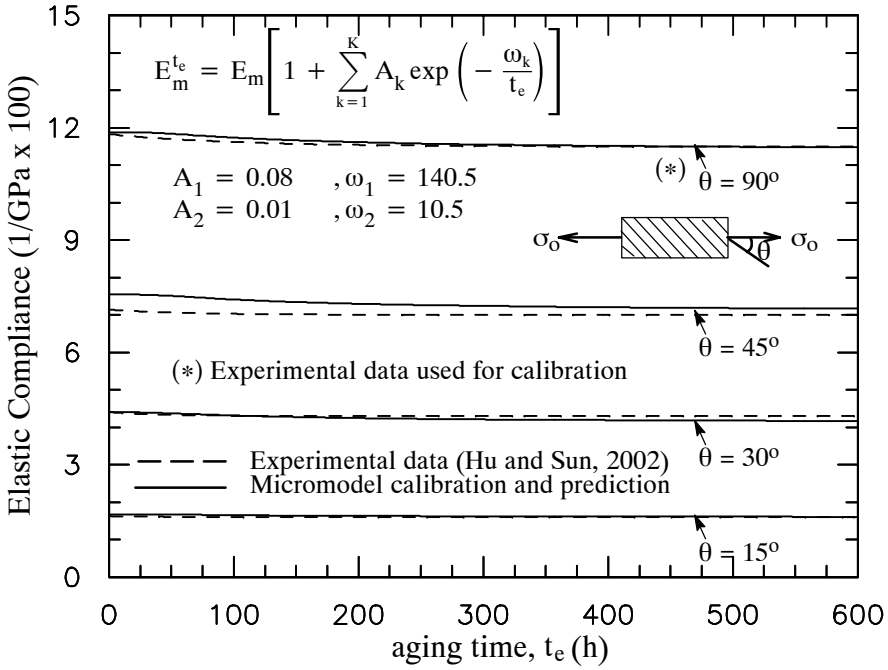

Figure 3.19 Elastic compliance from IM7/977-3 off-axis coupon versus aging time.

Table 3.9 Calibrated Prony series coefficients for the 977-3 epoxy matrix.

n	λ_n (sec^{-1})	D_n x 10^{-6} MPa^{-1} (ksi^{-1})	
1	1	1.00	(6.89)
2	10^{-1}	3.36	(23.17)
3	10^{-2}	3.50	(24.13)
4	10^{-3}	4.58	(31.58)
5	10^{-4}	32.60	(224.77)
6	10^{-5}	20.00	(137.89)

The aging shift rate, μ, Eq. (2.62), is used to characterize the aging effect on the transient creep response. The acceleration factor, a_{te}, is characterized at each sampled aging time. The inverse of the acceleration factor a_{te}, Eq. (2.61), is called the aging time-scale factor, a_e, used in Eq. (2.29). The 45° off-axis creep tests, given at t_e: 12, 24, 48, 72, and 96 hours were used to calibrate the matrix aging parameters. An a_e value for the in-situ matrix was

determined such that the overall creep from the micromodel exactly matches the 45° off-axis creep at each sampled aging time. The calibrated aging time-scale is shown in logarithmic scale in Figure 3.20. The slope from a linear regression determines the aging shift rate, μ, which in this case is 0.5827. The calibrated transient creep curves for the five sampled aging times are shown in Figure 3.22. The results show that using a constant aging shift rate is not sufficient to capture the creep response for aging times larger than the reference time. In order to correct this mismatch, the previously calibrated five aging time-scale values are used to yield a separate μ value for each case. Next, the new five μ values were assumed to be part of a polynomial function of t_e. The calibrated aging shift factor is shown in Figure 3.21 and it is strongly dependent on aging time. Figure 3.22 shows the creep response for 45° off-axis using the new calibrated aging time-scale with the $\mu(t_e)$ polynomial function. In this case the creep response is better matched when using a non-constant aging shift rate. Next, the creep response is predicted by the micromodel and examined for aged off-axis specimen, θ =15°, 30°, 45°, and 90°, that are not used in the calibration process. Figure 3.23 shows the transient creep strains for all off-axis cases taken at different aging times. Figure 3.24 shows the total creep strains for the same off-axis samples to demonstrate the ability of the proposed modeling approach in capturing the initial elastic strains. The aging model of the matrix in the micromodel is capable of capturing the overall multi-axial creep-aging effect of the lamina.

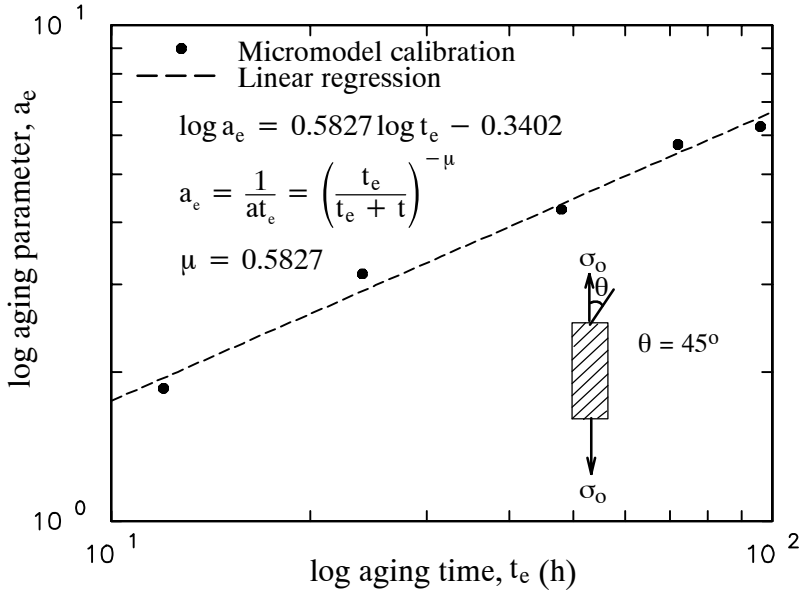

Figure 3.20 Logarithmic plot of aging parameter versus aging time.

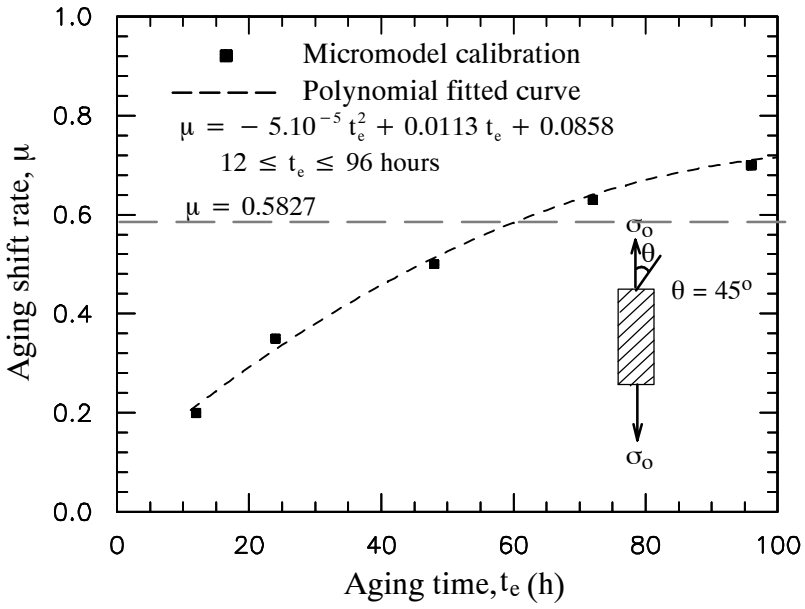

Figure 3.21 Shift rate factor versus aging time.

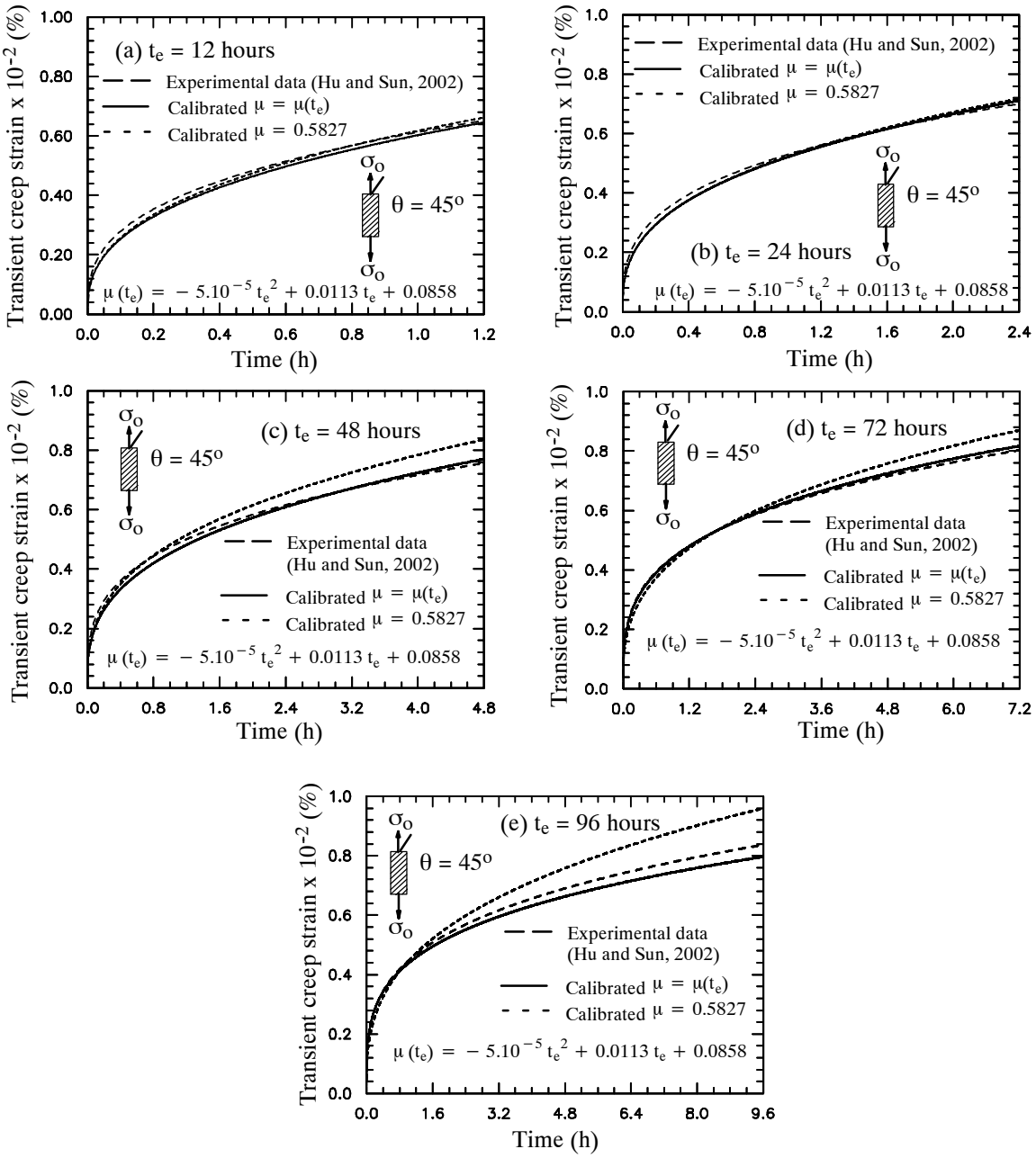

Figure 3.22 Calibrated creep strain from 45º off-axis coupon at various aging time.

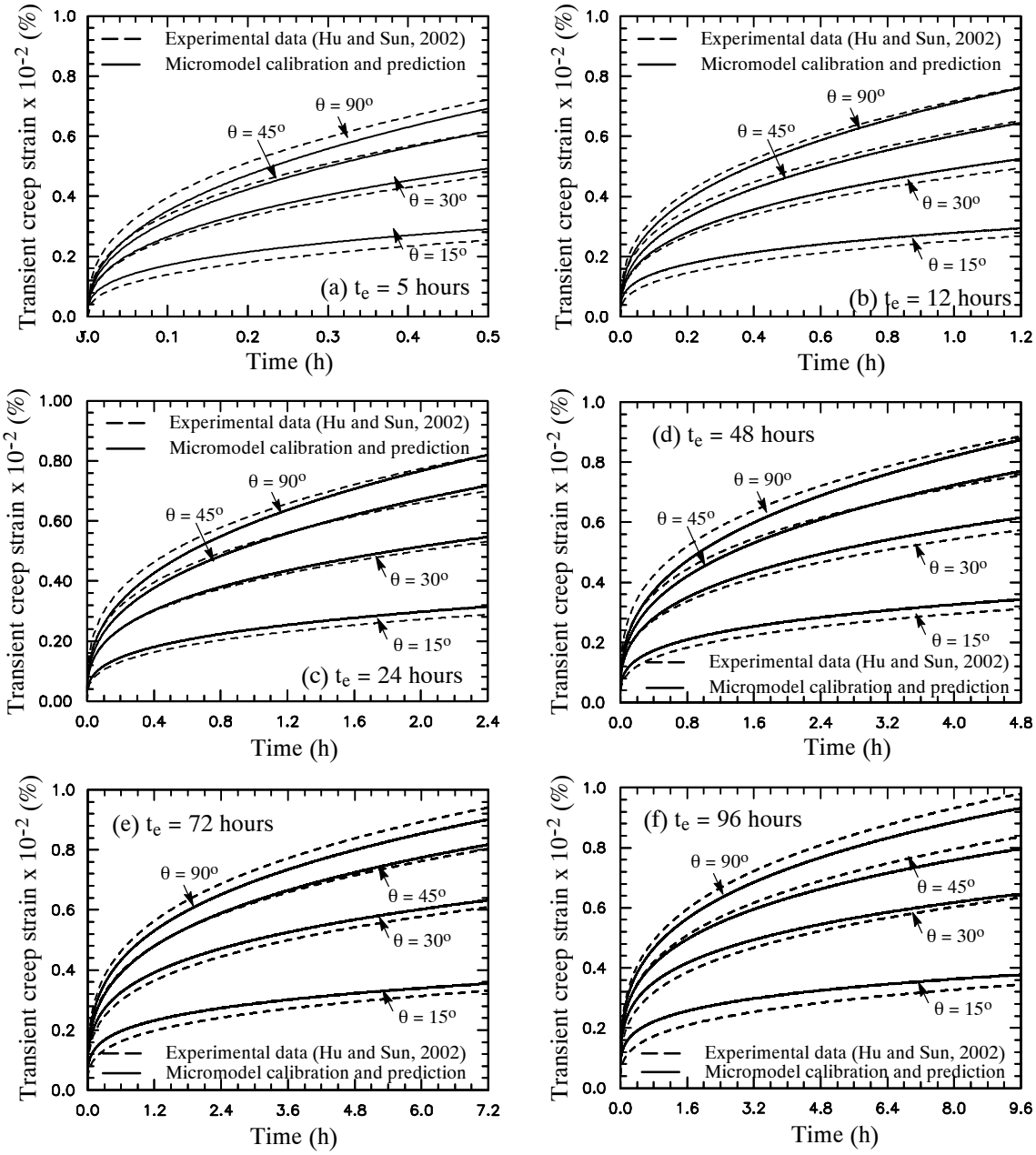

Figure 3.23 Predicted transient creep strain for off-axis coupons at different aging hours.

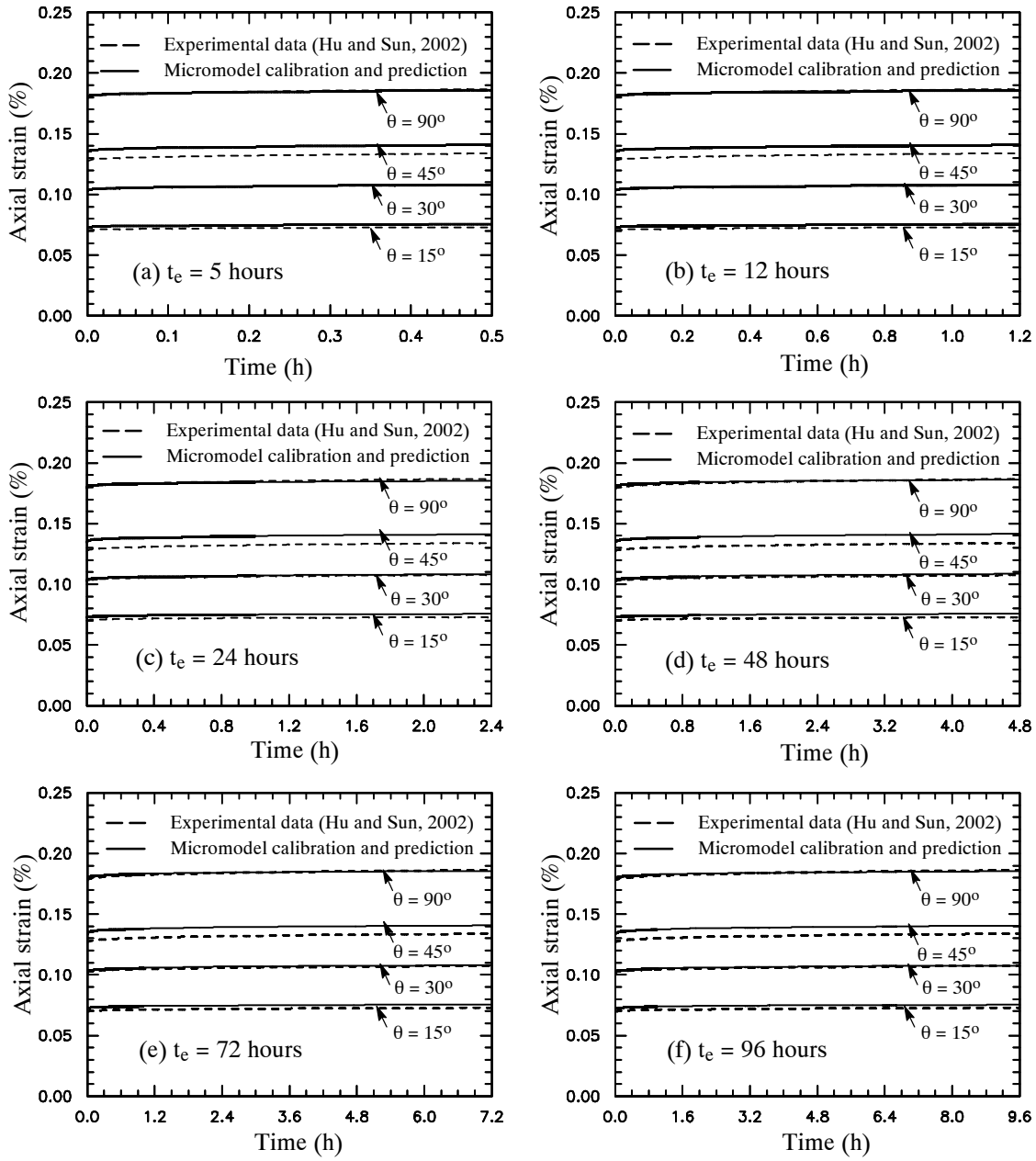

Figure 3.24 Predicted total strain for off-axis coupons at different aging hours.

CHAPTER IV

MICROMECHANICAL MODELS FOR THE NONLINEAR VISCOELASTIC BEHAVIOR OF PULTRUDED COMPOSITES

A micromechanical framework for the nonlinear viscoealstic analysis of pultruded composite materials and structures is presented in this chapter. The studied pultruded composite consists of repeating layers of roving and CFM. The nonlinear elastic micromechanical models for roving and CFM composite layers (Haj-Ali et al. 2001, Haj-Ali and Kilic 2002, 2003) are modified with additional numerical algorithm suitable for the time domain integration and nonlinear viscoelastic constitutive model for the matrix. The anisotropic viscoelastic responses of roving and CFM layers are homogenized using a sublaminate micromodel in order to develop an effective 3D nonlinear viscoelastic constitutive model of pultruded materials. The result is a multi-scale micromechanical framework that can be integrated as a material model in a displacement-based FE. This micromechanical framework is sampled at the material points (Gaussian integration points) in the FE model of a pultruded composite structure. Off-axis creep compression and tension tests are performed for E-glass/vinylester and polyester pultruded plates in order to calibrate the in-situ viscoelastic properties and predict the overall nonlinear viscoelastic response. This chapter describes the work of Haj-Ali and Muliana (2003) and extends it to include more experimental and analytical verifications.

4.1 Micromodel Formulation for Sublaminate, CFM and Roving

A micromechanical framework for the pultruded material systems, reinforced with roving and CFM layers, is schematically shown in Figure 4.1. This micromechanical frame-

work has been proposed for the nonlinear *time-independent* behavior of pultruded composites (Haj-Ali et al. 2001, Haj-Ali and Kilic 2002, 2003, and Kilic 2001). The current section generalizes this approach to include time-dependent viscoelastic behavior. A sublaminate model is used in order to generate a 3D effective anisotropic viscoelastic response of the alternating roving and CFM layers. Two independent 3D micromechanical material models are used for the roving and CFM layers. Roving is a long unidirectional fiber bundled embedded in the matrix system and is idealized as a doubly periodic array of fibers with rectangular cross section surrounded by the matrix. The roving unit-cell model consists of four fiber and matrix subcells, following configuration of Aboudi MOC (1991), as described in chapter III. CFM is long, swirl, and randomly oriented fiber filaments embedded in the matrix system. The CFM unit-cell is composed of a weighted average of two other unit-cells, which represent layers with two limited orientations. The first unit-cell is a matrix-mode layer (transverse), where all the fibers are surrounded by the matrix phase and the fibers are oriented in the transverse direction. The second unit-cell is a fiber-mode layer (unidirectional layer), in which fibers are oriented in the axial direction. Perfect bond is assumed between adjacent layers in the sublaminate model and also along the interfaces inside the unit-cell models. The traction and displacement continuity relations at all interfaces are approximated and written in terms of the average stress and strain variables of the different subcells or layers. The 3D stress-strain constitutive characterization for the fiber and matrix constituents is performed at the lowest level of the nested modeling framework. It is assumed that both matrix constituents in the roving and CFM systems have the same isotropic and nonlinear viscoelastic behavior; and both fibers in the roving and CFM systems are linear elastic.

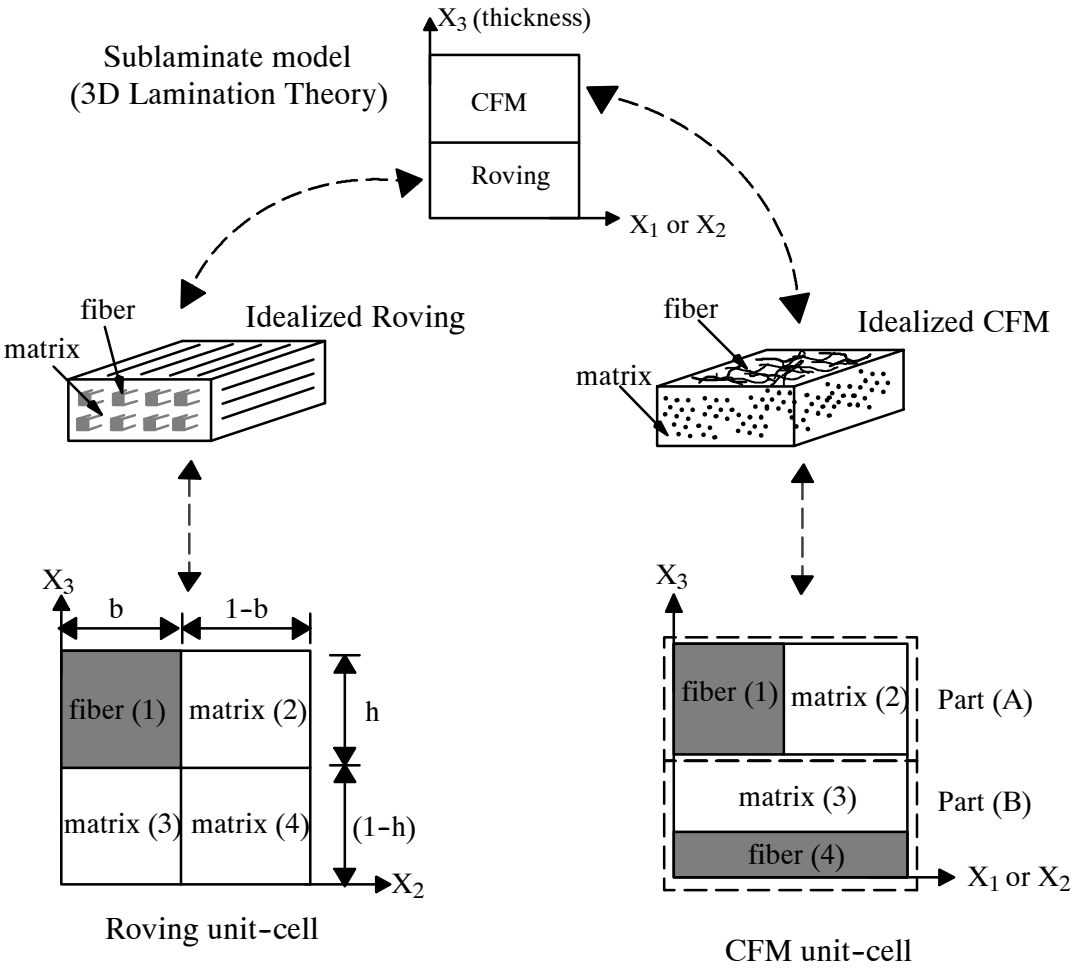

Figure 4.1 Micromechanical framework for the pultruded composite materials.

Micromodel for sublaminate

A sublaminate model is used to generate the nonlinear equivalent continuum response of a periodic layered medium with two alternating layers of roving and CFM. The sublaminate micromodel is a unit-cell that consists of CFM and roving subcells. The through thickness homogenization process is achieved using the 3D lamination theory assuming a perfect bond between the layers. The incremental stress and strain vectors for each subcell are transformed to material coordinates, and are partitioned into *in-plane* (x_1-x_2 axes) and *out-of-plane* (x_3 axis) components:

$$d\bar{\sigma}_i = \{ d\sigma_{11} \;\; d\sigma_{22} \;\; d\tau_{12} \} \;, \quad d\bar{\sigma}_o = \{ d\sigma_{33} \;\; d\tau_{13} \;\; d\tau_{23} \} \tag{4.1}$$

$$d\bar{\varepsilon}_i = \{ d\varepsilon_{11} \;\; d\varepsilon_{22} \;\; d\gamma_{12} \} \;, \quad d\bar{\varepsilon}_o = \{ d\varepsilon_{33} \;\; d\gamma_{13} \;\; d\gamma_{23} \} \tag{4.2}$$

where an overbar indicates a homogenized sublaminate quantity, i.e. a through-thickness average. The subscript "i" and "o" denote an in-plane and out-of-plane stress or strain vectors, respectively. The sublaminate incremental average stresses can be written as:

$$\begin{aligned} d\bar{\sigma} &= \frac{1}{V} \left(V_C \, d\sigma^{(C)} + V_R \, d\sigma^{(R)} \right) = \frac{1}{t} \left(t_C \, d\sigma^{(C)} + t_R \, d\sigma^{(R)} \right) \\ V &= V_C + V_R \qquad\qquad t = t_C + t_R \end{aligned} \tag{4.3}$$

where V is the unit-cell volume, C and R denote the CFM and roving layers, respectively. A similar equation can also be written for the average strain vector.

Displacement continuity requires that the in-plane strains to be continuous across the interface, while equilibrium of tractions across the interface requires that out-of-plane stresses to be continuous across the interface. These two requirements can be expressed in an incremental form:

$$d\varepsilon_i^{(C)} = d\varepsilon_i^{(R)} = d\bar{\varepsilon}_i \tag{4.4}$$

$$d\sigma_o^{(C)} = d\sigma_o^{(R)} = d\bar{\sigma}_o \tag{4.5}$$

The complementary stresses and strains may differ in the roving and CFM layers. The homogenized in-plane stresses and out-of-plane strains are taken as weighted averages, using the relative CFM and roving thickness, t_C and t_R, as:

$$d\bar{\sigma}_i = \frac{1}{(t_C + t_R)} \left(t_C \, d\sigma_i^{(C)} + t_R \, d\sigma_i^{(R)} \right) \tag{4.6}$$

$$d\bar{\varepsilon}_o = \frac{1}{(t_C + t_R)} \left(t_C \, d\varepsilon_o^{(C)} + t_R \, d\varepsilon_o^{(R)} \right) \tag{4.7}$$

Equations (4.4) through (4.7) define the micromechanical relations needed for the incremental formulation of the sublaminate model. The incremental stress-strain relations for the two layers are also needed to define an effective sublaminate model.

Micromodel for CFM

The CFM medium is reinforced with long and swirl filaments, that are randomly distributed in the in-plane of the layer. A simplified micromodel for the CFM is used to generate the 3D equivalent response for the CFM layer by a weighted-average of two other unit-cell models. The first is a matrix-mode layer unit-cell, where fibers are surrounded by a matrix phase. The second is a fiber-mode unit-cell, where the fibers are unidirectional and not shielded by the matrix.

The overall unit-cell model for the CFM consists of four subcells, as shown in Figure 4.1. Subcells 1 and 4 represent fiber constituent, while subcells 2 and 3 represent matrix constituent. The matrix-mode part (A) consists of subcells 1 and 2, while the fiber-mode part (B) consists of subcells 3 and 4. The FVFs within these parts should satisfy:

$$\begin{aligned} \frac{V_1}{V_1 + V_2} &= V_{f_C} & \frac{V_4}{V_3 + V_4} &= V_{f_C} \\ V_A &= \frac{V_1 + V_2}{V_C} & V_B &= \frac{V_3 + V_4}{V_C} \\ V_C &= V_A + V_B \end{aligned} \tag{4.8}$$

where v_{f_C} is the FVF for CFM layer.

We proceed with the micromechanical formulation by considering parts (A) and (B) of the unit-cell as separate layers in a sublaminate model. To this end, the relations in Eqs. (4.4) through (4.7) can be applied for the two parts. The out-of-plane traction continuity and in-plane displacement continuity requirements will yield the following relations:

$$d\sigma_o^{(C)} = d\sigma_o^{(A)} = d\sigma_o^{(B)} \qquad d\varepsilon_i^{(C)} = d\varepsilon_i^{(A)} = d\varepsilon_i^{(B)} \tag{4.9}$$

The relations for the CFM effective in-plane stresses and out-of-plane strains are:

$$\begin{aligned} d\sigma_i^{(C)} &= \frac{1}{V_C}\left(V_A\, d\sigma_i^{(A)} + V_B\, d\sigma_i^{(B)} \right) \\ d\varepsilon_o^{(C)} &= \frac{1}{V_C}\left(V_A\, d\varepsilon_o^{(A)} + V_B\, d\varepsilon_o^{(B)} \right) \end{aligned} \tag{4.10}$$

Within part A, the following equations should be satisfied between the subcells:

$$d\sigma^{(A)} = d\sigma^{(1)} = d\sigma^{(2)}$$
$$d\varepsilon^{(A)} = \frac{1}{V_A}\left(V_1\, d\varepsilon^{(1)} + V_2\, d\varepsilon^{(2)} \right) \tag{4.11}$$

Within part B, the following equations should be satisfied:

$$d\sigma_o^{(B)} = d\sigma_o^{(3)} = d\sigma_o^{(4)} \qquad d\varepsilon_i^{(B)} = d\varepsilon_i^{(3)} = d\varepsilon_i^{(4)}$$
$$d\sigma_i^{(B)} = \frac{1}{V_B}\left(V_3\, d\sigma_i^{(3)} + V_4\, d\sigma_i^{(4)}\right) \qquad d\varepsilon_o^{(B)} = \frac{1}{V_B}\left(V_3\, d\varepsilon_o^{(3)} + V_4\, d\varepsilon_o^{(4)}\right) \tag{4.12}$$

Equations (4.9) through (4.12) complete the micromechanical relations within subcells in the CFM micromodel. These equations along with the incremental stress-strain relations of the fiber and matrix subcells are used to define the effective incremental stress-strain relations of the CFM material.

Micromodel for roving

The roving layer is idealized as a doubly periodic array of rectangular cross-section fibers embedded in the matrix. The long fibers are aligned in the x_1 direction. The other cross-section directions are referred to as the transverse directions. The unit-cell is composed of four subcells similar to the MOC configuration proposed by Aboudi (1991). The current formulation is carried out using average stresses and strains in the subcells without the need of higher-order polynomial expansions for the displacement. Micromodel relations for roving system are similar to the one of the unidirectional composite model, Eqs. (3.9) to (3.15) in section 3.1.

4.2 Linearized Micromechanical Formulation

The strain-interaction matrix (B), which relates the subcell average strain increment, $d\varepsilon^{(\alpha)}$, to the overall unit-cell average strain increment, $d\overline{\varepsilon}$, is then defined for sublaminate, CFM and roving unit-cells. The general linearized formulation for pultruded micromodel

follows the one of unidirectional layer micromodel, Eqs. (3.1) through (3.7). The strain components in the sublaminate, CFM, and roving are grouped into displacement compatibility and traction continuity parts, as in Eq. (3.18). The strain vectors corresponds to displacement compatibility and traction continuity in sublaminate model are:

$$\underset{(1 \times 9)}{d\varepsilon_a^T} = \left\{ d\varepsilon_i^{(R)},\ d\varepsilon_i^{(C)},\ d\varepsilon_o^{(C)} \right\} \qquad \underset{(1 \times 3)}{d\varepsilon_b^T} = \left\{ d\varepsilon_o^{(R)} \right\} \tag{4.13}$$

The displacement compatibility and traction continuity strain vectors in the CFM model are:

$$\underset{(1 \times 12)}{d\varepsilon_a^T} = \left\{ d\varepsilon_i^{(1)},\ d\varepsilon_o^{(1)},\ d\varepsilon_i^{(3)},\ d\varepsilon_i^{(4)} \right\}$$

$$\underset{(1 \times 12)}{d\varepsilon_b^T} = \left\{ d\varepsilon_i^{(2)},\ d\varepsilon_o^{(2)},\ d\varepsilon_o^{(3)},\ d\varepsilon_o^{(4)} \right\} \tag{4.14}$$

The displacement compatibility and traction continuity strain vectors in the roving model are similar to the one of unidirectional lamina, as listed in Eqs. (3.16) and (3.17).

Next, the $\overline{A}$ and $\overline{D}$ matrices in Eq. (3.18) are determined for sublaminate, CFM, and roving micromodels after some algebraic manipulations. The $\overline{A}$ and $\overline{D}$ matrices for the sublaminate model are:

$$\overline{A} = \left[\begin{array}{c|c|c|c} \underset{(3 \times 3)}{I} & \underset{(3 \times 3)}{0} & \underset{(3 \times 3)}{0} & \underset{(3 \times 3)}{0} \\ \hline \underset{(3 \times 3)}{0} & \underset{(3 \times 3)}{I} & \underset{(3 \times 3)}{0} & \underset{(3 \times 3)}{0} \\ \hline \underset{(3 \times 3)}{0} & \underset{(3 \times 3)}{0} & \underset{(3 \times 3)}{I} & \underset{(3 \times 3)}{\frac{t_R}{t_C} I} \\ \hline \underset{(3 \times 3)}{-C_{oi}^{(C)}} & \underset{(3 \times 3)}{C_{oi}^{(R)}} & \underset{(3 \times 3)}{-C_{oo}^{(C)}} & \underset{(3 \times 3)}{C_{oo}^{(R)}} \end{array}\right] \tag{4.15}$$

$$\overline{D}^T = \begin{bmatrix} I_{(3\times3)} & I_{(3\times3)} & 0_{(3\times3)} & 0_{(3\times3)} \\ 0_{(3\times3)} & 0_{(3\times3)} & \frac{t}{t_C} I_{(3\times3)} & 0_{(3\times3)} \end{bmatrix} \tag{4.16}$$

where C is the stiffness matrix, and the subscripts "i" and "o" in the stiffness matrices indicate in-plane and out-of-plane components, respectively. The $\overline{A}$ and $\overline{D}$ matrices for the CFM micromodel are expressed as:

$$\overline{A} = \begin{bmatrix} I_{(3\times3)} & 0_{(3\times3)} & 0_{(3\times3)} & 0_{(3\times3)} & 0_{(3\times3)} & 0_{(3\times3)} & 0_{(3\times3)} & 0_{(3\times3)} \\ 0_{(3\times3)} & I_{(3\times3)} & 0_{(3\times3)} & 0_{(3\times3)} & 0_{(3\times3)} & 0_{(3\times3)} & 0_{(3\times3)} & 0_{(3\times3)} \\ 0_{(3\times3)} & 0_{(3\times3)} & I_{(3\times3)} & 0_{(3\times3)} & \frac{V_2}{V_1} I_{(3\times3)} & 0_{(3\times3)} & 0_{(3\times3)} & 0_{(3\times3)} \\ 0_{(3\times3)} & 0_{(3\times3)} & 0_{(3\times3)} & I_{(3\times3)} & 0_{(3\times3)} & \frac{V_2}{V_1} I_{(3\times3)} & \frac{V_3}{V_1} I_{(3\times3)} & \frac{V_4}{V_1} I_{(3\times3)} \\ 0_{(3\times3)} & 0_{(3\times3)} & -C^{(1)}_{oi\,(3\times3)} & -C^{(1)}_{oo\,(3\times3)} & C^{(2)}_{oi\,(3\times3)} & C^{(2)}_{oo\,(3\times3)} & 0_{(3\times3)} & 0_{(3\times3)} \\ 0_{(3\times3)} & 0_{(3\times3)} & -C^{(1)}_{ii\,(3\times3)} & -C^{(1)}_{io\,(3\times3)} & C^{(2)}_{ii\,(3\times3)} & C^{(2)}_{io\,(3\times3)} & 0_{(3\times3)} & 0_{(3\times3)} \\ C^{(3)}_{oi\,(3\times3)} & 0_{(3\times3)} & -C^{(1)}_{oi\,(3\times3)} & -C^{(1)}_{oo\,(3\times3)} & 0_{(3\times3)} & 0_{(3\times3)} & C^{(3)}_{oo\,(3\times3)} & 0_{(3\times3)} \\ 0_{(3\times3)} & C^{(4)}_{oi\,(3\times3)} & -C^{(1)}_{oi\,(3\times3)} & -C^{(1)}_{oo\,(3\times3)} & 0_{(3\times3)} & 0_{(3\times3)} & 0_{(3\times3)} & C^{(4)}_{oo\,(3\times3)} \end{bmatrix} \tag{4.17}$$

$$\overline{D}^T = \begin{bmatrix} I_{(3\times3)} & I_{(3\times3)} & \frac{V_1+V_2}{V_1} I_{(3\times3)} & 0_{(3\times3)} & 0_{(3\times3)} & 0_{(3\times3)} & 0_{(3\times3)} & 0_{(3\times3)} \\ 0_{(3\times3)} & 0_{(3\times3)} & 0_{(3\times3)} & \frac{V}{V_1} I_{(3\times3)} & 0_{(3\times3)} & 0_{(3\times3)} & 0_{(3\times3)} & 0_{(3\times3)} \end{bmatrix} \tag{4.18}$$

Finally, the $\overline{A}$ and $\overline{D}$ matrices for the roving micromodel are given in Eqs. (3.19) to (3.22).

4.3 Stress Correction Algorithm

The linearized micromechanical relations, derived in incremental formulation, will usually violate the constitutive equations because of the nonlinear and time-dependent response in the matrix subcells. An iterative correction scheme is needed in order to satisfy both the micromechanical constraints and the constitutive equations. The linearized micromechanical relations with tangential material matrices are used to generate trial incremental stresses and strains for the subcells (trial solution). The total micromechanical relations are then used to define a residual error for each micromodel. This residual is then used to correct the trial solution. This process is repeated until a converged solution that satisfies both micromechanical and nonlinear equations is reached.

A correction algorithm is needed in every nested micromodels, as shown in Figure 4.2. The incremental strain, the stress-strain states from previous step, and the history variables are the known variables for each nested micromodel. Inside the sublaminate model, the strain increment is distributed to the roving and CFM micromodels. Iterative correction schemes are developed separately for the roving and CFM models in order to minimize the errors and satisfy the micromechanical and constitutive relations. At the roving and CFM systems, the current stress-strain states, the tangent stiffness, together with the history variables are updated and sent to the sublaminate level. An iterative procedure is also performed inside the sublaminate system until the actual stress-strain relations as well as homogenization constraints are satisfied. Any iteration at sublaminate level requires the full calculation procedure from the lower levels of the framework. Once all levels of error are satisfied, the sublaminate effective nonlinear continuum state is defined and communicated to the FE structural level.

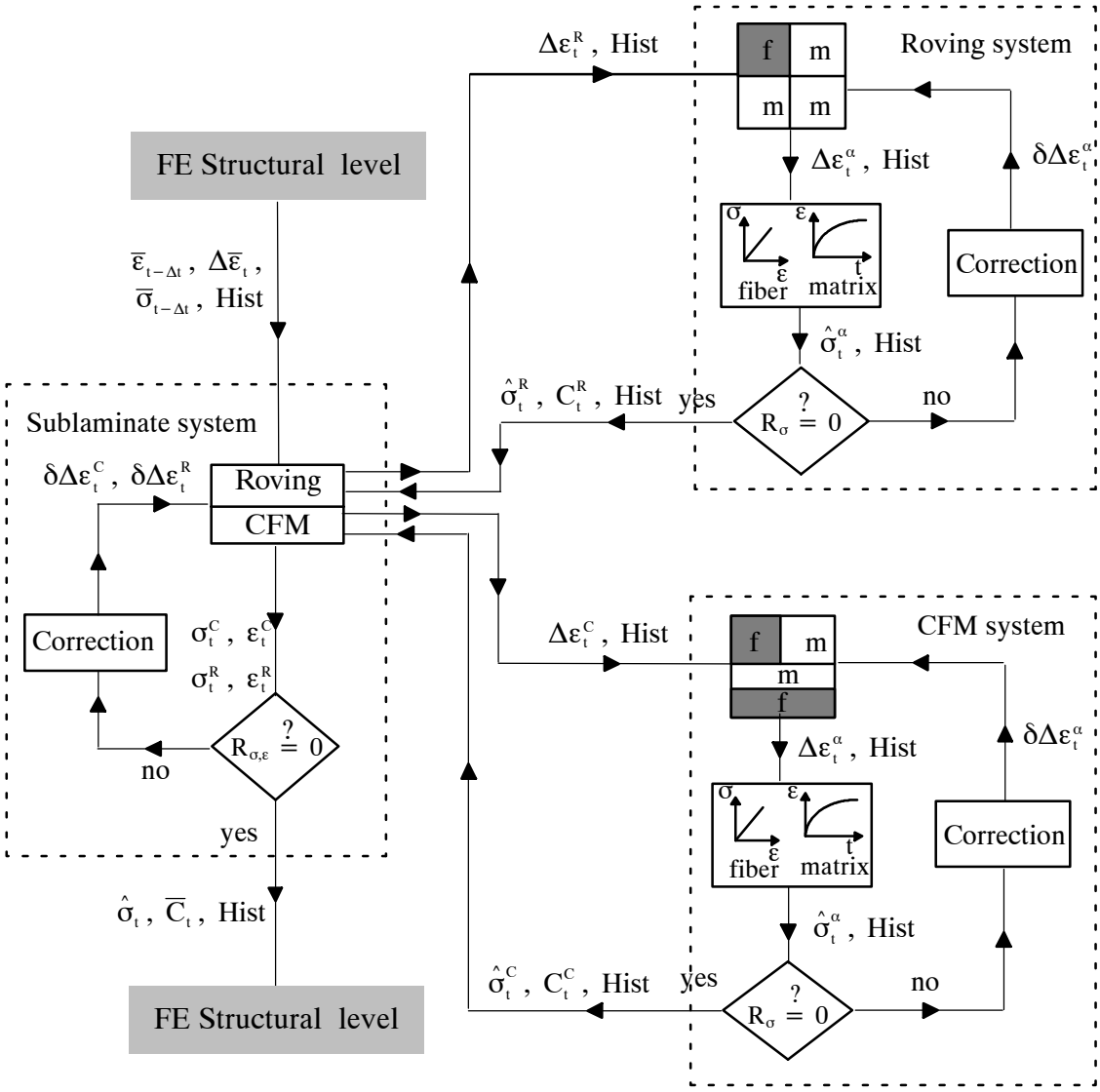

Figure 4.2 A micromechanical recursive-iterative integration algorithm for nonlinear viscoelastic behavior in pultruded composite materials.

4.4 Compression Creep Test on E-glass/Vinylester Pultruded Composite Materials

Uniaxial compression creep tests on off-axis pultruded coupons are performed in order to calibrate and verify the prediction of the pultruded's effective response under multi-axial plane stress conditions. Coupons were cut from a monolithic unidirectional pultruded plate, having 0.5 inches thickness, with different orientations for the roving layers. The pultruded

system is made of E-glass fiber and vinylester resin in both CFM and roving layers. The creep tests were conducted for one hour under uniaxial compression loads. The compression tests were performed because the nonlinear response is mainly due to matrix nonlinearity with little or no added damage, such as matrix microcracking which tend to reduce the initial stiffness. The short durations of the proposed creep tests are used to calibrate the in-situ viscoelastic properties of the matrix and to compare the predictions of the overall effective nonlinear viscoelastic response for different off-axis angles.

Five groups of specimens with off-axis angles: 0^o, 30^o, 45^o, 60^o, and 90^o were tested at room temperature with different applied stress taken as a ratio between 0.1-0.6 of the ultimate compression strength, σ_c^{ult}, of each coupon. Table 4.1 lists an array of off-axis creep coupons tested in this study. Some of the relevant compression test guidelines in ASTM D3410 are followed. The dimensions of the off-axis compression coupons are 7" length and 1.25" width. The measured average thickness of all coupons ranges from 0.490 to 0.498 in. The relatively thick and short coupon dimension allows for off-axis compression tests without buckling. Axial strains were monitored using strain gages attached at the center on both sides of the specimen. Transverse strain was also monitored from a strain gage mounted on one side of the specimen.

A static compression test was first performed for each off-axis coupon in order to determine its Young's modulus. The stiffness is measured as the slope of the line regressed from the stress-strain data between 1000 $\mu\varepsilon$ and 4000 $\mu\varepsilon$. Average off-axis stiffness, from the two axial gages, is compared with the test result performed by Haj-Ali and Kilic (2002) and is shown in Table 4.2. The elastic stiffnesses of the tested pultruded coupons are comparable with those of Haj-Ali and Kilic (2002). Thus, other properties such as the ultimate strength, fiber and matrix stiffness and FVFs of the material system followed those of Haj-Ali and Kilic (2002). An average Poisson's ratio is also calculated from both uniaxial and transverse coupons. Figure 4.3 shows the results of transverse strain measurements used to assess the

overall elastic properties. It indicates that less variability would occur if the effective elastic properties were to be calculated from 2000 με to 3000 με levels. Also, it shows that a maximum error of 10% may develop in the two measured in-plane Poisson's ratios.

Table 4.1 Creep tests with different off-axis E-glass/vinylester coupons subjected to various fractions of their ultimate load.

Cx − y − z ≡ off-axis angle - coupon number - loading ratio

	0°	30°	45°	60°	90°
	C0-1-0.1	C30-1-0.1	C45-1-0.1	C60-1-0.1	C90-1-0.1
	C0-2-0.2	C30-2-0.2	C45-2-0.2	C60-2-0.2	C90-2-0.2
	C0-3-0.4	C30-3-0.4	C45-3-0.4	C60-3-0.4	C90-3-0.4
	C0-4-0.4	C30-4-0.6	C45-4-0.6	C60-4-0.6	C90-4-0.6
	C0-5-0.6	C30-5-0.1	C45-5-0.1	C60-5-0.1	
		C30-5-0.2	C45-6-0.2	C60-5-0.2	
		C30-5-0.4	C45-7-0.4	C60-5-0.4	
		C30-5-0.6	C45-8-0.6	C60-5-0.6	
Total coupons	5	5	8	5	4

Table 4.2 Off-axis average Young's modulus (ksi) from compression tests.

θ	0°	30°	45°	60°	90°
Static test data	2704	1980	1719	1710	1703
Experimental data (Haj-Ali and Kilic, 2002)	2779	2124	1727	1806	1727

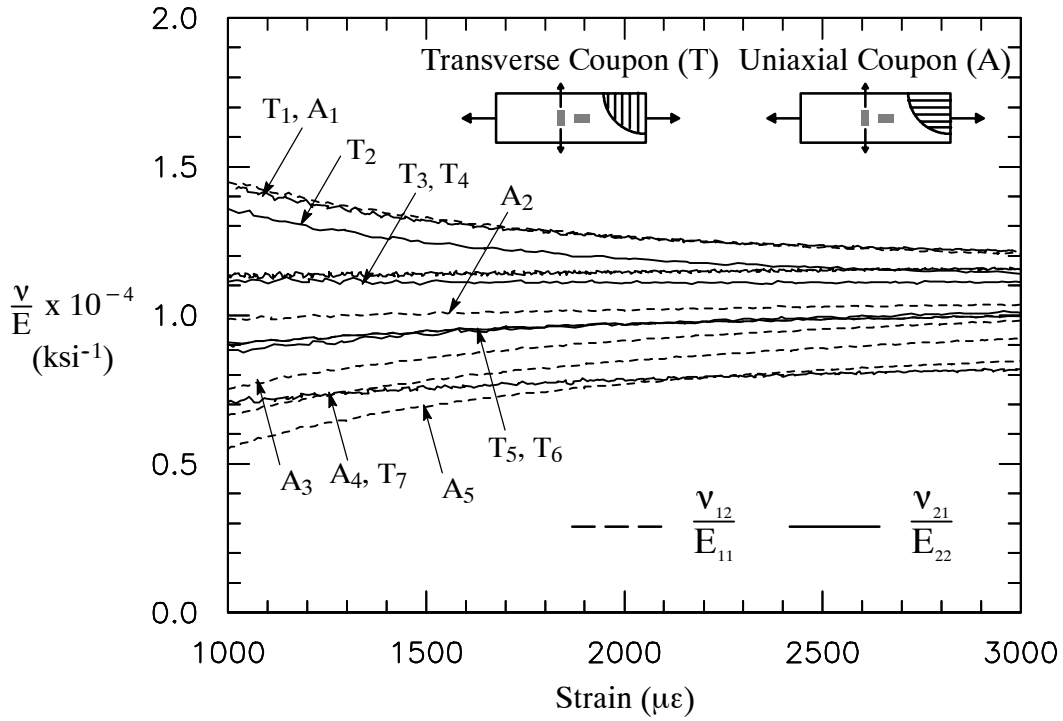

Figure 4.3 Symmetric compliance of the tested pultruded materials.

The in-situ properties of the fiber and matrix for the linear elastic behavior were previously calibrated for the E-glass/vinylester pultruded FRP composite (Haj-Ali and Kilic, 2002). In this study, the elastic stiffness for the matrix is taken as 600 ksi (instead of 730 ksi) in order to match the initial response from the transverse coupons. Table 4.3 shows the E-glass fiber and vinylester matrix properties. The total thickness of the roving layers is 0.172 inches while it is 0.328 inches for the CFM layers. The FVFs in the roving and the CFM layers were also determined as 0.407 and 0.305, respectively. These values are drastically changed when measured relative to the overall volume; they are 0.14 and 0.2, respectively. Thus, the overall FVF, from both the long and short filaments in the roving and CFM layers, is 0.34. The stiffness information along with the FVF's and relative thickness are sufficient for predicting the effective linear elastic behavior of the CFM and roving layers. The relative thickness of the layers can be used to generate an effective cross-section homogenized response. The predicted initial effective stiffness of the composite is listed in Table 4.4 and compared with some available experimental values.

Table 4.3 Elastic properties of fiber and matrix.

	E *(ksi)*	ν
Fiber (E-glass)	10500	0.25
Matrix		
Vinylester and additives	600	0.30
Polyester and additives	500	0.30

Table 4.4 Elastic effective properties of E-glass/vinylester pultruded system.

	E_{11}	E_{22}	E_{33} *(ksi)*	G_{12}	G_{13}	G_{23}	ν_{12}	ν_{13}	ν_{23}
Micromodel	2708	1598	1082	592	360	340	0.273	0.295	0.320
FE predictions (Haj-Ali and Kilic, 2002)	2800	1838		645			0.260		

Next, one hour creep followed by one hour recovery tests were conducted for each off-axis angle under different stress ratios: 0.1-0.6 σ_c^{ult}. The manner that simulates creep-recovery tests is described in Figure 4.4. The average ultimate compression stress for each off-axis specimen is followed the one of Haj-Ali and Kilic (2002) and listed in Table 4.5. Error estimates of strain measurements in pultruded off-axis tests due to the misalignment of the material symmetry were given by Haj-Ali and Kilic (2002). They found that the maximum error from the strain is about 1% in the center of the coupon, where the strain is measured. The added shear stress in tension is reduced by using longer coupons (12”). In addition, the relatively larger section area (0.625 in^2) reduces the added shear stress magnitude due to misalignment. As seen from Table 4.1, some of the coupons were subjected to single creep test while others were subjected to multiple tests after the specimen has been given sufficient

time for recovery. The specimens subjected to multiple creep tests were given at least 24 hours recovery duration between the consecutive tests. The purpose of the repeated tests is to examine the possibility of accumulated residual strain in the specimens. It should be noted that the off-axis tested were conducted over a month span. The environmental conditions in the lab have fluctuated; however, the average room temperature was 22°C and a 48% humidity.

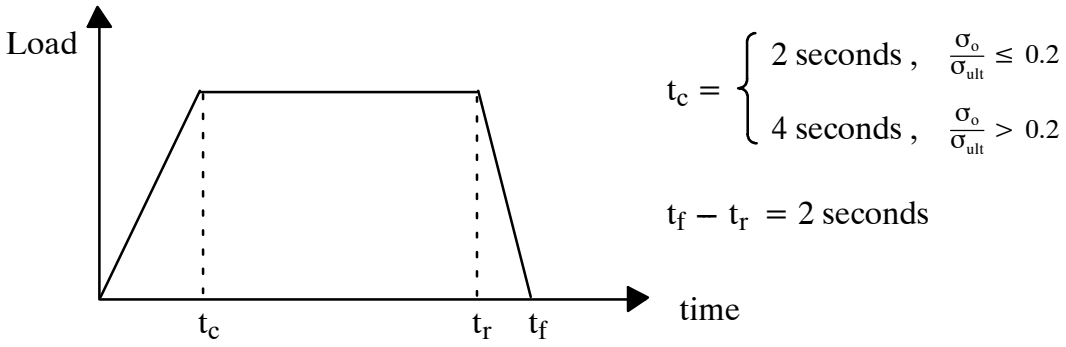

Figure 4.4 Step function during the creep-recovery test.

Table 4.5 Ultimate compression stress for different off-axis E-glass/vinylester coupons with nominal cross-sectional area (1.25 in x 0.5 in).

θ	0°	30°	45°	60°	90°
σ_c^{ult} *(ksi)* (Haj-Ali and Kilic, 2002)	40	25	24	24	24

Linear and nonlinear viscoelastic calibrations

The linear viscoelastic coefficients in the Prony series are determined in this study from a single creep test with transverse (90°) coupon under applied compression load of 0.1 σ_c^{ult}. The nonlinear viscoelastic parameters are equal to one for a linear response. The duration of the available creep data helps estimate the number of terms. The inverse of retardation

times , λ_n, were chosen as 10^{1-n}, which is usually one decade apart (Dillard et al 1987, Lai and Baker 1996). The corresponding Prony series coefficients D_n are varied until the overall effective creep response matches the experimental data for the 90° pultruded specimen. Figure 4.5 shows the experimental curve used for the linear response along with the calibrated curve from the proposed models. The calibrated Prony series coefficients are given in Table 4.6.

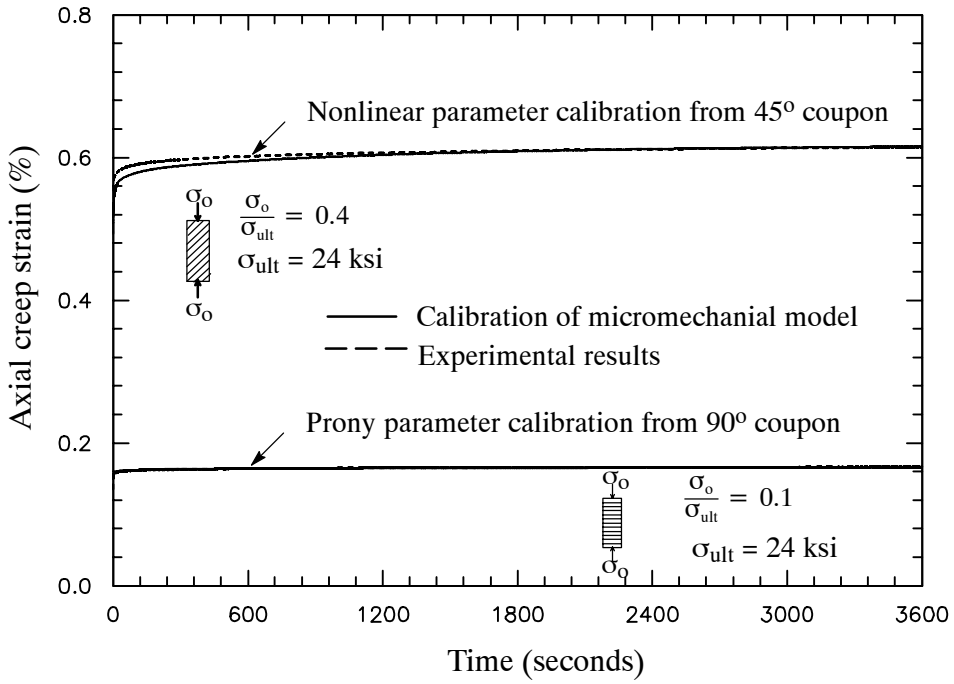

Figure. 4.5 Compression axial creep from off−axis coupons used for linear and nonlinear viscoelastic calibrations.

Table 4.6 Calibrated Prony series coefficients for the matrix.

n	λ_n (sec^{-1})	D_n x 10^{-6}(ksi^{-1})	
		Vinylester matrix	Polyester matrix
1	1	153.76	143.76
2	10^{-1}	71.00	130.99
3	10^{-2}	57.06	137.05
4	10^{-3}	73.83	140.83
5	10^{-4}	45.00	345.00
6	10^{-5}	25.00	580.00

The second calibration step is performed in order to determine the nonlinear viscoelastic parameters: g_0, g_1, g_2, and a_σ. The linear viscoelastic limit of the matrix is determined by the $\bar{\sigma}_o$ parameter in Eq. (2.45). This value was determined by examining the effective stress levels in all matrix subcells (roving and CFM) for the linear viscoelastic case (0.1 loading ratio). This effective stress value is initially used and then increased until a mismatch between the initial overall axial creep strains is found between the model and test results. In this study the effective stress that determines linear range, $\bar{\sigma}_o$, is chosen as 5.5 ksi. The nonlinear calibration starts with matching the g_0 parameter for the 45° off-axis specimen subjected to 0.4 loading ratio while monitoring the initial elastic strain values from specimens with the same off-axis angle and different loading ratios. The polynomial coefficients are changed to achieve the best possible match between all nonlinear curves. The calibrated nonlinear parameter, g_0, follows the general polynomial function of the effective stress in Eq. (2.45) with fourth order terms, as seen in Figure 4.6. The polynomial coefficients (α_0^i, i = 1 ... 4) are calibrated by varying these coefficients until the overall creep response of the pultruded specimen matches with the experimental data. The two top curves in Figure 4.5 show the axial shear response used for calibration. In this special case of an E-glass/vinylester pultruded system, the calibrated g_0 nonlinear function along with the Prony series coefficients were sufficient to capture the full nonlinear spectrum of response. The other non-

linear parameters were set to one. The creep test results are very limited due to the relatively short time involved, as well as, constant temperature, and no variation of environmental variables. However, the goal of this study is only to verify the ability of the micromodels in predicting the overall creep response under multiaxial loading. This is just one approach of calibration using polynomials for g values. Matching the curves progressively from the small stress level is needed to properly interface with linear viscoelastic response. Other approaches have been tried for example using R-O for g_0, which will be shown later. The advantage is that it gives faster convergence time and smoother convergence and behavior. However, there is no guarantee that one axial function (in terms of effective shear) will match all levels of applied stress. Therefore, segmental functions for the different ranges of applied stress may be a better alternative.

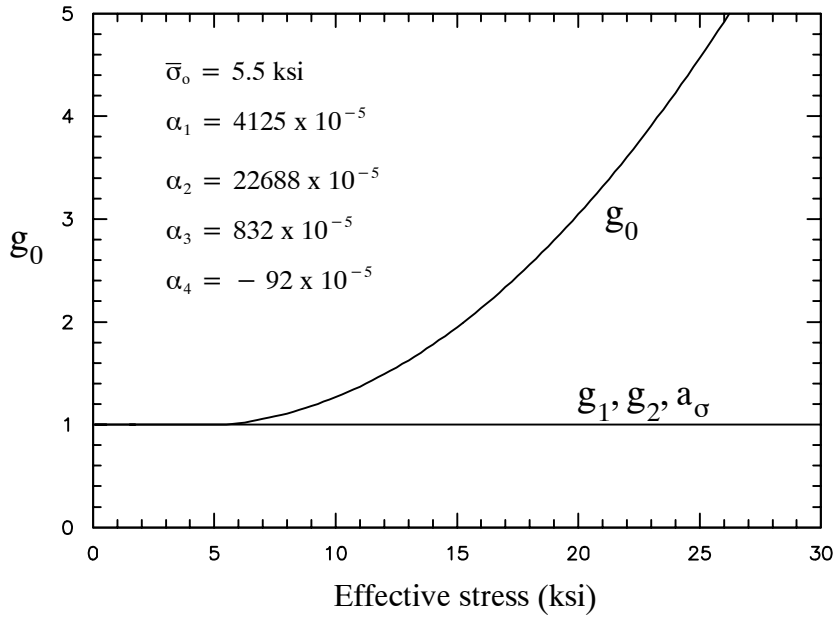

Figure 4.6 Calibrated polynomial coefficient for the vinylester matrix

Different nonlinear uniaxial stress-strain curve for the matrix phase has been used to characterize the nonlinear response. Haj-Ali et al. (2001) used the Ramberg-Osgood strain-stress representation for the matrix nonlinear response. The nonlinear parameters of the Ramberg-Osgood curve were calibrated for the in-situ matrix using axial-shear stress-

strain response measured using a V-notch test. The calibrated Ramberg-Osgood equation, Eq. (2.69), and polynomial function for the g_0 parameter are compared in Figure 4.7. As expected, the two curves are similar since they represent the same nonlinear elastic behavior. It has been shown in section 2.4 and Figure 2.8 that the Ramberg-Osgood strain-stress representation gives better numerical convergence over the polynomial function. It will be seen later that using the Ramberg-Osgood strain-stress representation may be an advantage in the numerical convergence over the polynomial form.

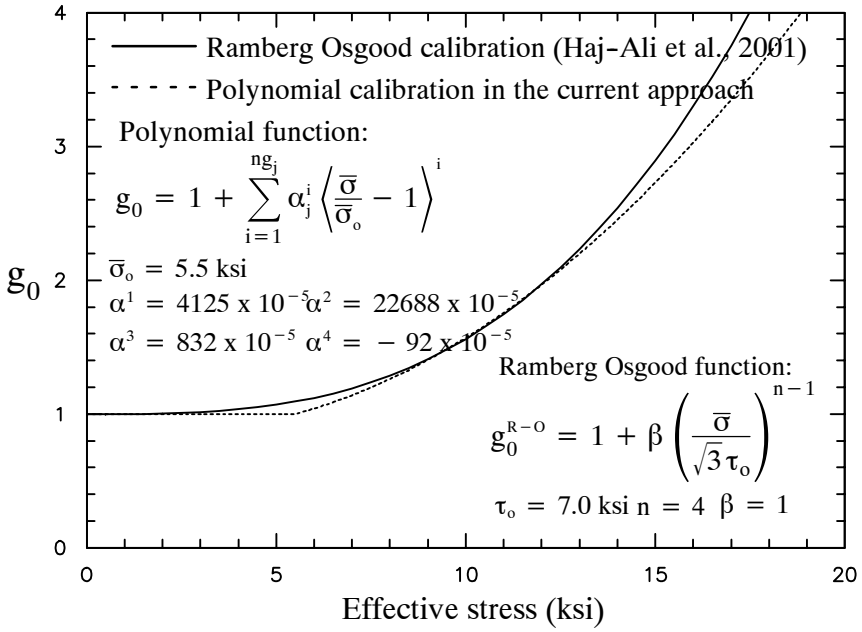

Figure 4.7 Nonlinear functions for vinylester matrix.

Prediction of the micromodel formulation

The proposed micromodeling approach is examined in its ability to generate the overall nonlinear response for the off-axis coupon tests that were not used in the calibration process. The reported experimental data are averaged from axial gages attached at the center of front and back sides of the specimen. The complete strain results from both front and back gages are shown in Appendix B. Figure 4.8 shows the predicted and the creep experimental results

for the uniaxial E-glass/vinylester pultruded coupons. A predominantly linear viscoelastic response is shown. The linear behaviors are due to the relatively low stress magnitude in the matrix. The transverse creep strain in the unidirectional coupon is shown in Figure 4.9. This shows a time-independent Poisson's ratio. The creep curves for the 30° off-axis coupons under different applied stresses are shown in Figure 4.10. The results from the proposed model are in good agreement to the experimental curves. Some deviations are shown from the two creep coupons. Material variability may be the reason for this difference, which is amplified with higher applied stresses. The creep curves for the 45° E-glass/vinylester pultruded system are shown in Figure 4.11. In this case, eight separate specimens were used and tested at 4 applied stress levels, where two coupons were used for each stress level. The experimental creep data for the two coupons under applied loading ratio of 0.4 are used for calibration. The rest of creep data are used to verify the proposed model. The overall responses from the micromechanical model show linear viscoelastic response for the low stress levels: $0.1\sigma_c^{ult}$ and $0.2\sigma_c^{ult}$. Nonlinear viscoelastic response is present at higher stress levels due to high stresses in the matrix. The overall creep curves for the 60° off-axis coupons are shown in Figure 4.12. Good prediction is shown by the micromodels for the linear and nonlinear curves. Some deviations at higher stress level are shown. Figure 4.13 shows creep results for the 90° transverse specimens under various applied loads: 0.1-0.6 of σ_c^{ult}. Good prediction is shown by the micromodels for the linear and nonlinear curves. Again, some deviation is shown for the test with the highest applied stress. The model shows more nonlinear response in this case. This may be explained by the fact that the nonlinear calibration was carried out with a 45° coupon having 0.4 load ratio, while the predicted transverse response is for a ratio of 0.6. The level of effective stress in the matrix is out of the calibrated range in the transverse coupon.

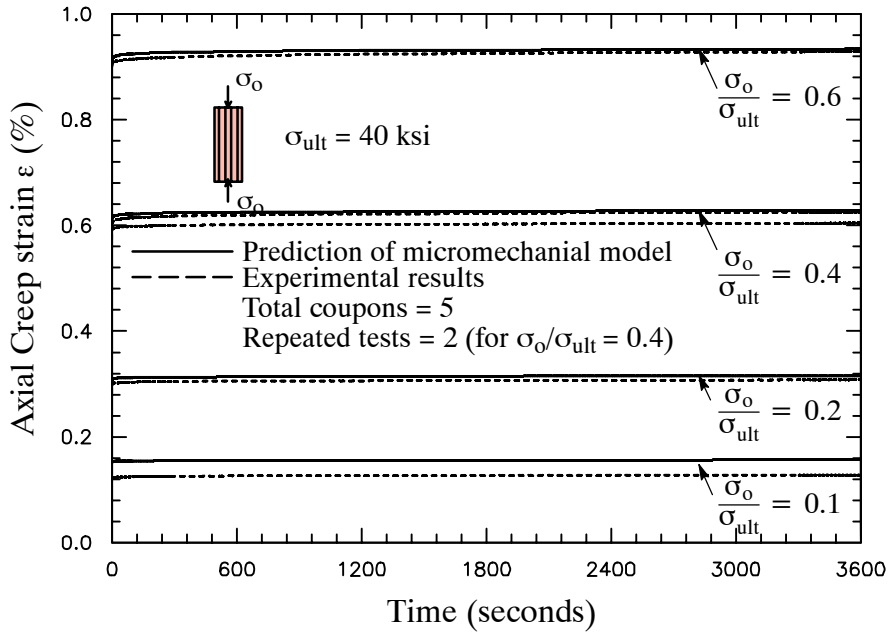

Figure 4.8 Compression axial creep for uniaxial pultruded FRP coupons.

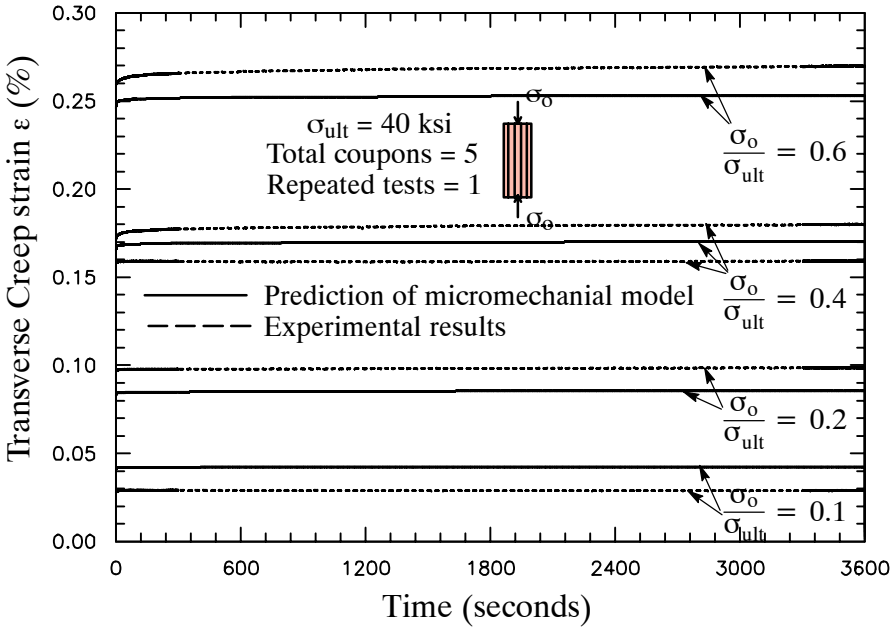

Figure 4.9 Compression transverse creep for uniaxial pultruded FRP coupons.

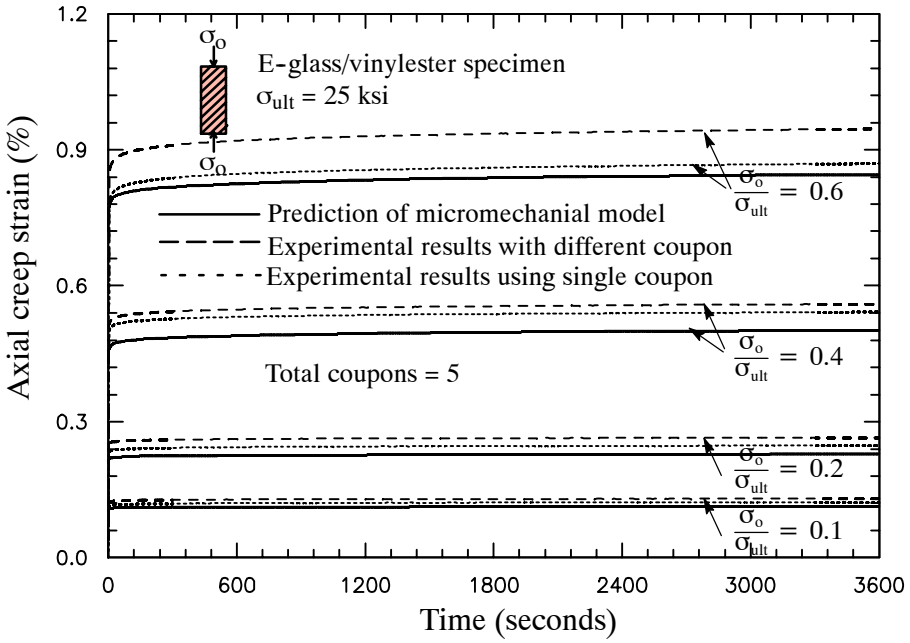

Figure 4.10 Compression axial creep for 30° off−axis pultruded FRP coupons.

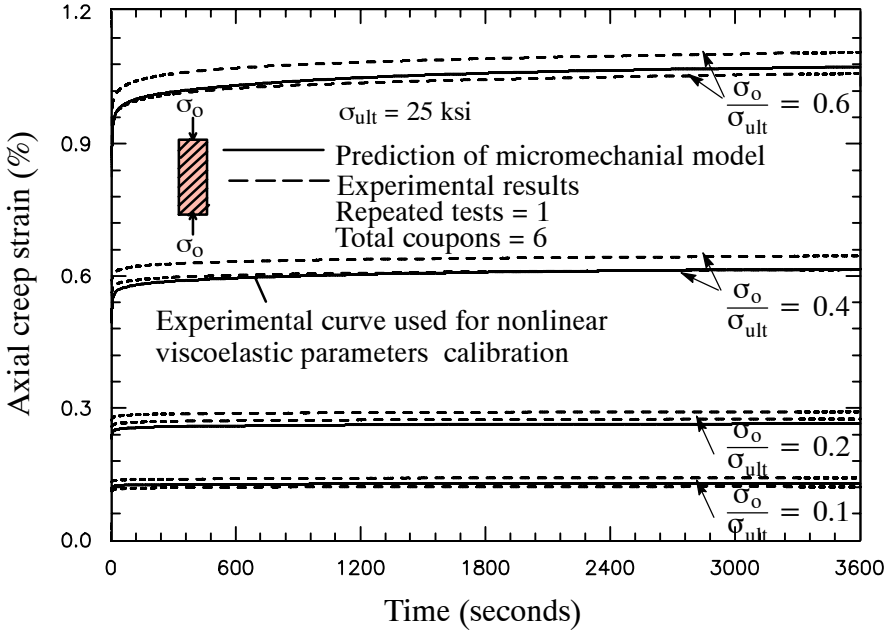

Figure 4.11 Compression axial creep for 45° off−axis pultruded FRP coupons.

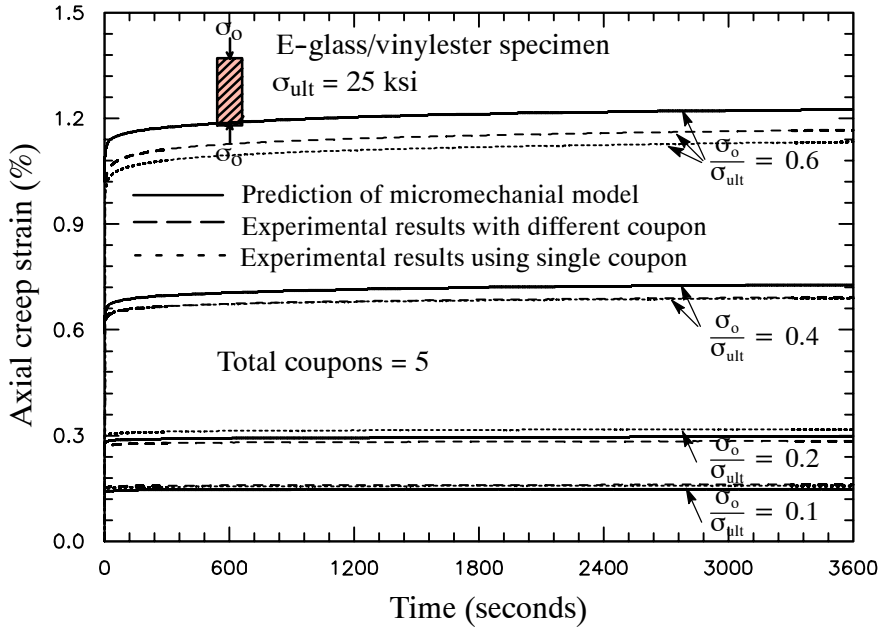

Figure 4.12 Compression axial creep for 60° off−axis pultruded FRP coupons.

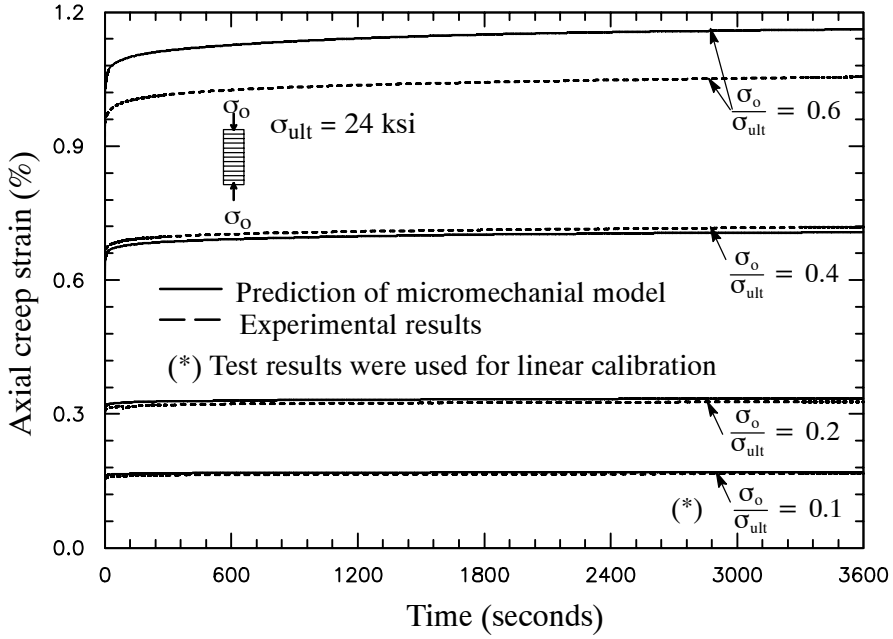

Figure 4.13 Compression axial creep for transverse pultruded FRP coupons.

4.5 Tension Creep Tests on E-glass/Polyester Pultruded Composite Materials

Another pultruded composite system that was calibrated in this study is the form of E-glass/polyester pultruded plate. The polyester coupons were subjected to creep tension tests. The creep response for this system is different from the vinylester due to the different matrix and different tension loading. Tension tests are performed because there is an added nonlinear transverse tension effect. Furthermore, there is an initial stiffness reduction due to opening of existing microcracks. In the case of increasing applied tensile stress, existing and initiating microcracks becomes important and may significantly alter the nonlinear material response.

Four coupons were cut from a unidirectional pultruded plate with different orientations in the roving layers: 0^o, 45^o, 60^o, and 90^o. Some of the relevant tension test guidelines in ASTM D3039 are followed. The dimensions of the off-axis tension coupons are 12" length and 1.25" width, following the one used by Haj-Ali and Kilic (2002). The measured average thickness of all coupons ranges from 0.490 to 0.498 in. The thickness and the configuration of the E-glass reinforcement layers are assumed to be the same as the previous E-glass/vinylester plate. Table 4.3 shows the in-situ properties of the polyester matrix used in the micromodels. The FVFs in the roving and the CFM layers are 0.407 and 0.305, respectively. The predicted initial effective stiffness of the composite is listed in Table 4.7 and compared with some available experimental values.

Table 4.7 Elastic effective properties of E-glass/polyester pultruded system.

	E_{11}	E_{22}	E_{33}	G_{12}	G_{13}	G_{23}	ν_{12}	ν_{13}	ν_{23}
			(ksi)						
Micromodel	2610	1452	919	538	302	285	0.271	0.296	0.323
Experimental data (Haj-Ali and El-Hajjar, 2003)	2484	1444		507			0.283		

The tests were conducted for one hour creep followed by one hour recovery at fixed environmental conditions. The test procedure is described in Figure 4.4. The average temperature and humidity during all tests were 21.8°C and 34%, respectively. Four E-glass/polyester off-axis specimens: 0°, 45°, 60°, and 90° were subjected to several tensile creep loading ratios between 0.1-0.6 of their ultimate tensile strength, σ_t^{ult}. The average ultimate tensile stress for each off-axis specimen is listed in Table 4.8. Axial average strains were reported from two strain gages that are attached at the center on both side of the specimens. The specimens were subjected to multiple creep tests and were given at least 24 hours recovery duration between the consecutive tests. The purpose of the repeated tests is to examine the possibility of accumulated residual strain in the specimens. The short duration of the proposed creep tests are used to calibrate the in-situ viscoelastic properties of the matrix and compare the predictions for the overall effective nonlinear viscoelastic response for different off-axis angles.

Table 4.8 Ultimate tension stress for different off-axis E-glass/polyester coupons with nominal cross-sectional area (1.25 in x 0.5 in).

θ	0°	45°	60°	90°
σ_t^{ult} *(ksi)* (Haj-Ali and El-Hajjar, 2003)	27	12	14	12

Linear and nonlinear viscoelastic calibration

The linear and nonlinear in-situ viscoelastic parameter calibration procedures follow the one for E-glass/vinylester pultruded specimens, as described previously. The linear viscoelastic coefficients in the Prony series were calibrated from a single creep test with 45° off-axis coupon under applied tension loading ratio of 0.1. The nonlinear viscoelastic parameters are equal to one for a linear response. The corresponding Prony series coefficients D_n

are varied until the overall effective creep response matches the experimental data for the 45° pultruded specimen. The calibrated Prony series coefficients for the polyester matrix are given in Table 4.6. The linear viscoelastic limit of the matrix, $\bar{\sigma}_o$, was determined as 1.37 ksi. The nonlinear viscoelastic parameters: g_0, g_1, g_2, and a_σ were calibrated from the 45° off-axis specimens starting with the 0.6 loading ratio and aiming to match the other nonlinear curves. The nonlinear calibration starts with matching the g_0 parameter to the initial elastic response. The g_1, g_2, and a_σ parameters are then calibrated by matching the transient creep response. The calibrated nonlinear parameters follow the general polynomial function of the effective stress in Eq. (2.45), as shown in Figure 4.14. The effective stress limit of the calibrated range is determined based on the maximum matrix effective stress from the test data used for calibration, which in this study, the value is determined as 15 ksi. Beyond this range, the nonlinear functions may not be accurate to represent the actual nonlinear behavior. It is interesting to note the difference of the nonlinear parameters between the polyester and vinylester cases.

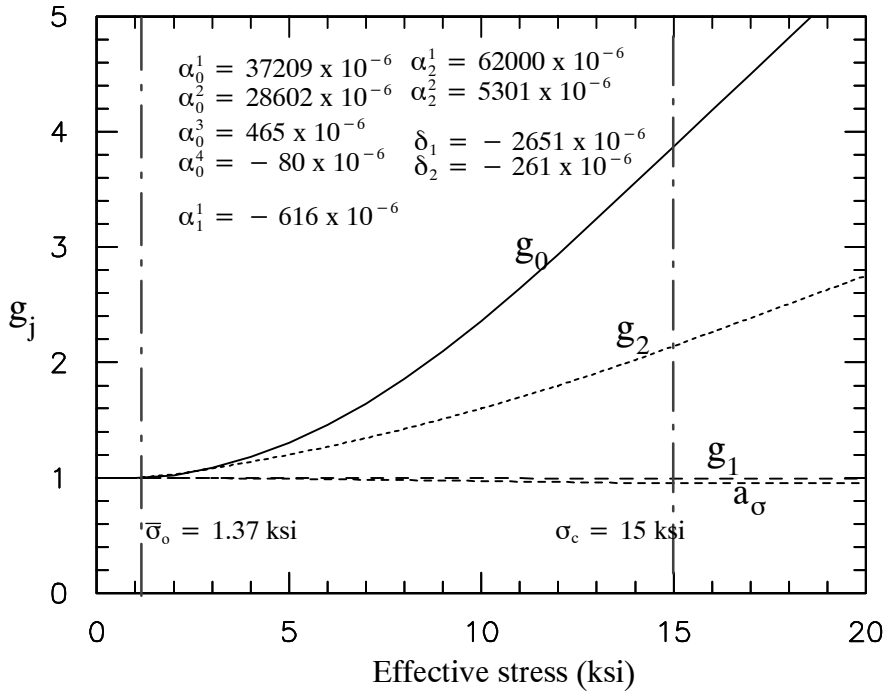

Figure 4.14 Calibrated polynomial coefficient for the polyester matrix.

Prediction of the micromodel formulation

The micromodel predictions of the overall nonlinear responses for the off-axis coupon tests are performed for specimens that are not used in the calibration process. The reported experimental data are averaged from axial gages attached at the center of front and back sides of the specimen. The complete strain results from both front and back gages are shown in Appendix B. Figure 4.15 shows the predicted and experimental creep response for a uniaxial coupon subjected to multiple tensile creep loading ratios between 0.1-0.6 of its ultimate tensile strength, σ_t^{ult}. A linear viscoelastic response is shown under relatively low applied stress ratios. Some deviations are shown at higher stress levels. This may be explained by the existence of microcracking, which is amplified with higher applied stresses. The matrix effective stresses for the uniaxial coupon tests are in the relatively low nonlinearity range. The predictions for the 45^o and 60^o off-axis E-glass/polyester pultruded specimens under tensile creep are shown in Figures 4.16 and 4.17, respectively. The experimental creep data for the 45^o coupon under applied loading ratio of 0.1 and 0.6 were used for linear and nonlinear calibration. The other experimental results are used to verify the proposed model. Good prediction is shown by the micromodels for the linear and nonlinear curves. Figure 4.18 shows creep results for the transverse specimens. Initial mismatch is shown for all the creep responses. Material variability may be the reason for this difference.

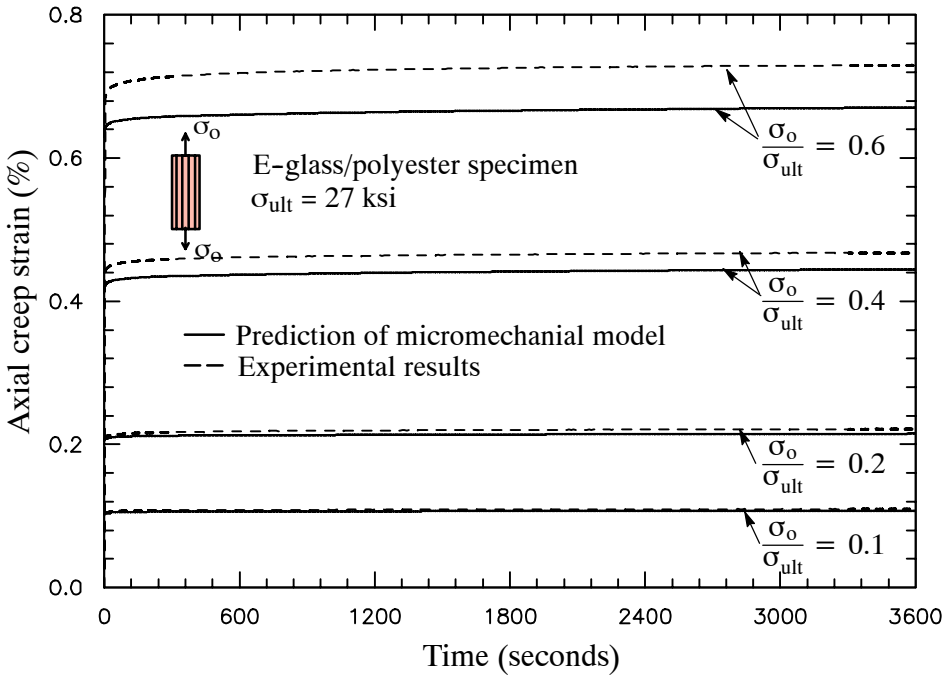

Figure 4.15 Tension axial creep for uniaxial pultruded FRP coupons.

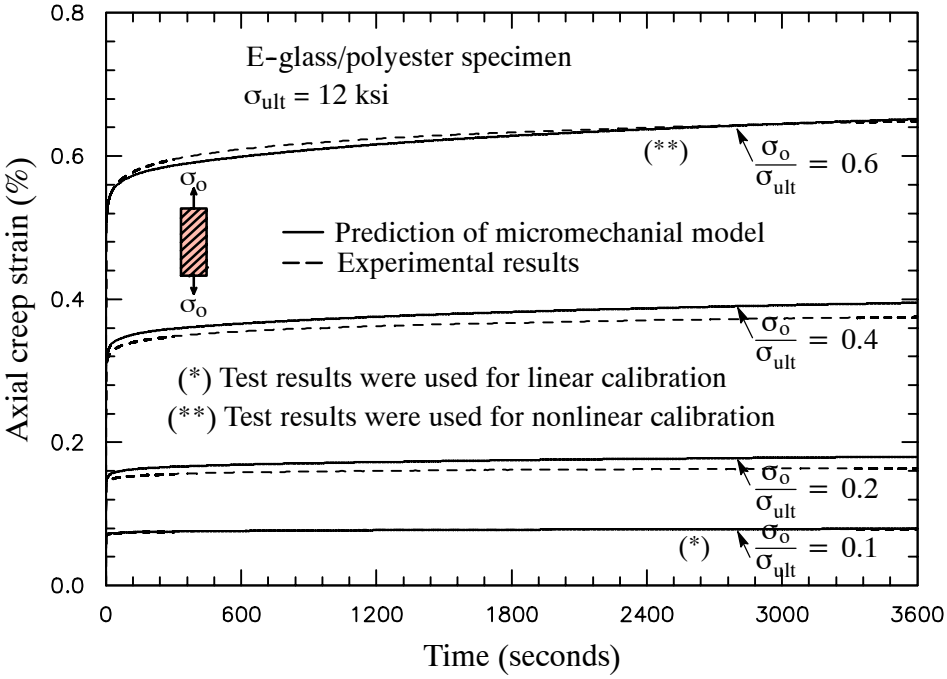

Figure 4.16 Tension axial creep for 45° off-axis pultruded FRP coupons.

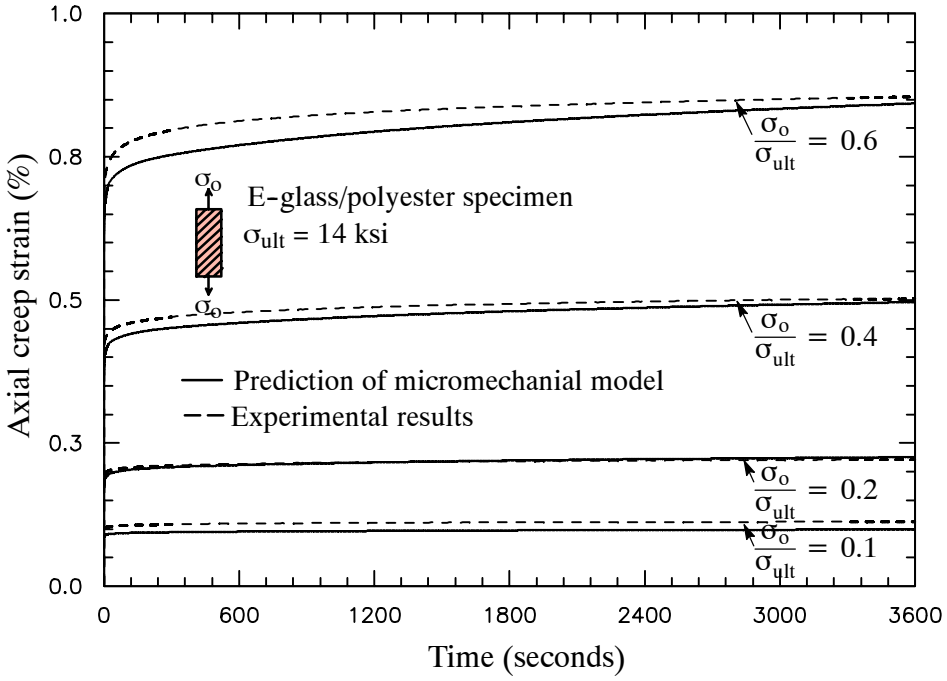

Figure 4.17 Tension axial creep for 60° off-axis pultruded FRP coupons.

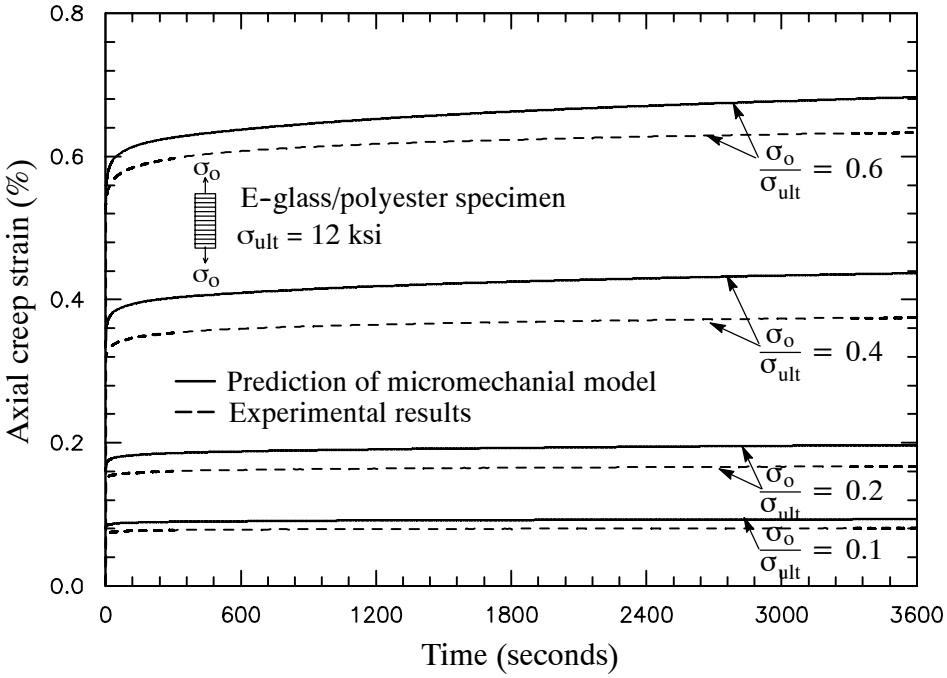

Figure 4.18 Tension axial creep for 90° off-axis pultruded FRP coupons.

CHAPTER V

INTEGRATED MICROMECHANICAL-STRUCTURAL ANALYSIS FRAMEWORK

The integrated micromechanical-structural framework is generated by applying the proposed viscoelastic micromechanical models within a displacement-based FE formulation to form the local-global nonlinear viscoelastic analysis of laminated and pultruded composite structures. The Schapery nonlinear viscoelastic constitutive model for the matrix along with the different nested micromodels for laminated and pultruded composites are implemented numerically as a material subroutine (UMAT) in the ABAQUS (2002) general FE code. The UMAT subroutine updates the stresses and stiffness matrix for given global strains and time increments assuming a constant strain rate within each time increment. History variables are used to define the state of deformations in the matrix and fiber levels of the micromodels. In the case of pultruded composite structures, the overall nonlinear viscoelastic response is generated using the nested micromodels of roving, CFM, and sublaminate at each material point (Gaussian integration point) within the elements. In the case of laminated composite structures, the four-cell micromechanical model is implemented at each material point for the nonlinear viscoelastic analysis of multi-layered composite. Off-axis creep compression and tension tests are performed for E-glass/vinylester and E-glass/polyester notched pultruded plates, respectively, in order to examine the ability of the proposed framework to predict the nonlinear viscoelastic response under multi-axial stress-strain states. The proposed multi-scale framework is also modeled in order to predict the creep responses of eccentrically loaded single-edge-notch-tension ESE(T) pultruded specimens made from E-glass fibers and polyester matrix. Finally, the integrated micromechanical-structural modeling approach is applied for the nonlinear viscoelastic analysis of different laminated composite structures.

5.1 Multi-scale Structural Framework

A general 3D multi-scale framework is proposed for the nonlinear viscoelastic analysis of laminated and pultruded composite structures. Figure 5.1 illustrates the integrated micro-mechanical-structural framework for multi-layered laminated composite structures using both 3D and shell based FE models. This approach was previously introduced by Haj-Ali and Pecknold (1996) in order to analyze the time-independent response in laminated composite structures. This study modifies and generalizes this multi-scale framework to include nonlinear viscoelastic and time-dependent effects in layered composite structures. In the case of 3D elements, the sublaminate model represents the nonlinear effective response at each material point (Gaussian point). In the case of shell elements, a sublaminate model reduces to the classical lamination theory due to the assumption of a plane stress state condition. Constant transverse-shear cross-sectional stiffness is assumed. This assumption is valid in the cases where the transverse stresses in the different layers are very small compared to the in-plane stresses. The nonlinear constitutive behavior is used to integrate the through-thickness response using integration points for each layer. Each layer can be explicitly modeled using one or more integration points. A micromechanical model is implemented at each of these points.

A new micromechanical-structural framework for the nonlinear viscoelastic analysis of pultruded composite structures is also derived in this study. It is schematically illustrated in Figure 5.2. Different micromechanical models are used for the reinforcement systems in the pultruded layers. In addition, both structural and continuum finite elements can be used. Haj-Ali et al. (2001, 2002, and 2003) was first to introduce this combined nonlinear 3D micromechanical modeling approach for pultruded composites. Their framework was time-independent and mainly focused on applying continuum elements. Kilic (2001) and Kilic and Haj-Ali (2003a) extended their material model to include quasi-static damage behavior. The upper level of this framework, in Figure 5.2, depicts FE models for pultruded structures

using 1D (beam, truss), 2D (plane, shell), and 3D (brick) elements. The 3D viscoelastic nested micromodels are implemented at each Gaussian point of every element. Different stress-strain constraints are imposed on the 3D constitutive micromodel in order to properly interface with the 1D, 2D, or 3D elements. A sublaminate model is used at each Gauss point in order to generate a 3D effective anisotropic viscoelastic response of the combined roving and CFM layers. Two independent 3D micromechanical material models are then used for the roving and CFM layers. The constitutive characterization for the fiber and matrix constituents is performed at the lowest level of the nested micro-macro modeling framework. It is assumed that both matrix constituents in the roving and CFM unit-cells have the same nonlinear viscoelastic behavior.

A material model in a displacement-based FE code is required to update the stresses and the tangent or algorithmic stiffness matrix for a given strain increment. The input data to this subroutine consists of the fiber and matrix material properties, the calibrated viscoelastic parameters for the matrix constituents, and internal convergence tolerances as well as control flags. In the case of laminated composite structures, additional input data of lamination sequence is needed. Different convergence tolerances can be used in the stress update and correction algorithms at the sublaminate, micromechanical, and matrix levels. An allocated storage for the solution dependent state variables (SDV), at each material point (Gaussian point), is used and updated at the end of each convergent increment. This vector contains all the history variables of the model at all levels of hierarchy.

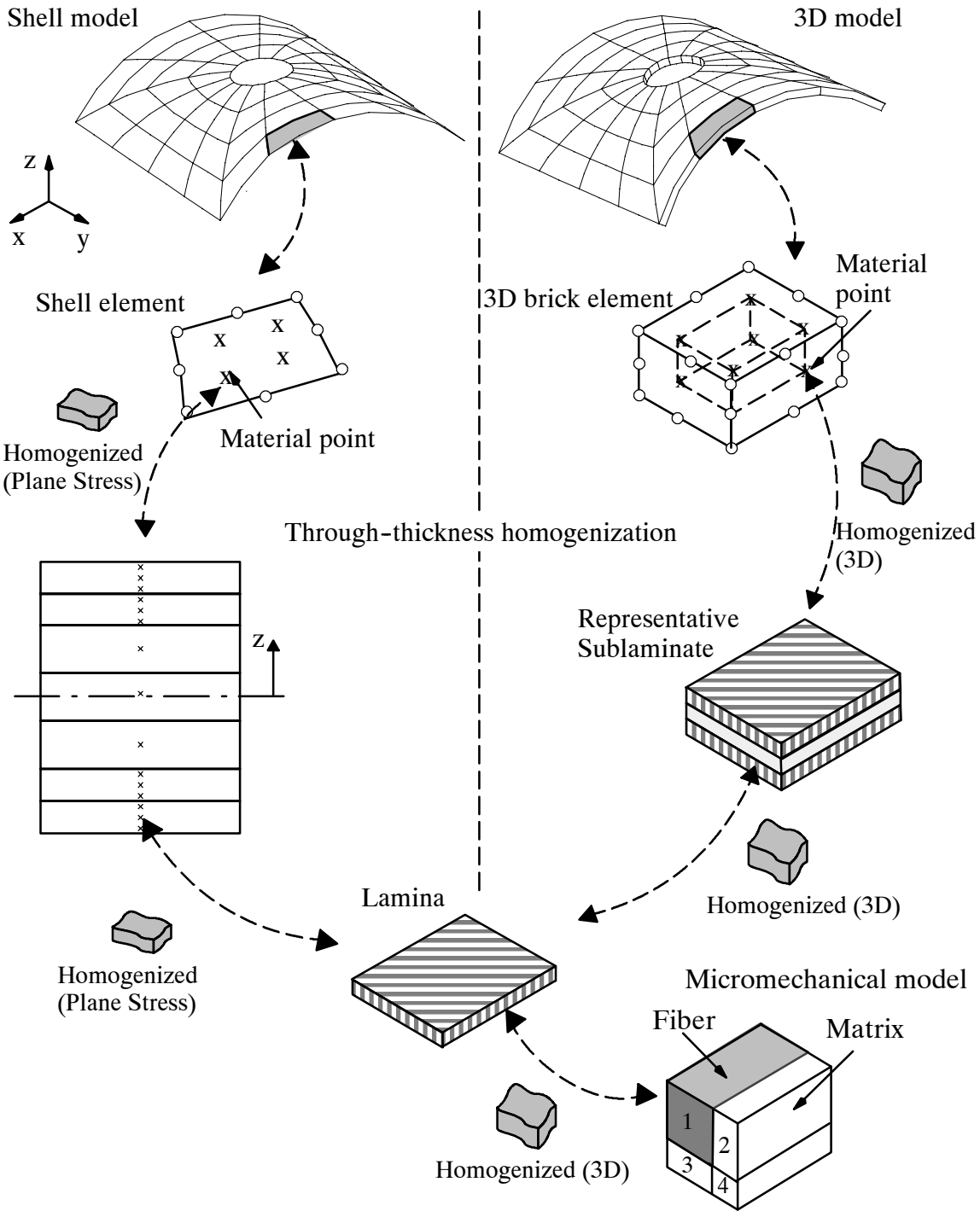

Figure 5.1 A multi-scale micromechanical-structural framework for nonlinear viscoelastic analysis of laminated composites.

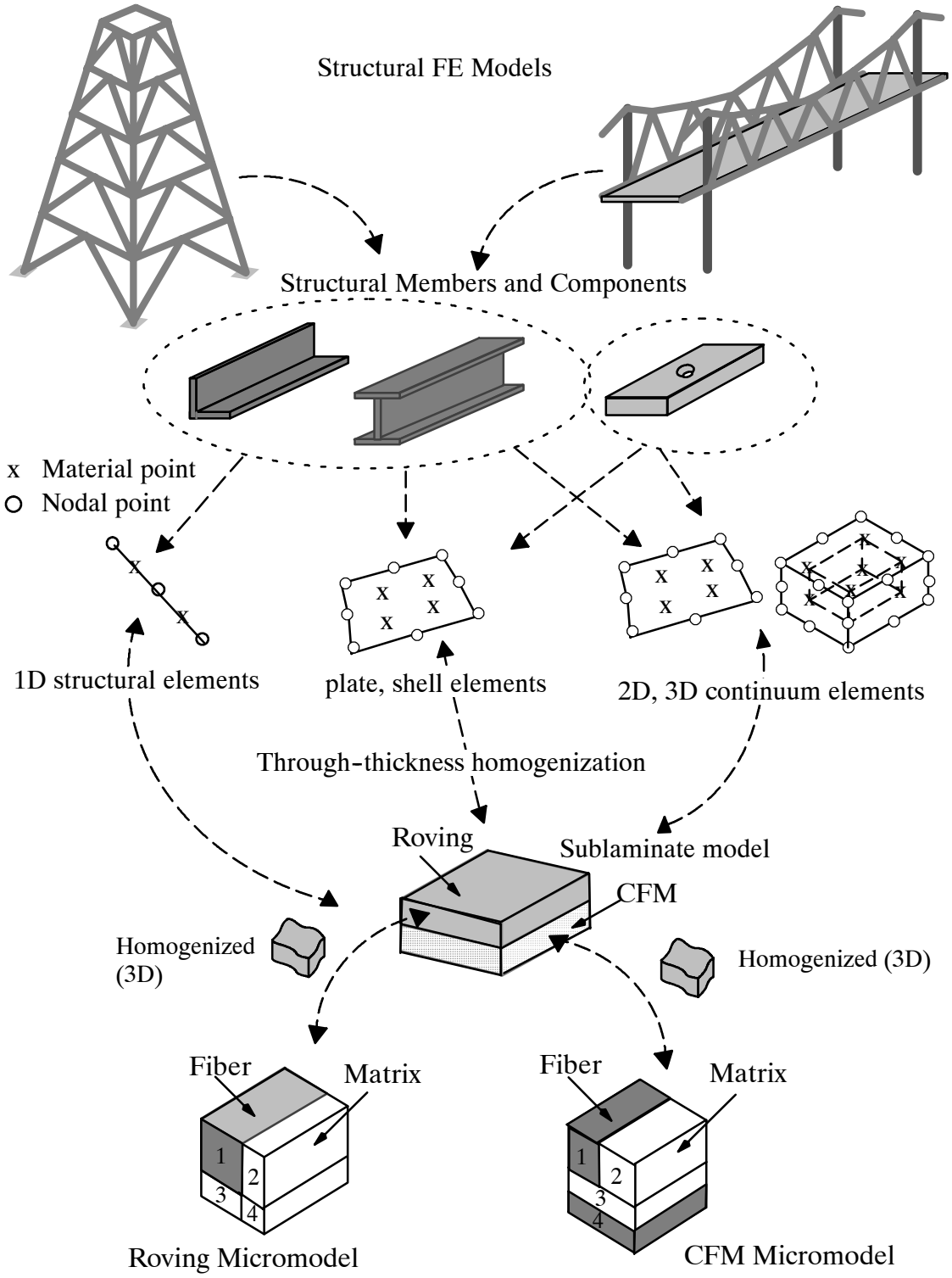

Figure 5.2 Integrated structural and micromechanical framework for the analysis of pultruded composite materials and structures.

5.2 Experimental Tests and FE Models for Notched Plate Pultruded Specimens

The combined micromechanical and structural analysis framework is verified using FE models on creep behavior of off-axis pultruded plates with a circular hole. Off-axis creep compression and tension tests are conducted on E-glass/vinylester and E-glass/polyester notched plates, respectively. The geometry of the notched plates follows the study of Kilic (2001) and Kilic and Haj-Ali (2003a) as shown in Figure 5.3. Axial strain gages are attached at three locations: G_1, G_2, and G_3 on the front surface; additional strain gage, G_4, is attached at the back surface in the case of compression specimens. Gages G_3 from the front surface and G_4 from the back surface are mounted at the same location, which are used to monitor possible bending effect due to compression loading. Different plate dimensions are used for the compressive and tensile specimens, as listed in Table 5.1. FE model is generated using continuum 20-node brick elements with reduced integration (C3D20R) and one element is used through the thickness. The FE is modeled only for a free span area. The double symmetric geometry allows a quarter plate model as seen in Figure 5.3. A total of 2874 nodes and 380 elements are generated. The area near the hole has a finer mesh in order to capture a nonlinear response, which is very pronounced in the hole area. The dimensions of the elements near gage G_1 is 0.22x0.0875 inches; around gage G_2 is 0.04x0.02 inches; and around gages G_3 and G_4 is 0.0425x0.05625 inches. The gages G_1, G_3 and G_4 are monitored at the exact location of the center point of the strain gage, while gage G_2 is monitored at the distance of 0.07 inches from the notched tip. Symmetric boundary conditions are imposed along the two symmetric edges. The top edge nodes are constrained to have a uniform axial displacement. Loading is applied through these nodes.

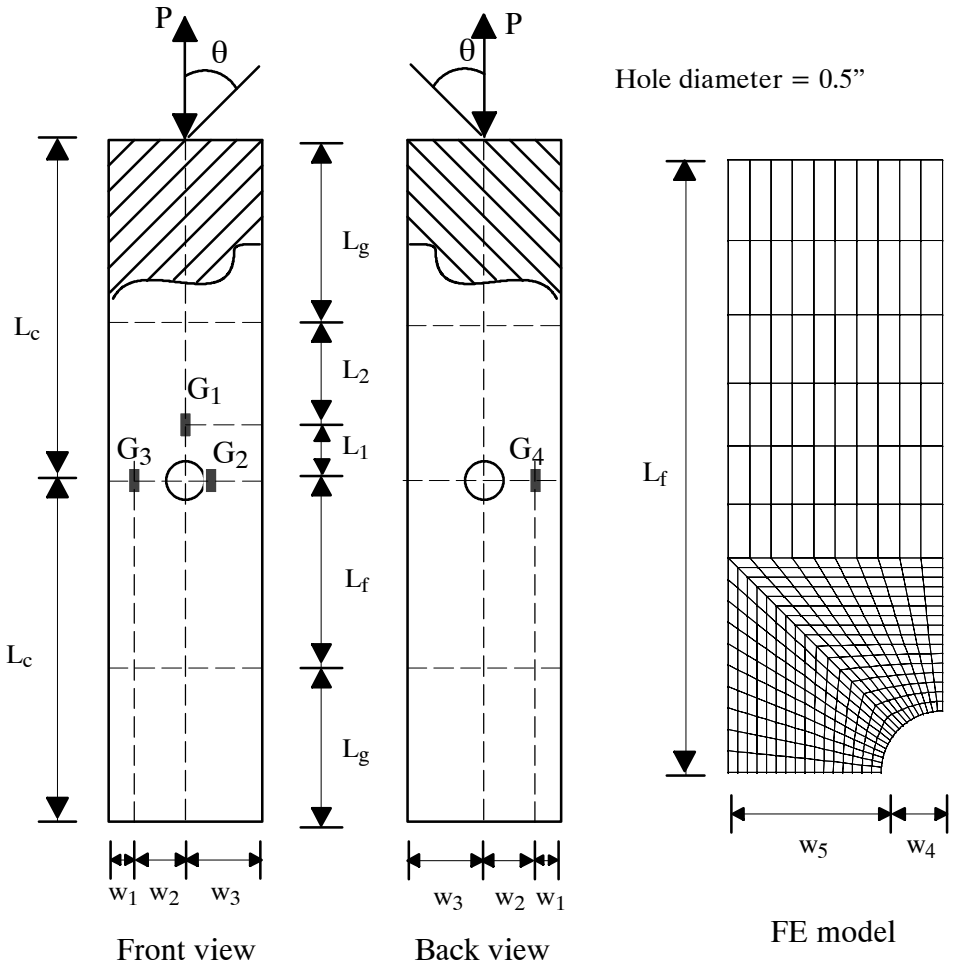

Figure 5.3 Geometry of the notched pultruded plate and FE model.

Table 5.1 Dimension of notched plates.

Dimension (inches)	L_c	L_g	L_f	L_1	L_2	w_1	w_2	w_3	w_4	w_5
Compression plate	5.0	2.5	2.5	1.0	1.5	0.3125	0.5625	0.875	0.25	0.625
Tension plate	6.0	2.5	3.5	1.0	2.5					

Compression creep responses on notched pultruded plates

Compression creep tests were performed on off-axis E-glass/vinylester notched pultruded plates with 0^o, 45^o, and 90^o roving fiber orientations. Two specimens were used for each off-axis case. Coupons were cut from the same monolithic pultruded plates as the ones of unnotched specimens in section 4.4. The plate has dimensions of 10 x 1.75 inches with a hole diameter of 0.5 inches. The measured thickness of all tested plates ranges from 0.490-0.494 inches. The load ratio for the notched off-axis specimen is defined as the applied load divided by half of the corresponding unnotched ultimate compression strength. The ultimate compression strength for unnotched off-axis specimen is reported in Table 4.5. Four compression loading ratios: 0.1, 0.2, 0.4, and 0.6, were applied to each specimen consecutively giving sufficient time, at least 24 hours, for deformation recovery after each test. All tested specimens are listed in Table 5.2. Creep tests were conducted for one hour under room temperature. The step function used during the creep loading is given in Figure 4.4. Axial strain gages were attached at four locations on the surfaces; three gages at the front surface and one gage at the back surface as shown in Figure 5.3. Detail strain gage position is given in Table 5.1. The corresponding front and back surface gages G_3 and G_4 were used to monitor a possible bending effect or buckling during the test. Each specimen was gripped along 2.5 inches from both ends with a grip pressure of 2 ksi. No mechanical conditioning was performed for each sample since the stress concentration in notched plate specimens during mechanical conditioning may cause damage to the material (Dillard et al. 1987). Conditioning may also cause plastic yielding in the matrix material (Hiel et al. 1983).

Table 5.2 Stress levels for notched-plate specimens under compression load (unit in ksi)

θ	σ_c^{ult}	Specimen	$\frac{\sigma}{\sigma^c_{ult}} = 0.1$	$\frac{\sigma}{\sigma^c_{ult}} = 0.2$	$\frac{\sigma}{\sigma^c_{ult}} = 0.4$	$\frac{\sigma}{\sigma^c_{ult}} = 0.6$
90^o	12	CS-90^o-h1	1.22	2.44	4.88	7.31
		CS-90^o-h2	1.21	2.43	4.86	7.29
45^o	12.5	CS-45^o-h1	1.25	2.50	5.00	7.50
		CS-45^o-h2	1.24	2.48	4.97	7.46
0^o	20	CS-0^o-h1	2.04	4.08	8.16	12.24

FE analyses are performed to predict the experimental creep results for the off-axis notched plates. The previously calibrated elastic and time-dependent material parameters for E-glass/vinylester off-axis pultruded coupons are used as the material properties in the subroutine UMAT. The thickness of the plate is taken as 0.492 inches. All nodes on the top of notched plate are linked together to one master node. Loading is applied through the master node. Due to a symmetric model, only half of the actual force is given to the master node. Multiple loading steps are used in the FE analyses. The first step simulates the instantaneous loading with duration of 0.001 seconds. The constant load is then held for 20 seconds with initial time increments of 1 second to capture the transient response. The next viscoelastic step is carried for 200 seconds with initial time increments of 10 seconds. The constant load for the last step is continued until 1 hour with increments of 100 seconds. These are suggested initial time increments and are likely to increase during analysis due to automated time-increment scheme in ABAQUS. The strains from the FE models are extracted at the corresponding locations of the center of each strain gage.

Figures 5.4 (a)-(d) and 5.5 (a)-(d) show the comparison of FE analysis and experimental tests for the transverse and 45^o off-axis notched plates, respectively, under several load ratios: 0.1-0.6. The creep strains from gages G_1, G_2, and averaged of G_3 and G_4 are reported. The complete strain results from both G_3 and G_4 gages are listed in Appendix B. For every

load level, two tests were performed from different coupons. Overall, the FE models show good nonlinear prediction of the experimental results. The FE prediction and creep test data for the uniaxial notched plate under various compression loads are illustrated in Figure 5.6 (a)-(d). Only one coupon was used for all load levels. For the applied stress of 0.6 σ_{ult}, the tests were repeated twice from the same coupon. A limited linear viscoelastic response is shown from the strain gages of the uniaxial notched plate tests. This is due to the high uniaxial reinforcement of the material.

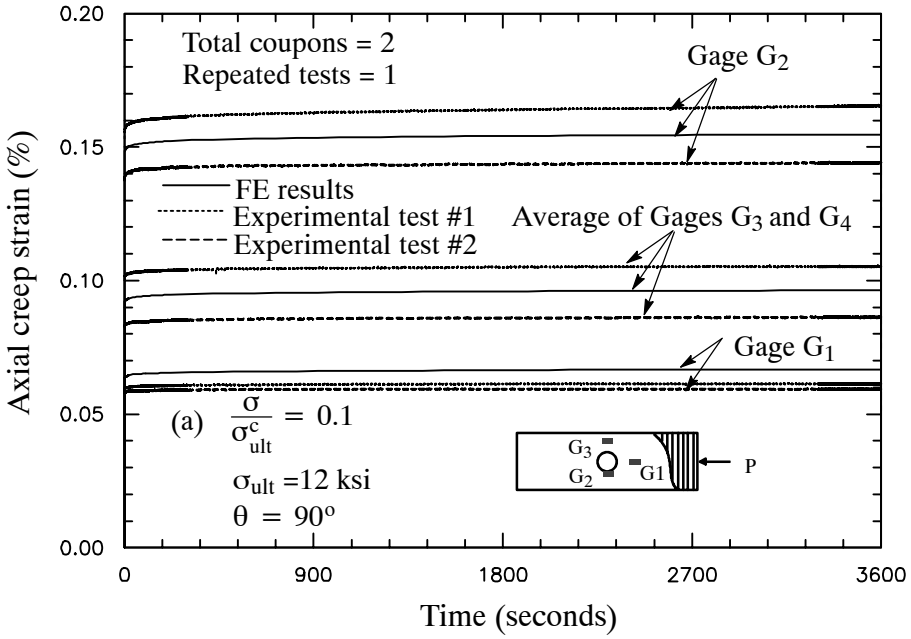

Figure 5.4 (a) Prediction of FE with micromodel compared to axial creep compression tests for notched pultruded plates with 90° off-axis angle under load ratio 0.1.

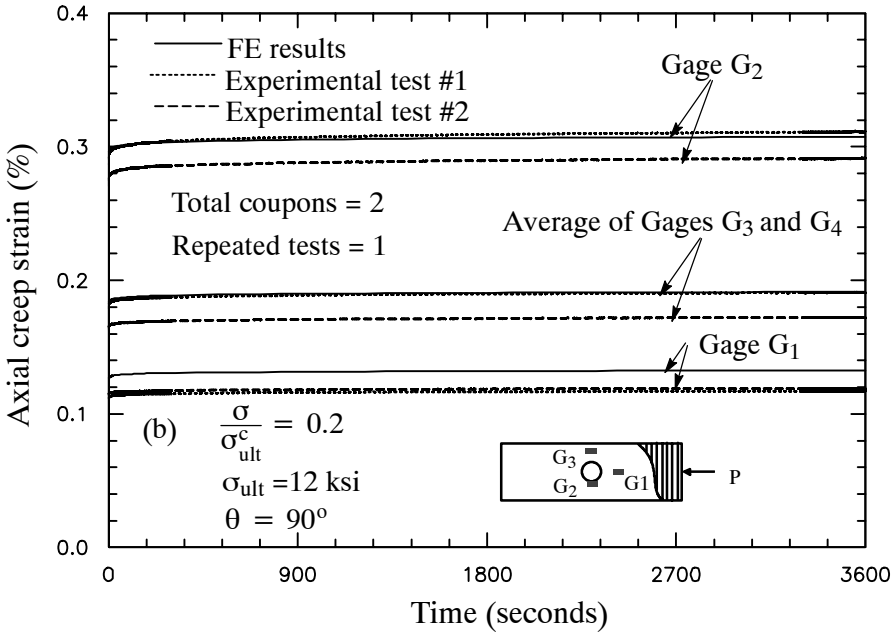

Figure 5.4 (b) Prediction of FE with micromodel compared to axial creep compression tests for notched pultruded plates with 90° off-axis angle under load ratio 0.2.

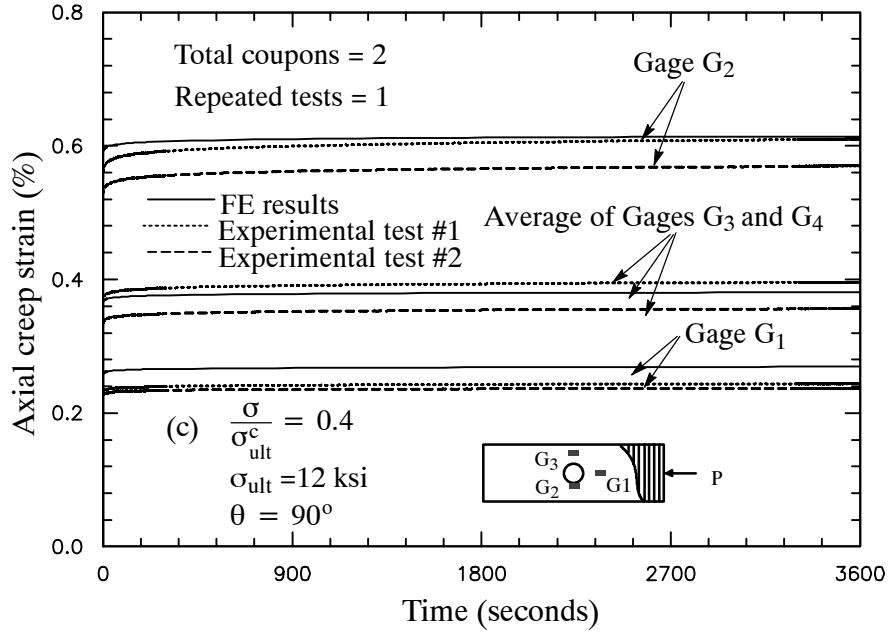

Figure 5.4 (c) Prediction of FE with micromodel compared to axial creep compression tests for notched pultruded plates with 90° off-axis angle under load level 0.4.

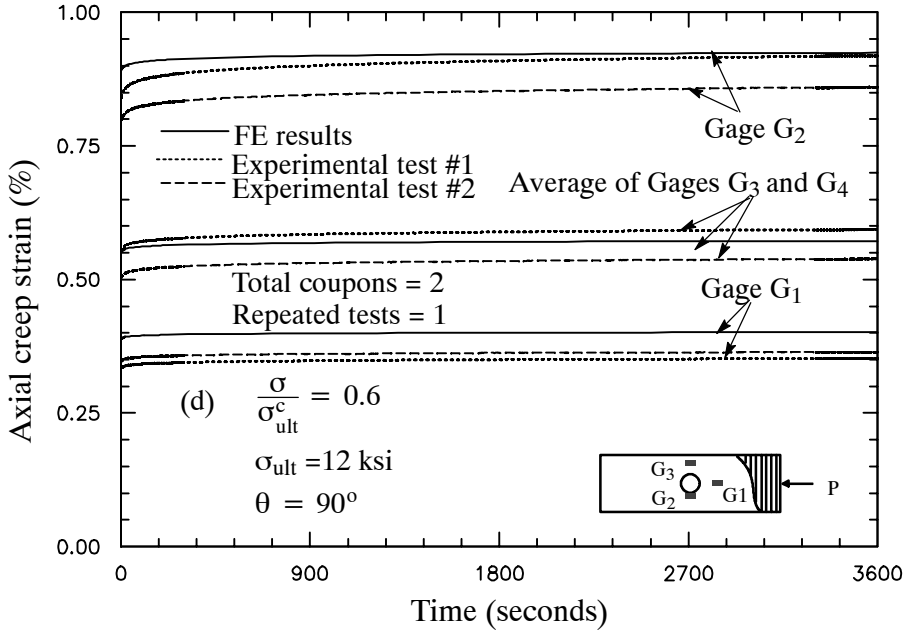

Figure 5.4 (d) Prediction of FE with micromodel compared to axial creep compression tests for notched pultruded plates with 90° off-axis angle under load level 0.6.

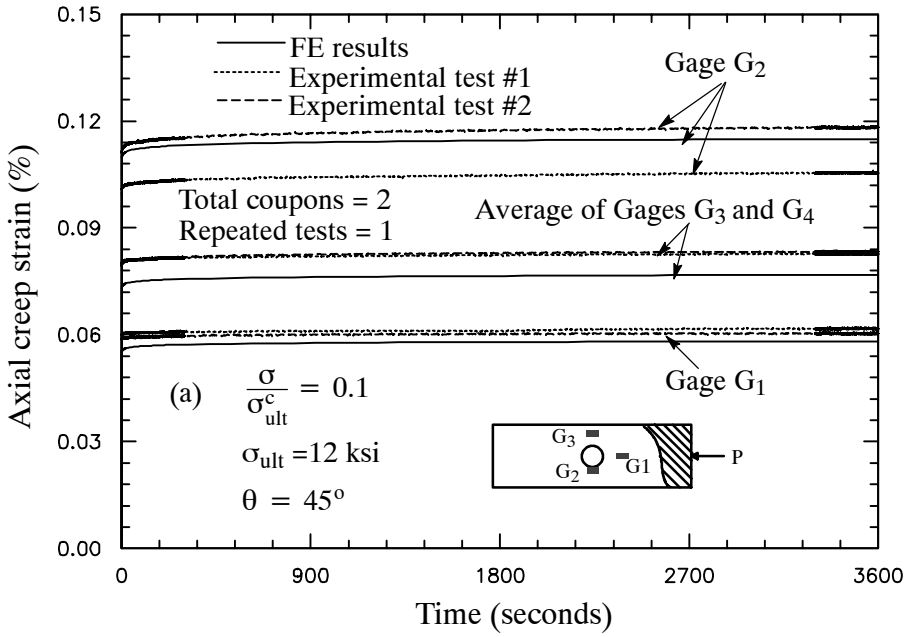

Figure 5.5 (a) Prediction of FE with micromodel compared to axial creep compression tests for notched pultruded plates with 45° off-axis angle under load level 0.1.

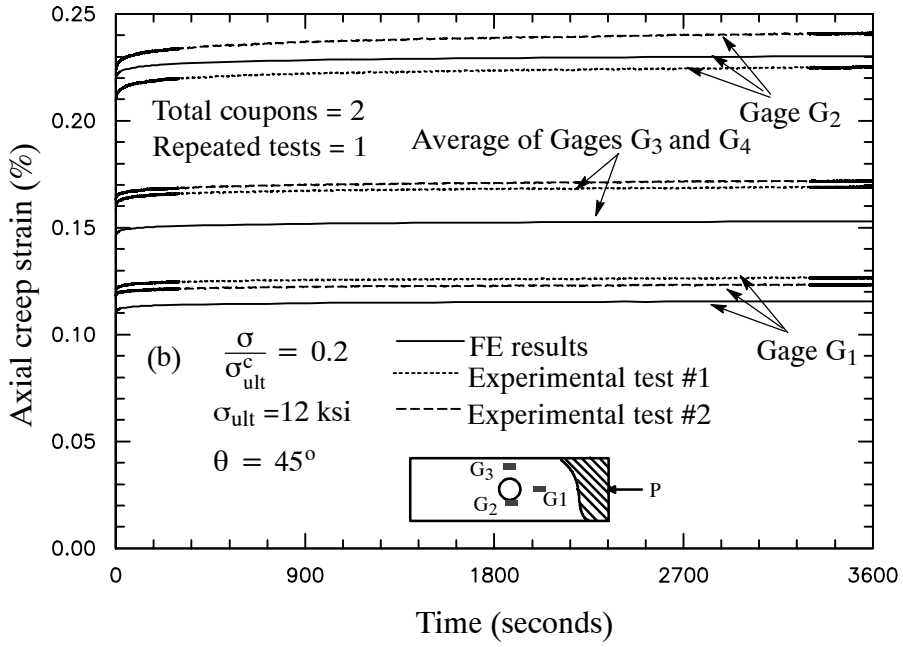

Figure 5.5 (b) Prediction of FE with micromodel compared to axial creep compression tests for notched pultruded plates with 45° off-axis angle under load level 0.2.

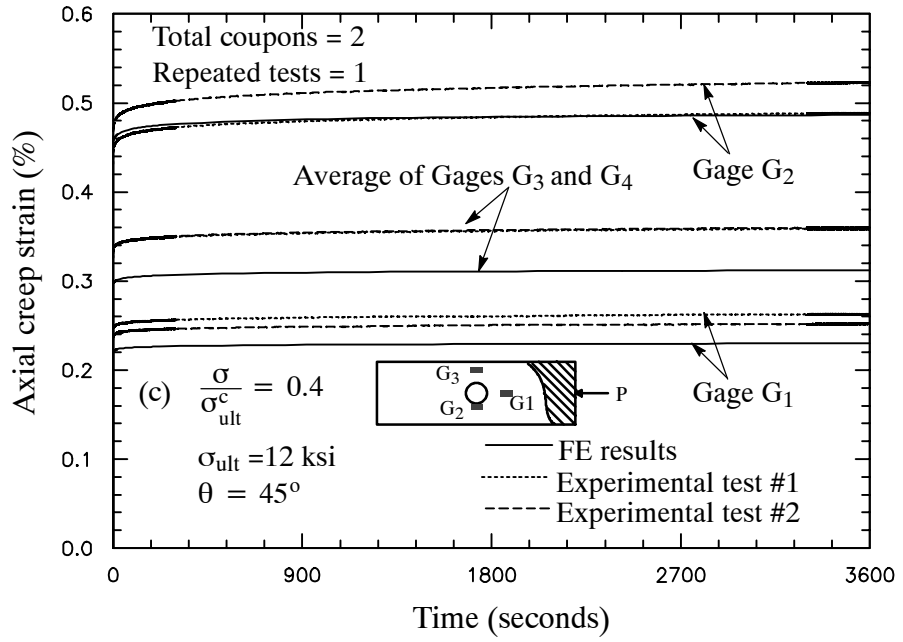

Figure 5.5 (c) Prediction of FE with micromodel compared to axial creep compression tests for notched pultruded plates with 45° off-axis angle under load level 0.4.

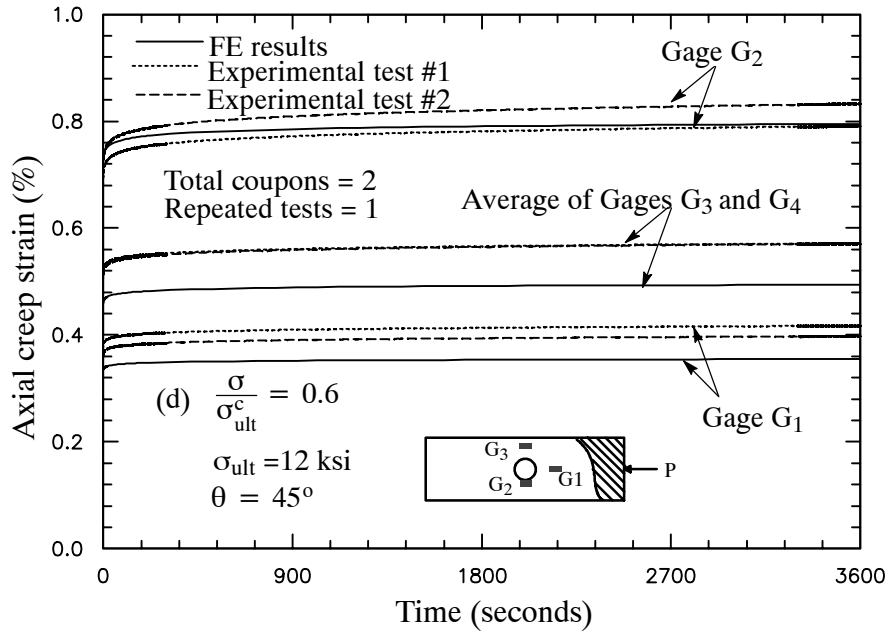

Figure 5.5 (d) Prediction of FE with micromodel compared to axial creep compression tests for notched pultruded plates with 45° off-axis angle under load level 0.6.

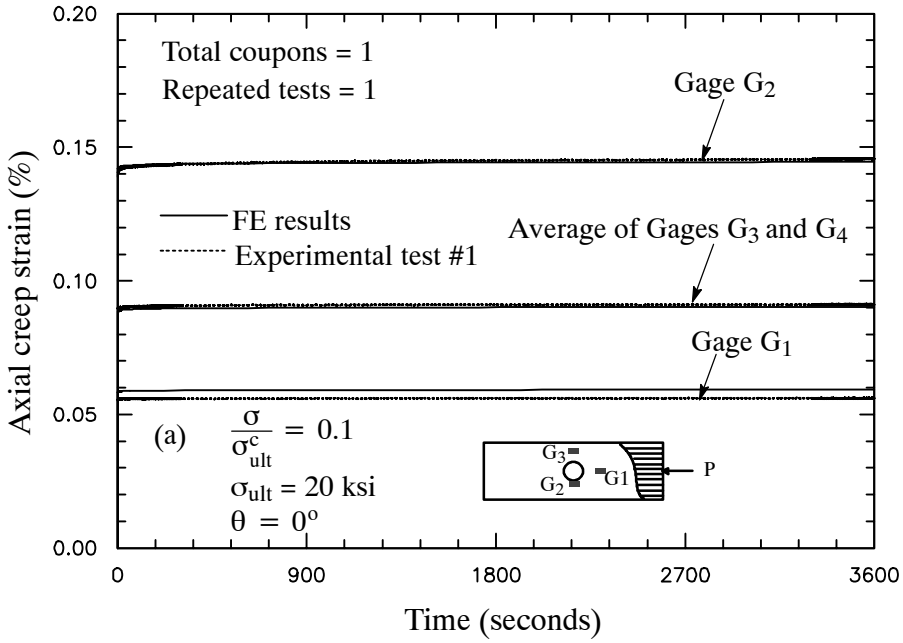

Figure 5.6 (a) Prediction of FE with micromodel compared to axial creep compression tests for uniaxial notched pultruded plates under load level 0.1.

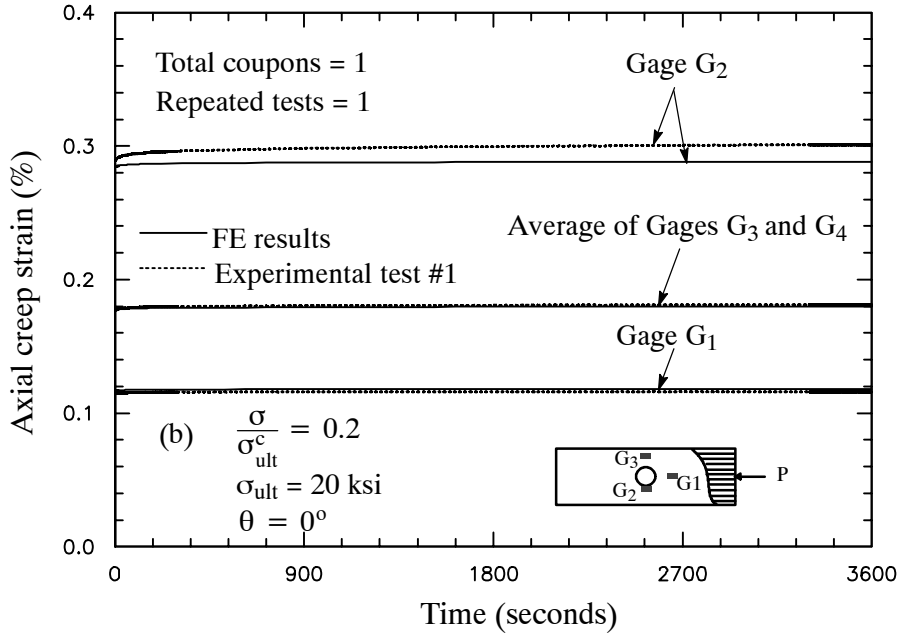

Figure 5.6 (b) Prediction of FE with micromodel compared to axial creep compression tests for uniaxial notched pultruded plates under load level 0.2.

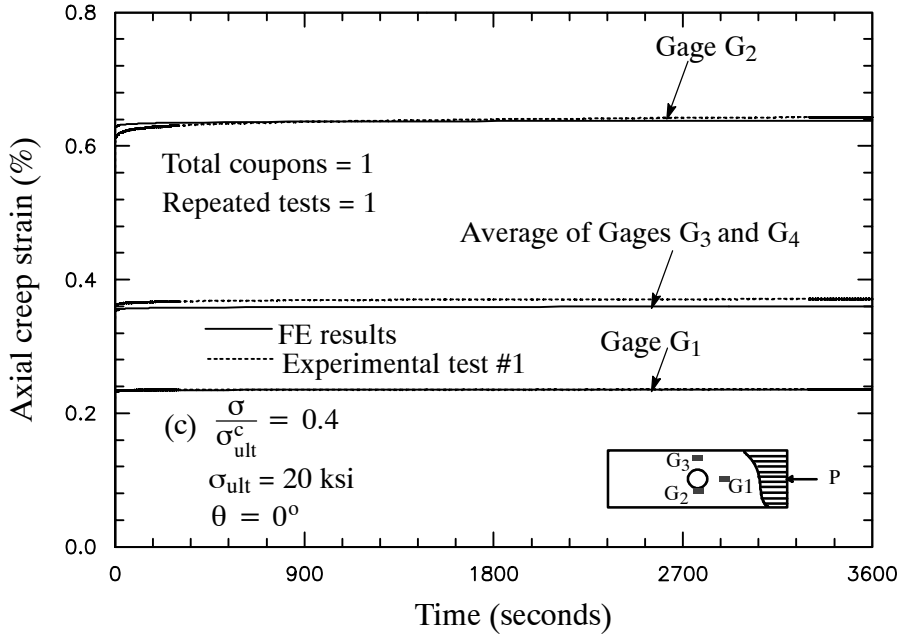

Figure 5.6 (c) Prediction of FE with micromodel compared to axial creep compression tests for uniaxial notched pultruded plates under load level 0.4.

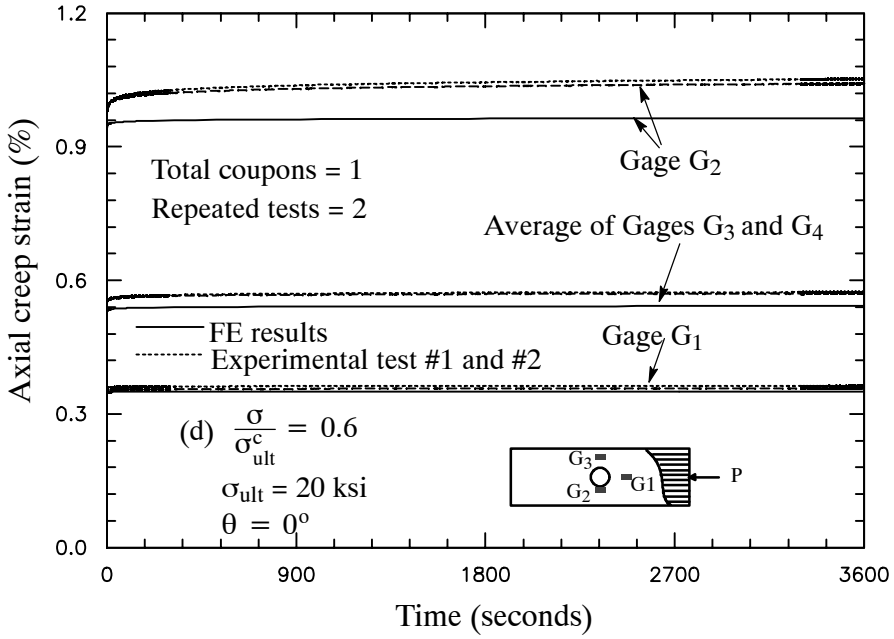

Figure 5.6 (d) Prediction of FE with micromodel compared to axial creep compression tests for uniaxial notched pultruded plates under load level 0.6.

Tension creep responses on notched pultruded plates

One-hour tensile creep tests were performed on three off-axis E-glass/polyester pultruded plates, having 0°, 45°, and 90° roving fiber orientations. A single plate is used for each off-axis angle. The dimensions of the plate are 12 x 1.75 inches with the hole diameter of 0.5 inches. The measured thickness of all tested plates ranges from 0.482-0.485 inches. The ultimate static load levels for these structural components were assumed to be half of the unnotched ultimate tension strength, as listed in Table 4.8. Four tension load ratios: 0.1, 0.2, 0.4, and 0.6 of the notched plate ultimate tensile strength were applied consecutively and each specimen was given sufficient time for strain recovery after each test. The instantaneous step loading in Figure 4.4 is used for the creep test. Axial strain gages were attached at three locations on one surface as shown in Figure 5.3. Each specimen was gripped along 2.5 inches from both edges with a grip pressure of 2 ksi. The tests were done under fixed environmental condition with the average test temperature and humidity of 24°C and 38.6%, respectively.

FE models are generated to analyze the nonlinear viscoelastic response of these notched specimens. The plate thickness is modeled as 0.482 inches. The previously calibrated material parameters on E-glass/polyester coupons are used as the material properties in the subroutine UMAT. Multiple loading steps are simulated, as previously explained. The strains from the FE models are extracted at the corresponding locations of the center of each strain gage. The FE model and test results for the uniaxial notched plate under tension loading ratios: 0.1-0.6 are shown in Figure 5.7 (a)-(d). The FE models predict the experimental data very well. The creep strain predictions for transverse and 45° off-axis notched pultruded specimens under various tensile load levels: 0.1-0.6 of the ultimate strength, are shown in Figures 5.8 (a)-(d) and 5.9 (a)-(d), respectively. Relatively large deviation between FE prediction and experimental data is shown for the test with the highest applied stress. Under this load level, the stress distributions at the notched pultruded plate are higher than the stress level used for the calibration, especially near the hole area.

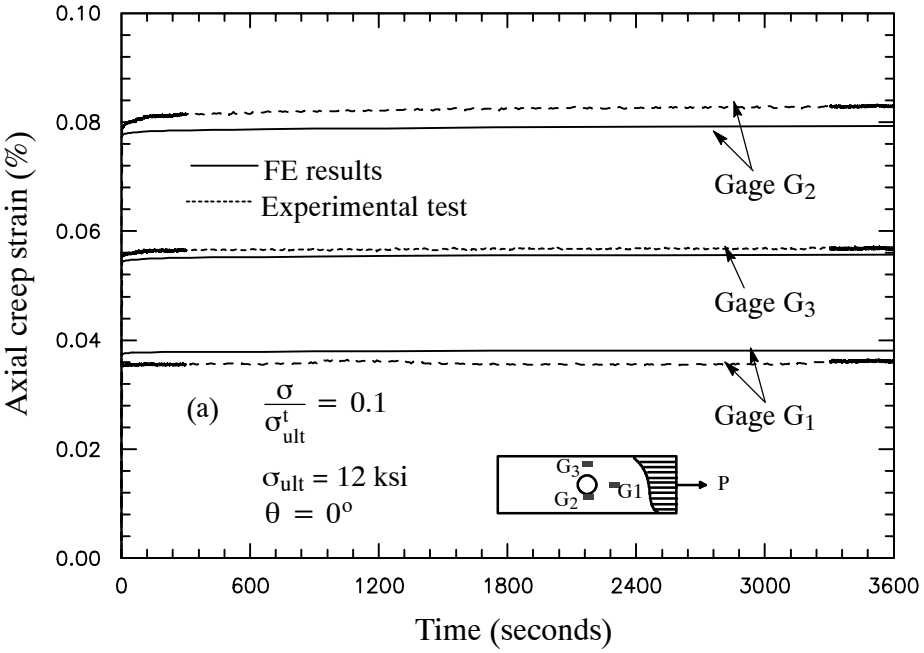

Figure 5.7 (a) Prediction of FE with micromodel compared to axial creep tension tests for uniaxial notched pultruded plate under load level 0.1.

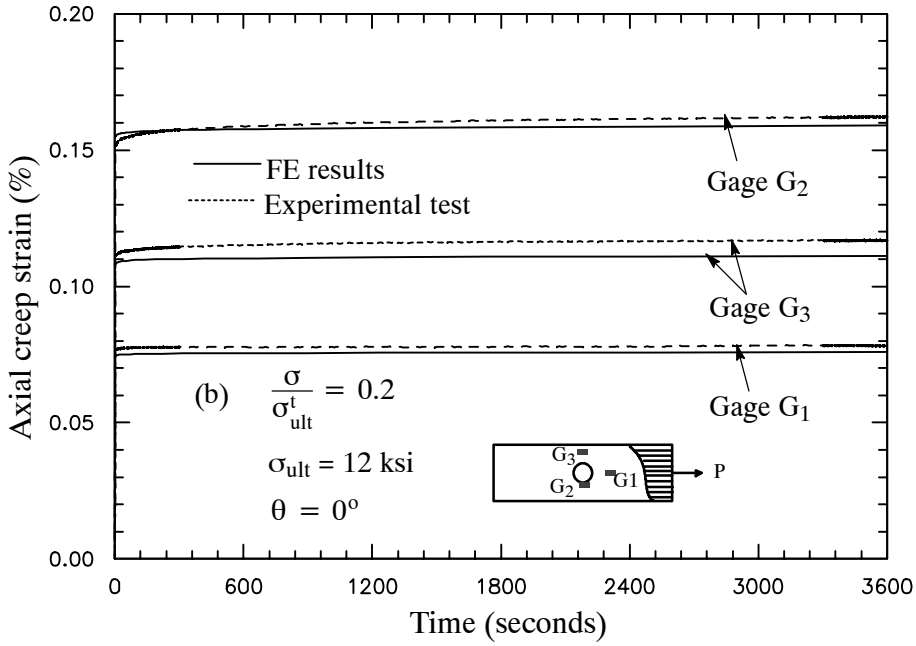

Figure 5.7 (b) Prediction of FE with micromodel compared to axial creep tension tests for uniaxial notched pultruded plate under load 0.2.

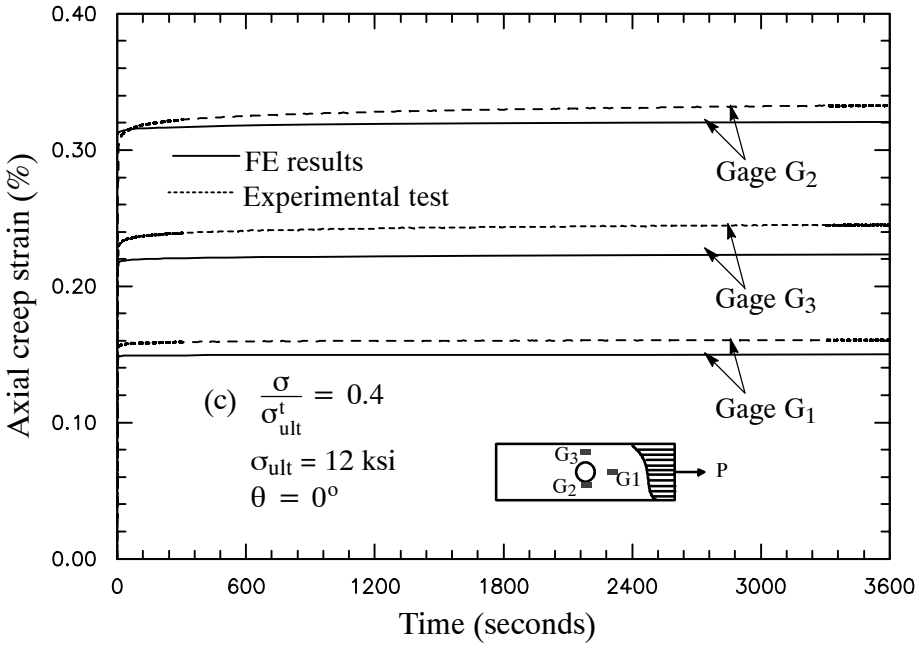

Figure 5.7 (c) Prediction of FE with micromodel compared to axial creep tension tests for uniaxial notched pultruded plate under load 0.4.

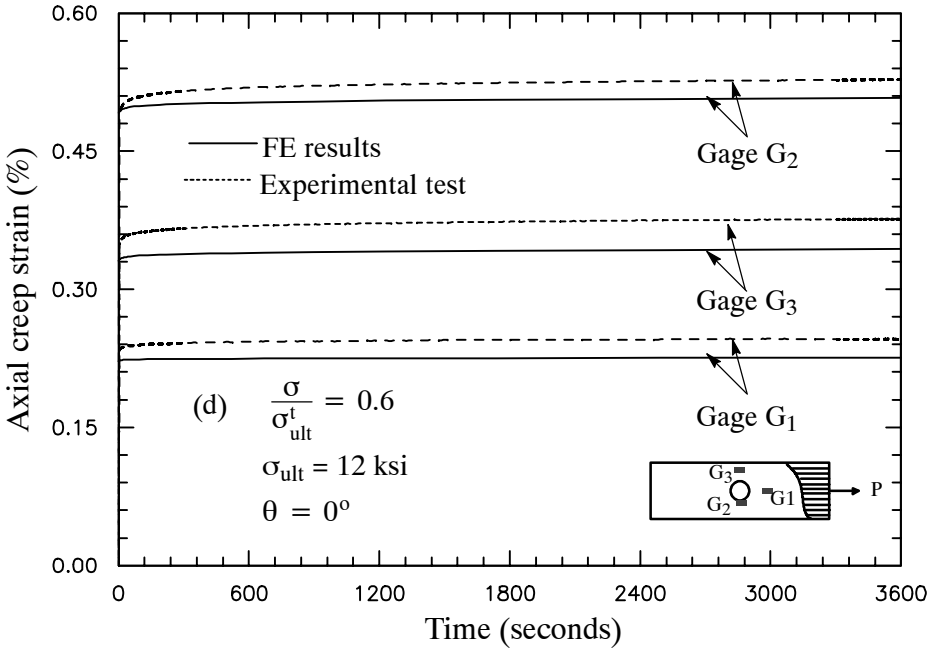

Figure 5.7 (d) Prediction of FE with micromodel compared to axial creep tension tests for uniaxial notched pultruded plate under load level 0.6.

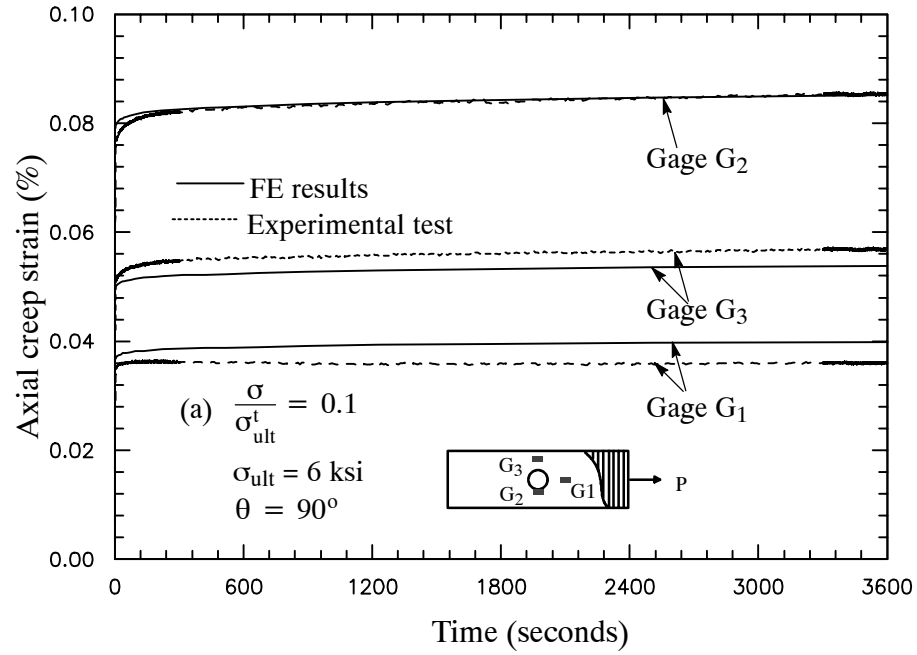

Figure 5.8 (a) Prediction of FE with micromodel compared to axial creep tension tests for transverse notched pultruded plate under load 0.1.

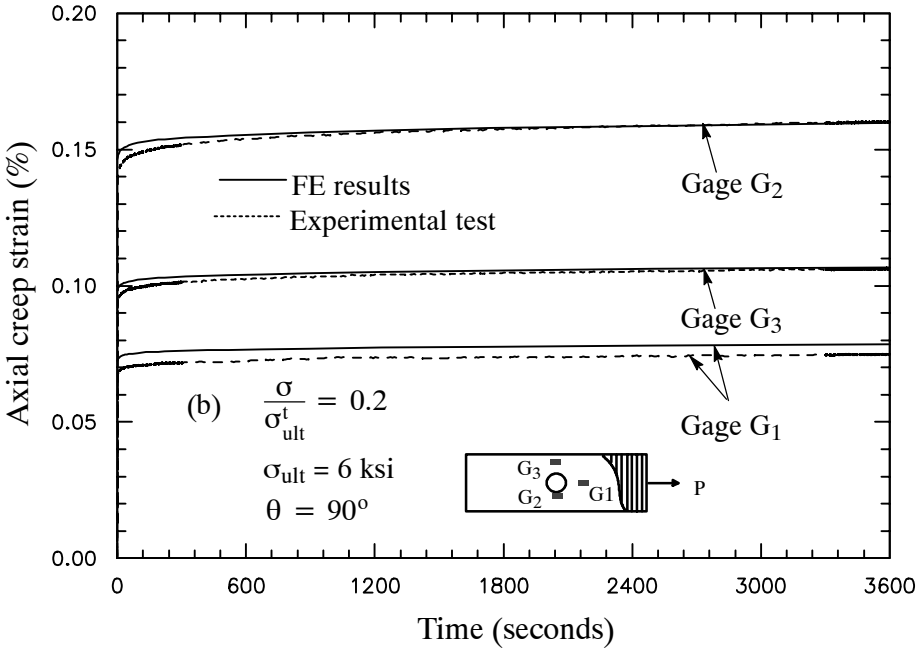

Figure 5.8 (b) Prediction of FE with micromodel compared to axial creep tension tests for transverse notched pultruded plate under load 0.2.

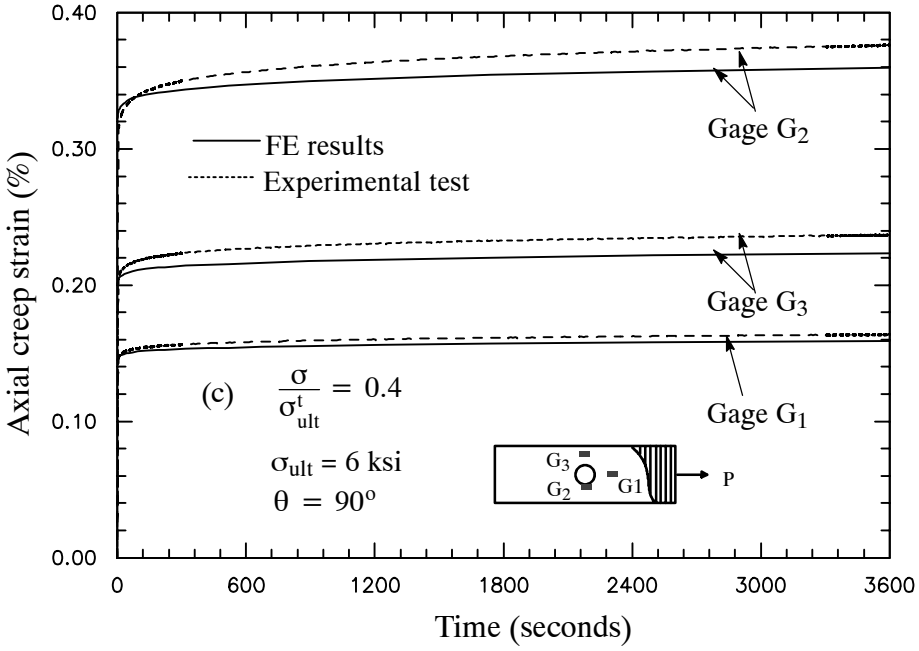

Figure 5.8 (c) Prediction of FE with micromodel compared to axial creep tension tests for transverse notched pultruded plate under load 0.4.

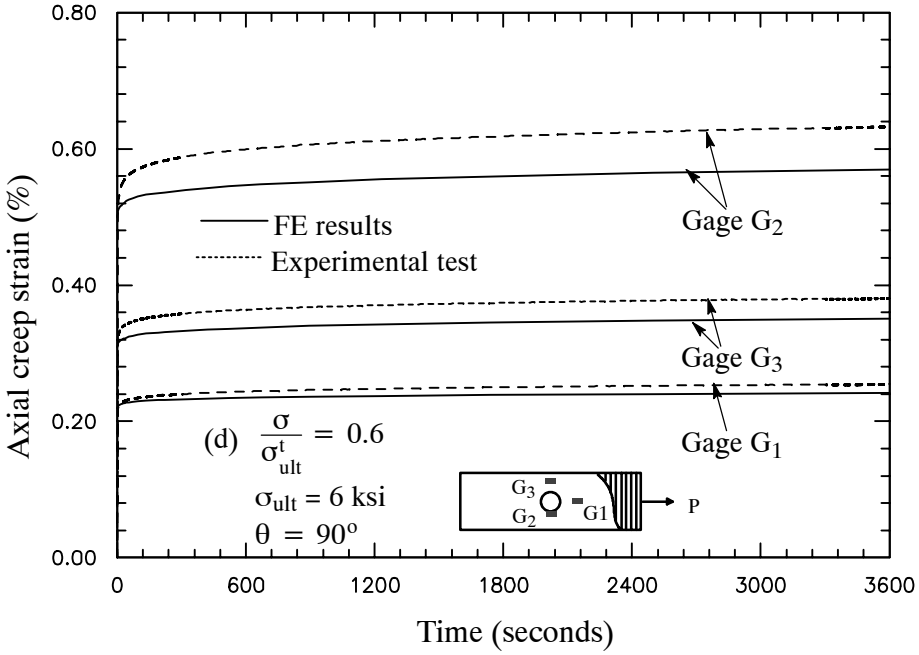

Figure 5.8 (d) Prediction of FE with micromodel compared to axial creep tension tests for transverse notched pultruded plate under load 0.6.

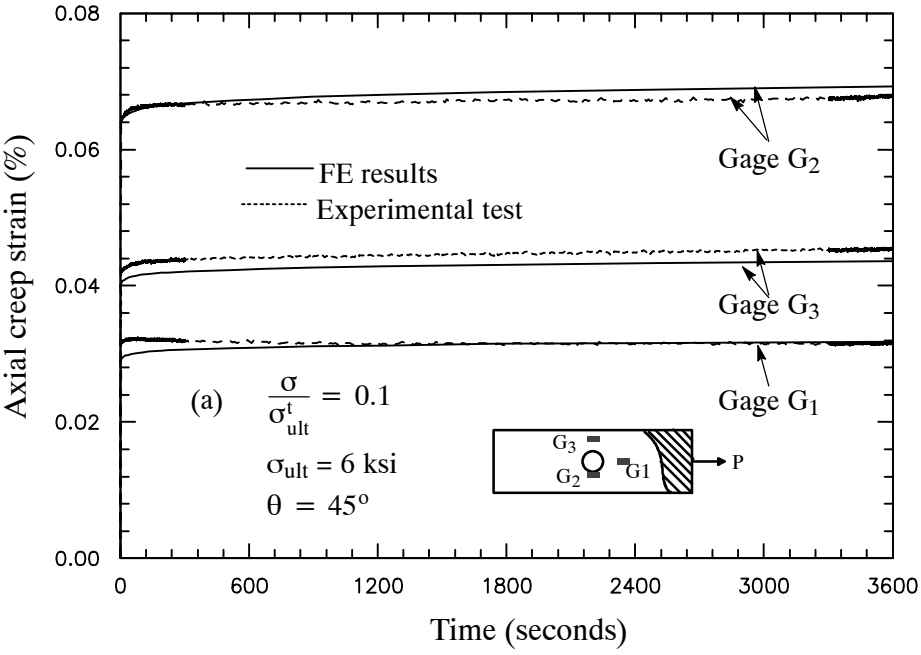

Figure 5.9 (a) Prediction of FE with micromodel compared to axial creep tension tests for 45° off-axis notched pultruded plate under load level 0.1.

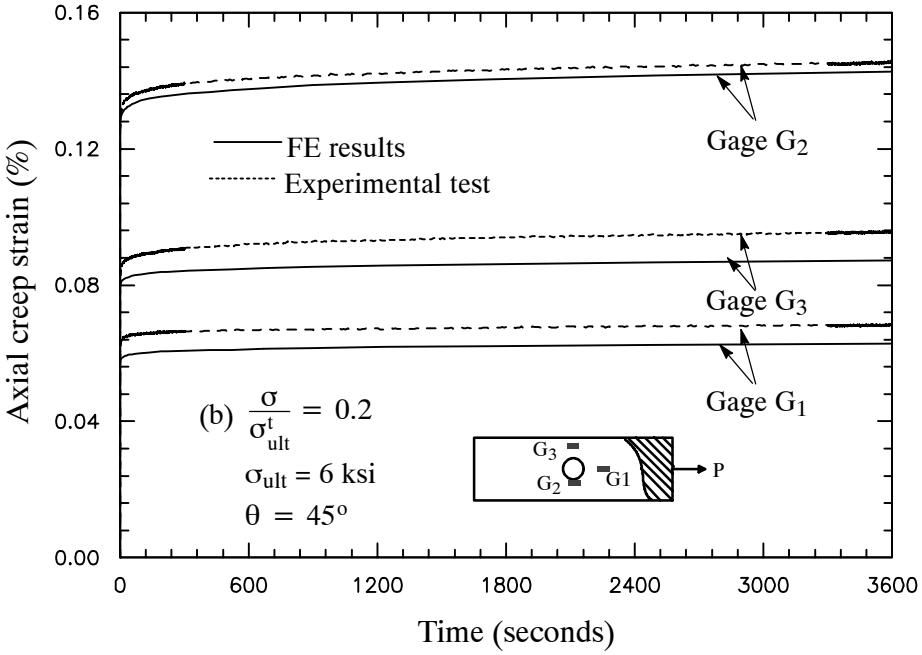

Figure 5.9 (b) Prediction of FE with micromodel compared to axial creep tension tests for 45° off-axis notched pultruded plate under load level 0.2.

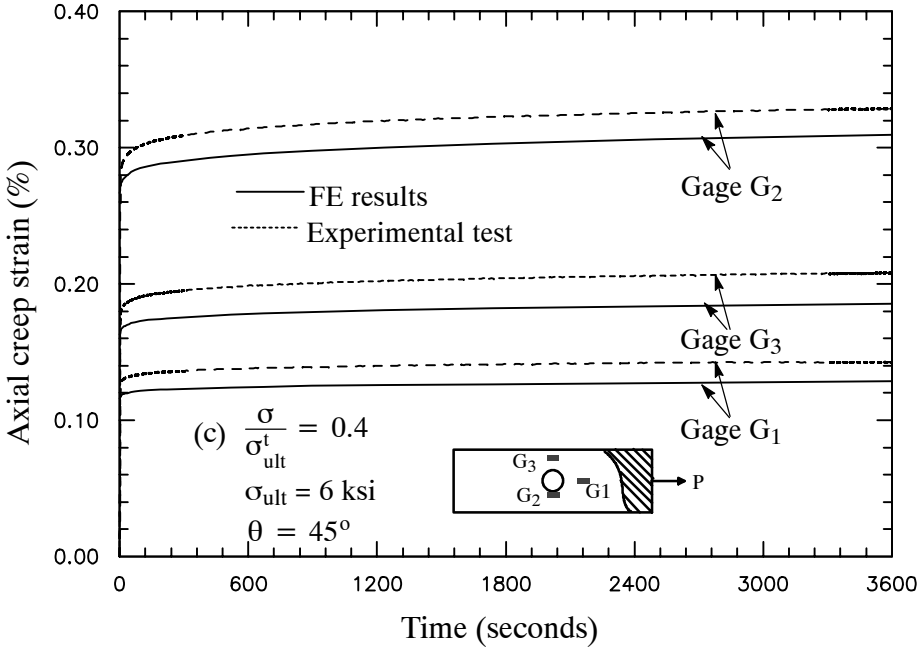

Figure 5.9 (c) Prediction of FE with micromodel compared to axial creep tension tests for 45° off-axis notched pultruded plate under load level 0.4.

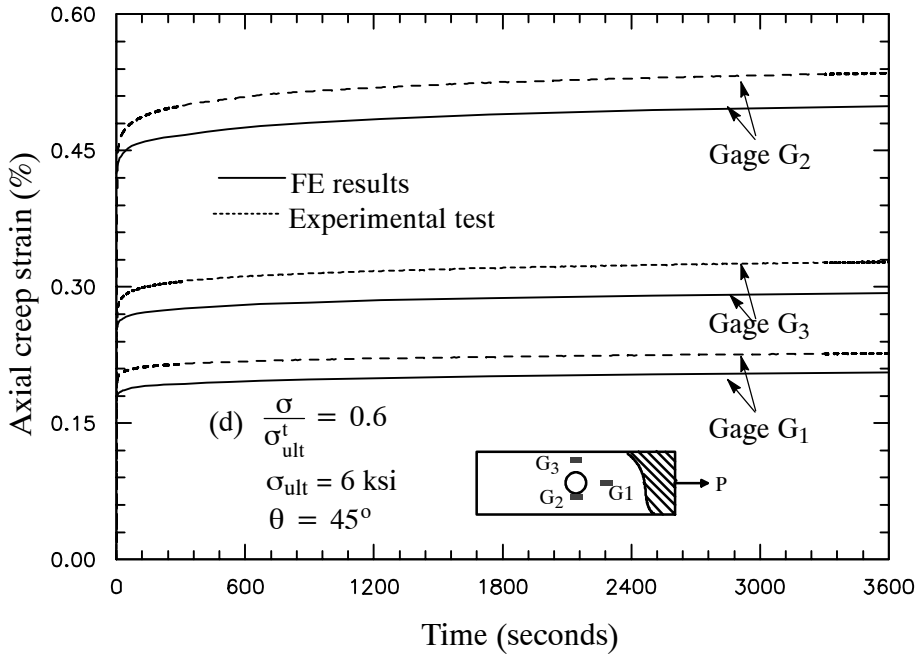

Figure 5.9 (d) Prediction of FE with micromodel compared to axial creep tension tests for 45° off-axis notched pultruded plate under load level 0.6.

5.3 Creep Analysis of Mode-I Fracture Specimens

The proposed micromechanical-structural analysis is applied to model the creep response of eccentrically loaded single-edge-notch-tension ESE(T) fracture specimens. To that end, ESE(T) specimens were cut from E-glass/polyester monolithic pultruded plate similar to the tensile coupons, in section 4.5. The geometry of the ESE(T) pultruded specimen is shown in Figure 5.10. It follows the one used by Haj-Ali and El-Hajjar (2003) to study time-independent crack propagation and toughness of pultruded composites. The specimen has dimension of 2.5x10 inches with a notch at the center. The notch length, a, can be varied. An extensometer is usually attached at the notch edge and is used to measure the crack mouth opening displacement (CMOD). Loading is applied through a rod mounted at the pin loading. FE models are generated using the ABAQUS C3D20R brick elements with a single element through the thickness. The FE mesh is symmetry as shown in Figure 5.10. In a typical ESE(T) model, a total of about 7000 nodes and 900 elements are used.

The area near the notch has a finer mesh in order to capture the nonlinear elastic and viscoelastic responses that are pronounced near the crack tip. Symmetric boundary conditions are imposed along the mid-surface of the specimen. Forces are assumed to act at the nodes located on the contact line between the pin and the specimen. The vertical displacements of these nodes are linked together to a master node to impose a uniform axial displacement. Tensile force is applied through the master node.

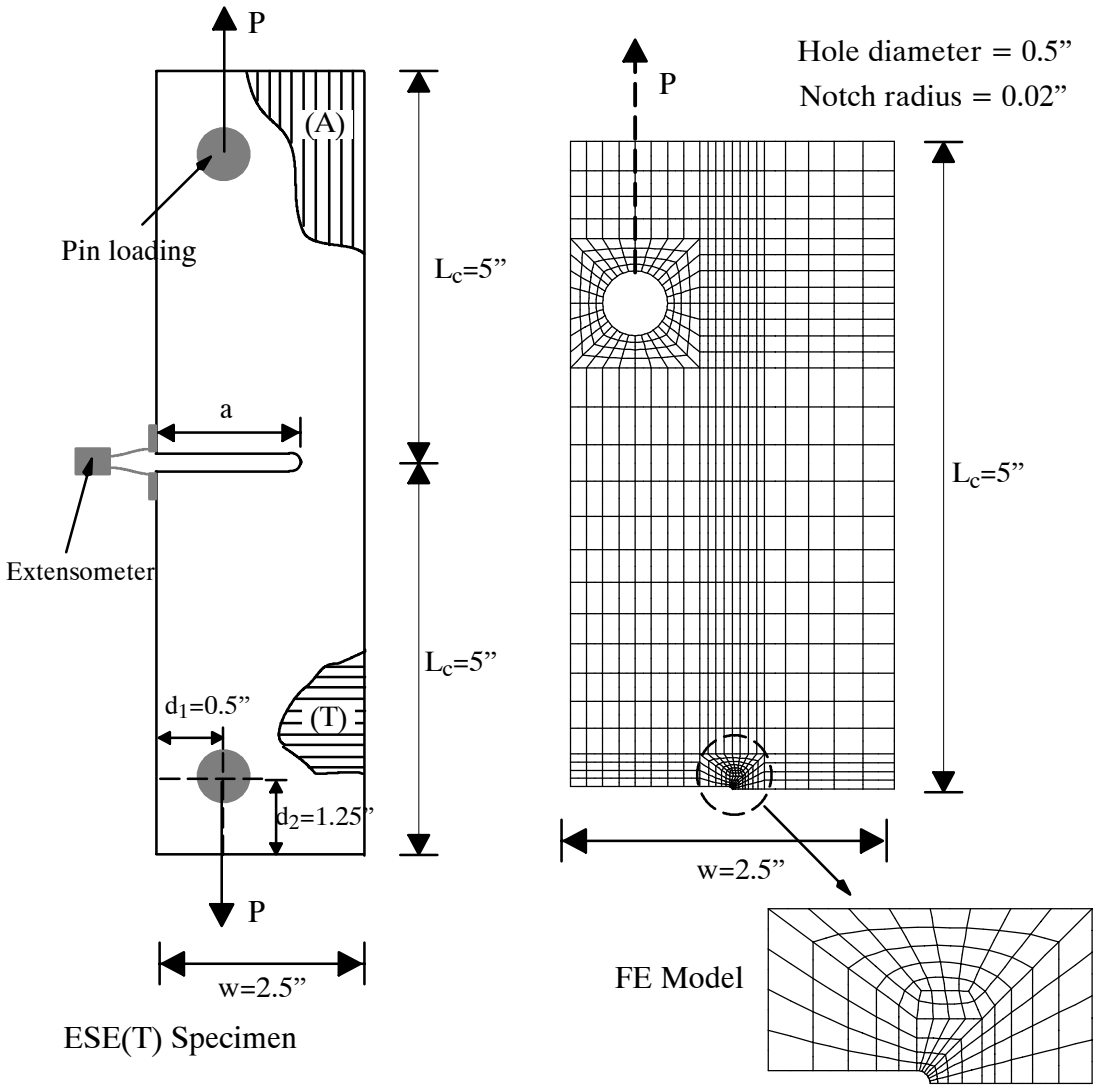

Figure 5.10 Dimension of ESE(T) pultruded plate and FE model.

The ESE(T) specimens include two possible roving orientations. The first is a uniaxial orientation where the fibers in the roving layers are in the loading direction. The second is a transverse orientation where the fibers in the roving layers are aligned with the crack line. Six specimens included three a/w ratios: 0.3, 0.5, and 0.7 in both uniaxial and transverse orientations were tested. Creep tests were performed for 90 minutes. The average temperature and humidity during the tests were 18^{o}C and 33%, respectively. Three loading ratios: 0.2, 0.4, and 0.6 of the specimen ultimate tensile force, P_{cr}, were applied consecutively to each specimen, given a sufficient time for deformation recovery after each test. The value of P_{cr} for uniaxial and transverse specimens with different a/w ratios are taken from the static fracture study of Haj-Ali and El-Hajjar (2003) and is listed in Table 5.3. The values of P_{cr} were determined based on maximum load reached with or without initial crack growth. Figure 5.11 describes the manner that the creep load was applied during the tests in order to simulate a 'step function'. The elastic stiffness of the ESE(T) specimens was obtained prior to each creep test in order to monitor the formation of a permanent damage including crack growth. This was achieved in separate static tests, prior and after the creep tests, by applying a load with a 0.1 P_{cr} magnitude. The change of stiffness was determined by calculating the initial slope of the load versus CMOD curve termed herein as $\Delta P/\Delta CMOD$. The measured changes in the elastic stiffness for both uniaxial and transverse specimens are given in Tables 5.4 and 5.5, respectively. Sufficient time for creep recovery was possible by storing the samples before the next creep test. This was independently verified by monitoring stiffness during recovery. It is seen that damage may accumulate under higher applied loads. This is used later to explain the inaccuracy in the prediction of creep response because the proposed constitutive models do not include damage.

Table 5.3 Ultimate load for E-glass/polyester ESE(T) specimens.

a/w		0.3	0.5	0.7
Pcr (kip)	uniaxial	3.4	1.8	0.8
	transverse	1.75	1.0	0.625

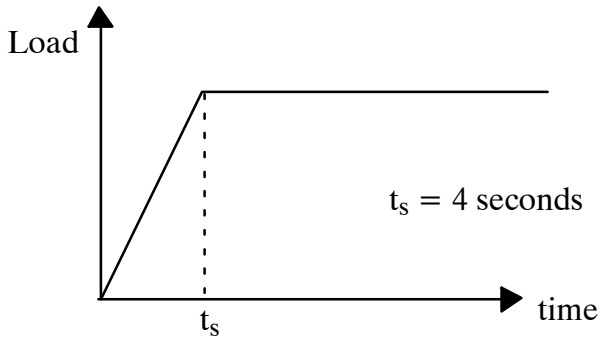

Figure 5.11 Step function during the creep test.

Table 5.4 Elastic stiffness for the uniaxial specimen measured before and after creep test (samples were given sufficient time for recovery after creep tests)

a/w	ΔP/ΔCMOD (kip/in)			
	Initial state	After creep test (0.2)	After creep test (0.4)	After creep test (0.6)
0.3	117.5	114.0	115.0	109.2
	-	2.9%	2.1%	7.1%
0.5	39.0	38.0	37.0	36.0
	-	2.3%	5.1%	7.7%
0.7	12.3	12.1	11.8	11.3
	-	1.6%	4.0%	8.1%

Table 5.5 Elastic stiffness for the transverse specimens measured before and after creep test.
(samples were given sufficient time for recovery after creep tests)

a/w	ΔP/ΔCMOD (kip/in)			
	Initial state	After creep test (0.2)	After creep test (0.4)	After creep test (0.6)
0.3	94.0	91.0	90.0	85.0
	-	3.2%	4.3%	8.5%
0.5	30.0	27.0	27.0	26.0
	-	10.0%	11.7%	11.7%
0.7	9.7	9.5	9.6	9.2
	-	2.1%	1.0%	1.0%

Next, the predicted creep response in the form of CMOD versus time is compared to the experimental results. Figures 5.12, 5.13, and 5.14 show the creep response, CMOD versus time, for the uniaxial ESE(T) specimens with a/w=0.3, 0.5, and 0.7, respectively. Better predictions are demonstrated for the smaller load levels, while the largest mismatch is shown for the creep response under the load level 0.6 P_{cr}. This is due to damage that occurred in the materials during the instantaneous or creep loading in these tests, as evident from the stiffness decrease in Table 5.4 and 5.5. In the case of the uniaxial specimen with a/w=0.3, the damage starts from load ratio 0.4. It is also seen in Figure 5.13 that the material nonlinearity increases in the transient creep response. The response for the transverse ESE(T) specimens with a/w=0.3, 0.5, and 0.7 are shown in Figures 5.15, 5.16, and 5.17, respectively. Overall, the FE models show good predictions compared with the experimental results only for the lower applied loads. Higher material nonlinearity is exhibited with the 0.6 load ratio.

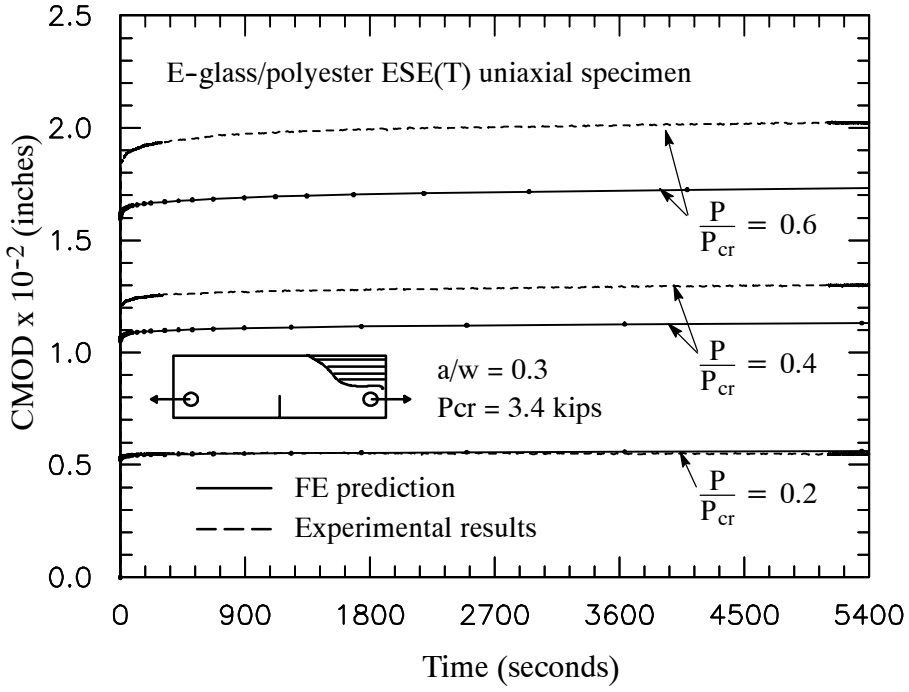

Figure 5.12 CMOD creep response on uniaxial ESE(T) specimen with a/w=0.3

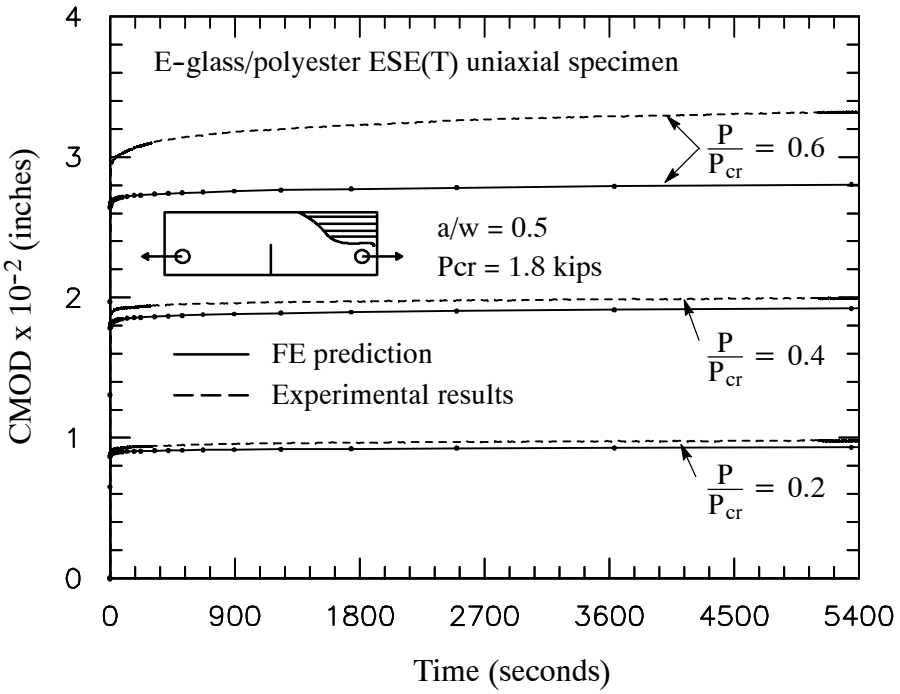

Figure 5.13 CMOD creep response on uniaxial ESE(T) specimen with a/w=0.5

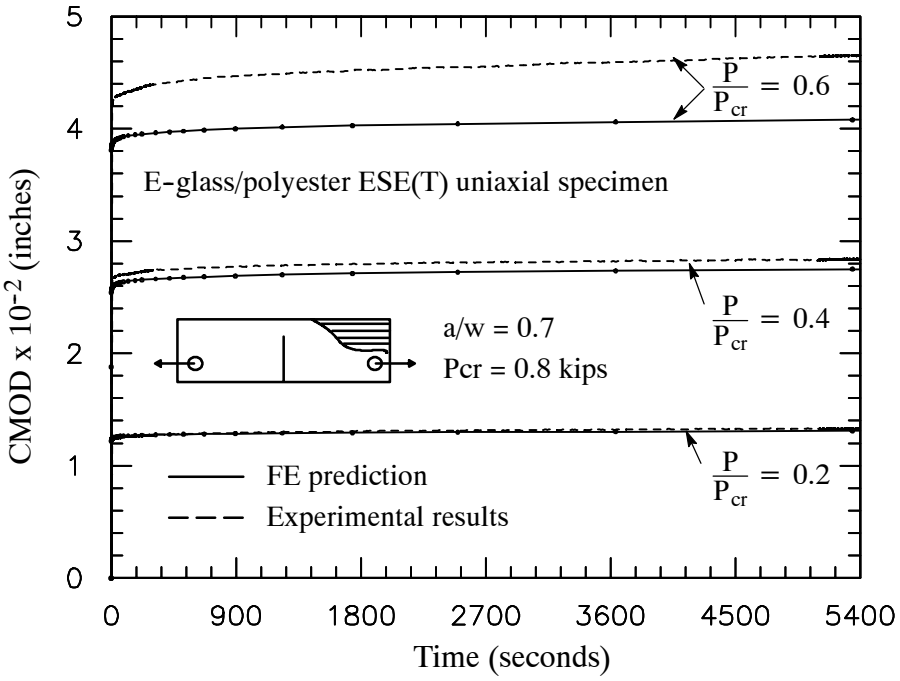

Figure 5.14 CMOD creep response on uniaxial ESE(T) specimen with a/w=0.7

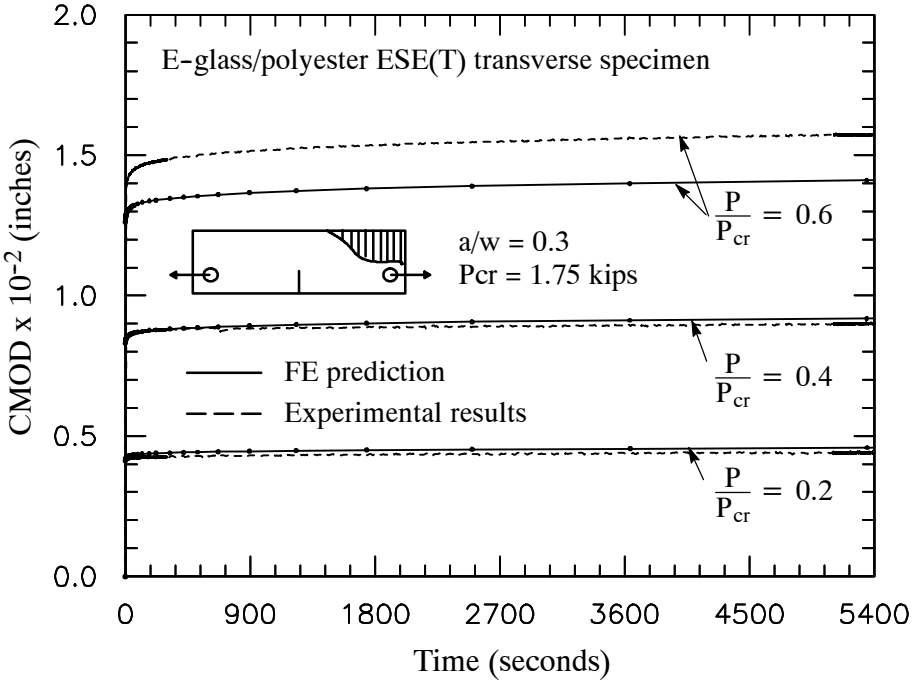

Figure 5.15 CMOD creep response on transverse ESE(T) specimen with a/w=0.3

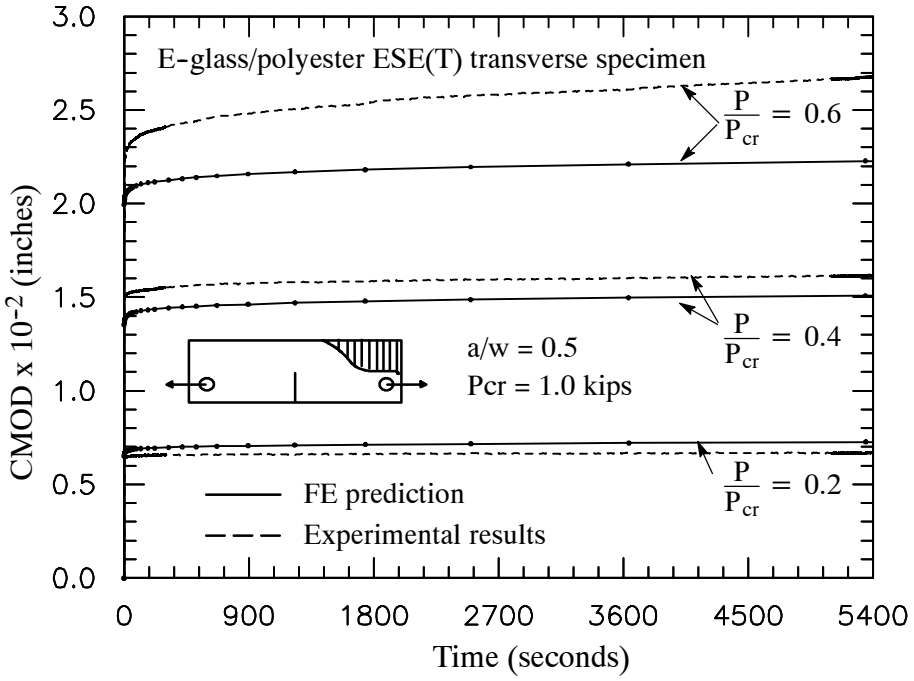

Figure 5.16 CMOD creep response on transverse ESE(T) specimen with a/w=0.5

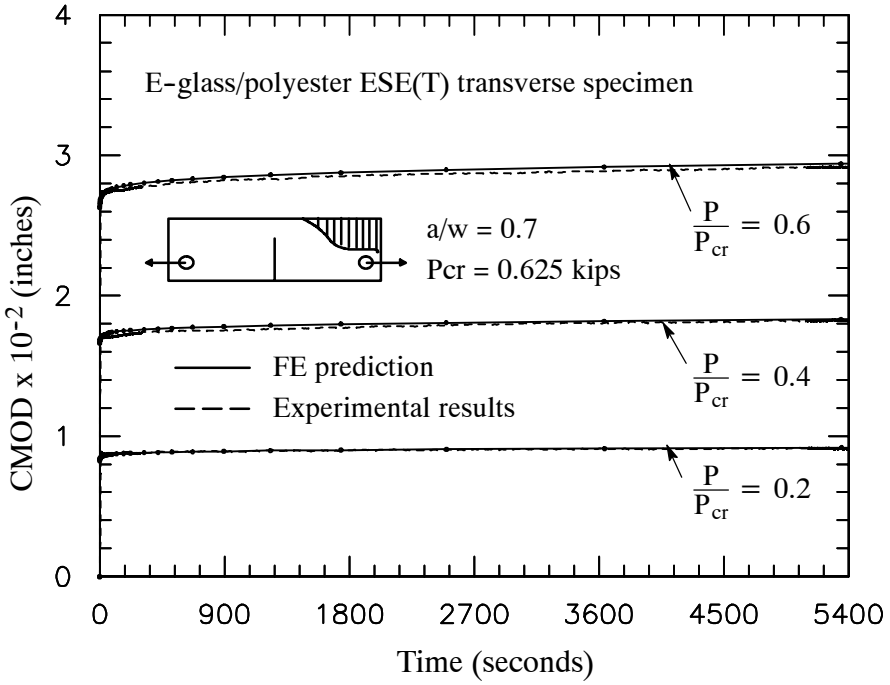

Figure 5.17 CMOD creep response on transverse ESE(T) specimen with a/w=0.7

5.4 Creep Analysis of Laminated Composite Structures

The multi-scale viscoelastic constitutive framework is applied for the creep analysis of graphite/epoxy laminated composite structures. Viscoelastic problems are considered in this section including the response of a composite lap joint and a cylinder under external pressure. A simple lap joint configuration, made from laminated composite plates, is subjected to axial tensile load. The second case involves a thick composite cylinder under hydrostatic pressures. The composite structures are made of T300/5208 graphite/epoxy materials (Tuttle and Brinson, 1986). The material of each layer is T300/5208 graphite/epoxy. The elastic properties for the fiber and matrix are listed in Table 3.3. Originally, the Prony series parameters were calibrated from short-term creep experiments of Tuttle and Brinson (1986) up to 480 minutes, as shown in Table 3.5. In order to extend the range of analysis and to examine the long-term structural response (1 year), a new Prony series was simulated and calibrated such that the rate of creep is fixed after the experimental range of 480 minutes. The modified Prony coefficients from the new calibrated series are listed in Table 5.6. The nonlinear viscoelastic micromechanical framework is implemented as a material subroutine (UMAT) in the ABAQUS (2002) FE code.

Table 5.6 Modified Prony series coefficients for the 5208 epoxy matrix to allow long-term analysis.

n	λ_n $\left(\text{min}^{-1}\right)$	D_n long-term creep (1 year) x 10^{-5} MPa^{-1} (ksi^{-1})
1	1	7.77 (53.57)
2	10^{-1}	6.32 (43.58)
3	10^{-2}	3.60 (24.82)
4	10^{-3}	7.44 (51.30)
5	10^{-4}	3.95 (27.23)
6	10^{-5}	3.95 (27.23)
7	10^{-6}	4.96 (34.20)
8	10^{-7}	1.93 (13.31)

The first structural creep analysis deals with the viscoelastic behavior of a simple lap joint made of T300/5208 graphite/epoxy laminates with $[0/\pm 45/90]_s$ layups. The geometry of this model follows a previous static analysis study by Muliana et al. (2001). It consists of two plates having 152.4 mm length, 25.4 mm width, and 1.016 mm thickness as described in Figure 5.18. The two plates are attached symmetrically to each other along an interface of 50.8 mm from their edges. In the actual geometry, the plates contain 20-degree tapers at both ends of the lap joint. The taper was constructed by staggering the plies in the ply termination region. The purpose of the taper was to reduce stress concentration and the possibility of resin accumulation at the joint ends. In this study, the lap-joint model is simplified by not including the taper at the edge and an adhesive layer of 0.125 mm thickness is considered along the interface. The adhesive is assumed to have the same properties as epoxy-5208. A FE model, with 400 shell (S4R) elements for the laminated composite plates, and 160 brick (C3D8R) elements for the adhesive layer between the two plates, is generated. The creep response is simulated using the FE model at load levels: 0.5 and 0.75 of the joint static failure load (P_{fail}). The ultimate load is taken as 20 kN, estimated from the

study by Muliana et al. (2001). The creep shear strain is plotted as a function of time for two locations along the interface: 5 mm and 12.7 mm from the edge and shown in Figure 5.19. As expected more shear stress is accumulated near the end of the adhesive layer. Figure 5.20 shows the axial strain inside the adhesive layer at two locations: 5 and 12.7 mm from the edge. Also, it is seen that the shear strain is the dominant strain component.

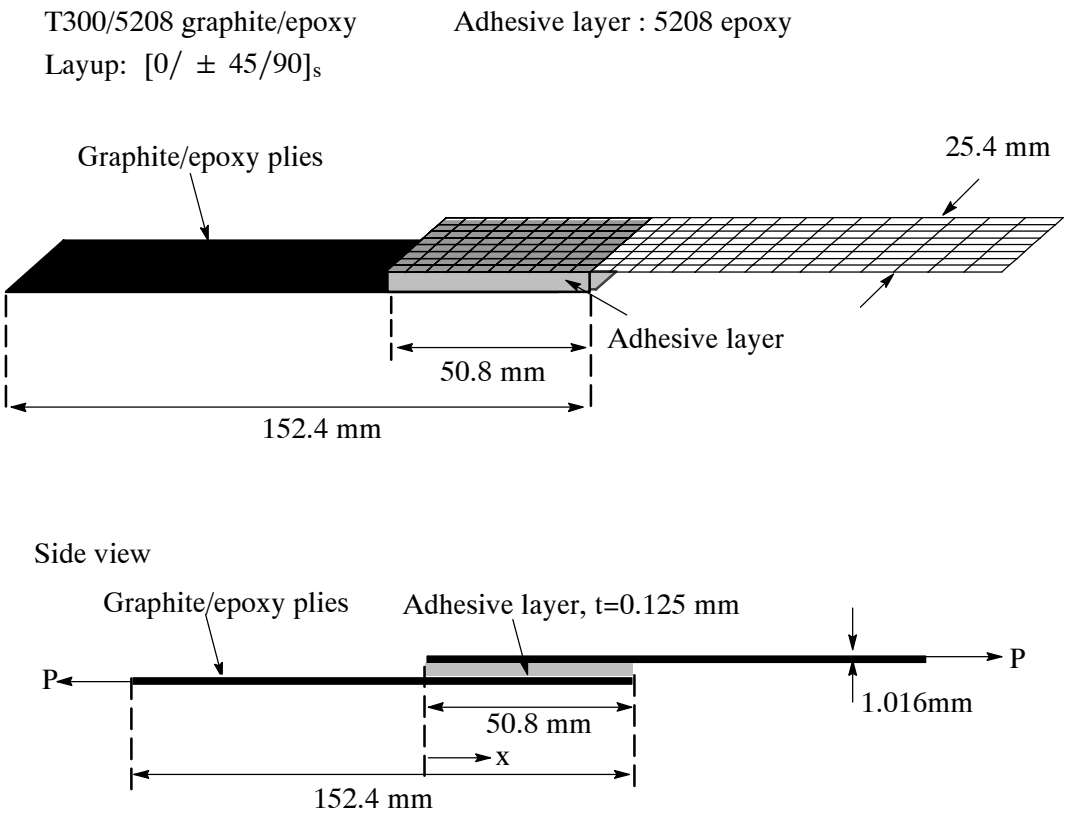

Figure 5.18 Geometry and FE model of the laminated composite lap-joint (not to scale).

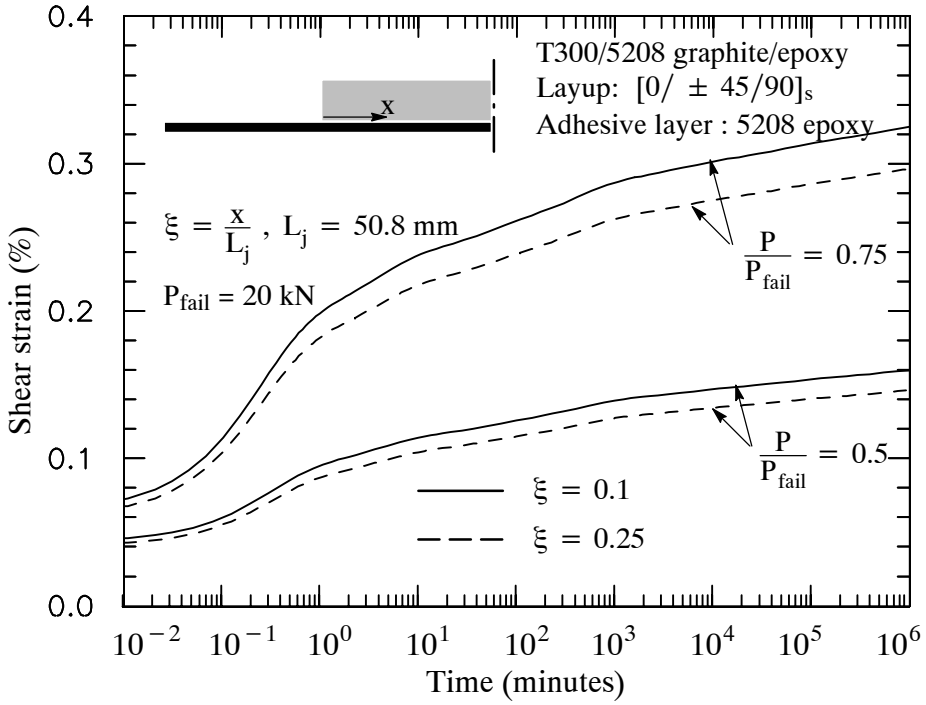

Figure 5.19 Shear strain in the adhesive layer of a single-lap joint.

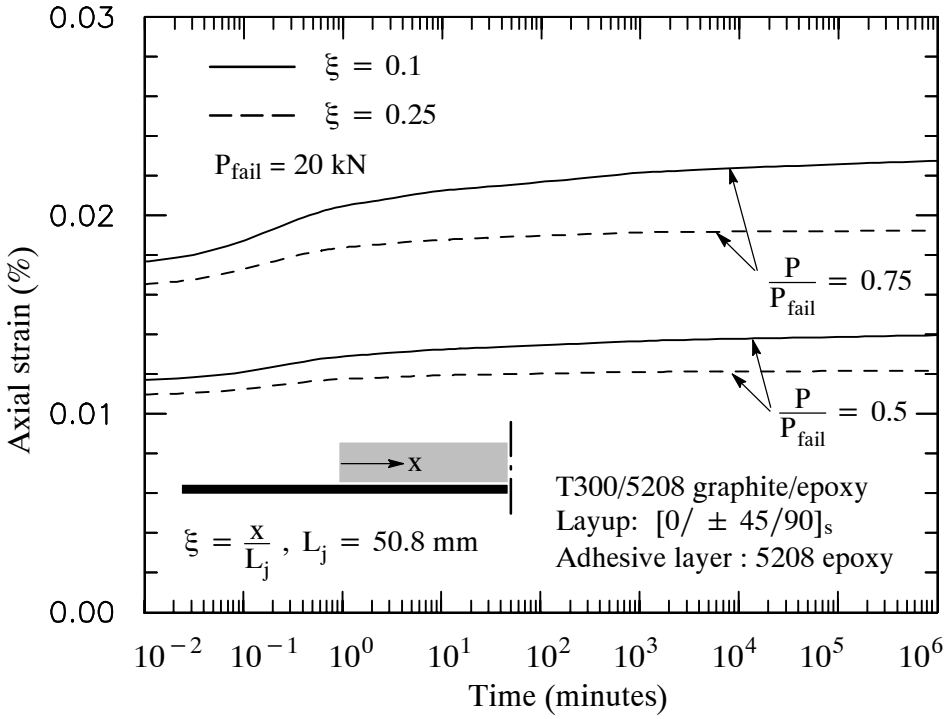

Figure 5.20 Adhesive axial strain for a laminated single-lap joint.

The second FE modeling deals with the viscoelastic analysis of a thick laminated composite cylinder with a cutout under hydrostatic pressures. The geomety of this model is taken from the static post-buckling study by Pecknold and Haj-Ali (1993) and is shown in Figure 5.21. The laminated cylinder has a 240 inch length and a 144 inch outer diameter. It is made of T300/5208 graphite/epoxy with a layup $[0/90/\pm 45]_{4s}$ through its 1.8 inch thickness. A circular cutout is located at the mid-section of the cylinder, which has a 40 inch diameter in a projected flat plane to the cylindrical surface. The FE mesh includes 896 shell (S8R) elements. The geometry and FE mesh are shown in Figure 5.21.

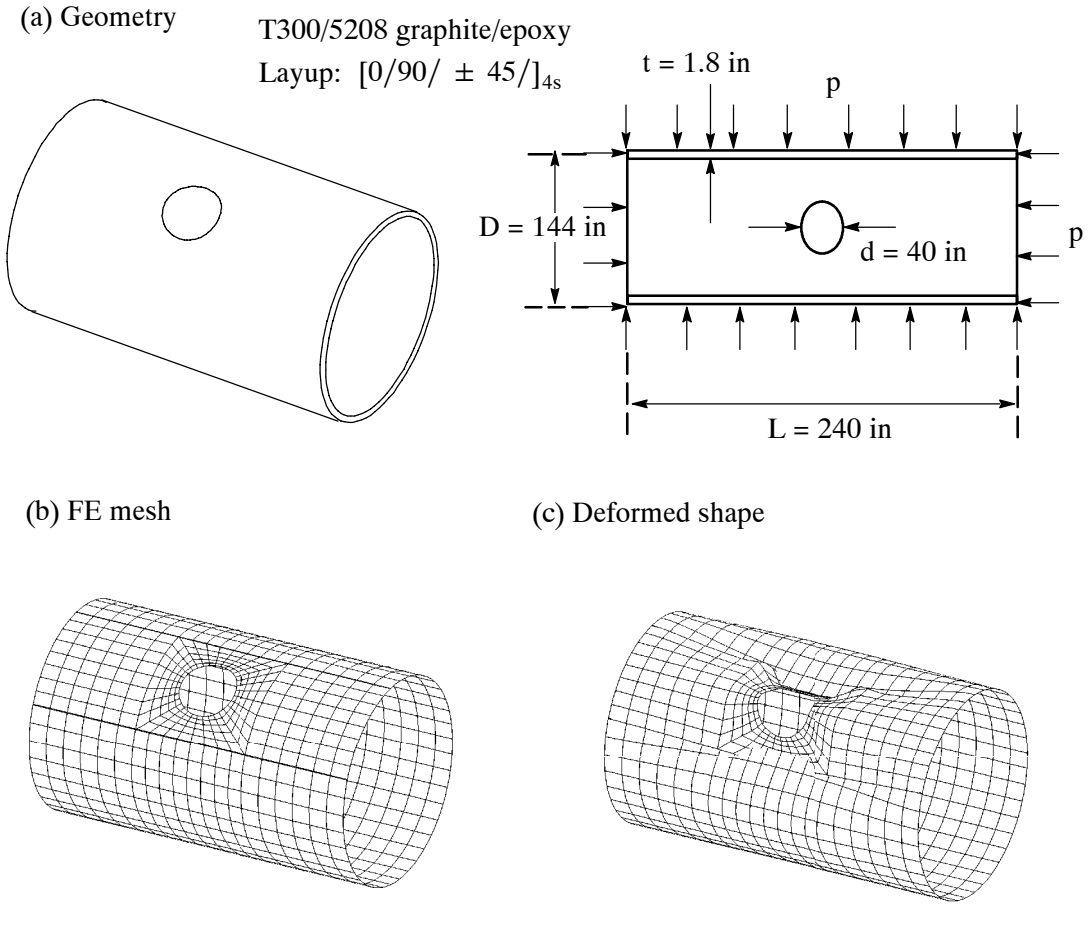

Figure 5.21 Thick laminated composite cylinder under hydrostatic presssure.

The creep response under hydrostatic pressure at the depth of 50 meters (164 feet) is simulated by applying a uniform creep-step pressure on the cylinder external surface. The maximum longitudinal and transverse creep strains along the cutout perimeter are shown in Figure 5.22. A typical deformed shape is also shown in 5.21(c).

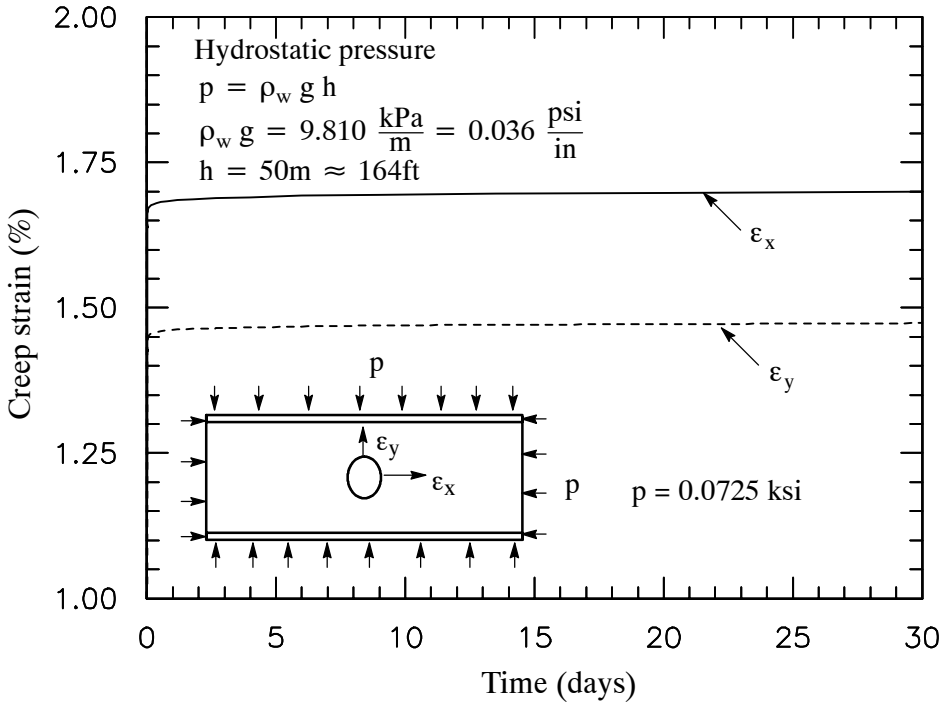

Figure 5.22 Maximum creep strains in thick laminated cylinder under hydrostatic pressure.

CHAPTER VI

CREEP BUCKLING AND COLLAPSE ANALYSES OF COMPOSITE STRUCTURES

Time-dependent response of imperfect composite structures under compressive loads may ultimately lead to buckling and collapse. Creep deformation increases continuously with time and can be classified into three creep phases: primary, secondary, and tertiary phases. In the primary phase (transient creep), an elastic deformation occurs immediately after the structure is loaded and the structure continues to deform with a decreasing deformation rate. If the deformation increases with a constant rate, a secondary creep phase is exhibited. The tertiary creep phase occurs when the deformation grows with an increasing rate until the structure collapses. At a critical collapse time, the deformation rate is close to infinity. Creep or viscoelastic buckling can be defined as an unstable deformation using classical 'static' or time-dependent criteria. In most cases viscoelastic (creep) buckling is numerically analyzed using imperfection methods. This allows investigating the structure response both in time domain and in the postbuckling range. The problem is that such numerical methods may not lead to the precise critical load and time combinations.

Problems of creep buckling and postbuckling of imperfect structures have been extensively addressed for isotropic columns. Hilton (1952, 1961) studied the critical time for columns based on their material properties, levels of applied load, and arbitrary imperfection. Combination of bending and compression was considered during creep using Euler-Bernoulli beam theory. Maxwell model was used to represent the time-dependent material response. The critical time was determined when the internal moment is less than the applied moment due to creep in an imperfect column. At this stage, an unstable equilibrium was reached and the lateral deflection went to infinity. Kempner (1954) analyzed creep bending and buckling of isotropic columns with an initial deflection from a straight centroidal axis.

The material was considered linear viscoelastic and represented by series and parallel arrangements of springs and dashpots. Euler buckling theory was used to determine the critical buckling load. Deflection of the column increased significantly with time and approach infinity under applied loads including those with magnitude less than the critical static buckling load. Sharad et al. (1956) conducted creep buckling tests of 2024-T4 aluminum alloy columns at 600^{o}F. The slenderness ratio of the columns was 111. It was shown that the critical time to buckling decreased much more significant with increasing applied load than with adding imperfection. Huang (1976) studied creep buckling of an imperfect column and considered large deformations. The material behavior followed a Findley-type power law model for a creep response and a Ramberg-Osgood relation to represent the nonlinear elastic response. Euler buckling theory was used in the creep buckling analysis. It was shown that creep buckling at a finite time would occur only when the magnitude of load is between the elastic buckling and the steady creep deformation range. Vinogradov (1985) presented the creep buckling analysis of eccentrically loaded viscoelastic columns. Linear and nonlinear geometry were considered and governed by the Euler-Bernoulli theory. The viscoelastic material model was defined by a linear integral equation (Volterra-type), in which the kernel function in the integral equation was determined experimentally. The creep responses from small (linear) and large (nonlinear) deformation solutions were comparable only in the case of small creep deformation. Using the linear solution, the lateral deformation increased continuously with time and became infinite, while the nonlinear solution predicted no infinite deformation. Touati and Cederbaum (1998c) investigated the postbuckling response of imperfect columns made of linear viscoelastic materials. The viscoelastic material model is defined by a single integral equation. A creep deformation was formulated and solved numerically in order to describe the postbuckling response of imperfect viscoelastic columns.

Creep buckling of anisotropic plates and shells has been studied using both linear and nonlinear viscoelastic material models. Wilson and Vinson (1984) analyzed creep buckling

of laminated plates. The effective creep compliances of the anisotropic lamina were determined using the Halpin-Tsai micromechanical equations assuming linear elastic fiber (orthrotopic) and an isotropic linear viscoelastic matrix. Time-dependent Young's modulus with a constant bulk modulus was used for the matrix. Applications were reported for a simply supported laminated plate having $[0/\pm 45/90]_s$ and $[0/\pm 60]_s$ layups. Touati and Cederbaum (1998a, 1998b) studied the postbuckling behavior of imperfect laminated plates using the Schapery nonlinear viscoelastic material model. The Schapery single integral constitutive equation, directly describing the stress-strain relation in the time-domain, was applied independently to characterize each nonlinear anisotropic stiffness of a unidirectional layer under plane stress condition. The nonlinear strain-dependent material parameters were calibrated from experimental tests. The von Karman nonlinear plate theory was used for the postbuckling analysis.

This chapter presents a new modeling approach for the analysis of creep buckling and collapse of pultruded and laminated composite structures. The proposed multi-scale nonlinear viscoelastic constitutive framework is implemented numerically as a material subroutine (UMAT) in the ABAQUS (2002) FE code. Therefore, it is possible to generate a wide-range of FE models (beam, plate, shell, solids) for composite structures and to determine their critical load and corresponding critical time. The first part of this chapter is concerned with verification and stability modeling for isotropic structures. Analyses are presented for creep buckling of PMMA polymeric tubes with different geometry and imperfection parametric studies. The second part deals with creep buckling and collapse of I-shaped pultruded composite columns. Different FE models are examined using beam, shell, and 3D continuum elements. The general 3D micromodeling framework is condensed in the case of structural elements to allow for plane stress and uniaxial stress-strain overall behavior at each Gaussian point. Finally, postbuckling and creep analyses are studied for a laminated composite panel and a thick composite ring under surface pressures.

6.1 Creep Collapse of PMMA Polymeric Tubes

The numerical integration method for an isotropic nonlinear viscoelastic model, presented in Chapter II, is used in this section along with FE models for the stability analysis of polymeric columns. Two parametric studies are performed on PMMA polymeric tubes with both fixed and pinned supports. The elastic and viscoelastic material properties of PMMA polymer, reported by Lai and Bakker (1996), are given in Table 2.1. The first parametric study investigates the effects of the cross sectional geometry and slenderness ratio on viscoelastic buckling of the tubes. Slender and stocky tubes, having square and circular cross sections, are modeled with both fixed and pinned supports. All tubes are 144 inches long. The square and circular cross sections are constrained to have close moments of inertia. Detailed dimensions and slenderness ratio for each tube are presented in Table 6.1. FE model with 5223 nodes and 720 brick (C3D20R) elements are generated. Elastic critical loads, P_{cr}, were computed and compared with Euler buckling loads, P_E, as reported in Table 6.1. The computed buckling loads from the square and circular cross sections are comparable only for slender columns. In this case, their global buckling modes are not affected by their detailed cross sectional geometries but strongly depend on their slenderness ratios. In the case of stocky tubes, the circular and square cross sections do not exhibit the same buckling modes. Local buckling mode is pronounced for the stocky tube with square cross section, while the circular tube shows a global buckling mode. This may be due to the axisymmetric condition in the circular cross section. As expected, the critical loads for geometries with lower slenderness ratio are not properly predicted by the Euler equations and better captured using the FE models. The first five buckling modes of the stocky tube having circular and square cross sections with pinned support are illustrated in Figure 6.1.

Table 6.1 Theoretical and numerical critical loads for PMMA tubes (elastic material).

Geometry		A (in^2)	I (in^4)	r_g (in)	$\lambda = \frac{L}{r_g}$	Boundary condition	Critical buckling loads (kips)		
							P_E	P_{cr}	% Diff
Square  t=0.5 in L=144 in	b=4 in	7.0	14.58	1.44	99.8	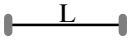	14.86	14.66	1.39
						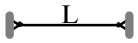	3.72	3.66	1.50
	b=12 in	23.0	507.92	4.70	30.6	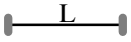	517.65	93.41	82.00
						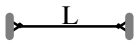	129.41	51.32	60.34
Circle  t=0.5 in L=144 in	r=2.35 in	6.6	14.79	1.50	96.2	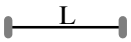	15.07	14.89	1.22
						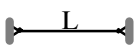	3.77	3.74	0.80
	r=7.11 in	21.6	508.59	4.86	29.7	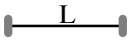	518.34	345.92	33.26
						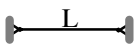	129.58	144.92	11.84

Note: λ is slenderness ration; r_g is radius of gyration $\left(\sqrt{\frac{I}{A}}\right)$

P_E is Euler theoretical buckling load; P_{cr} is the critical FE load

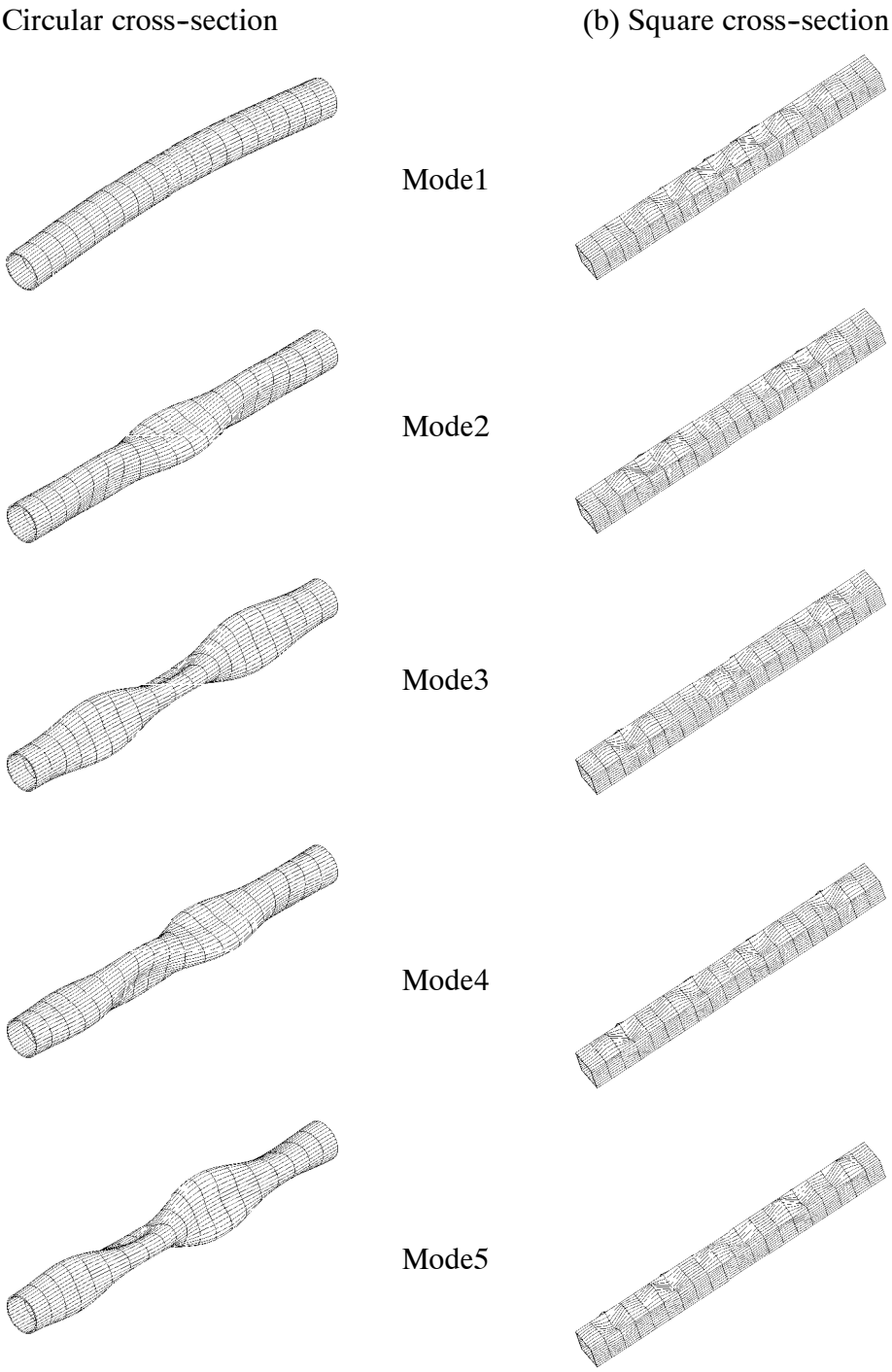

Figure 6.1 The first five buckling modes for circular and square stocky tubes with pinned supports

The main goal of this section is to determine the creep buckling and collapse for polymeric tubes. To that end, the second parametric study is conducted to determine the critical time of slender tubes with different geometric imperfections. The imperfection of the tube is modeled as linear superposition of the first five buckling modes. These buckling modes are scaled and added to the nodal coordinates of a perfectly straight column; this is expressed by:

$$x_i = x_i^o + \frac{e}{m}\sum_{j=1}^{m} \phi_i^{(j)} \tag{6.1}$$

where e is the imperfection scale factor or amplitude, m is the number of eigen-modes used in the superposition, and $\phi_i^{(j)}$ is the j^{th} normalized eigen-mode vector. Two slender PMMA tubes ($\lambda \geq 90$), having square and circular tubular cross-sections with fixed supports, are modeled. The creep responses for near 'perfect' and imperfect structures are simulated. The near 'perfect' tubes are modeled by choosing a scale factor of L/5760 (0.025 in), where L is a total length of the tube. The imperfect tubes are simulated by giving a scale factor L/200 (0.72 in). In both cases, the first five eigen-modes are used in the imperfection analysis (m=5). A material subroutine UMAT is implemented to model the time-dependent response of PMMA polymer at each material point in the FE model following the numerical formulation and integration method developed in Chapter II. Compression creep analyses are conducted for several loading levels: 0.4 to 0.8 of the critical buckling load, P_{cr}. The analyses consist of multiple loading steps. The first step simulates the instantaneous loading with duration of 0.001 seconds. The constant load is then held for 20 seconds with refined time increments of 0.02 seconds to capture the transient response. The next consecutive viscoelastic steps are carried for 250, 4000, 80000, and 10^8 seconds with time increments of 1, 20, 200, and 1000 seconds, respectively. These are suggested initial time increments and are likely to increase during the analysis due to the automated time-incrementation scheme in ABAQUS. Linear viscoelastic responses are exhibited during the analyses. This is probably

due to the relatively low critical loads of the current slender columns that are not sufficient to trigger nonlinear elastic response.

Normalized axial creep deformations (end-shortening) for the near 'perfect' and imperfect columns under several loading levels are shown in Figures 6.2 and 6.3, respectively. Both the near 'perfect' tubes having square and circular cross sections, which have nearly equal moment of inertia, show identical creep behaviors under the same loads. After buckling occurs, some creep analyses are terminated due to an excessive nonlinearity, which causes convergence problems. Similar creep behaviors are also demonstrated for imperfect tubes having square and circular cross sections. Small deviations in creep responses after structural buckling is exhibited are shown by the two cross sections at the large load levels where local effects become important. Transverse creep deformations are also calculated at the mid-span of the tubes and normalized by the corresponding initial elastic deformations due to instantaneous static loadings at any time. The normalized transverse creep deformations for the near 'perfect' and imperfect columns are given in Figures 6.4 and 6.5, respectively. Both tubes with square and circular cross sections exhibit comparable creep responses under the same applied loads. This indicates that cross sectional geometry has no significant effect in creep behaviors of slender tubes, except at load level near the elastic critical buckling load. It is shown that under the same load levels, the imperfect tubes buckle at earlier time than the near 'perfect' columns. Thus, structural imperfections accelerate creep buckling.

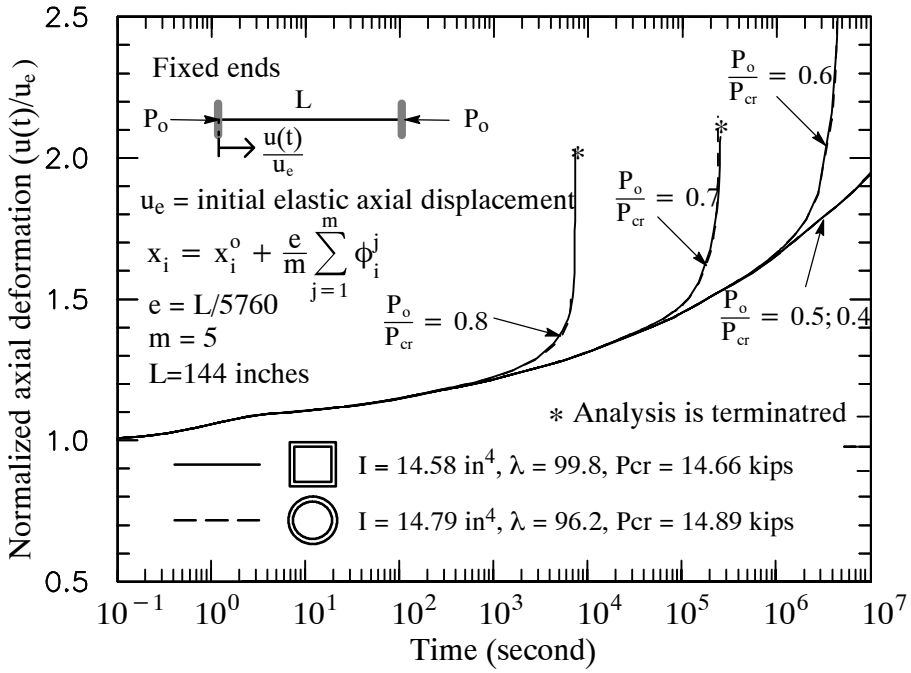

Figure 6.2 Normalize axial creep deformation for near 'perfect' fixed end tubes.

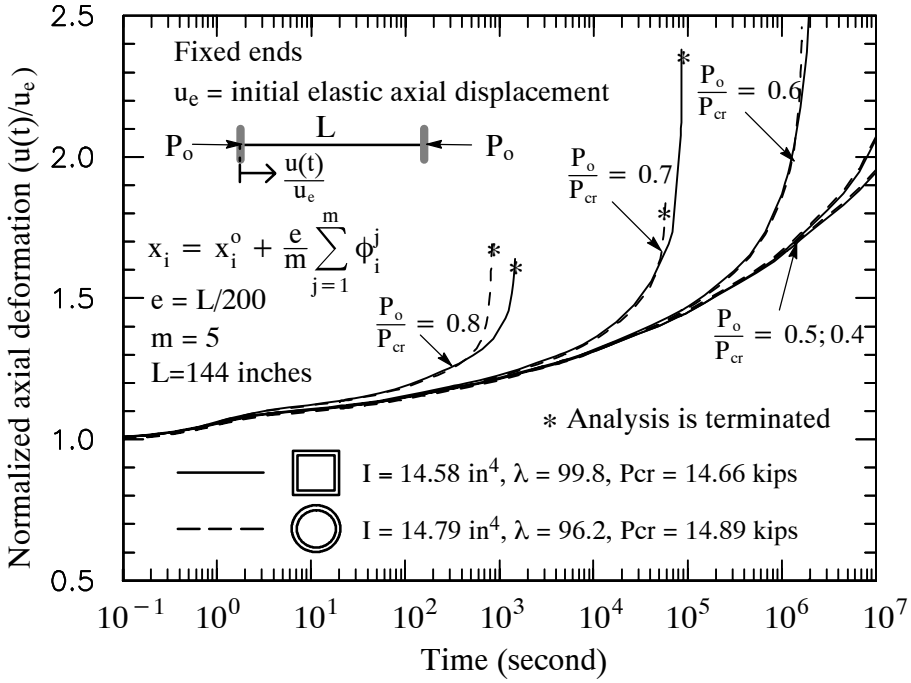

Figure 6.3 Normalize axial creep deformation for imperfect fixed end tubes.

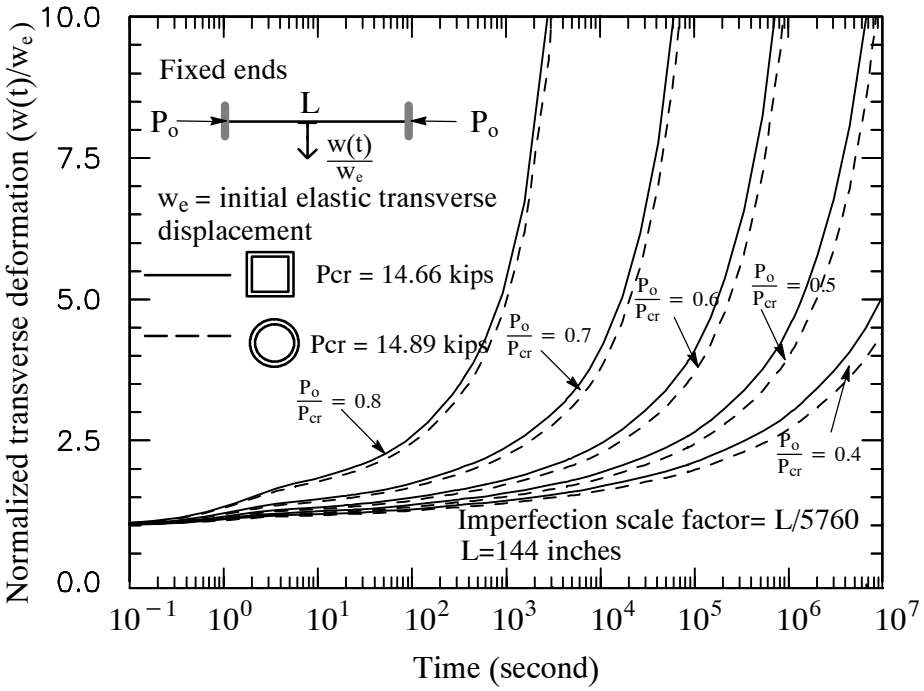

Figure 6.4 Normalize transverse creep deformation for 'perfect' fixed end tubes.

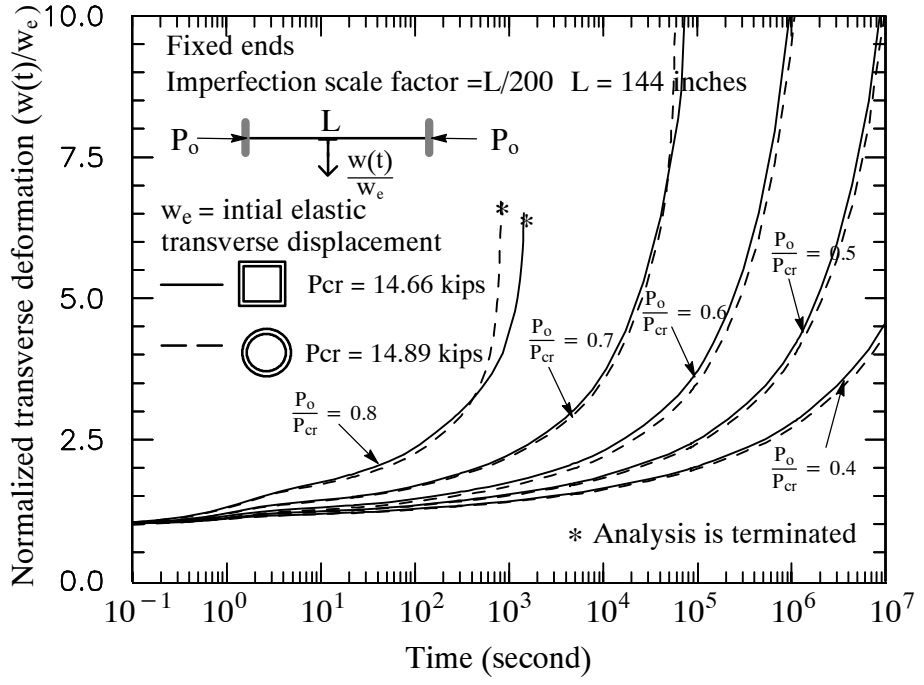

Figure 6.5 Normalize transverse creep deformation for imperfect fixed end tubes.

A critical time is determined numerically from the current two analyses as the time when the slope of the normalized creep response (deformation rate) reaches the value of 4, i.e. when the slope of the normalized creep response is approximately 76°. This criterion is chosen due to the rapidly increasing deformation beyond this point. It is important to note that the numerical critical time is not exactly a collapse time nor it is the theoretical buckling time for perfect columns; it is however bounded by the above two. Figure 6.6 shows the critical time for the imperfect PMMA fixed end tubes with square and circular cross sections under different applied loading. Critical times are calculated from both axial and transverse creep deformations. The time measured from the transverse creep curves is lower than that measured from axial creep deformation. This is probably due to the relatively more sensitive transverse deformation compared to the end-shortening. Therefore, critical times in the tubes are better calculated from transverse creep responses. It should be noted that the time-dependent parameters for PMMA materials were calibrated from experimental data with short term (30 minutes) linear creep. Therefore, the numerical models are not accurate in their critical time predictions. The predicted time to buckling is a lower bound that can be improved if the time-dependent material properties are calibrated from long-term creep tests.

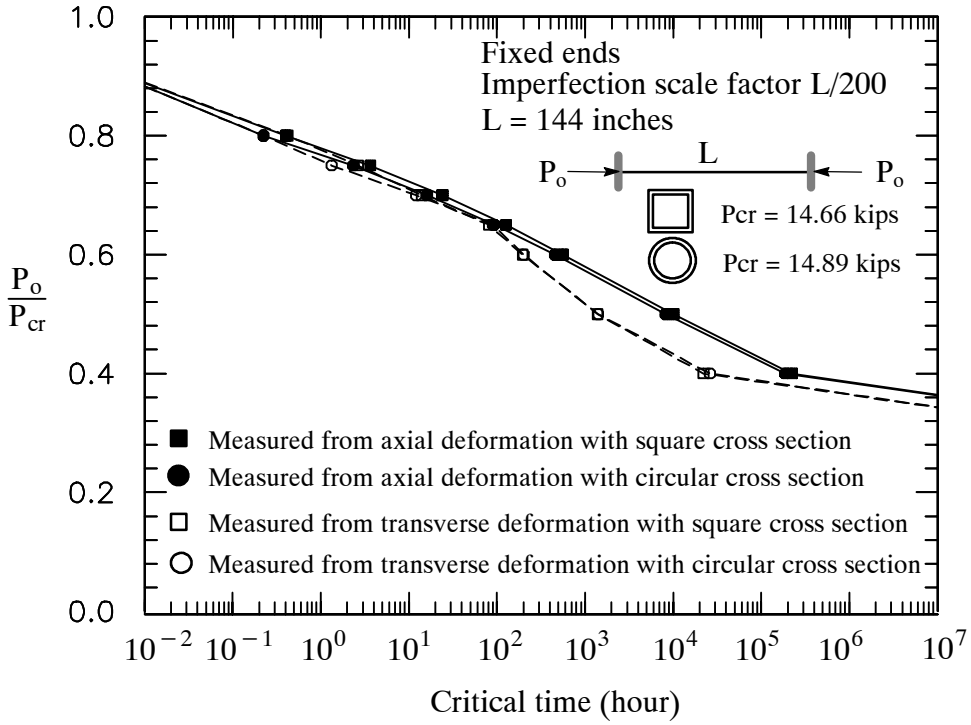

Figure 6.6 Critical time for imperfect fixed end tubes.

Creep buckling responses for a slender pinned end tube with a circular tubular cross section ($\lambda = 96$) are also performed. Geometry imperfection is accounted for by superimposing the first five buckling modes of a perfectly straight column with equal scale factors (amplitudes) of L/200 (0.72 in). A creep buckling analysis is performed by multiple steps in the same manner as the previous case of a slender fixed end tube. Linear viscoelastic responses are exhibited during these analyses. Normalized axial and transverse creep deformations under various load levels are shown in Figures 6.7 and 6.8, respectively. The critical buckling time is determined from both axial and transverse creep deformations using the same criterion as described in the previous analyses. Figure 6.9 shows the creep critical time for different applied loads. Again, time taken from the transverse deformation rates is more conservative.

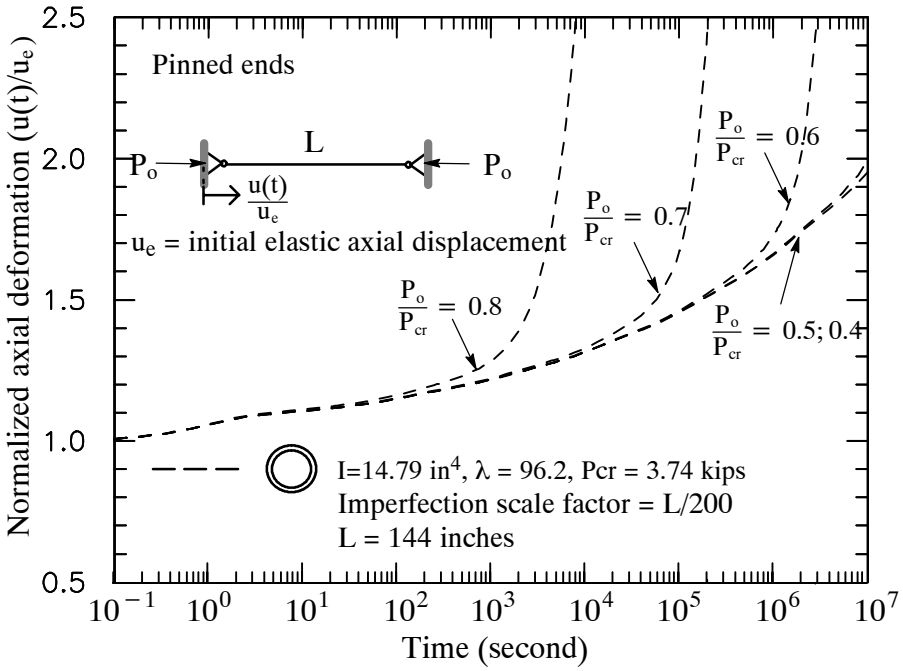

Figure 6.7 Normalize axial creep deformation for the imperfect pinned end tube.

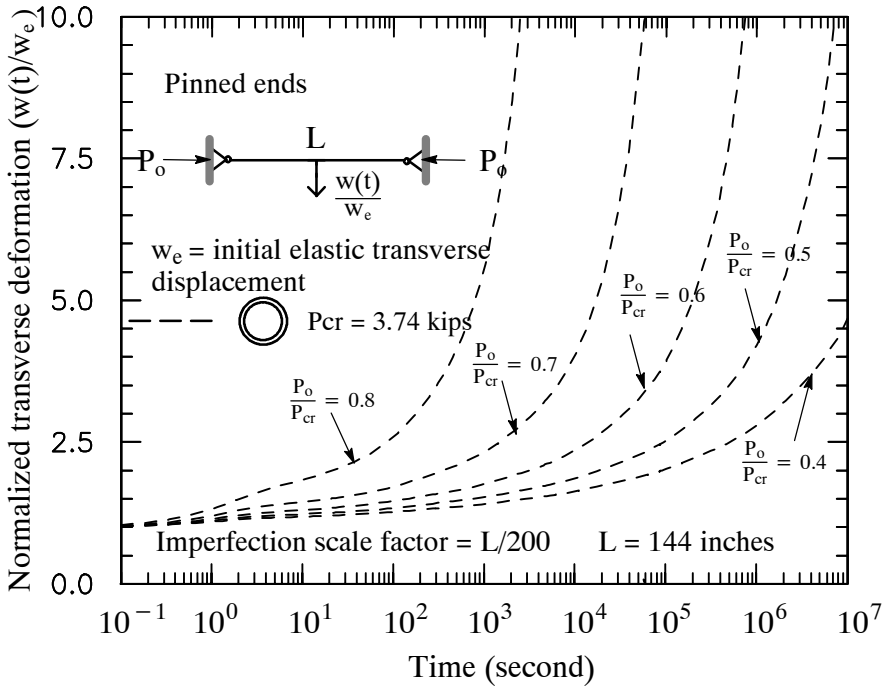

Figure 6.8 Normalize transverse creep deformation for the imperfect pinned end tube.

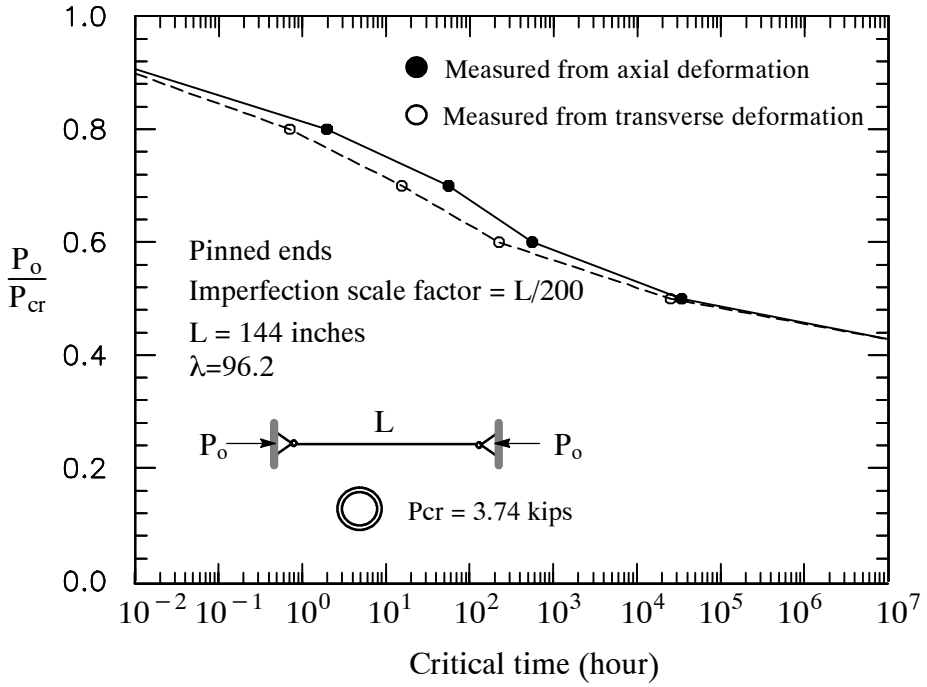

Figure 6.9 Critical time for the imperfect pinned end tube.

6.2 Postbuckling and Creep Collapse of I-Shaped Pultruded Columns

The new multi-scale viscoelastic framework, Chapter IV, for pultruded composites is used in this section for static postbuckling and creep collapse analysis of I-shaped pultruded columns. The studied pultruded composite materials consist of vinylester resin reinforced with layers of E-glass roving and CFM. I-shaped pultruded columns with fixed cross sectional area of 4 x 4 x 0.49 inches and spans ranging from 20 to 240 inches are analyzed using beam (B23), shell (S8R) and 3D brick (C3D20R) elements. Effects of nonlinear elastic and time-dependent material behavior on the postbuckling and creep collapse responses are investigated. In order to have a reliable predicted critical collapse times, the model must be calibrated for long-term behavior from test data. For this purpose, the time-dependent viscoelastic model of the matrix subcells in the CFM and roving micromodels are calibrated from 8-month compression creep tests on uniaxial E-glass/vinylester pultruded coupons, reported by Scott and Zureick (1998). Uniaxial coupons were cut from an I-shaped pul-

truded beam at three different locations: top flange, bottom flange, and web, as illustrated in Figure 6.10. Thickness of the coupons was 0.25 inches. Overall FVF of this pultruded material system is 0.3. Elastic properties for fiber and matrix are assumed to be the same as the tested and calibrated (short-term) E-glass/vinylester pultruded coupons in Table 4.3. Scott and Zureick (1998) conducted their long-term creep tests with different applied compression loads: 0.2, 0.4, and 0.6 of the ultimate compression strength. The Prony series coefficients, Eq. (2.30), are calibrated from the linear creep response under low load level of 0.2 of ultimate. Figure 6.11(a) shows the calibrated creep response from the micromodels with the creep tests. The creep responses from the three different coupon locations are shown. Time-dependent properties with 8 Prony terms were used with an hour unit time. The calibrated Prony coefficients are reported in Table 6.2. The nonlinear stress-dependent parameters in the Schapery equation were taken form the previously short-term (1 hour) nonlinear calibration of the tested in this study, Figure 4.6 in section 4.4. Verifications of the micromodel predictions for creep stress-strain response are performed for load fraction of 0.4 and 0.6. Figures 6.11(b) and (c) compare the predicted creep response from the micromechanical model for 16 and 8 months tests that were not used in the calibration process. It should be noted that during the calibration process the material linear and nonlinear response was considered the same for the three samples cut from the web and flange locations. In addition, material variability was not considered due to the limited data available for long-term creep tests. Nevertheless, the overall predictions of the proposed viscoelastic model are acceptable and can be used for long-term analysis of pultruded columns.

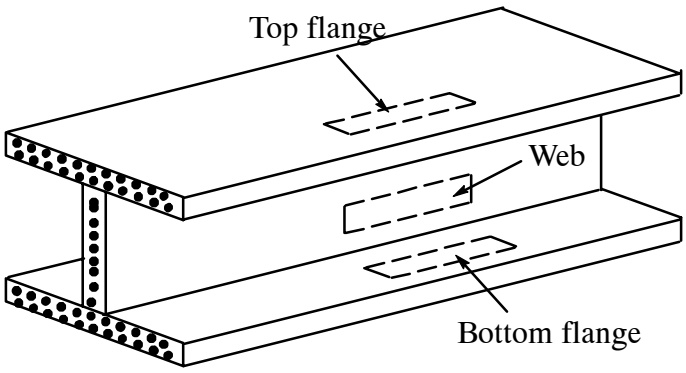

Figure 6.10 I shaped uniaxial E-glass/vinylester pultruded beam (Scott and Zureick, 1998).

Table 6.2 Prony series coefficients for the vinylester matrix from 8 month calibrations.

n	λ_n (hour^{-1})	D_n x 10^{-6}(ksi^{-1})
1	1	93.76
2	10^{-1}	50.99
3	10^{-2}	87.06
4	10^{-3}	120.83
5	10^{-4}	345.00
6	10^{-5}	790.00
7	10^{-6}	4500.00
8	10^{-7}	3800.00

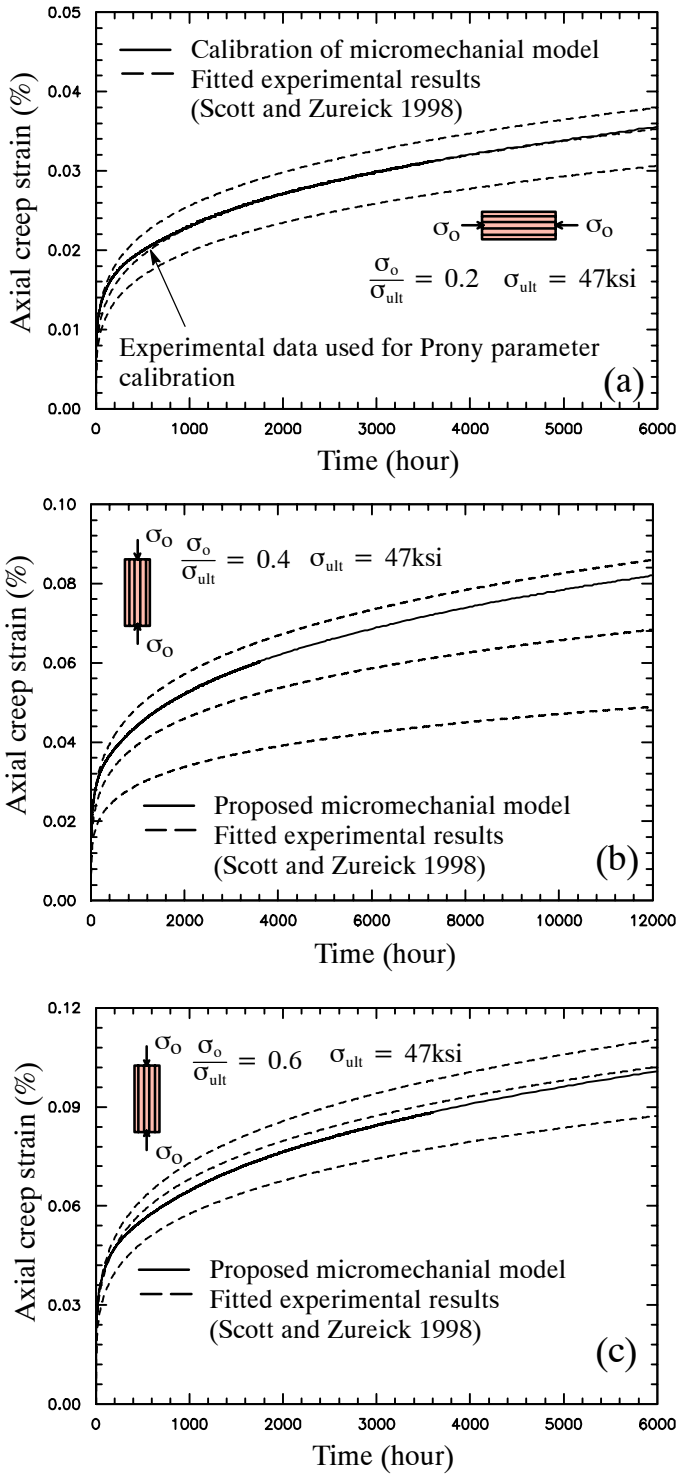

Figure 6.11 Compression creep response from uniaxial E-glass/vinylester pultruded coupons: (a) linear response under stress ratio 0.2; (b) linear response under stress ratio 0.4; (c) nonlinear response under stress ratio 0.6.

Convergence Study

Convergence study is first performed for four pin-pin columns with different lengths: 50, 60, 80, and 100 inches in order to determine an adequate mesh size. The cross sectional dimensions and slenderness ratios of the columns are given in Table 6.3. Two FE models with 1360 and 7680 brick (C3D20R) elements are generated for each column. Plane views of the two meshes are shown in Figure 6.12. All nodes at the two end sections are constrained to two master nodes that represent the 6-DOFs of a rigid plane. Uniaxial load is applied through the master node. The calculated buckling loads from mesh 1 and mesh 2 are close, as seen in Table 6.3. The results are compared with Euler buckling loads using the effective axial modulus of the composite. Euler buckling can be used for pultruded composite columns with slenderness ratio $\lambda \geq 80$. The first five buckling modes for the 80 inch pin-pin column are illustrated in Figure 6.13.

Table 6.3 Buckling loads for pultruded I shaped cross sections (convergence study).

Geometry	L (in)	$\lambda = \frac{L}{r_g}$	Critical buckling loads (kips)				
			P_E	Mesh 1		Mesh 2	
			(Euler)	P_{cr}	% Diff	P_{cr}	% Diff
b = d = 4.0 in $t_f = t_w$ = 0.49 in r_g = 0.9866 in A = 5.3998 in^2 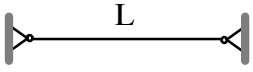	50	51	56.20	45.75	18.58	46.53	17.20
	60	61	39.02	35.81	8.23	36.44	6.63
	80	81	21.95	21.70	1.24	21.68	1.23
	100	101	14.05	13.93	0.86	13.93	0.85

Note: λ is slenderness ratio; r_g is radius of gyration $\left(\sqrt{\frac{I}{A}}\right)$

P_E is Euler buckling load; P_{cr} is critical load computed from FE

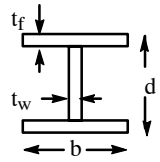

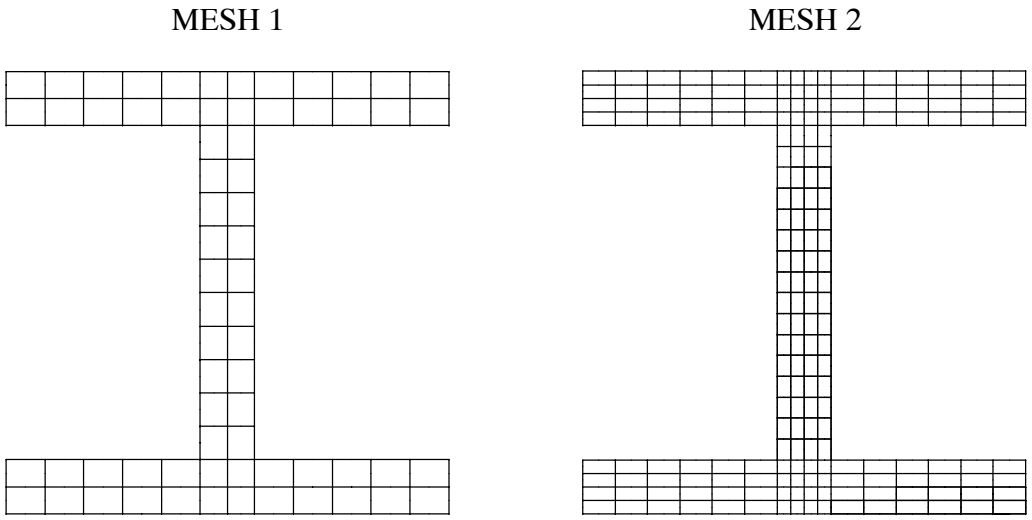

Figure 6.12 FE model for I-shaped pultruded beams.

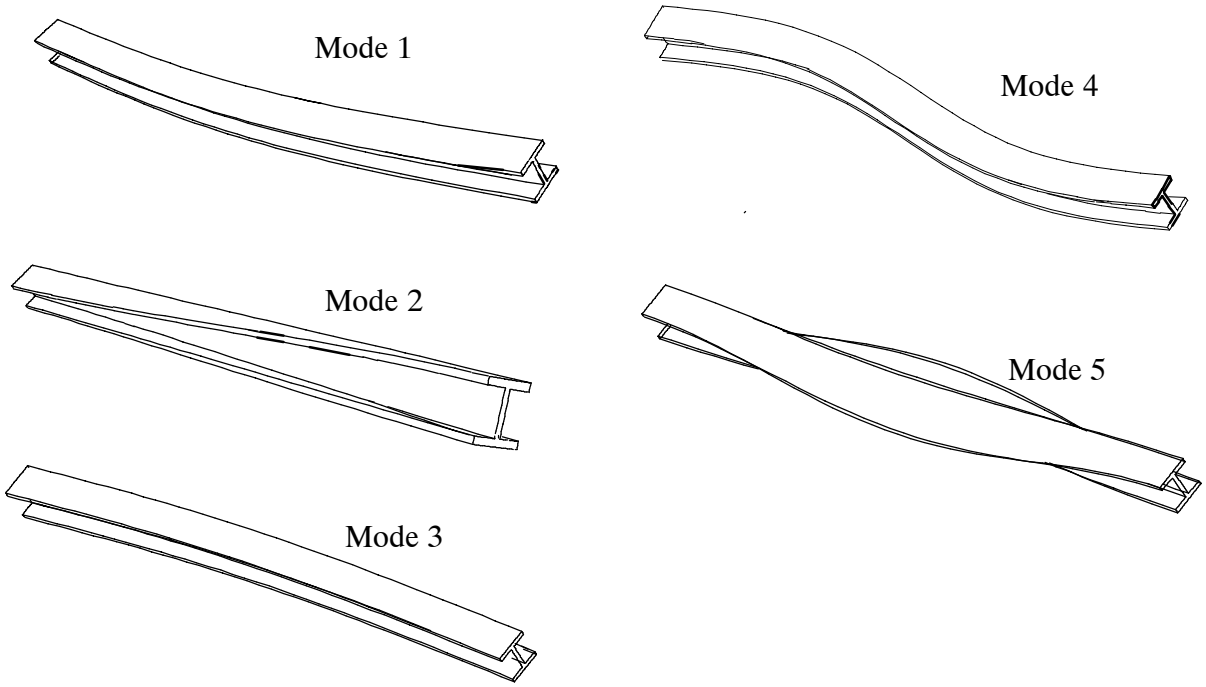

Figure 6.13 Buckling modes for I-shaped pultruded composite beam, L=80 inches, λ=81.

Next, nonlinear postbuckling (static) analysis is performed with mesh 1 and mesh 2. Column imperfections are included using the first five buckling modes scaled by L/200, where L is length of the column. The pultruded composite materials are assumed to be nonlinear elastic. The material constitutive micromodel is implemented using the UMAT subroutine in the ABAQUS (2002) FE code. Load-displacement responses from mesh 1 and mesh 2 for various column lengths are shown in Figure 6.14. Both axial and transverse deformations from mesh 1 and mesh 2 are very close. Thus, the smaller mesh with a total of 7921 nodes and 1360 C3D20R elements is chosen for the 3D nonlinear viscoelastic modeling of the I-shaped columns.

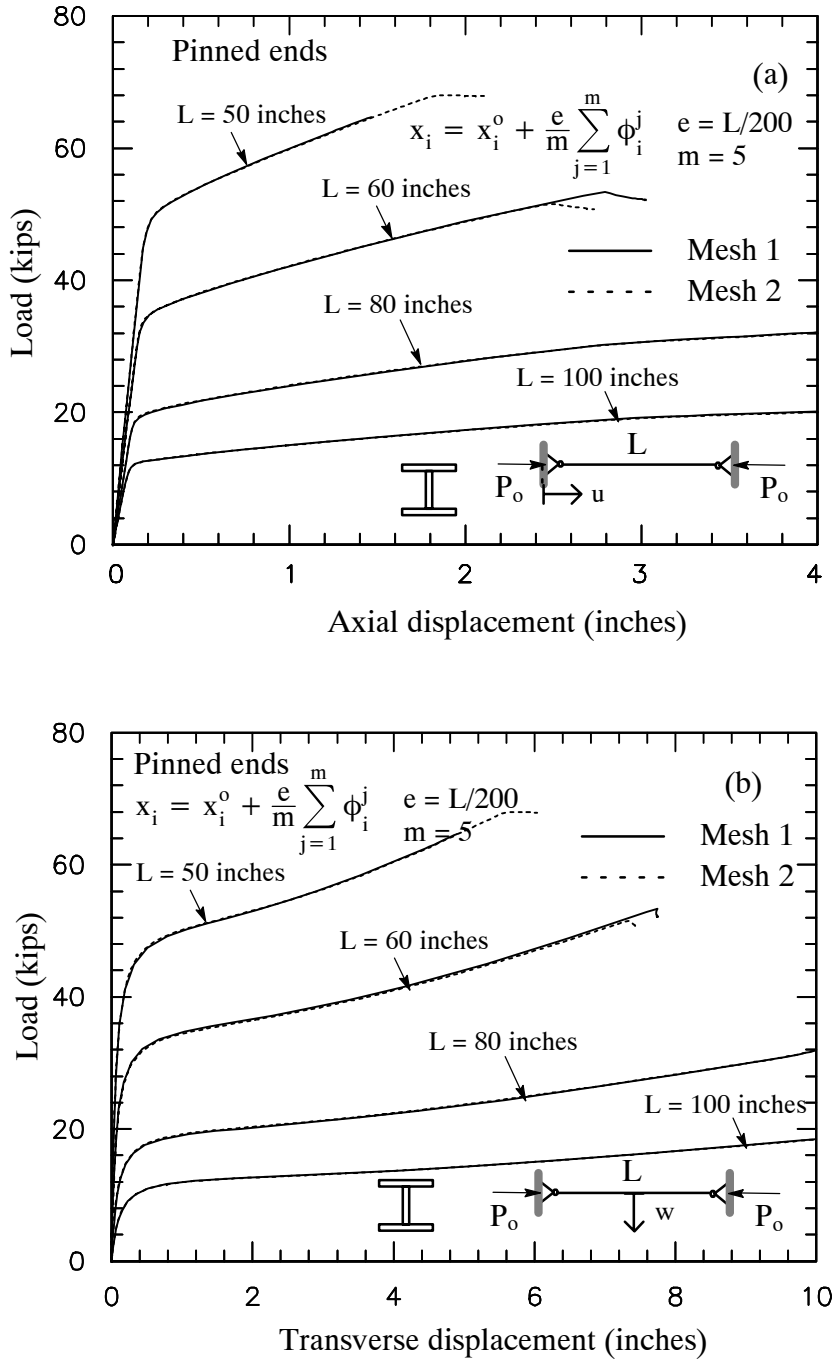

Figure 6.14 Load displacement for uniaxial I shape pultruded pinned end columns: (a) axial deformation; (b) transverse deformation.

Static postbuckling using structural beam and shell elements

Next, static postbuckling analysis of pultruded composite columns is also performed using structural beam and shell elements. The purpose of this study is to show the flexibility of the proposed multi-scale micromodel to interface with wide-range of FE structural elements. Nonlinear elastic material behavior is accounted for by using the previously developed micromodels. FE models using 20 beam (B23) elements, 600 shell (S8R) elements, and 1360 brick (C3D20R) elements are generated for three I-shape pultruded columns having 60, 100, and 160 inch lengths. Constraints are imposed to the 3D nonlinear constitutive micromodel in order to properly represent the stress-strain relation at each integration (material) point. In the case of a beam element is used, a uniaxial stress-strain relation is imposed to the sublaminate micromodel by setting the transverse stress components (σ_{22}, σ_{33}, σ_{12}, σ_{13}, σ_{23}) to zero. In the case of a shell element, a plane-stress condition is imposed.

Postbuckling analyses are performed for the above I-shaped columns in order to verify the nonlinear micromodels along with using beam, shell, and 3D models. Figure 6.15 (a) and (b) show the end-shortening and out-of-plane deformations, respectively, for the stocky (60 inches) and slender (160 inches) pinned end columns using beam (B23) elements. The end-shortening is measured at the position of the applied load, while the out of-plane deformation is measured at the mid-section of the column. It is also seen that the nonlinear response is pronounced only for the stocky column. Figure 6.16 illustrates the postbuckling responses for 60 and 100 inch columns under fixed end restrained using beam (B23), shell (S8R), and brick (C3D20R) elements. It is shown that using different type elements for the slender columns yield to comparable postbuckling behaviors with similar global postbuckling deformed shape (mode-1). Convergence problems arouse during the analyses on the slender columns due to highly nonlinear material and excessive deformations. Significant differences are shown in the nonlinear postbuckling response of the stocky columns using

B23, S8R, and C3D20R type elements. In the 3D and shell cases, the flange local buckling modes are exhibited; the beam element model can not capture the flange local buckling. It is also seen that high nonlinear material responses causes convergence problems during the analysis.

Postbuckling behavior for pin-pin columns having 60, 100, and 160 inch lengths using beam (B32) and brick (C3D20R) elements are illustrated in Figure 6.17 (a) and (b). Both linear and nonlinear material behaviors are considered. Different postbuckling responses are exhibited by using beam and brick elements for the stocky columns. This is due to the flange local buckling in the stocky columns. The differences decrease with increasing slenderness. The highly nonlinear response is exhibited for the stocky columns, which also causes convergence problems during the analysis. Similar postbuckling behavior for fixed end columns having 60 and 100 inch lengths are shown in Figure 6.18.

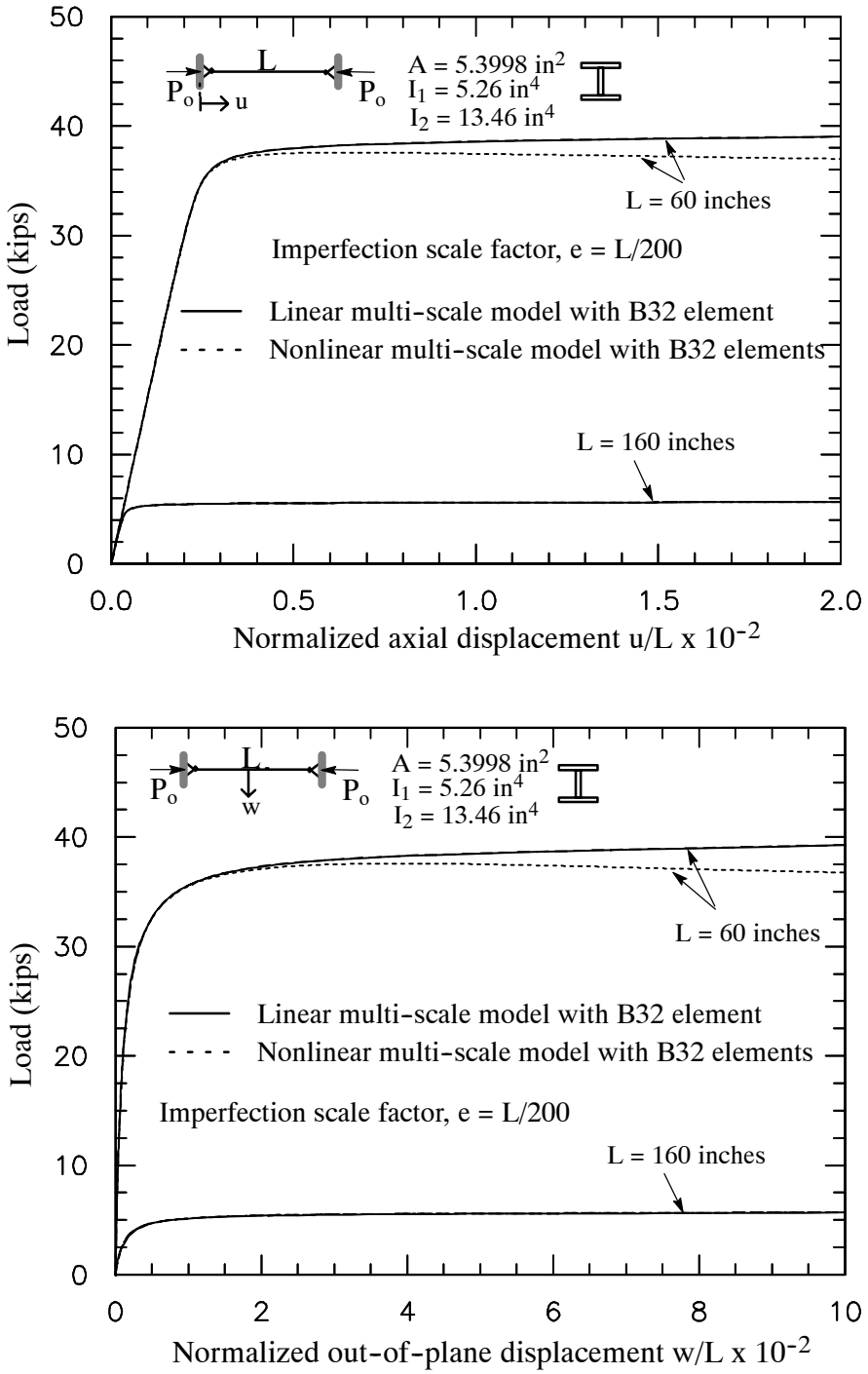

Figure 6.15 Postbuckling responses using beam (B23) elements for pinned end columns: (a) axial deformation; (b) transverse deformation.

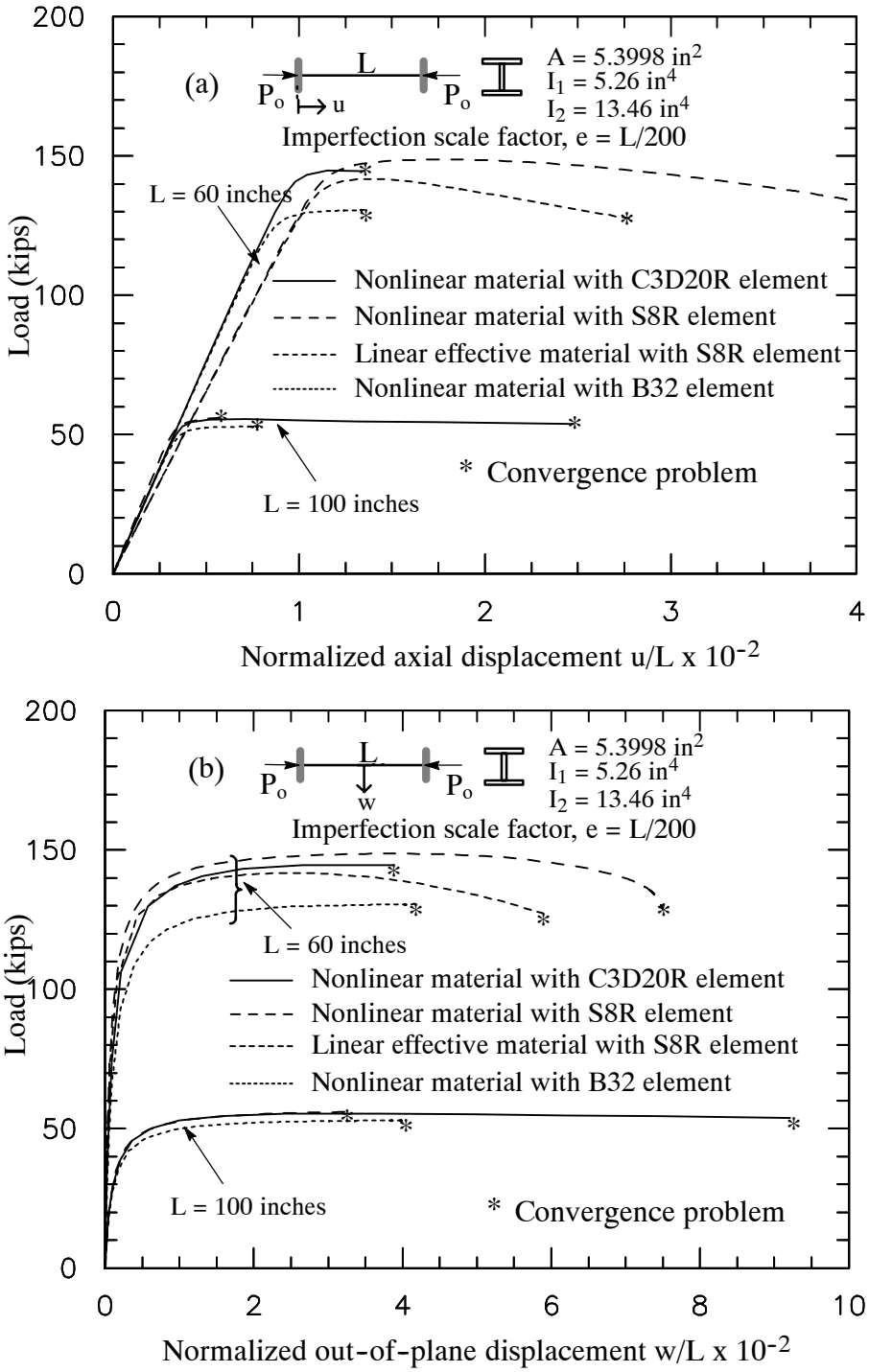

Figure 6.16 Postbuckling responses from 1D, 2D, and 3D elements: (a) axial deformation; (b) transverse deformation.

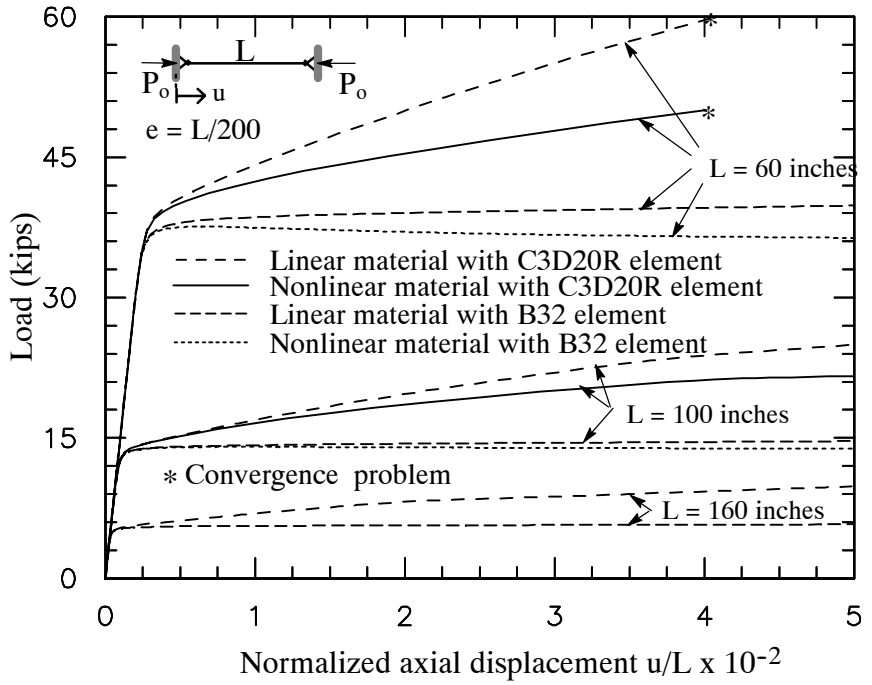

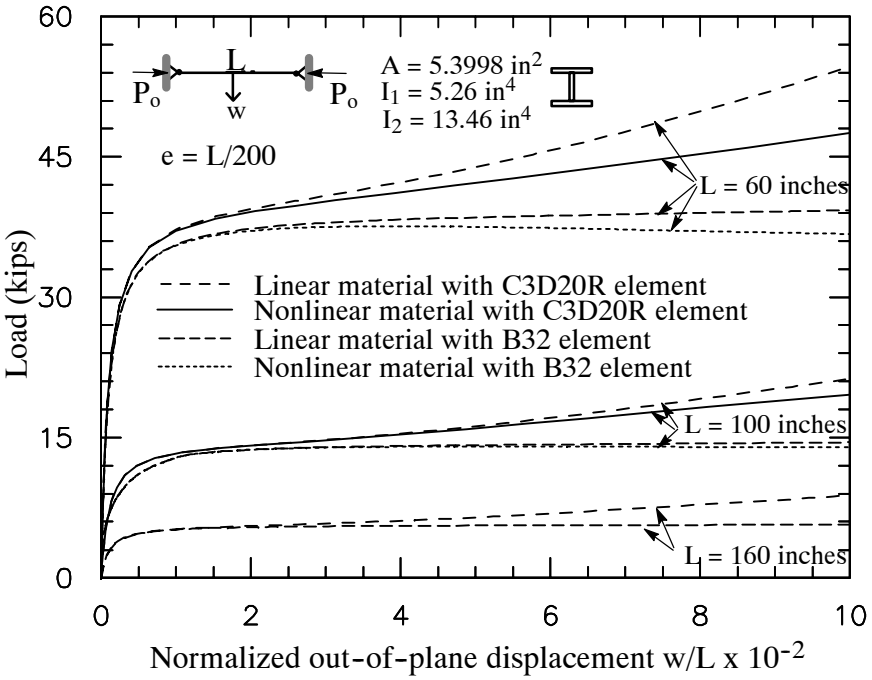

Figure 6.17 Postbuckling responses using linear and nonlinear materials for pinned end columns: (a) axial deformation; (b) transverse deformation.

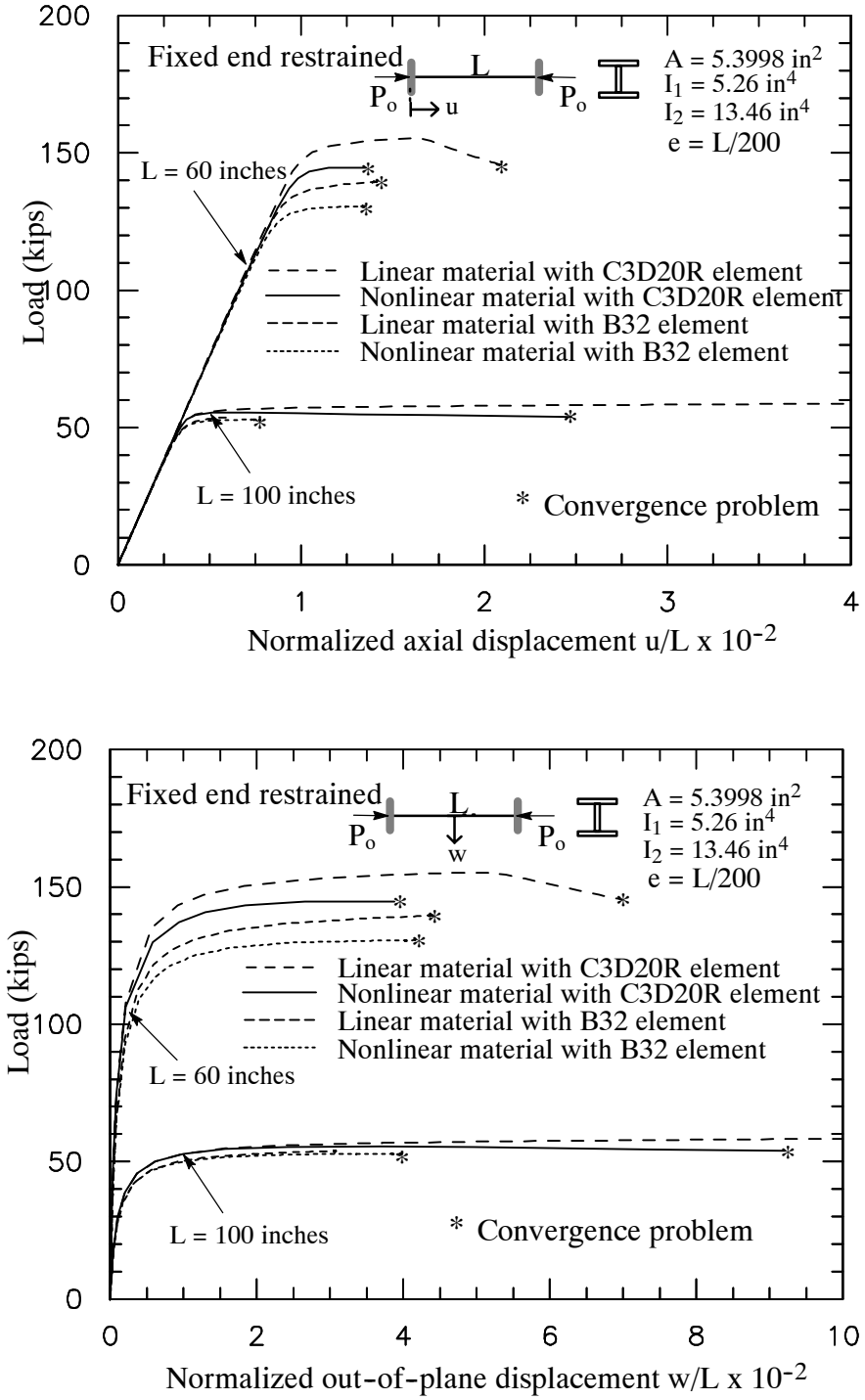

Figure 6.18 Postbuckling responses using linear and nonlinear materials for fixed end columns: (a) axial deformation; (b) transverse deformation.

Effect of nonlinear material on static postbuckling response

The effect of nonlinear material behavior on the postbuckling response of pultruded columns is investigated. Linear and nonlinear responses of E-glass/vinylester pultruded material are considered. The column lengths vary from 20 to 240 inches. FE model with brick (C3D20R) elements is used. Static buckling loads are first computed for several lengths of pultruded columns with pinned and fixed supports under axial compression. The computed critical loads are normalized by Euler buckling load, as shown in Figure 6.19. The effect of nonlinear material response is minimal and it is shown to be small at lower slenderness values. Only for the fixed stocky composite columns that the nonlinear material behavior affects the buckling loads.

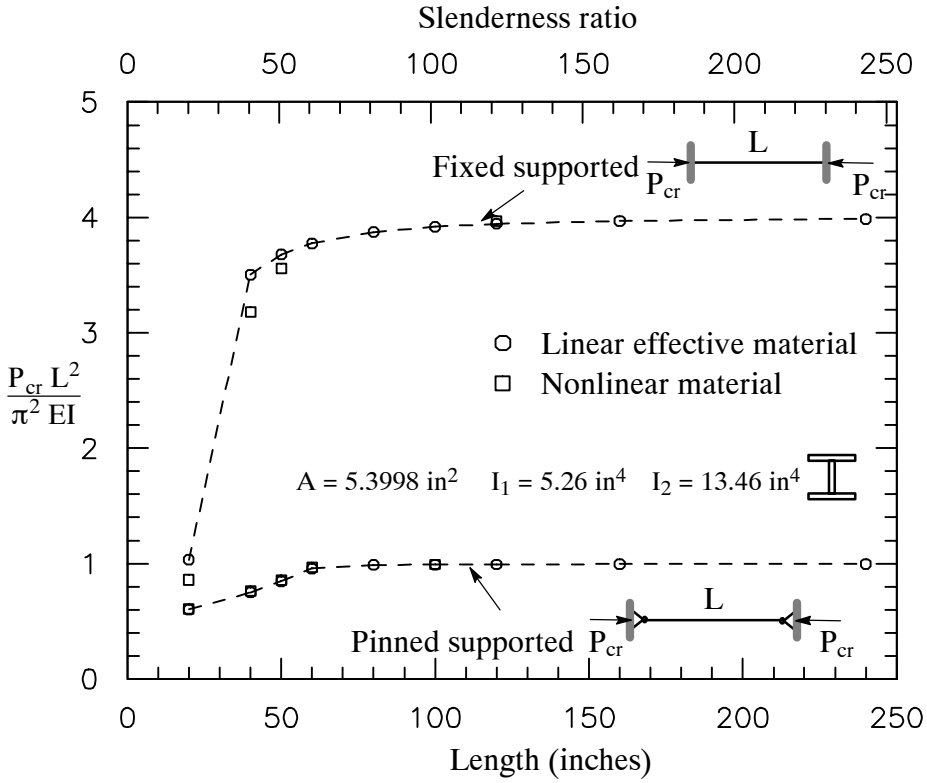

Figure 6.19 Normalized buckling loads for pinned and fixed ends columns.

Next, postbuckling analysis is performed for pinned and fixed support pultruded columns having different lengths: 50, 60, 80, 100, and 120 inches. Column imperfection is considered using the first five buckling modes with a scale factor of L/200. The effect of nonlinear material behavior on the postbuckling responses is investigated. For this purpose, the J2-deformation theory with the Ramberg-Osgood nonlinear 1D strain-stress curve are used to model for the vinylester matrix (Haj-Ali et al., 2001). The Ramberg-Osgood curve is used in order to avoid numerical convergence arouse by using polynomial function at the highly nonlinear range. Figure 4.7 shows the nonlinear shear 1D parameter using Ramberg-Osgood and polynomial representations. The axial load-displacement responses of the two columns are shown in Figures 6.20 and 6.21, respectively. It is shown that the nonlinear material behavior increases significantly for the stockier column. This is due to a relatively large stress level distributed in the column, in which the material responses are beyond the elastic linear range. In order to provide postbuckling response without material failure, the Tsai-Wu criterion is also monitored at each integration point and applied load level. The Tsai-Wu material failure criterion can be expressed by:

$$
\begin{aligned}
&F = F_1\,\sigma_{11} + F_2\,\sigma_{22} + F_{11}\,\sigma_{11}^2 + F_{22}\,\sigma_{22}^2 + F_{66}\,\sigma_{12}^2 + 2F_{12}\,\sigma_{11}\,\sigma_{22} \\
&F_1 = \frac{1}{\sigma_A^+} - \frac{1}{\sigma_A^-} \qquad F_2 = \frac{1}{\sigma_T^+} - \frac{1}{\sigma_T^-} \qquad F_{66} = \frac{1}{\tau_A^2} \\
&F_{22} = \frac{1}{\sigma_T^+\,\sigma_T^-} \qquad F_{11} = \frac{1}{\sigma_A^+\,\sigma_A^-} \qquad F_{12} = -\frac{1}{2}\sqrt{F_{11}\,F_{22}}
\end{aligned}
\tag{6.2}
$$

The ultimate strength values needed in the second part of Eq. (6.2), for E-glass/pultruded system are taken from the study by Haj-Ali and Kilic (2002) and are listed in Table 6.4. Both stocky and slender columns under pinned supports do not exhibit material failure during the postbuckling analyses. While for the 50 and 60 inch columns under fixed supported, the ultimate strength of the material is reached before initial elastic buckling is occurred.

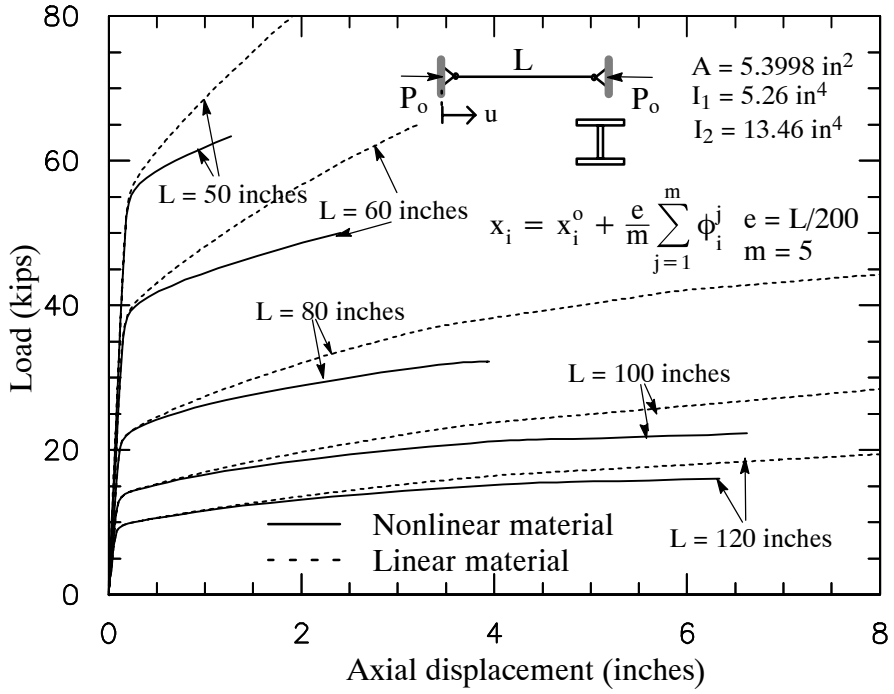

Figure 6.20 Postbuckling behavior for pinned supported pultruded columns.

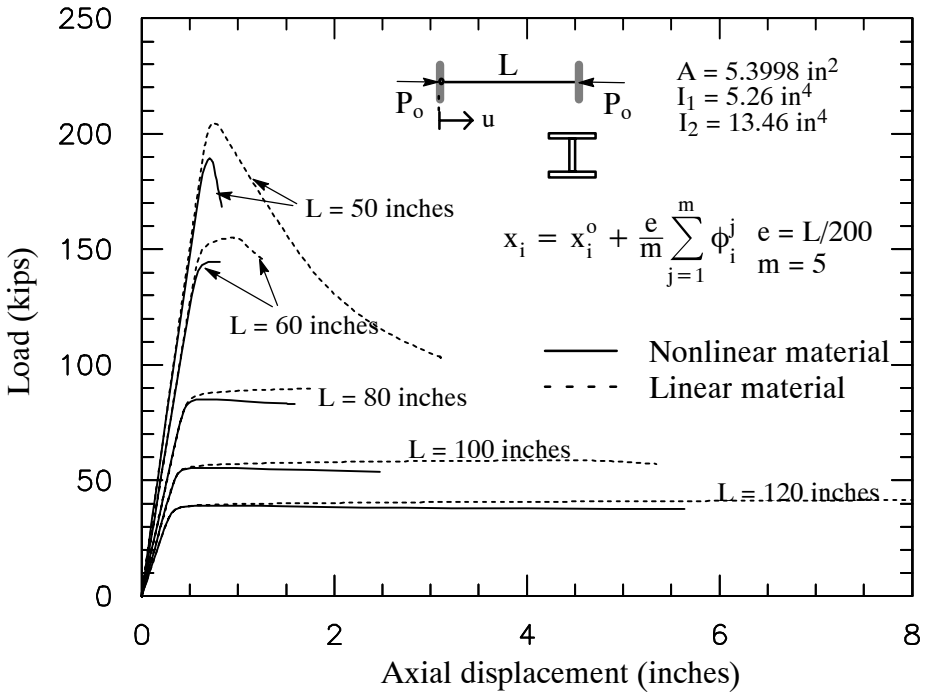

Figure 6.21 Postbuckling behavior for fixed supported pultruded columns.

Table 6.4 Strength of E-glass/vinylester pultruded system, v_f=0.34. (Haj-Ali and Kilic, 2002)

σ_A^+	σ_A^-	σ_T^+ (ksi)	σ_T^-	τ_A
35	40	12	24	12

Creep buckling and collapse of pultruded columns

In this section, a critical creep collapse and its corresponding critical time are examined for slender pultruded columns. Long-term creep data for pultruded coupons, reported by Scott and Zureick (1998) are used to calibrate the micromodels, as shown in Table 6.2. Pinned and fixed ends uniaxial pultruded columns with various length: 80, 120, and 160 are studied. FE model with brick (C3D20R) elements are generated. Critical loads are computed from nonlinear FE buckling analyses and are compared with Euler buckling loads, as given in Table 6.5. Effect of geometry imperfection on creep collapse is first analyzed for pinned supported pultruded columns with L=120 inches (λ = 122). Two geometric imperfections are included by superimposing the first five buckling modes with two scale factors L/20000 (near perfect) and L/200 (imperfect). Creep response is then simulated under several load levels: 0.7, 0.8, and 0.9 of the static buckling load. Figure 6.22 shows the normalized axial creep responses under several load levels for the near 'perfect' and imperfect I-shaped pultruded columns. It is shown that the geometry imperfections accelerate critical and creep collapse times.

Table 6.5 Critical buckling loads for pultruded I shaped cross sections.

Geometric	L (in)	$\lambda = \frac{L}{r_g}$	Critical buckling loads (kips)					
			L			L		
			P_E	P_{cr}	% Diff	P_E	P_{cr}	% Diff
b = d = 4.0 in $t_f = t_w$ = 0.49 in rg = 0.9866 in A = 5.3998 in^2	80	81	87.80	85.03	3.16	21.95	21.68	1.24
	120	122	39.02	38.48	1.40	9.76	9.70	0.64
	160	162	221.95	21.78	0.77	5.49	5.47	0.41

Note: λ is slenderness ration; r_g is radius of gyration $\left(\sqrt{\frac{I}{A}}\right)$

P_E is Euler buckling load; P_{cr} is the critical FE load

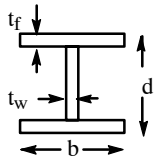

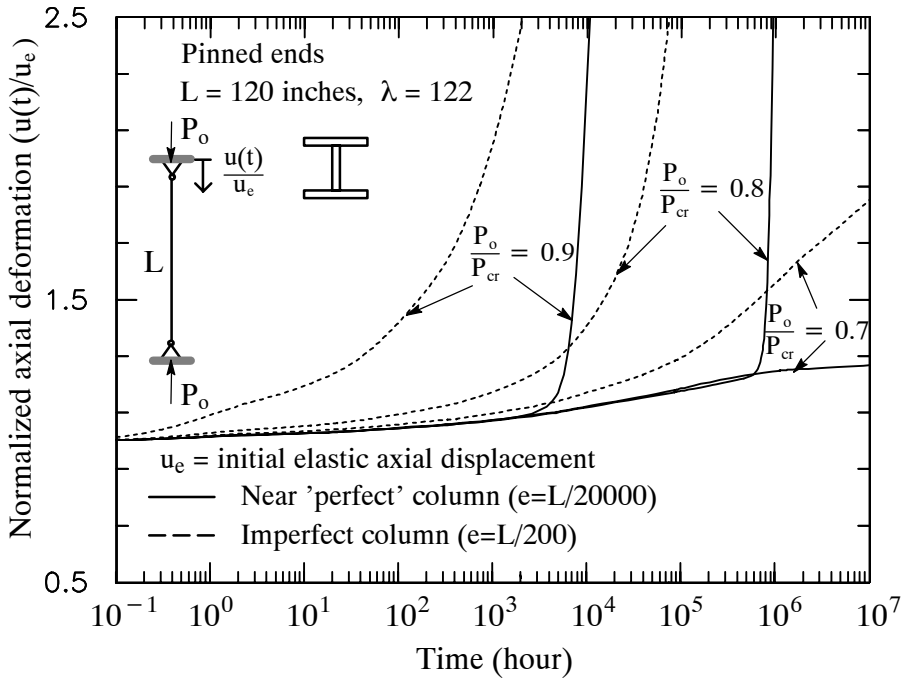

Figure 6.22 Normalize axial creep deformation for I shaped pultruded fixed end columns for the near 'perfect' and imperfect columns.

Next, long term creep collapse of the columns with various lengths: 80, 120, and 160 inches are performed. Different load fractions: 0.7, 0.8, and 0.9 of the elastic critical load are applied. Geometry imperfection is accounted for using the first five eigen-modes and a scale factor of L/200. Figure 6.23(a) and 6.23(b) show the normalized axial and transverse creep responses, respectively, for slender pultruded columns with pin-pin supports under various load levels: 0.7, 0.8, and 0.9. Figure 6.24(a) and 6.24(b) show the normalized axial and transverse creep responses, respectively, for slender pultruded columns under fixed end supports. The critical collapse time, in which unstable deformed configuration is reached, is determined when the slope normalized axial deformation reaches the value of 4. Figure 6.25 shows the critical collapse time for columns with pinned ends under various load levels. The critical times for fixed end columns under several load levels are illustrated in Figure 6.26. It is shown that the structural instability occurs faster for the slender columns than the stocky columns at the same loading ratios. There is also a load limit, below which the instability of the FRP composite column will not occur. In the current case, based on 8 month calibrated creep response of FRP pultruded composites, a load level of about 0.7 of P_{cr} can be considered as a save load limit in the design of pultruded structures. In order to provide a more accurate load carrying capacity and serviceability life of the FRP columns, the longer time-dependent material responses need to be characterized.

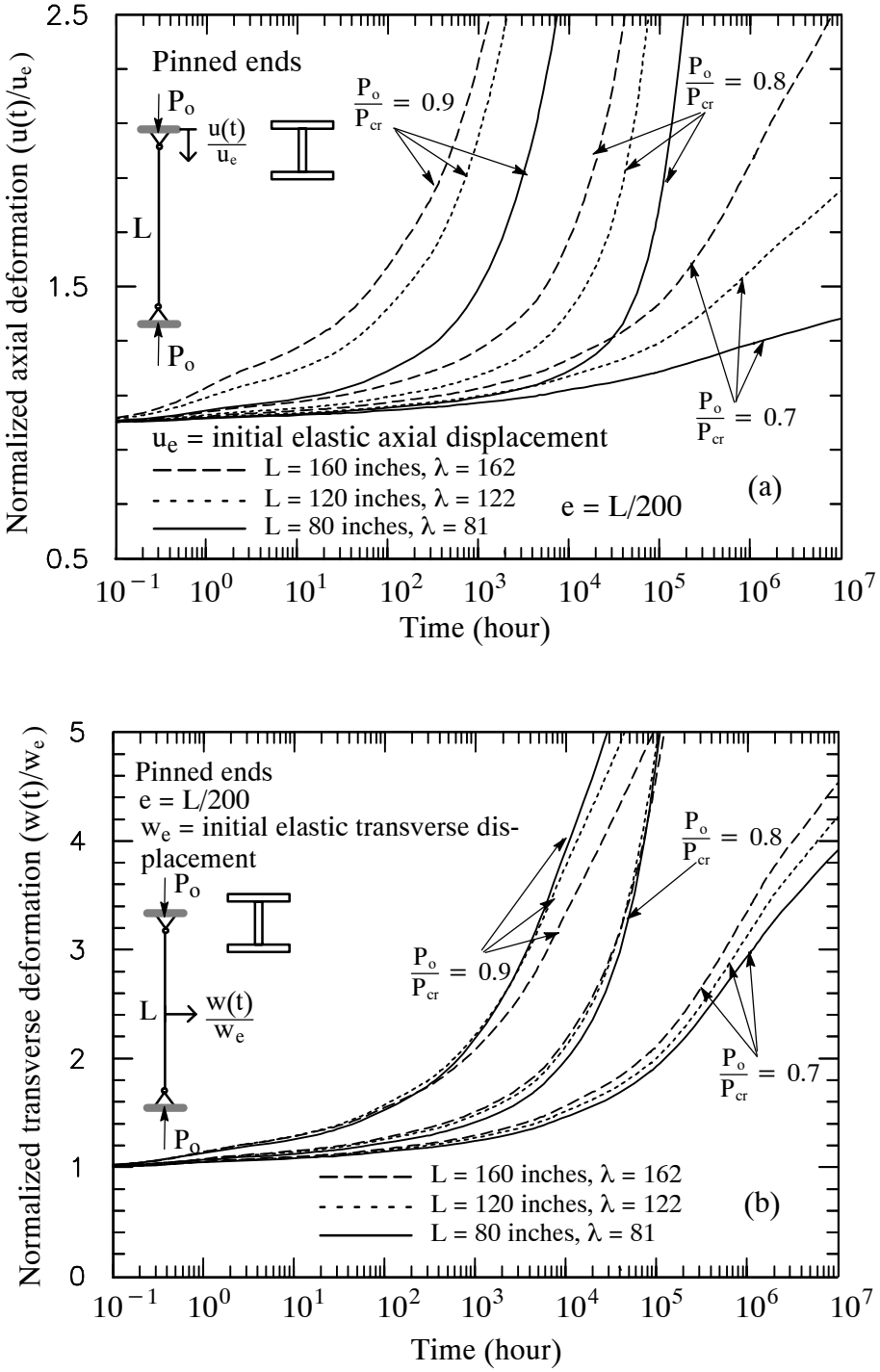

Figure 6.23 Normalize creep strain for I-shape pultruded pinned end columns: (a) axial deformation; (b) transverse deformation.

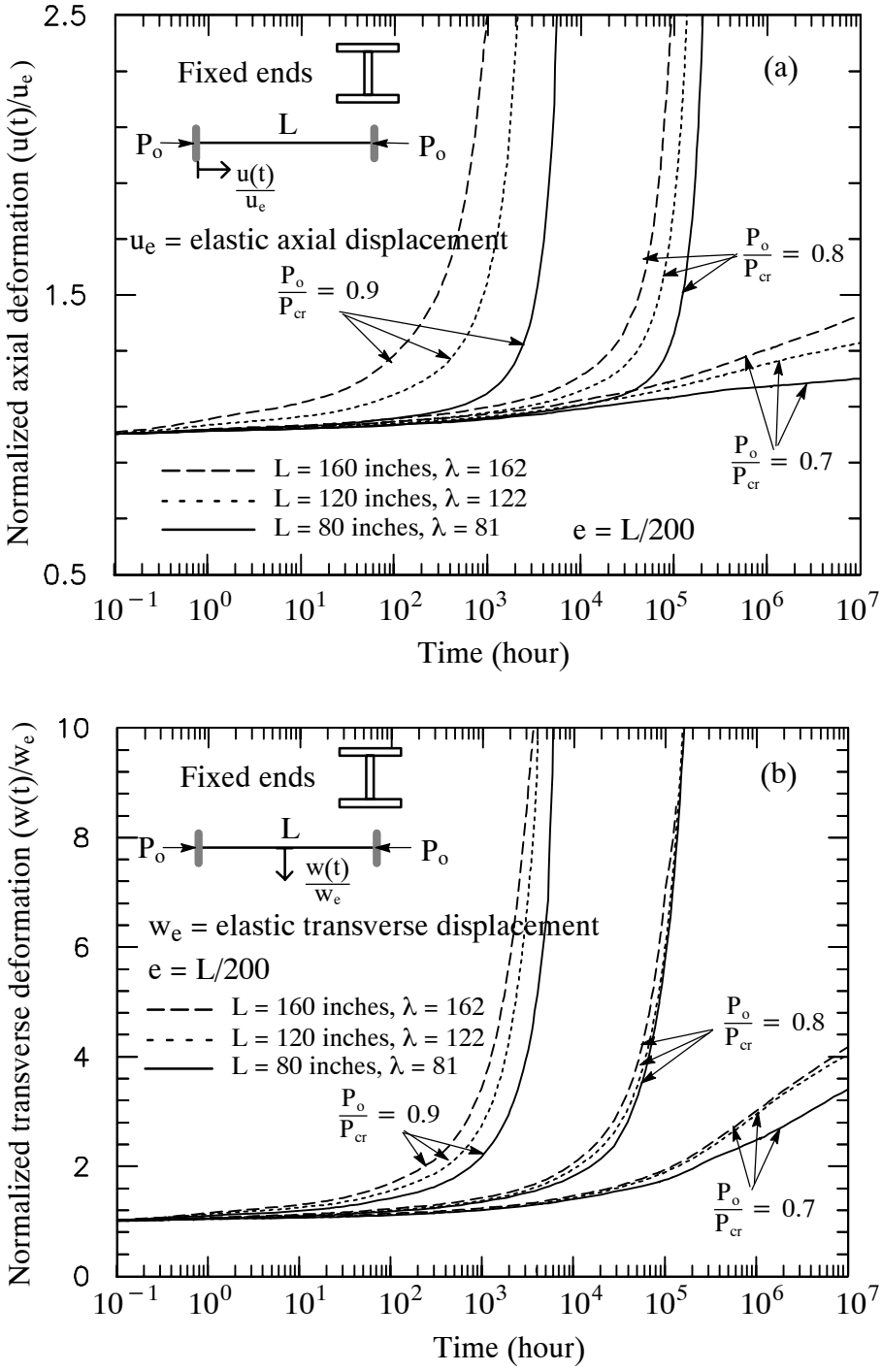

Figure 6.24 Normalize creep strain for I-shape pultruded fixed end columns: (a) axial deformation; (b) transverse deformation.

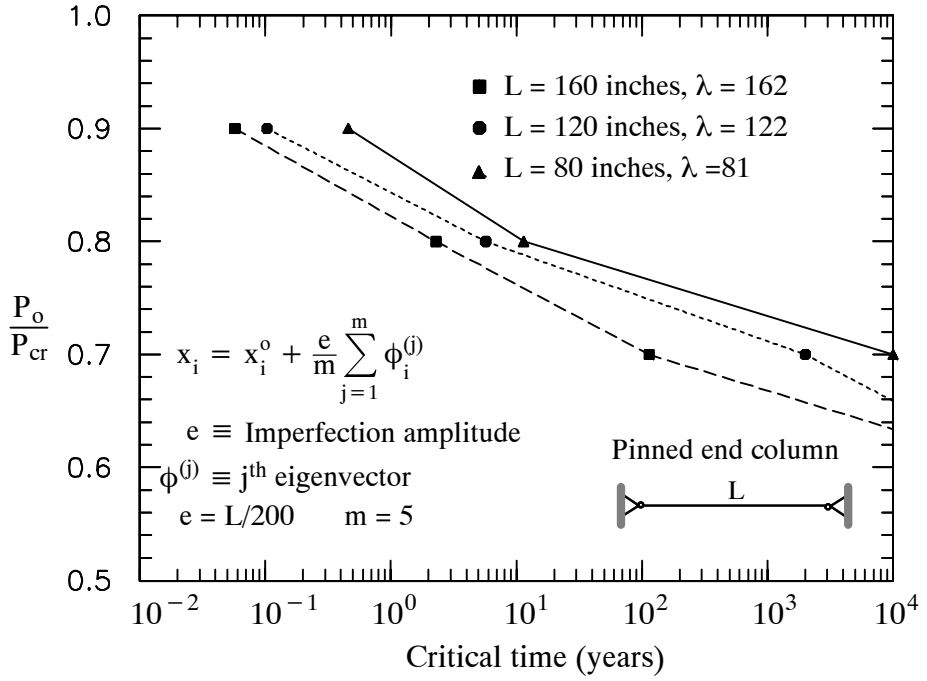

Figure 6.25 Critical buckling time for imperfect I-shaped pultruded columns.

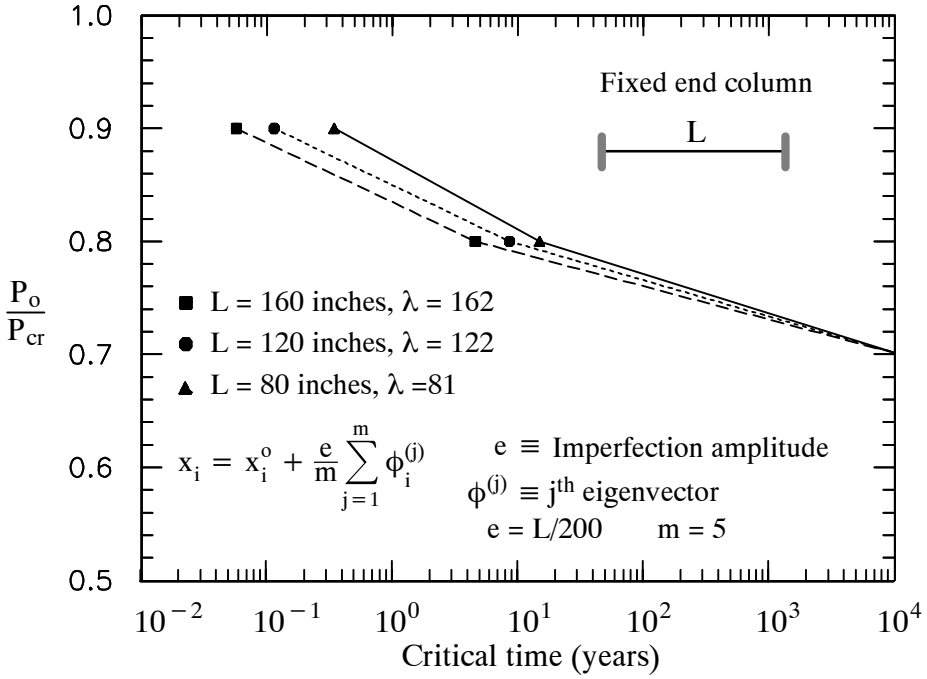

Figure 6.26 Critical buckling time for imperfect I-shaped fixed end pultruded columns.

6.3 Postbuckling and Creep Analysis of Laminated Composite Structures

In the following, the integrated multi-scale constitutive framework for the creep analysis of graphite/epoxy laminated composite structures is presented. Two examples of laminated composite panel and thick composite ring under surface pressures are performed. The studied composite structures are made of T300/5208 graphite/epoxy materials (Tuttle and Brinson, 1986). FE model is generated for both structures using a quadratic nine-node shell element with a reduced integration (S9R5). The nonlinear viscoelastic micromechanical framework is implemented as a material subroutine (UMAT) in the ABAQUS (2002) FE code.

T300/5208 graphite/epoxy composite panel under surface pressures

The first example is concerned with the viscoelastic response of a laminated composite panel subjected to an external uniform pressure. Figure 6.27 shows the geometry of the panel and the FE mesh along with the layup used through the thickness. The geometry of this panel is taken from the postbuckling study performed by Knight and Starnes (1985). A total of 2112 nodes and 512 S9R5 elements are used in the FE model. The composite panel has $[\pm 45/90/0_2/\mp 45]_s$ layup. The material used for each layer is the T300/5208 graphite/epoxy, where the elastic properties for the fiber and matrix are listed in Table 3.3. The long-term Prony series parameters are used for this purpose, as previously calibrated in Table 5.6. A uniform pressure is applied on the panel's top surface using a Heaviside step function. An elastic static critical buckling pressure, p_{cr}, is first computed. A geometric imperfect mesh is constructed using the first five eigen modes and scaled by 1/20 of the panel's thickness. The first five eigen-modes are shown in Figure 6.28.

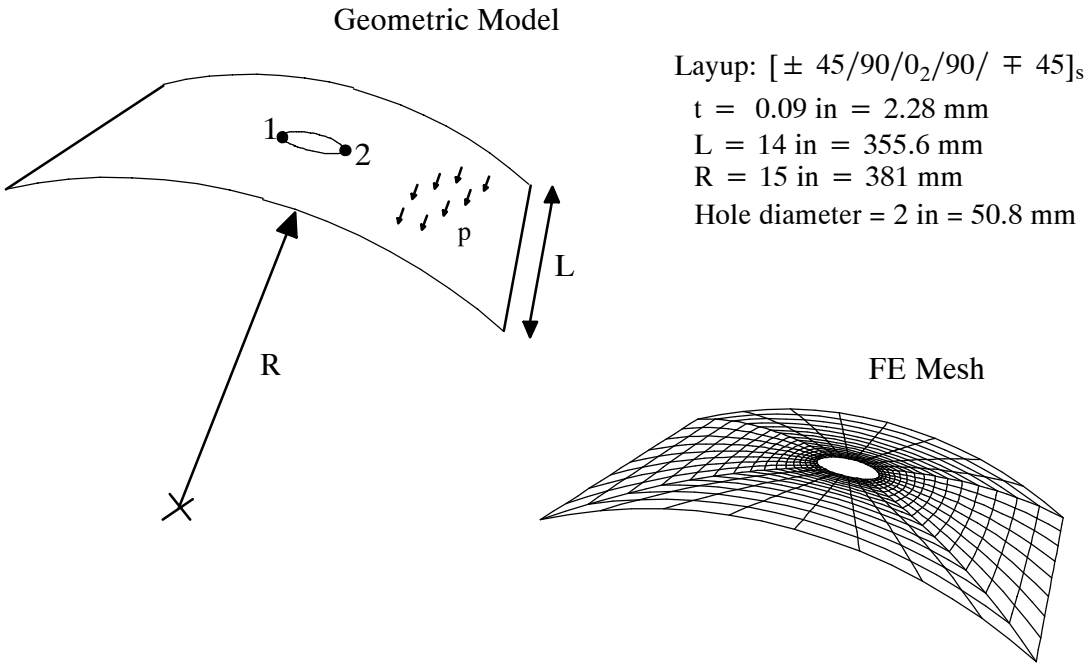

Figure 6.27 Geometry and FE mesh for the laminated composite panel.

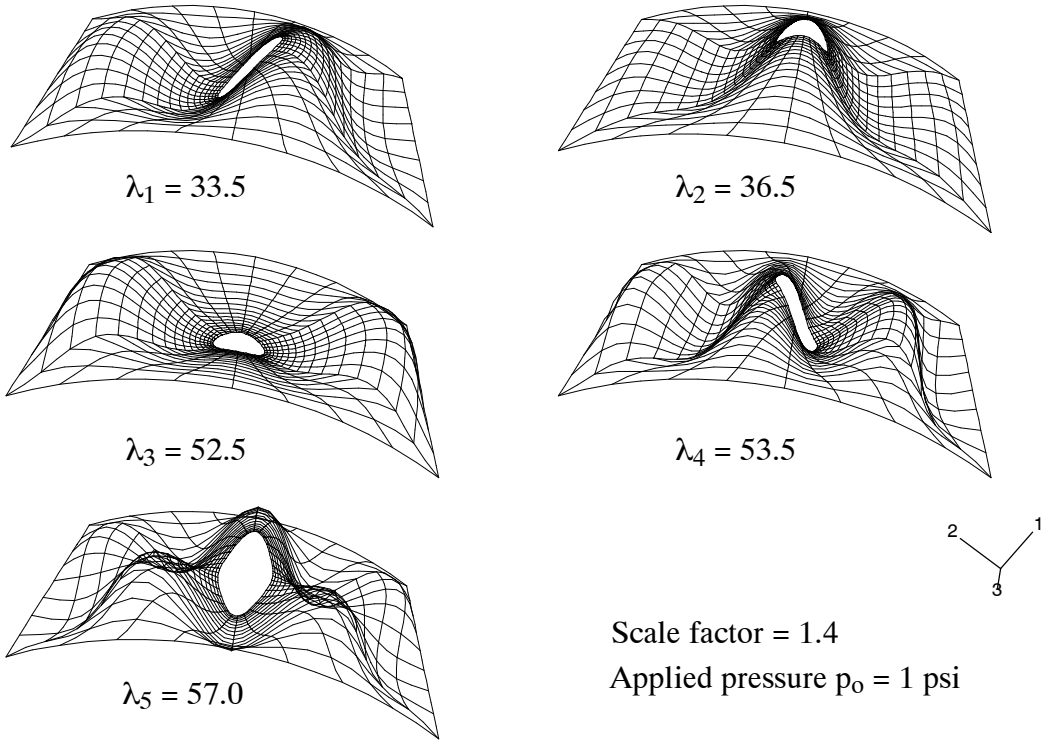

Figure 6.28 The first five eigen-modes for a laminated composite panel under a surface pressure.

A postbuckling analysis of the imperfect composite panel, having linear and nonlinear matrix behavior, is then simulated, as seen in Figure 6.29. The displacement is measured by an average radial displacement of the two points on the edge of the circular notch. The nonlinear material response is only exhibited at the localized stress area. Therefore, the material nonlinearity is not very significant in this case. The elastic critical buckling limit is never reached even at the failure point. Tsai-Wu failure criterion is also monitored during the analysis. The typical T300/5208 composite strength having FVF 0.65 is listed in Table 6.6. Postbuckling path and some deformed shapes along the equilibrium path are shown in Figure 6.30.

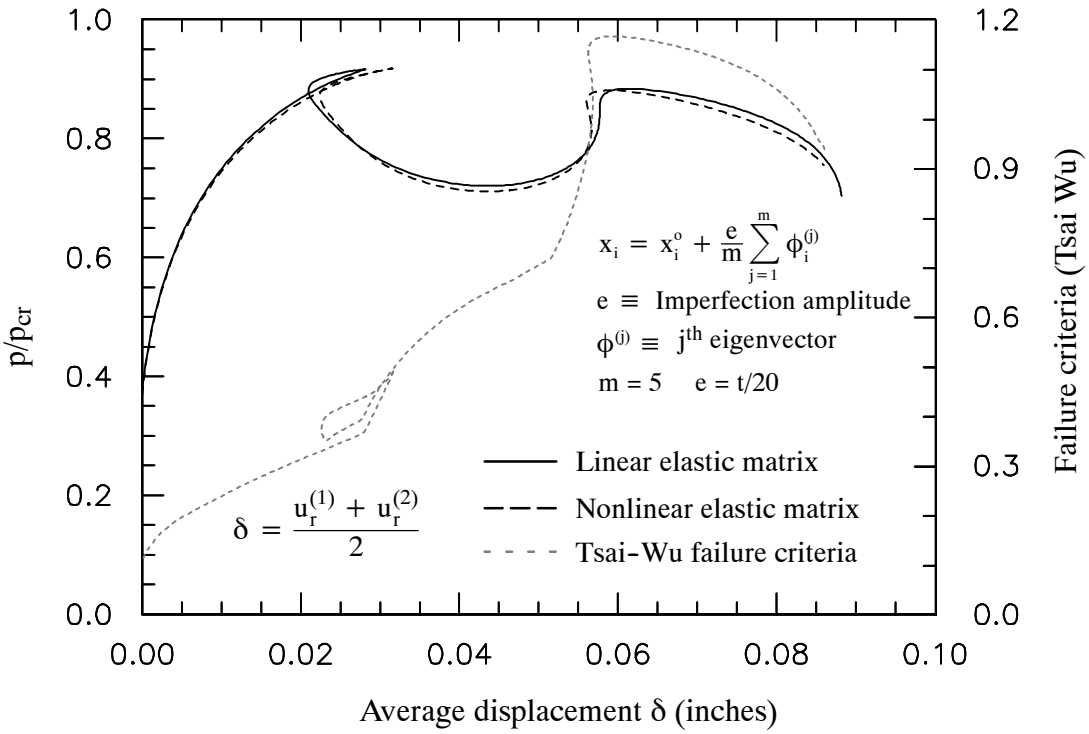

Figure 6.29 Postbuckling response in the form of normalized pressure and Tsai-Wu failure criteria againts out-of plane average displacement.

Table 6.6 Strength of T300 Graphite and 5208 Epoxy, v_f=0.65.

σ_A^+	σ_A^-	σ_T^+	σ_T^-	τ_A
MPa (ksi)				
1500 (220)	1650 (240)	48.3 (7)	276 (40)	82.7 (12)

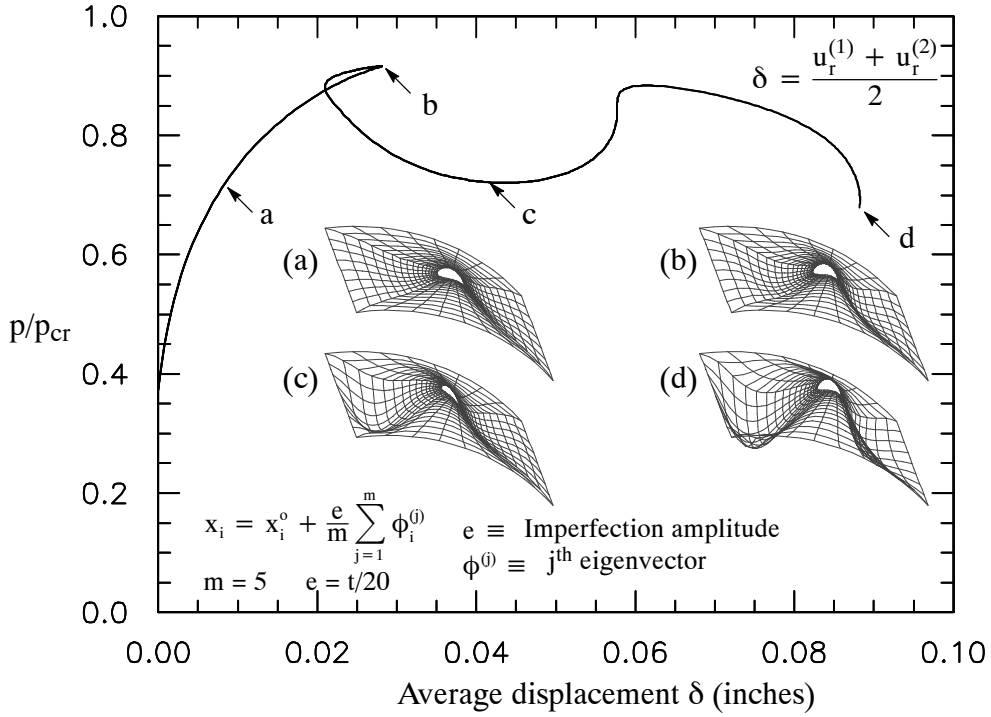

Figure 6.30 Postbuckling response depicted from the equilibrium path in the form of normalized pressure againts out-of plane average displacement.

Next, a relatively long-term creep response of the imperfect composite panel, under applied pressure of 0.8 and 0.9 p_{cr}, is simulated for 6000 hours, as shown in Figure 6.31. Figure 6.31 also shows a typical deformed configuration. An average radial displacement of the two points on the edge of the circular notch is defined and used to quantify the creep response of the panel. The nonlinear material response is evident near the hole area for the applied pressures of 0.8 and 0.9 p_{cr}, while below applied pressure 0.8 p_{cr} time-dependent response is not significantly nonlinear. At this load level, the Tsai-Wu failure criteria, in Figure 6.29, is less than 0.4.

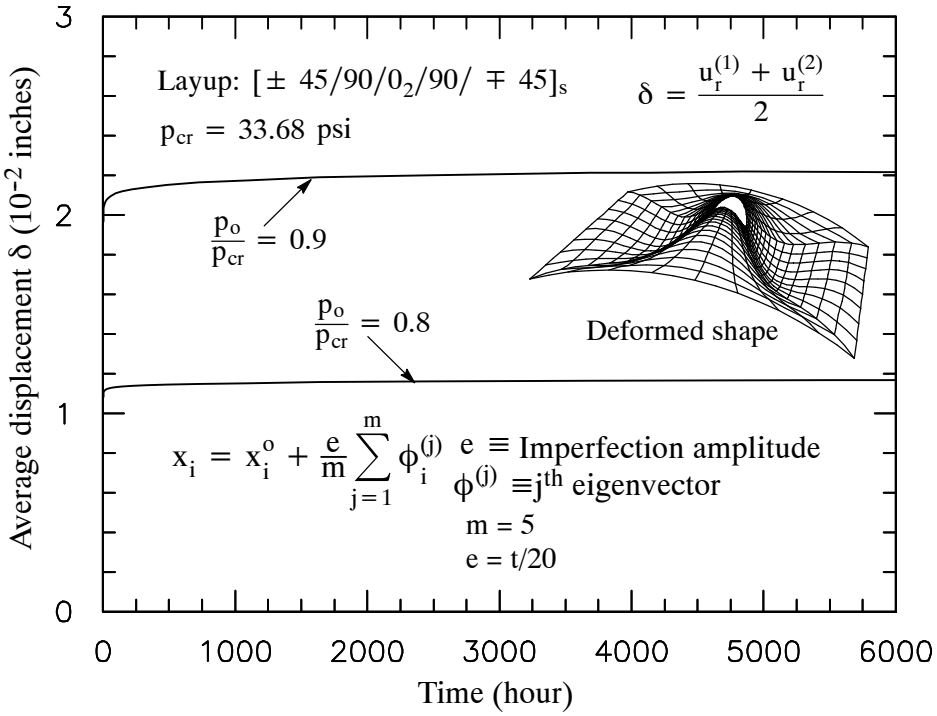

Figure 6.31 Out-of plane creep displacement responses.

T300/5208 graphite/epoxy thick composite ring under external pressures

The second structural application consists of a thick composite ring subjected to an external pressure. The ring is made of the same lamina as in the previous example. The geometry and layup are shown in Figure 6.32. The composite ring has outer radius of 30 inches and thickness of 0.27 inches, with $[0/90/\pm 45]_{6s}$ layup. FE model with S9R5 typed element is then generated. A concentric external pressure is applied along the outer surface of the ring. Buckling analysis was first performed to obtain the critical load and the first ten eigen-modes used in the postbuckling analysis. The first ten eigen-modes are illustrated in Figure 6.33. The postbuckling response of the ring is shown in Figure 6.32 for two different imperfection amplitudes, e: D/100 and D/500. A typical postbuckling deformation is also shown in Figure 6.32. A stable postbuckling response is exhibited due to the positive stiffness that the structure retains in the post-buckling range.

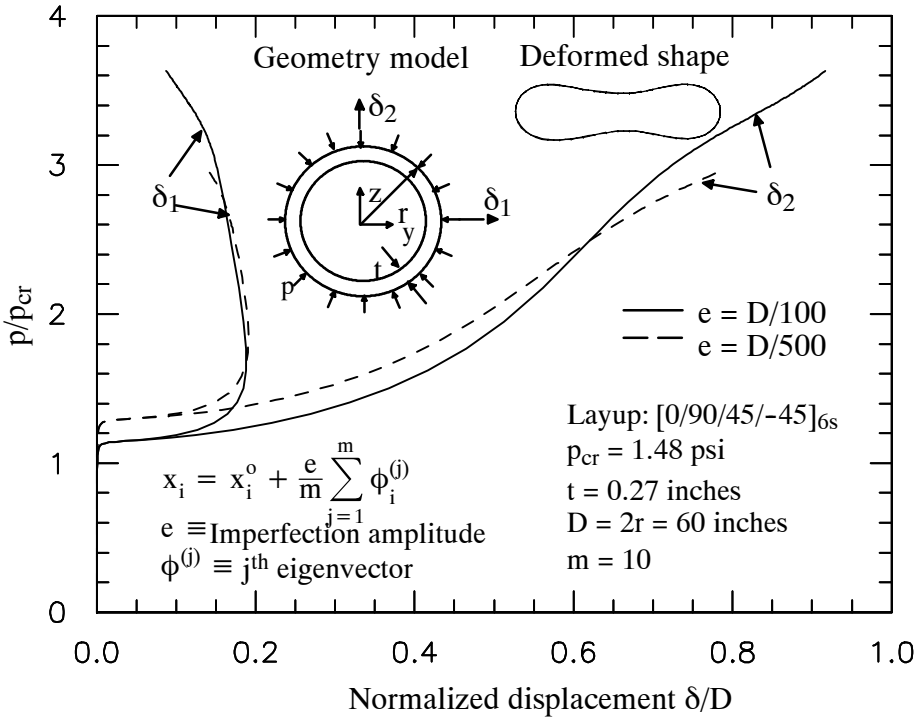

Figure 6.32 Postbuckling responses of the laminated composite circular ring.

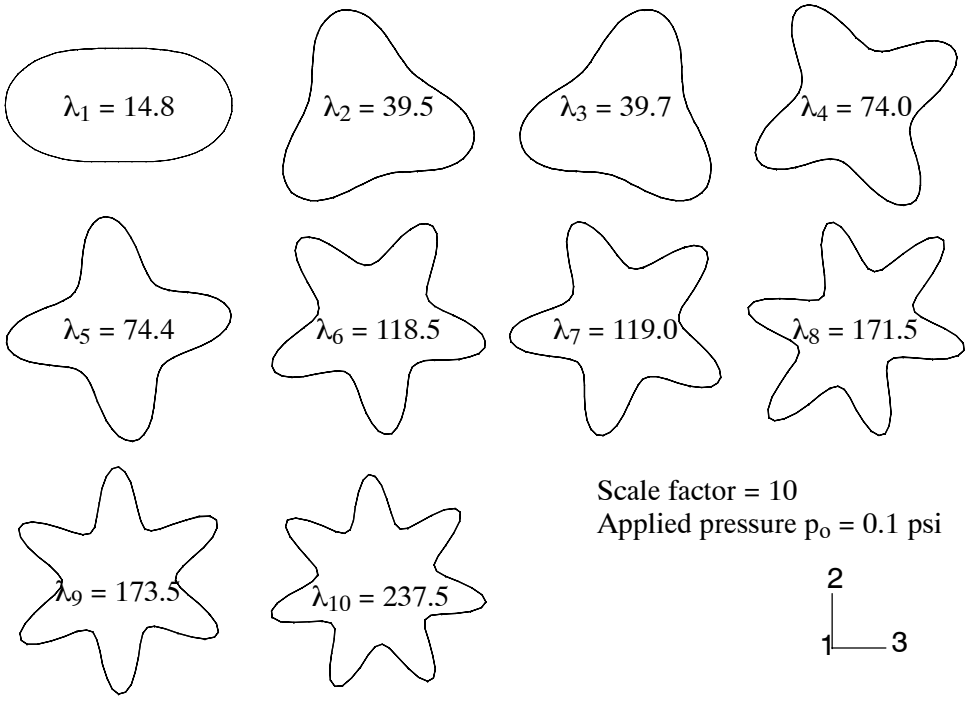

Figure 6.33 The first ten eigen-modes of a thick composite ring under an external pressure.

Long term creep under different pressure levels: 0.8-3.1 p_{cr} are simulated with the initial imperfection e=D/100. Figures 6.34(a), 6.34(b), and 6.34(c) present the long-term creep response of the ring when subjected to step pressure loads reported as a fraction of the critical buckling pressure. The creep response is monitored from the maximum radial displacement normalized by ring's initial radius. Loading ratios larger than one are also examined because of the positive residual stiffness of the ring after initial elastic buckling. The three figures are grouped according to the deformed shape. For $\frac{p}{p_{cr}} = 0.8$ to 1.1, the deformed shape follows the first mode and it is clear that viscoelastic buckling will ultimately occur for the cases where the loading ratio is greater than one. The second group of curves has loading ratio of $\frac{p}{p_{cr}} = 1.3$ to 1.7. The deformed shape in these cases is combined from both mode one and two. It is very interesting to note that while the applied load is greater than the buckling load, the likelihood of viscoelastic buckling has decreased perhaps due to the transition from mode-I to mode-II deformed configurations. Figure 6.34(c) illustrates the curves for $\frac{p}{p_{cr}} = 1.8$ to 3.1. Nonlinear response and early viscoelastic buckling is easily observed. Creep failure in the structures is also monitored. Figure 6.35 shows critical times as a function of pressure level when the structure collapses. The critical time is determined numerically when the normalized radial displacement rate reaches the value of 4, in which the slope of the creep response in Figures 6.34(a), 6.34(b), and 6.34(c) is approximately 76°. The deformation changes from the initial loading to the last stable point is given in Figure 6.36.

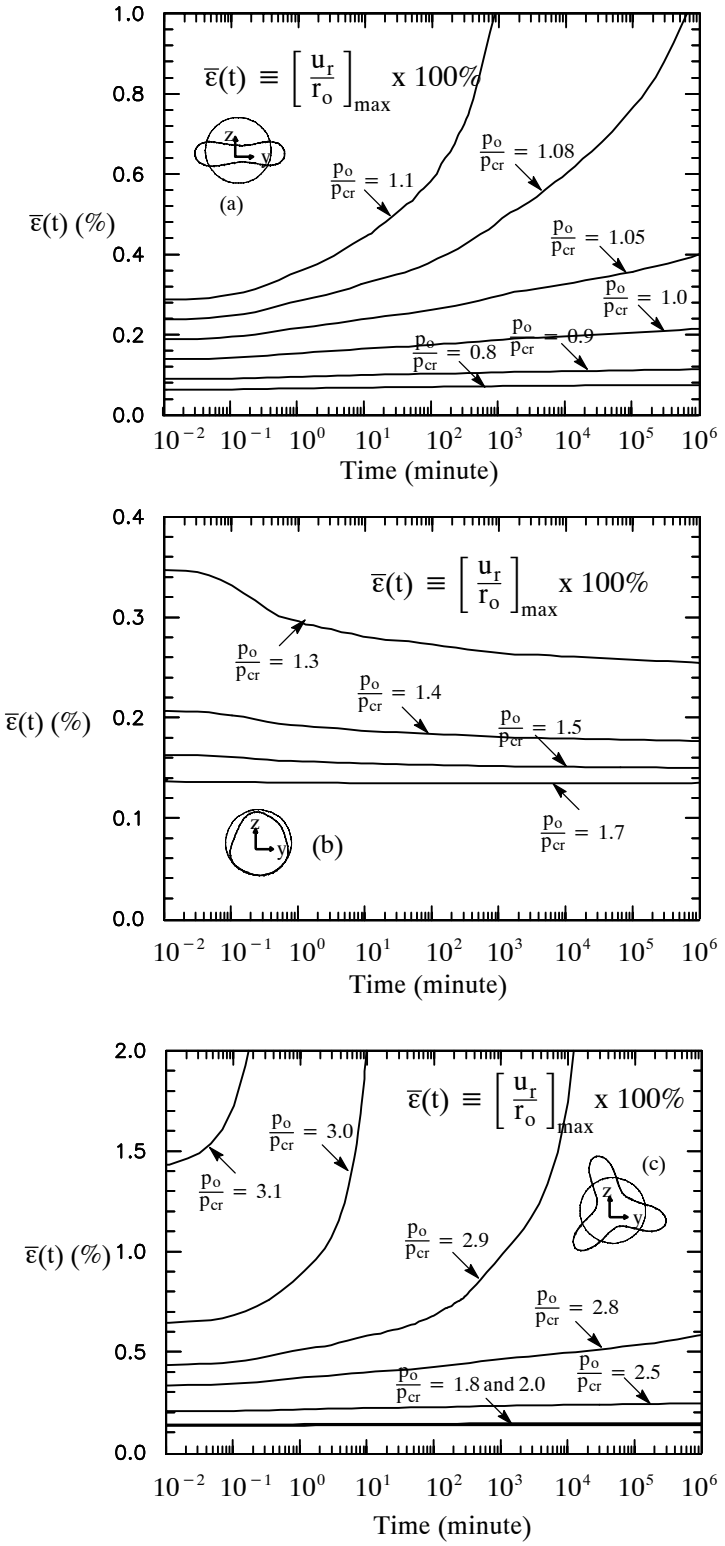

Figure 6.34 Long-term creep response.

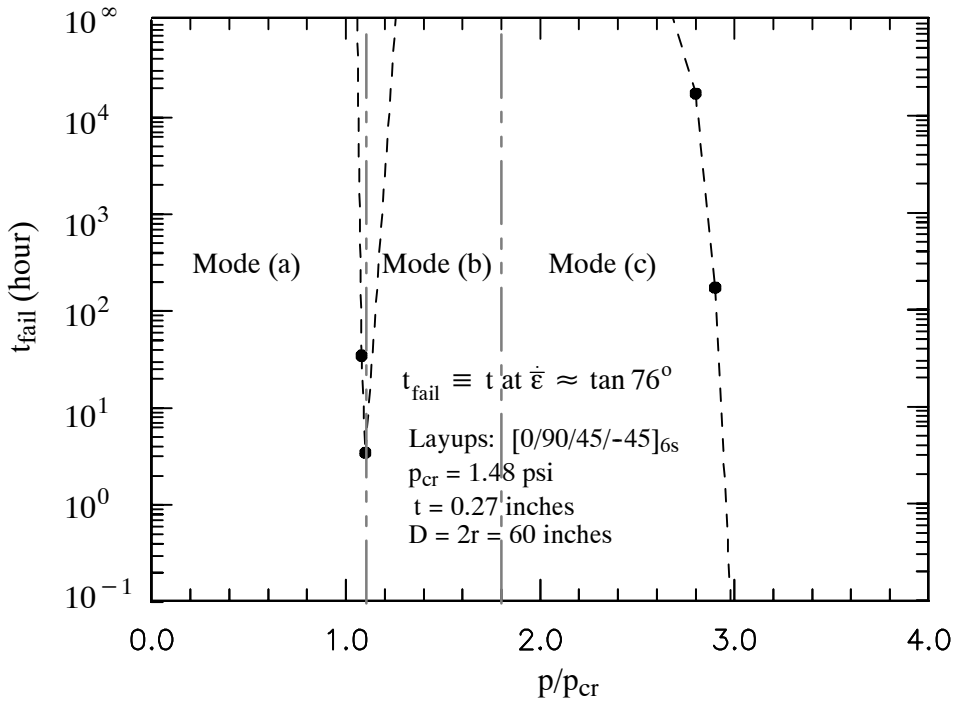

Figure 6.35 Critical time at failure point.

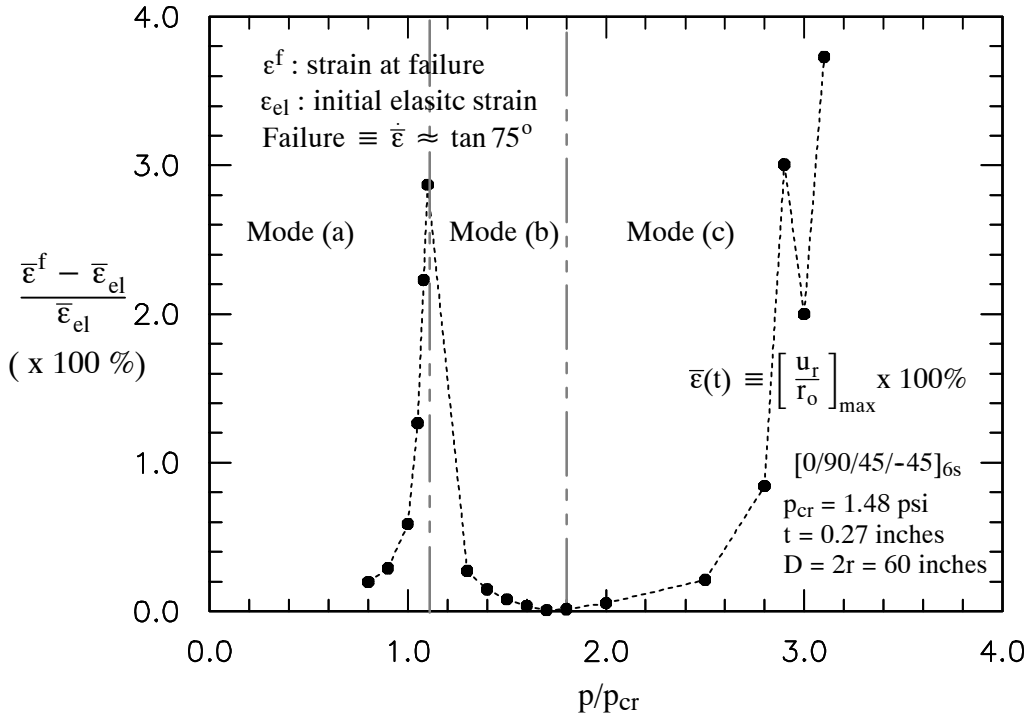

Figure 6.36 Dilatation at failure point.

CHAPTER VII

CONCLUSIONS AND FURTHER RESEARCH

7.1 Conclusions

A new 3D multi-scale constitutive framework is formulated for the nonlinear viscoelastic analysis of laminated and pultruded composite materials and structures. The proposed micromodeling framework recognizes the fiber and matrix responses in each reinforcement system within a laminated or pultruded layer. Two previously developed 3D micromodels are used and modified to include time-dependent nonlinear behavior for the matrix. A sublaminate micromodel, with two roving and CFM layers, is developed in order to generate an effective anisotropic viscoelastic response for the pultruded composite. A new recursive-iterative numerical integration method is developed for the Schapery nonlinear viscoelastic model used for the isotropic matrix. The lower level constitutive models for the fiber and matrix are nested to the upper level micromodels through different stress-update algorithms. The constitutive framework is integrated with a displacement-based FE code in order to form a combined micromechanical-structural method for the nonlinear and time-dependent analysis of composite structures. Several nonlinear viscoelastic structural models are presented to demonstrate the accuracy and efficiency of the numerical and mechanical models. The numerical integration methods used for the Schapery nonlinear viscoelastic model, the 3D micromodels for the layers, and for the overall effective material that directly interfaces with the FE Gaussian integration points are all shown to be effective in analyzing the time-dependent response of wide-range of composite structures.

The experimental part of this study includes short-term (1 hour) creep tests on unnotched off-axis pultruded coupons to calibrate and verify the prediction for multi-axial material re-

sponse. In addition, short-term creep tests of pultruded specimens in the form of notched off-axis and ESE(T) fracture coupons were conducted and simulated with different FE models. The calibration of nonlinear viscoelastic material is performed only at the matrix level. Thus, there is no need for separate calibrations for each mode of loading: uniaxial, transverse, and shear. Moreover, additional nonlinear viscoelastic effects at the matrix level, such as aging, temperature, and moisture can be easily incorporated in the constitutive framework. The new modeling approach is able to predict the complete 3D multiaxial viscoelastic response only from one viscoelastic kernel in the matrix.

A new recursive-iterative numerical algorithm

A new recursive-iterative numerical method is developed for the integration of the Schapery-type nonlinear viscoelastic model with stress-dependent state variables. The new numerical algorithm modifies the linearized time-dependent stress-strain relation of Lai and Baker (1996). An iterative scheme and an equation for the consistent tangent stiffness matrix are developed to enhance numerical convergence for fast and accurate equilibrium state. Numerical examples are presented to demonstrate the numerical performance of the recursive-iterative constitutive model with a FE code. It is shown that the algorithm accelerates the convergence and decreases residual at the global level. Accurate modeling of the viscoelastic behavior of isotropic materials is also shown, especially for highly nonlinear viscoelastic response. It is found that having a stress-dependent elastic compliance part that is monotonic function in terms of the equivalent stress, leads to a faster convergent solution.

Stress correction algorithms

The micromechanical models for laminated and pultruded composite materials are expressed using a linearized formulation in term of subcell's average stress and strains in order to satisfy traction continuity and strain compatibility along the interface of the subcells. Due to the nonlinear and time-dependent response in the matrix subcells, the linearized formula-

tion will usually violate the constitutive equations. A predictor-corrector stress-update algorithm is implemented for each micromodel to satisfy both the micromechanical relations and the constitutive equations. Therefore, accurate results are guaranteed in every level of the multi-scale framework. This enhances the convergence and leads to accurate and efficient analysis at the structural level. While no extensive numerical evaluation and performance was carried out for the different micromechanical models, the added computational premium is comparable to that of using computational plasticity models for a given time-increment. In addition to stress update, there is an additional small computational fraction needed for the recursive viscoelastic part of the algorithm.

An integrated micromechanical-structural framework.

A micromechanical-structural framework for the nonlinear viscoelastic analysis of laminated and pultruded composite structures is developed by implementing the 3D multi-scale constitutive model at each Gaussian point. Different stress or strain constraints are imposed on the overall response from the 3D constitutive framework in order to properly interface with beam or shell elements. This adds flexibility where it is possible to generate a wide-range of practical models for time-dependent structural analysis.

7.2 Further Research

The current modeling approach does not account for damage behavior due to the applied loading or the sustained deformation with time. However, the current formulation is general and allows incorporating damage in the static compliance functions. In addition, time-dependent damage due to long-term deformations or rate effects can potentially be incorporated within the viscoelastic stress-dependent parameters. It is also possible to include a viscoplastic behavior in the decomposition of the strains at the isotropic matrix material. For example, interphase subcells can be added to model the traction separation type damage between fiber and matrix subcells.

Combined environmental effects such as temperature and moisture on the creep response of FRP composites can be implemented using the proposed modeling framework. The limited available test data can be extended to recalibrate the proposed models for long-term behavior (years). The use of temperature to scale the time response enhances the performance of the current models. This was not considered in this study in order to focus on the analytical formulation.

The proposed viscoelastic modeling framework can be extended and applied for other type reinforcement systems such as woven and braided composites by having proper micromechanical equations.

APPENDIX A

VISCOELASTIC MATERIAL MODEL

This appendix deals with fundamental concepts of viscoelastic material. A viscoelastic (time-dependent) material describes a material that exhibit strain-rate effects due to applied load. These materials have elasticity characteristic, which allows them to respond instantaneously under loading, and viscous characteristic, which delays the response. The behaviors of these materials are often described by creep under a constant stress (Figure A.1) and stress relaxation under a constant strain (Figure A.2).

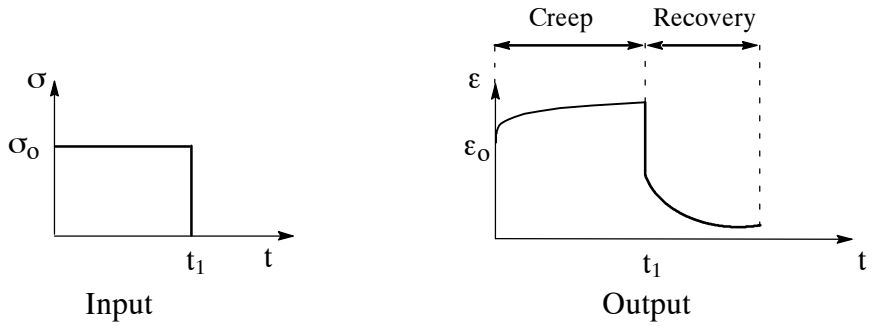

Figure A.1 Creep and recovery response due to a constant stress.

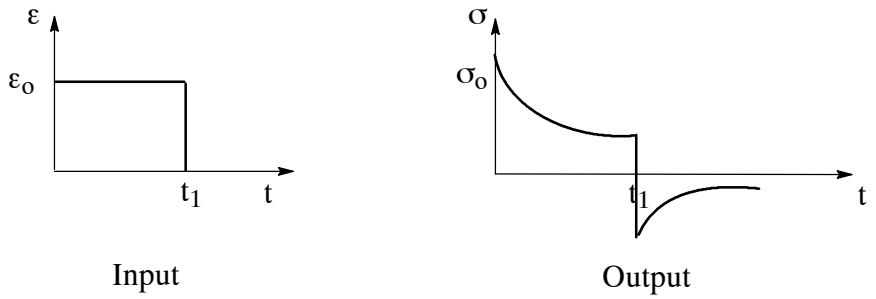

Figure A.2 Relaxation response due to a constant strain.

Creep is a slow continuous deformation of a material under a constant stress (Findley et al., 1976). A constant stress, σ_0, is applied using a step function and is hold for duration of

time t_1, as in Figure A.1. Upon loading, an intantaneous elastic strain, ε_0, is exhibited and the strain increases continuosly until time t_1. When the stress is removed, a full strain recovery will occur in a sufficient time. Creep response can be categorized by three different stages based on its strain rate, as illustrated in Figure A.3. The first stage is a primary creep, in which decreasing strain rate occurs during creep. The second stage is a secondary creep, which proceeds at almost constant strain rate. A tertiary creep occurs when the strain rate increases during creep until failure point is reached.

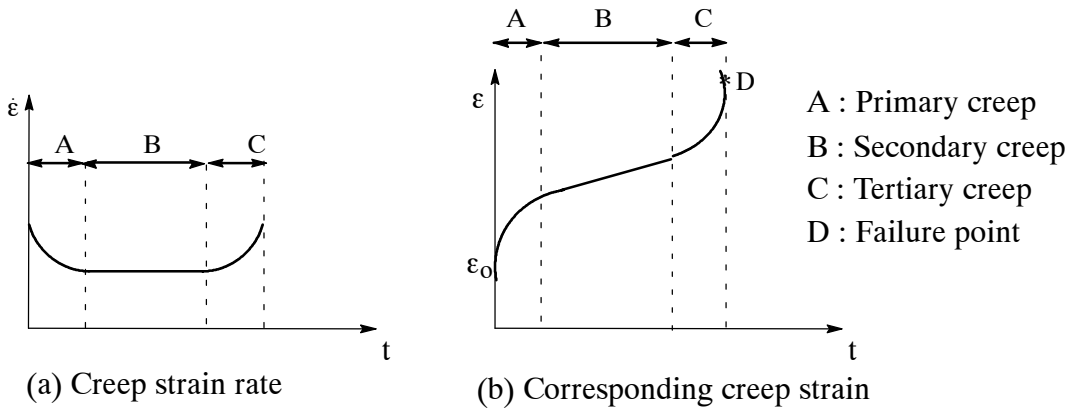

(a) Creep strain rate (b) Corresponding creep strain

Figure A.3 Three differentcreep stages: (a) creep strain rate and (b) corresponding creep strain.

Linear viscoelastic response

A linear viscoelastic response is considered whenever stress is proportional to strain at a certain time and a superposition principle is hold. Consider a response, R, at any time due to an input load, I, and R is a functional of I. The proportionality and superposition conditions are expressed as:

$$R(cI) = cR(I) \quad ; \quad c = \text{constant}$$
$$R(I_1 + I_2) = R(I_1) + R(I_2) \tag{A.1}$$

In a linear viscoelastic model, the stress-strain relation, which is a function of time, is interrelated and permit the construction of one from the other. A time-dependent stress-

strain relation can be represented by a differential or an integral forms. The integral form describes the time-dependent constitutive model more generally, although it may lead to difficulty in solving the integral equation. Boltzmann integral formulation is commonly used to express a linear time-dependent constitutive material model. Consider a time-dependent stress input $\sigma(t)$, illustrated in Figure A.4, which is approximated by the sum of a series of constant stress inputs, as:

$$\sigma(t) = \sum_{i=0}^{s} \Delta\sigma_i \, H(t - \xi_i) \tag{A.2}$$

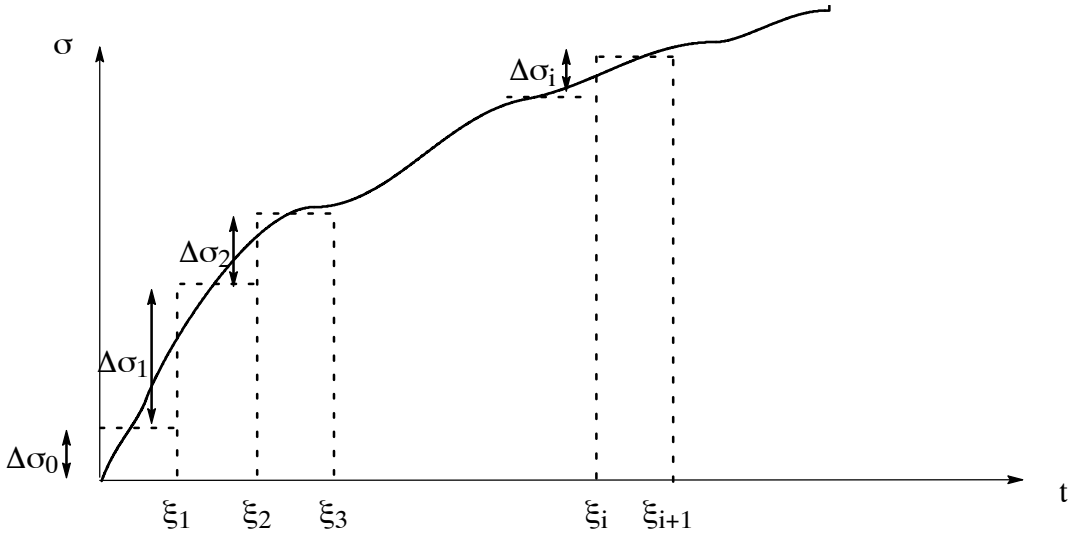

Figure A.4 Stress variable as sum of a series of constant stress inputs.

According to Boltzman superposition principle, the sum of the strain outputs resulting from each component of stress input is the same as the strain output resulting from the sum of stress input. The strain output due to stress variable $\sigma(t)$ is:

$$\begin{aligned} \varepsilon(t) &= \sum_{i=0}^{s} \varepsilon_i \, (t - \xi_i) \\ &= \sum_{i=0}^{s} \Delta\sigma_i \; D(t - \xi_i) \; H(t - \xi_i) \end{aligned} \tag{A.3}$$

where $D(t - \xi_i)$ is the creep compliance, $H(t - \xi_i)$ is the Heaviside function, and ξ_i is the time when a step load is applied. In the case of the step number goes to infinity, stress history is differentiable at ξ_i, and ξ is always less than or equal to t, then Eq. (A.3) can be expressed as:

$$\varepsilon(t) = \int_0^t D(t - \xi) \frac{\partial \sigma(\xi)}{\partial \xi} \partial \xi \tag{A.4}$$

Equation (A.4) is a single integral model of creep, which can be used to predict creep strain under a given stress history and creep compliance. The creep compliance can be separated into an elastic (time-independent) compliance, D_0, and a transient (time-dependent) compliance, $\Delta D(t)$. Thus the strain response in Eq. (A.4) becomes:

$$\varepsilon(t) = D_0 \sigma(t) + \int_0^t \Delta D(t - \xi) \frac{\partial \sigma(\xi)}{\partial \xi} \partial \xi \tag{A.5}$$

If the input strain variable $\varepsilon(t)$ is applied, the stress relaxation also can be formulated using Boltzmann superposition principle as:

$$\sigma(t) = \int_0^t E(t - \xi) \frac{\partial \varepsilon(\xi)}{\partial \xi} \partial \xi \tag{A.6}$$

The relaxation modulus E(t) can be separated into an elastic modulus, E_0, and time dependent modulus $\Delta E(t)$, which allows for the stress relaxation in Eq. (A.6) to be expressed by:

$$\sigma(t) = E_0 \sigma(t) - \int_0^t \Delta E(t - \xi) \frac{\partial \varepsilon(\xi)}{\partial \xi} \partial \xi \tag{A.7}$$

Differential forms have been widely used to express the rate-dependent constitutive material model. The time-dependent constitutive equation can be determined based upon the representative mechanical model, which consists of combinations of linear spring and dashpot. Stress-strain relation is then formulated as a linear function of stress, strain and their

derivatives. Figure A.5(a) represents a linear spring and a linear dashpot connected in series (Maxwell model). Stress σ and strain ε are time dependent and the dot represents the time derivation. The viscoelastic response from the Maxwell model is obtained by solving the following equation:

$$\dot{\varepsilon} = \frac{\dot{\sigma}}{E} + \frac{\sigma}{\eta} \tag{A.8}$$

This model describes the stress relaxation under a constant strain. Maxwell model does not show a time-dependent recovery and a decreasing strain rate under constant stress at primary creep, instead it represents a permanent strain which does not disappear.

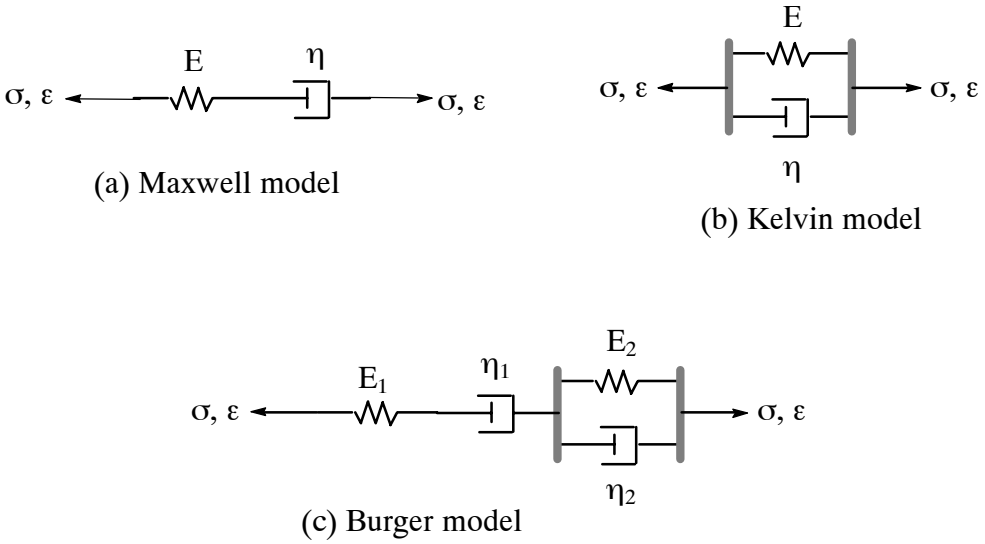

Figure A.5 Viscoelastic mechanical models.

Another mechanical model is Kelvin model, shown in Figure A.5(b), which consists of spring and dasphot connected in parallel. The stress-strain relation is expressed by:

$$\dot{\varepsilon} + \frac{E}{\eta}\,\varepsilon = \frac{\sigma}{\eta} \tag{A.9}$$

Kelvin model describes creep response under constant stress, but it does not show time-dependent relaxation nor exhibit an instantaneous strain due to loading and unloading.

Burger model, illustrated in Figure A.5(c), combines Maxwell and Kelvin models in series. The stress-strain relation for the Burger model is:

$$\sigma + \left(\frac{\eta_1}{E_1} + \frac{\eta_1}{E_E} + \frac{\eta_2}{E_2}\right)\dot{\sigma} + \frac{\eta_1 \eta_2}{E_1 E_2}\ddot{\sigma} = \eta_1 \dot{\varepsilon} + \frac{\eta_1 \eta_2}{E_2}\ddot{\varepsilon} \qquad \text{(A.10)}$$

Creep response of the Burger model is the sum of the creep responses from Maxwell and Kelvin models. Thus the creep-recovery response can be well described. The stress relaxation can also be obtained using this model.

Nonlinear viscoelastic response

A nonlinear viscoelastic material is considered whenever proportionality and/or superposition conditions are violated. There are two types of nonlinear viscoelastic behavior, reversible and irreversible nonlinearities. In reversible nonlinearity, full recovery of the specimen after loading is gained by allowing it to rest for sufficient period of time. The material will have the same properties as it has before any loading; there is no permanent strain in the material; and the effects of previous loading are faded away. This nonlinearity is due to high stress dependent viscosity (mainly in amorphous polymer), fatigue loading, increase in temperature during loading, and environmental effects such as elevated temperatures and high moisture. While the source of irreversible nonlinearity is microstructural changes in the material; such as existence of damage, crack growth, and high stress concentration.

The nonlinear viscoelastic constitutive model for the reversible nonlinearity (fading memory) can be obtained from either a single-integral or a multiple integral formulations. The single integral representation has been derived using the thermodynamic of irreversible process (Biot 1954, Coleman 1964, Coleman and Gurtin 1967, and Schapery 1969) and finite elasticity theory (Coleman and Noll 1961). In this equation, there are additional time-independent material constants that carry the sources of nonlinearity. The multiple integral formulation is an extension of linear superposition to the nonlinear range. The time-dependent strain output, $\varepsilon_i(t)$, resulting from a constant stress input, $\Delta\sigma_i$, is represented by polyno-

mial function of $\Delta\sigma_i$. The strain, as in Eq. (A.3), is composed of the sum of all terms and also their products to account for nonlinearity. At an arbitrary stress function and infinite number of steps the multiple integrals are formulated.

Characterization of viscoelastic parameters of the Schapery single integral model

Linear and nonlinear viscoelastic material parameters in the Schapery single integral equation for an isotropic material are characterized from a set of creep-recovery test under various load levels (Schapery, 1969). Consider two step uniaxial creep loadings:

$$\sigma = \begin{cases} \sigma_a, & 0 < t < t_a \\ \sigma_b, & t_a < t < t_b \end{cases} \tag{A.11}$$

The creep responses due to the two step loading are determined by substituting Eq. (A.11) into the creep strain model in Eq. (2.28) as:

$$\varepsilon(t) = \left[g_0^{\sigma_a} D_0 + g_1^{\sigma_a} g_2^{\sigma_a} \Delta D\left(\frac{t}{a_\sigma^{\sigma_a}}\right) \right] \sigma_a \qquad , \quad 0 < t < t_a \tag{A.12}$$

$$\varepsilon(t) = g_0^{\sigma_b} D_0 \sigma_b + g_1^{\sigma_b} \left[g_2^{\sigma_a} \sigma_a \Delta D\left(\frac{t_a}{a_\sigma^{\sigma_a}} + \frac{t - t_a}{a_\sigma^{\sigma_b}}\right) + \Delta D\left(\frac{t - t_a}{a_\sigma^{\sigma_b}}\right)\left(g_2^{\sigma_b}\sigma_b - g_2^{\sigma_a}\sigma_a\right) \right] \quad , \quad t > t_a \tag{A.13}$$

Next, creep-recovery test is simulated by taking $\sigma_a = \sigma_o$ and $\sigma_b = 0$. In this case, all nonlinear parameters will depend only on the applied load σ_o, since the nonlinear parameters at load removal is unity. Thus Eqs. (A.12) and (A.13) become:

$$\varepsilon_{creep}(t) = \left[g_0 D_0 + g_1 g_2 \Delta D\left(\frac{t}{a_\sigma}\right) \right] \sigma_o \qquad , \quad 0 < t < t_a \tag{A.14}$$

$$\varepsilon_{rec}(t) = g_2 \sigma_o \left[\Delta D\left(\frac{t_a}{a_\sigma} + t - t_a\right) - \Delta D(t - t_a) \right] \qquad , \quad t > t_a \tag{A.15}$$

The material parameters in the Schapery equations can be characterized by fitting the above equations into linear and nonlinear creep-recovery responses. The time-dependent

compliance ΔD is commonly modeled using a power law (Findley et al., 1976) or Prony series (exponential function) and can be characterized by fitting these equations to a linear creep response ($g_0 = g_1 = g_2 = a_\sigma = 1$). The stress-dependent parameters are then determined from the nonlinear creep-recovery response. The parameter g_0, which is the nonlinear instantaneous elastic compliance, is measured by comparing the instantaneous compliance for the linear case with the instantaneous compliance for the nonlinear case, $\varepsilon(0) = \varepsilon_0$, under the applied stress σ_o:

$$g_0 = \frac{\varepsilon_0}{D_0 \sigma_o} \tag{A.16}$$

The parameter g_1 can be performed from creep data by measuring the ratio of transient strain accumulated during the nonlinear creep and the transient strain under linear condition:

$$g_1 = \frac{\varepsilon(t_a) - \varepsilon_0}{\Delta D(t_a) \sigma_o} \tag{A.17}$$

It should be noted that under a linear transient creep the strain drop due to unloading at time t_a is similar to the instantaneous strain due to loading. Once, the parameter g_1 is known, the parameter g_2, which is corresponding to the loading rate, can be determined using curve fitting on nonlinear creep response. While the nonlinear parameter a_σ is calculated numerically using curve fitting from nonlinear recovery data or can be produced from horizontally shifting the nonlinear creep response.

Temperature, moisture, and aging effects on creep responses

Environmental effects such as temperatures and moisture contents and physical aging can affect creep behaviors of the material. Thus, creep compliance and relaxation modulus are modeled to account for temperature, T, moisture, H, and aging effects. For a thermorheologically simple material, eg: amorphous polymer, the combined time and environmental effects on creep and relaxation responses can be made through a single parameter (reduced time), similar to Eq. (2.29):

$$\psi(t) = \int_0^t \frac{d\xi}{a_T\,[T(\xi)]\;\; a_H\,[H(\xi)]\;\; a_e[t_e(\xi)]} \tag{A.18}$$

where ψ is the reduced time, t is the actual time measured from the beginning of creep or relaxation test, T is the current temperature, H is the moisture content, t_e is the aging time, and a_T, a_H, and a_e are the temperature, moisture and aging shift factors, respectively. If the environmental conditions are constant during the loading, then Eq. (A.18) is simplified to:

$$\psi = \frac{t}{a_T(T)\; a_H(H)\; a_e(t_e)} \tag{A.19}$$

Thus, for a thermorheologically simple material, it is possible to produce the modulus or compliance at different temperature, moisture, or aging conditions by shifting the time-dependent modulus or compliance, in a logarithmic scale, at the reference state using their shift factors, which is described as:

$$E\,(t, T) = E\,(\psi, T^0) \qquad E\,(t, H) = E\,(\psi, H^0) \qquad E\,(t, t_{e)} = E\,(\psi, t_e^0) \tag{A.20}$$

where the superscript 0 indicates the reference state. This concept is known as time-temperature superposition principle (TTSP). Since certain environmental conditions, such as elevated temperature, accelerate the creep deformation in a viscoelastic material, TTSP can be used to predict long-term time-dependent material response from series of short-term data under different temperature range (Brinson et al. 1978, Yeow et al. 1979, and Hiel et al. 1983). Figure A.6 shows short-term time-dependent modulus at several temperatures. A master curve, which represents a long-term time-dependent compliance or modulus, at the reference temperature T_3 is constructed by horizontally shifting the moduli at different temperatures to create a constinuous curve. The amount of each modulus is shifted is determined by the shift factor.

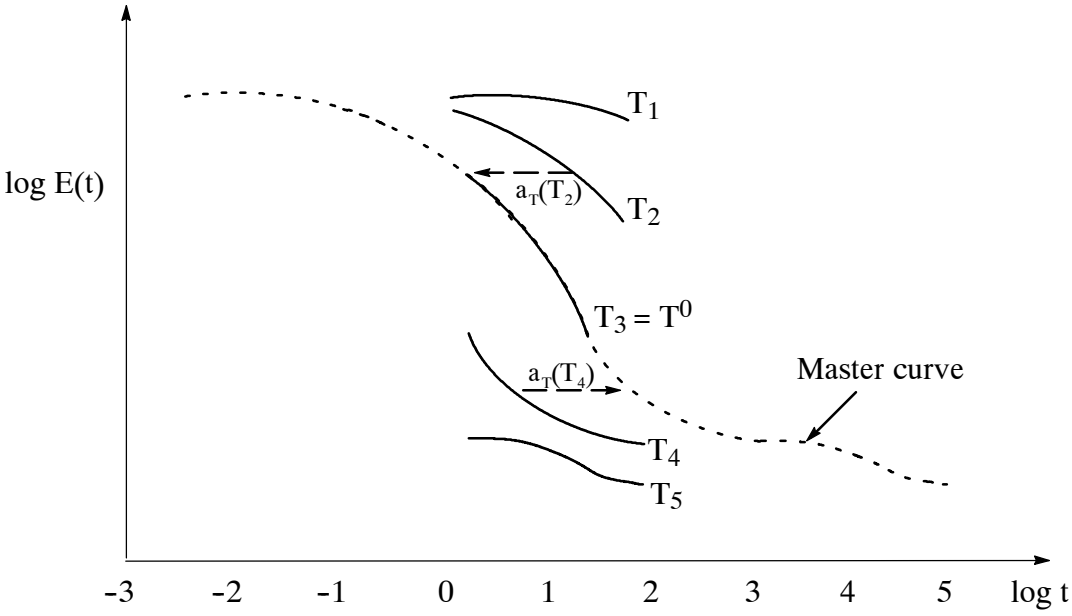

Figure A.6 Time-dependent modulus master curve at the reference temperature T_3.

APPENDIX B

EXPERIMENTAL CREEP DATA

This appendix consists of creep test data for the unnotched and notched off-axis pultruded coupons. Tables of the test coupons are first presented and followed by plots of the strains. The strain data is read from axial gages attached at the same location on both front and back surfaces of each specimen.

B.1 Creep Compression Tests for E-glass/vinylester Off-axis Coupons

Tabel B.1. Creep compression tests with different off-axis E-glass/vinylester specimens subjected to various loads.

Cx − y − z ≡ off-axis angle - coupon number - loading fraction of ultimate

Specimens	Creep test	
	σ_o (ksi)	F_o (kips)
C0-1-0.1	4.08	2.5
C0-2-0.2	8.23	5.0
C0-3-0.4	16.13	10.0
C0-4-0.4	16.40	10.0
C0-5-0.6	24.39	15.0
C45-1-0.1	2.44	1.5
C45-2-0.2	4.85	3.0
C45-3-0.4	9.76	6.15
C45-4-0.6	14.94	9.3
C45-5-0.1	2.42	1.5
C45-6-0.2	4.88	3.0
C45-7-0.4	9.88	6.15
C45-8-0.6	15.04	9.25
C90-1-0.1	2.40	1.5
C90-2-0.2	4.85	3.0
C90-3-0.4	9.64	6.0
C90-4-0.6	14.46	9.0

Specimens	Creep test	
	σ_o (ksi)	F_o (kips)
C30-1-0.1	2.49	1.5
C30-2-0.2	5.04	3.0
C30-3-0.4	9.98	6.15
C30-4-0.6	14.98	9.25
C30-5-0.2	2.49	1.5
C30-5-0.1	4.99	3.0
C30-5-0.4	10.25	6.15
C30-5-0.6	15.22	9.25
C60-1-0.1	2.47	1.5
C60-2-0.2	4.93	3.0
C60-3-0.4	9.99	6.1
C60-4-0.6	14.99	9.24
C60-5-0.1	2.49	1.5
C60-5-0.2	4.90	3.0
C60-5-0.4	9.96	6.1
C60-5-0.6	15.08	9.24

Axial strain results

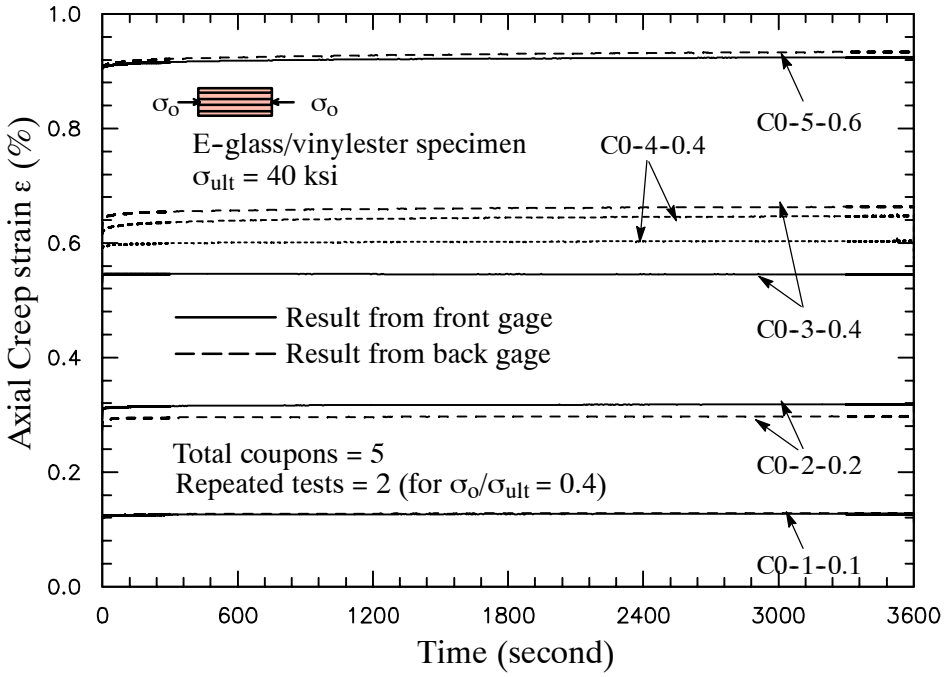

Figure B.1 Axial compression for uniaxial coupons.

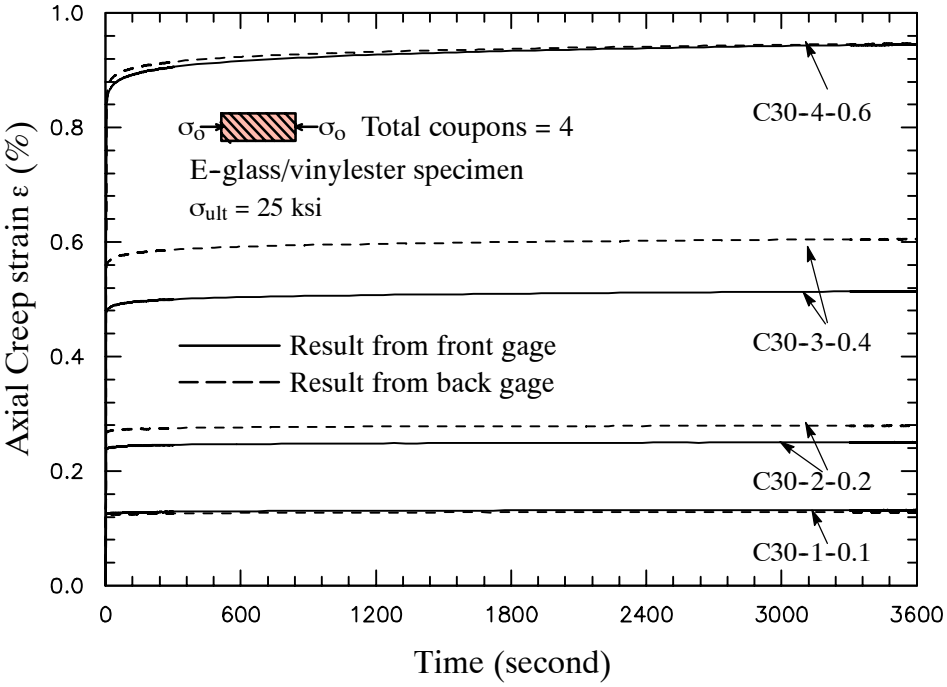

Figure B.2 Axial compression strain for 30° off axis coupons.

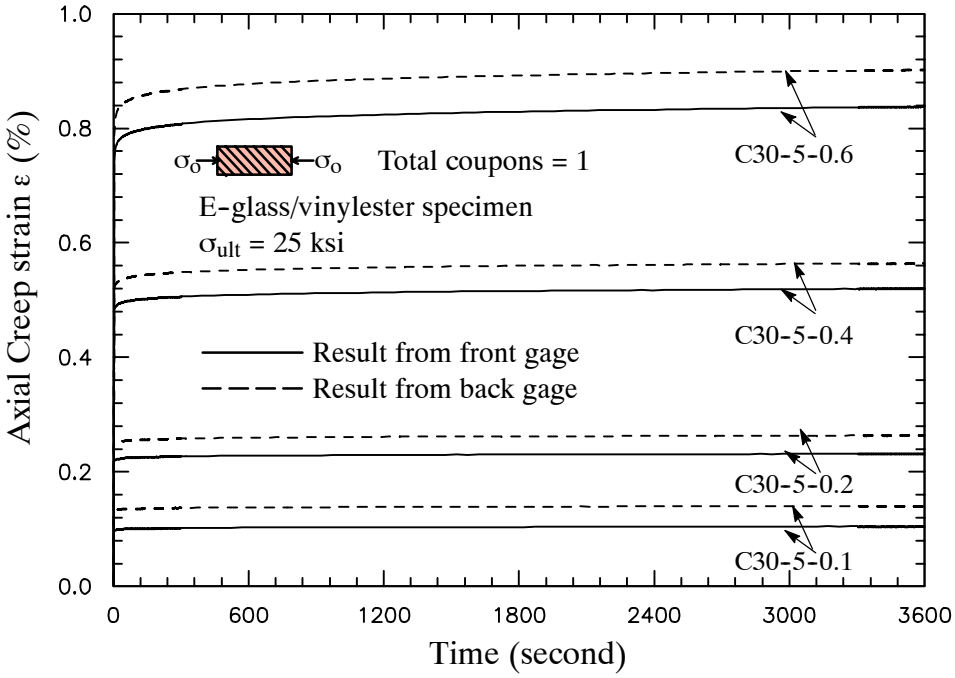

Figure B.3 Axial compression strain for 30° off axis coupons.

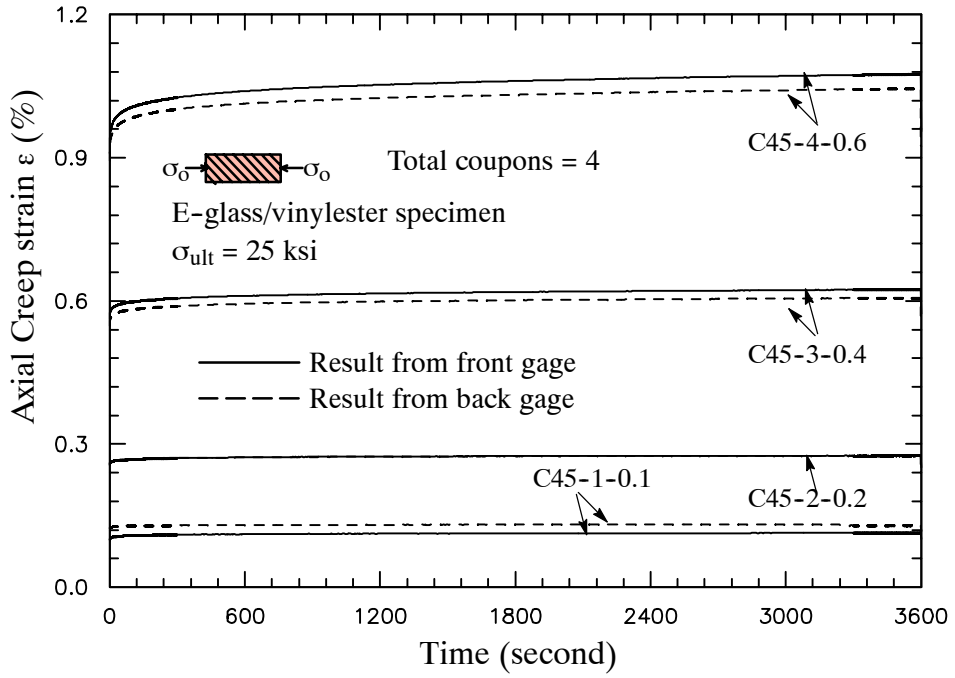

Figure B.4 Axial compression strain for 45° off axis coupons.

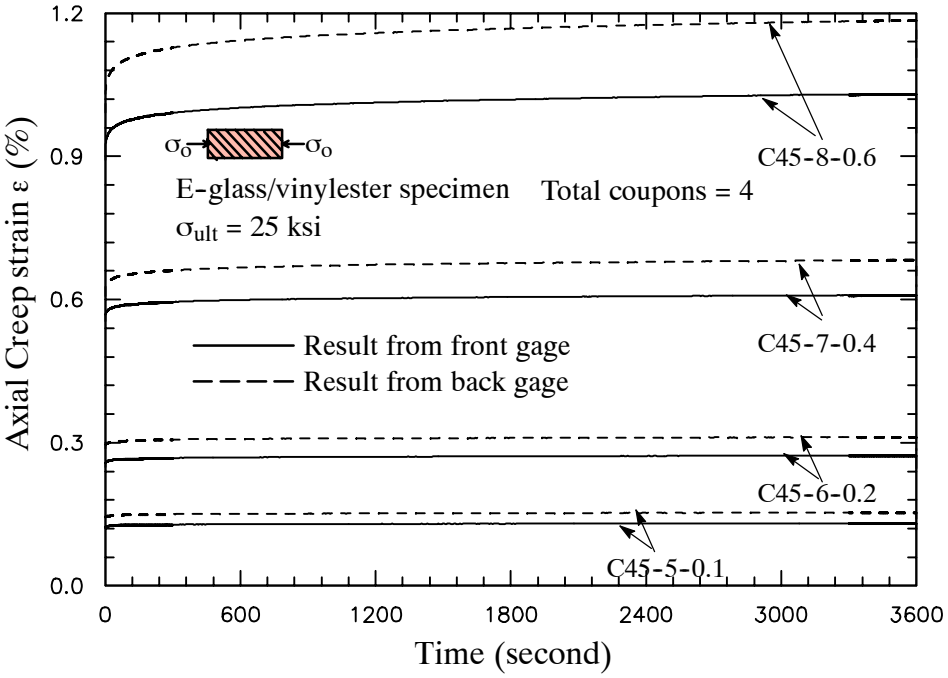

Figure B.5 Axial compression strain for 45° off axis coupons.

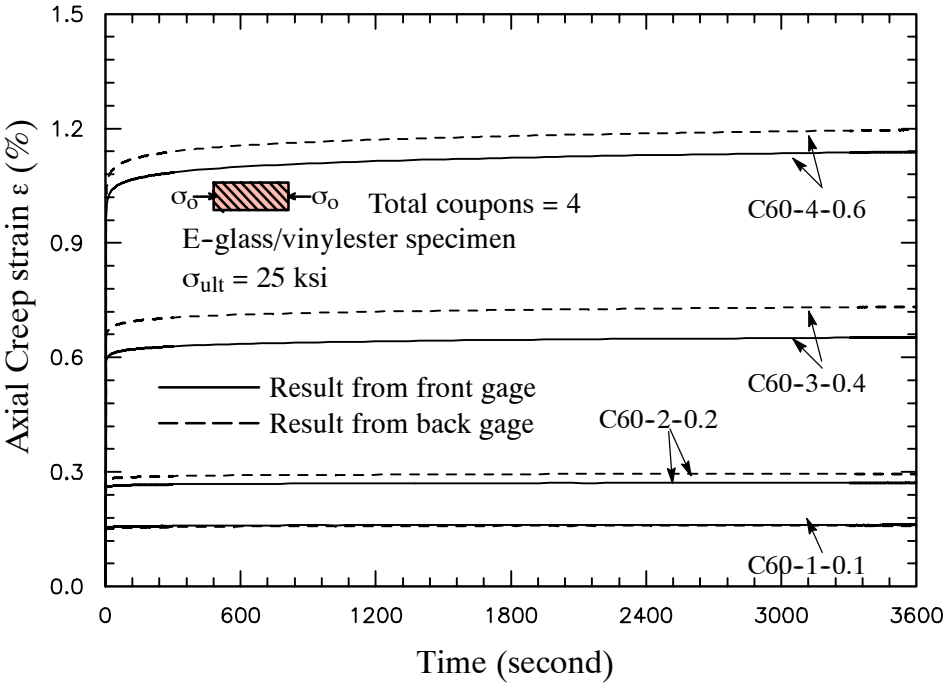

Figure B.6 Axial compression strain for 60° off axis coupons.

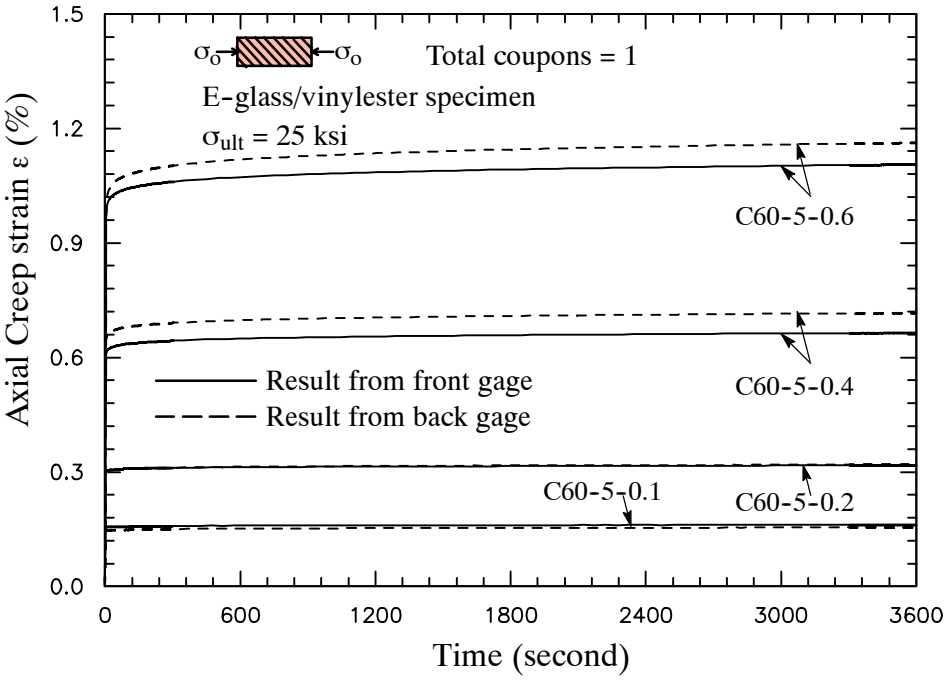

Figure B.7 Axial compression strain for 60° off axis coupons.

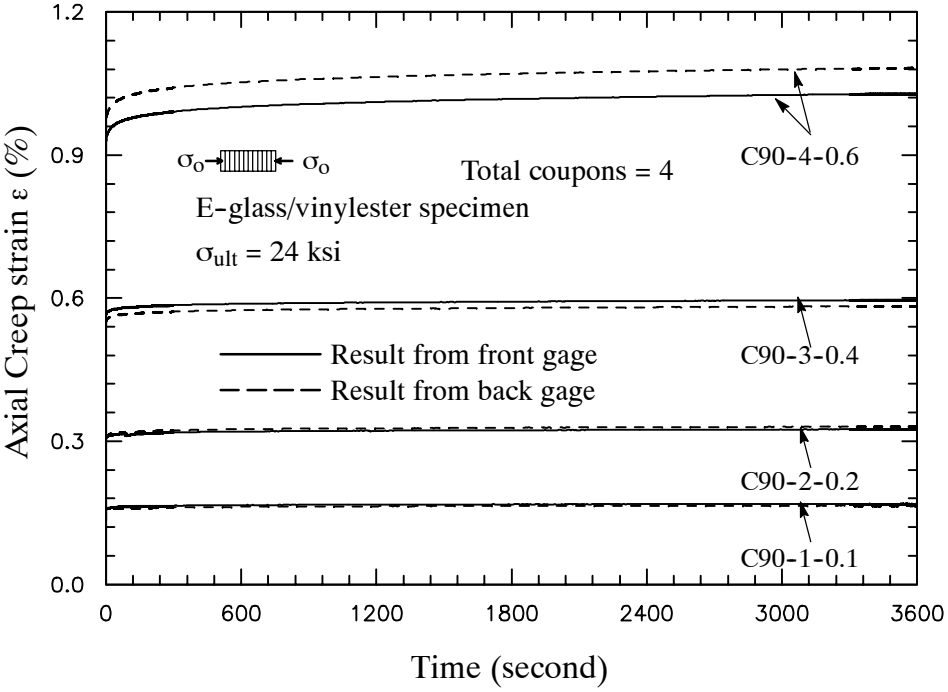

Figure B.8 Axial compression strain for transverse coupons.

Transverse strain results

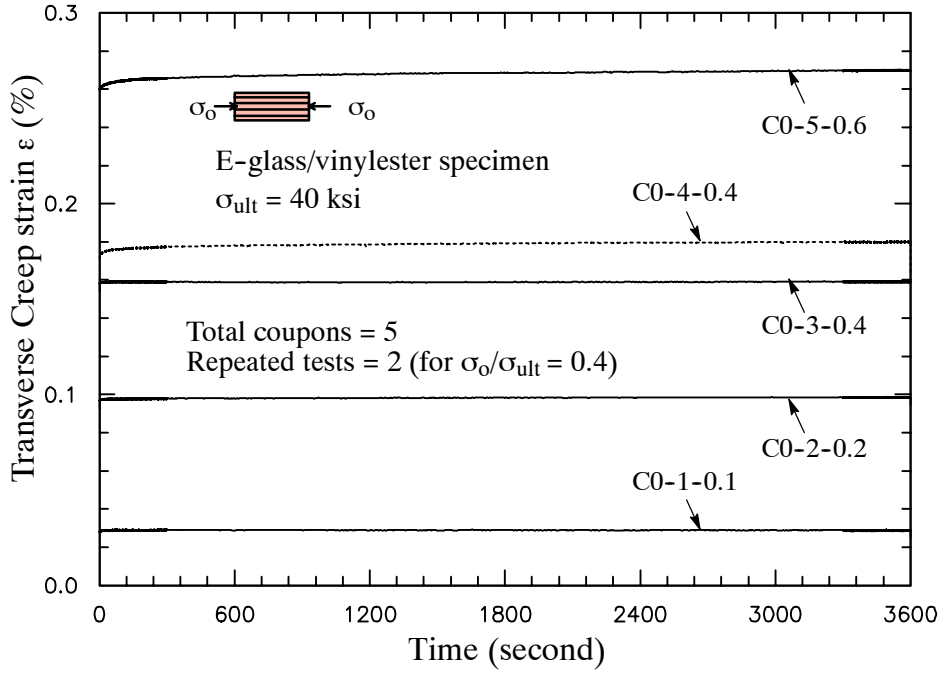

Figure B.9 Transverse compression strain for uniaxial coupons.

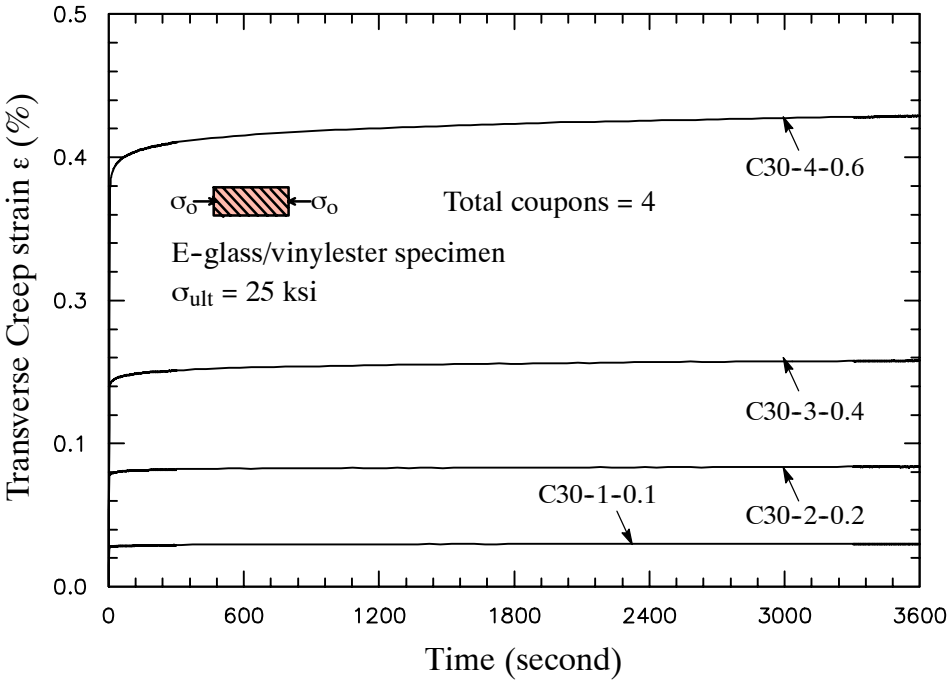

Figure B.10 Transverse compression strain for 30^{o} off aixs coupons.

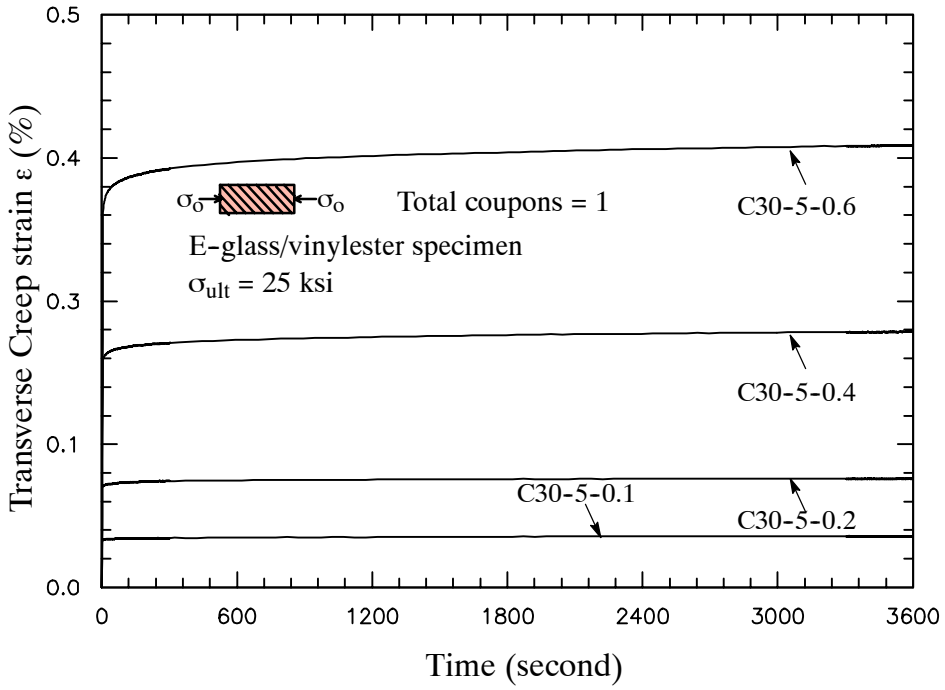

Figure B.11 Transverse compression strain for 30^{o} off aixs coupons.

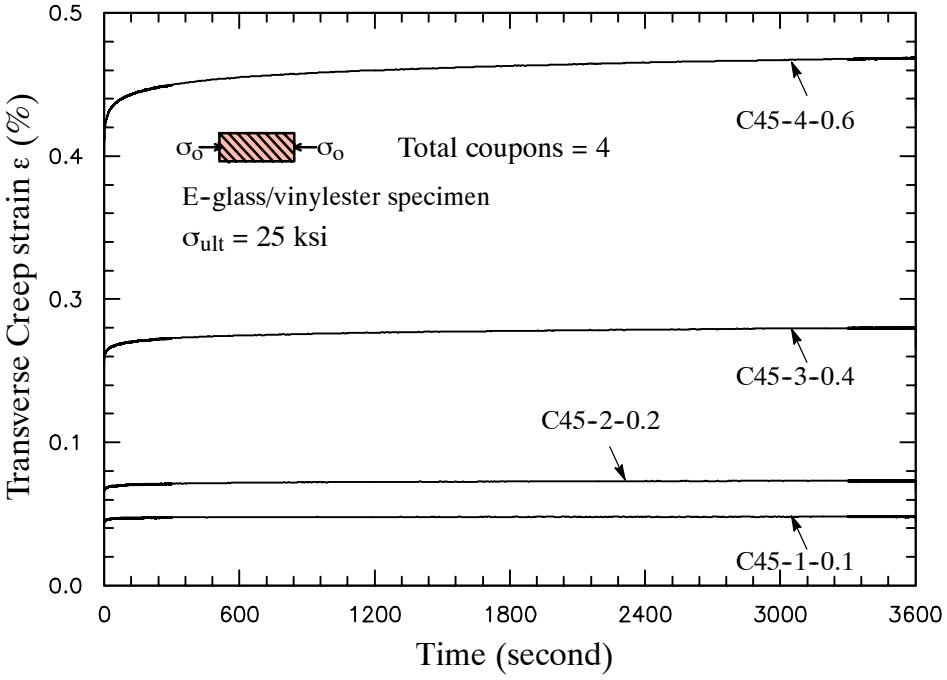

Figure B.12 Transverse compression strain for 45^{o} off aixs coupons.

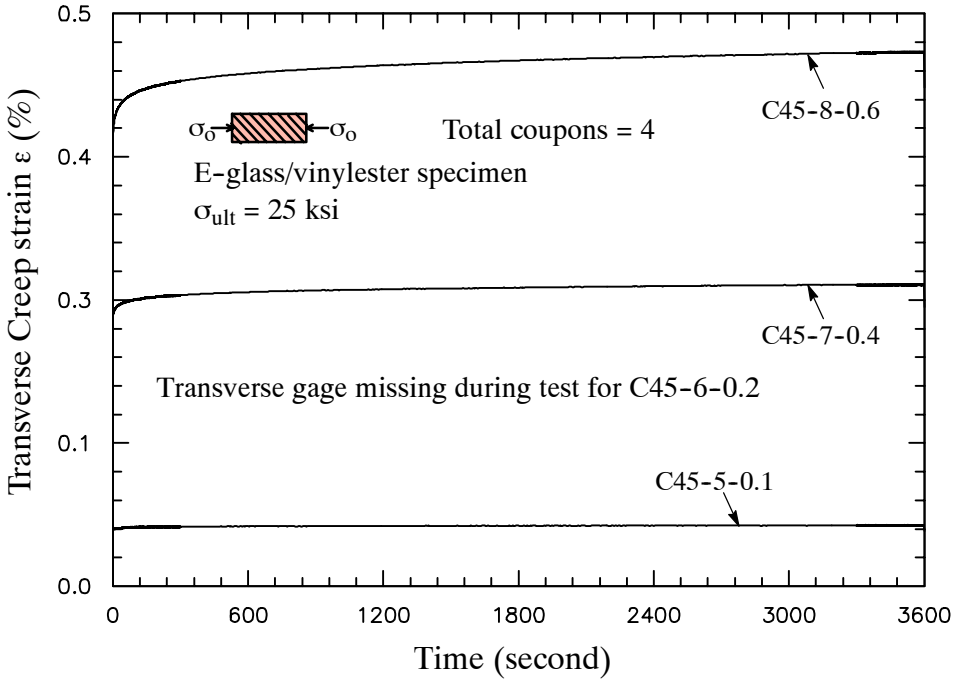

Figure B.13 Transverse compression strain for 45° off aixs coupons.

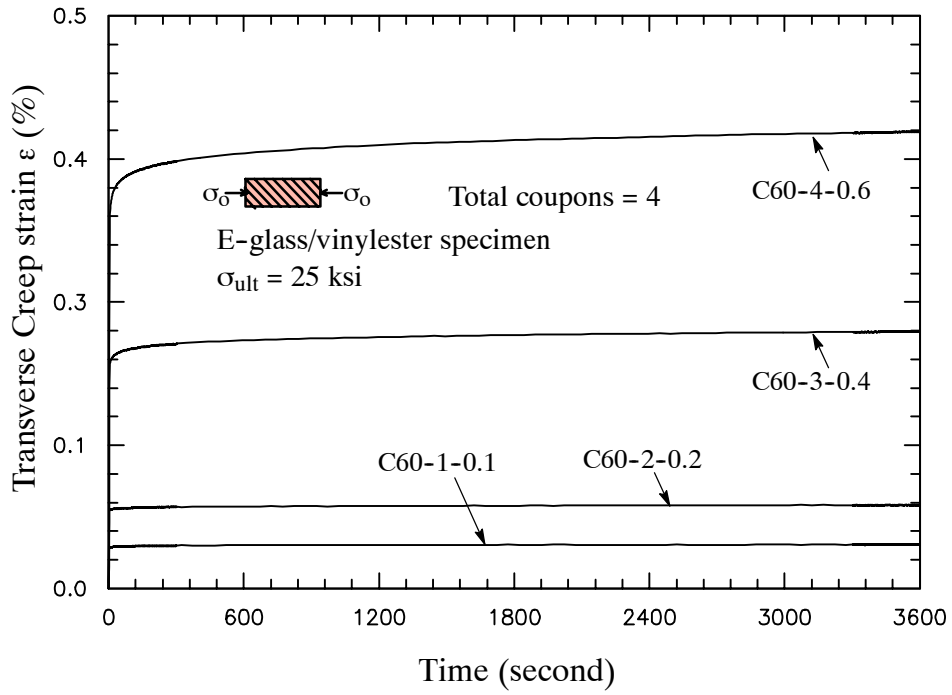

Figure B.14 Transverse compression strain for 60° off aixs coupons.

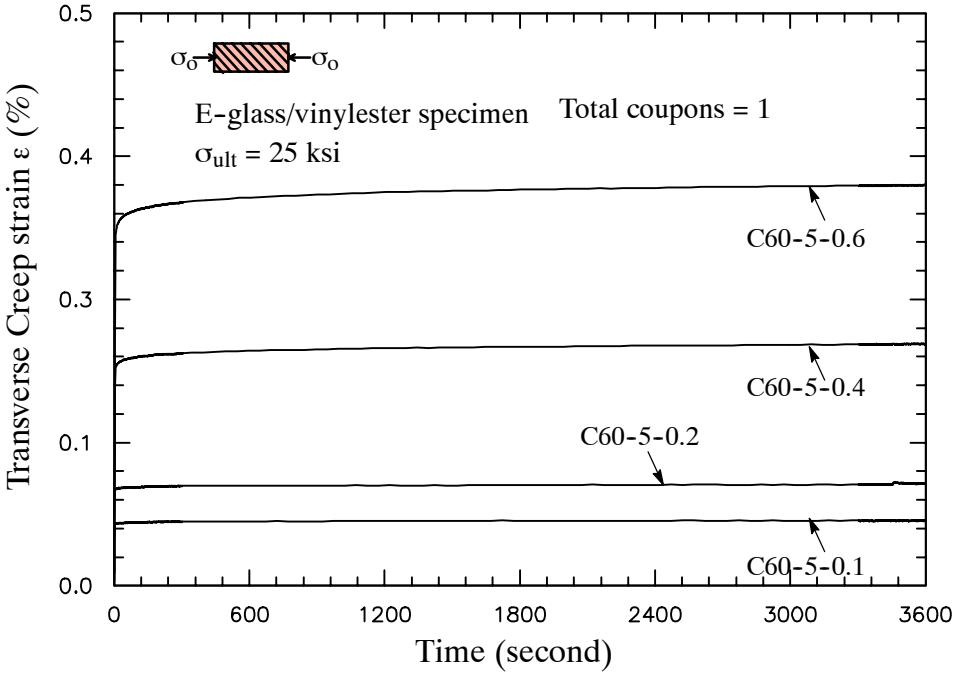

Figure B.15 Transverse compression strain for 60° off aixs coupons.

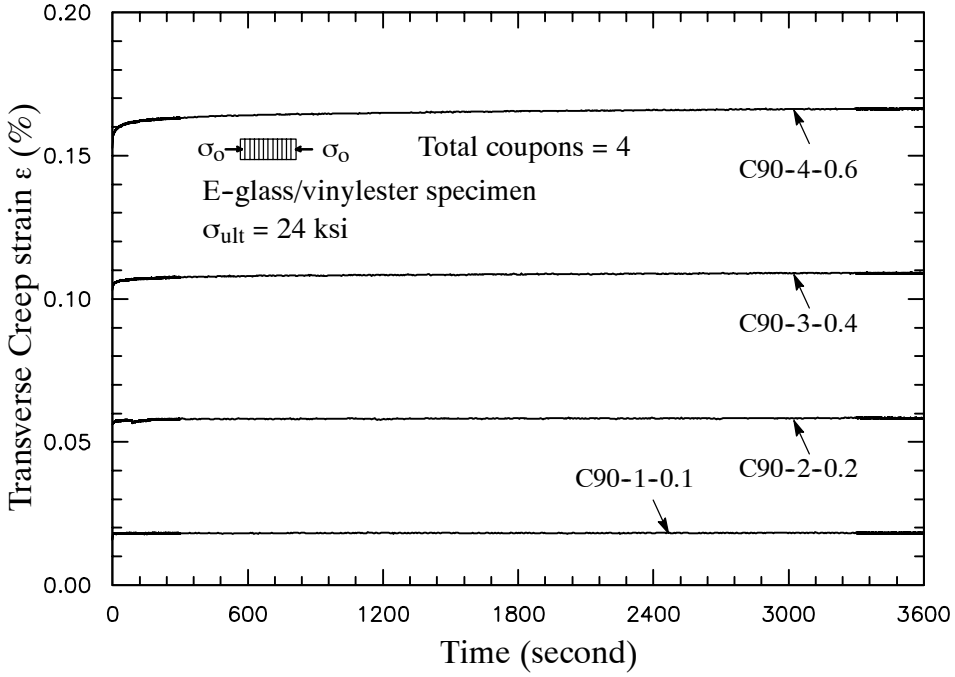

Figure B.16 Transverse compression strain for transverse coupons.

B.2 Creep Tension Tests for E-glass/polyester Off-axis Coupons

Tabel B.2 Creep tension tests with different off-axis E-glass/polyester specimens subjected to various fractions of their ultimate load.

Tx − y − z ≡ off-axis angle - coupon number - loading fraction of ultimate

Specimens	Creep test			
	σ_o (ksi)	F_o (kips)	Temp(^{o}C)	Humidity (%)
T0-1-0.1	2.68	1.6	20.4	34
T0-1-0.2	5.36	3.2	22.2	37
T0-1-0.4	10.71	6.4	23.3	31
T0-1-0.6	16.07	9.6	22.3	32
T45-1-0.1	1.29	0.75	20.0	34
T45-1-0.2	2.57	1.5	21.9	34
T45-1-0.4	5.14	3.0	21.0	34
T45-1-0.6	7.72	4.5	22.3	39
T60-1-0.1	1.40	0.83	21.9	35
T60-1-0.2	2.80	1.66	22.0	35
T60-1-0.4	5.60	3.32	22.7	39
T60-1-0.6	8.43	5.0	22.5	31
T90-1-0.1	1.18	0.75	19.3	33
T90-1-0.2	2.35	1.5	21.4	34
T90-1-0.4	4.71	3.0	23.1	31
T90-1-0.6	7.06	4.5	22.8	32

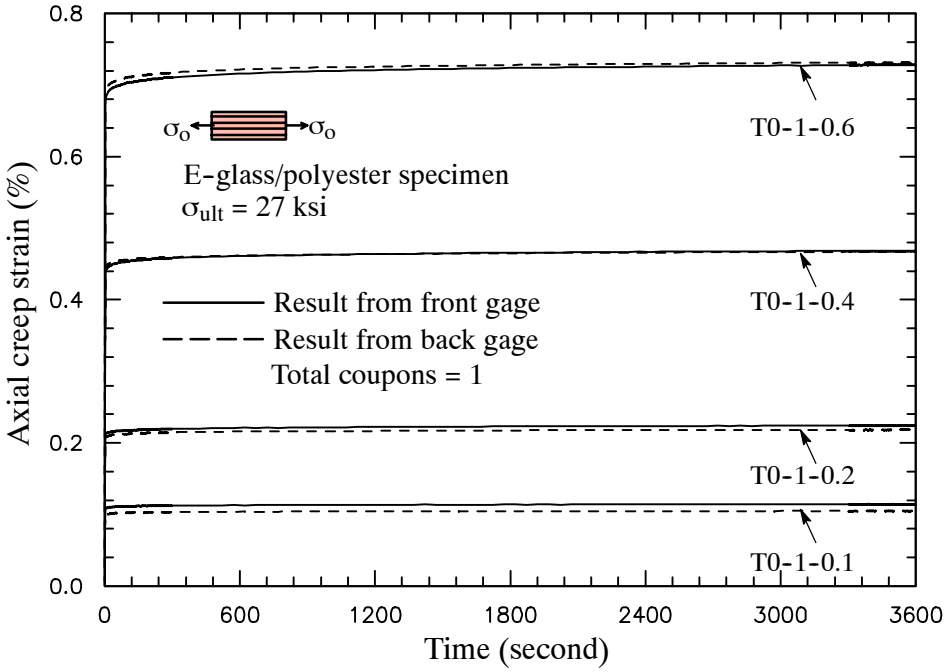

Figure B.17 Axial tension for uniaxial coupons.

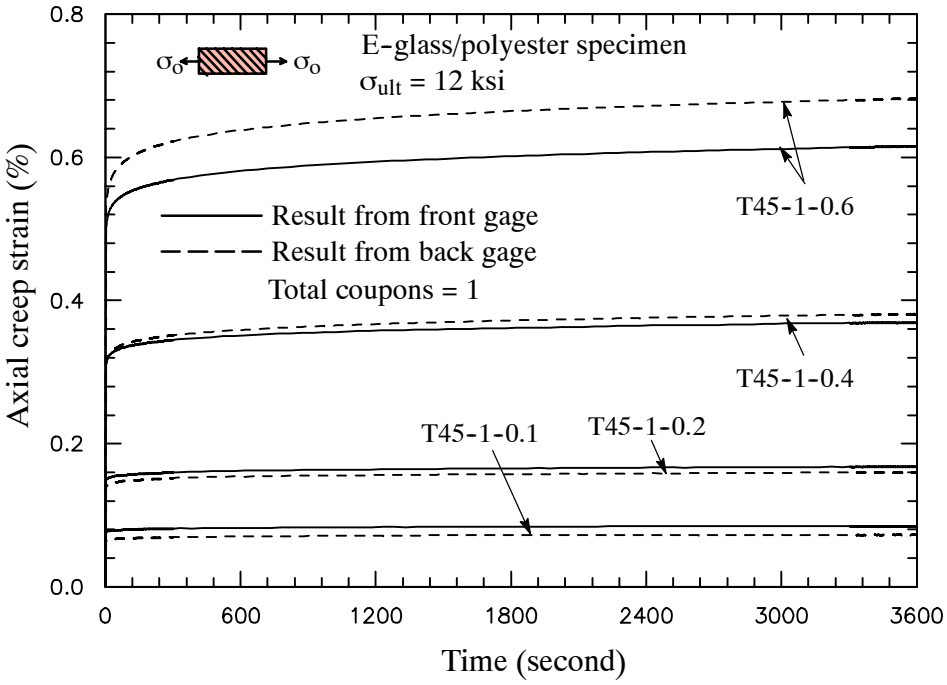

Figure B.18 Axial tension for 45° off-axis coupons.

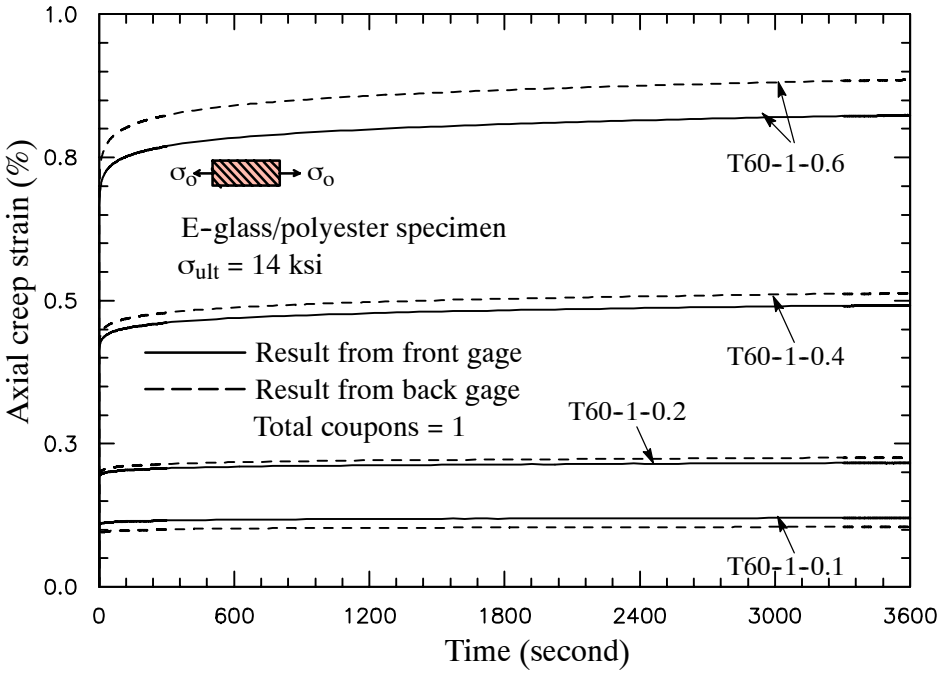

Figure B.19 Axial tension for 60° off-axis coupons.

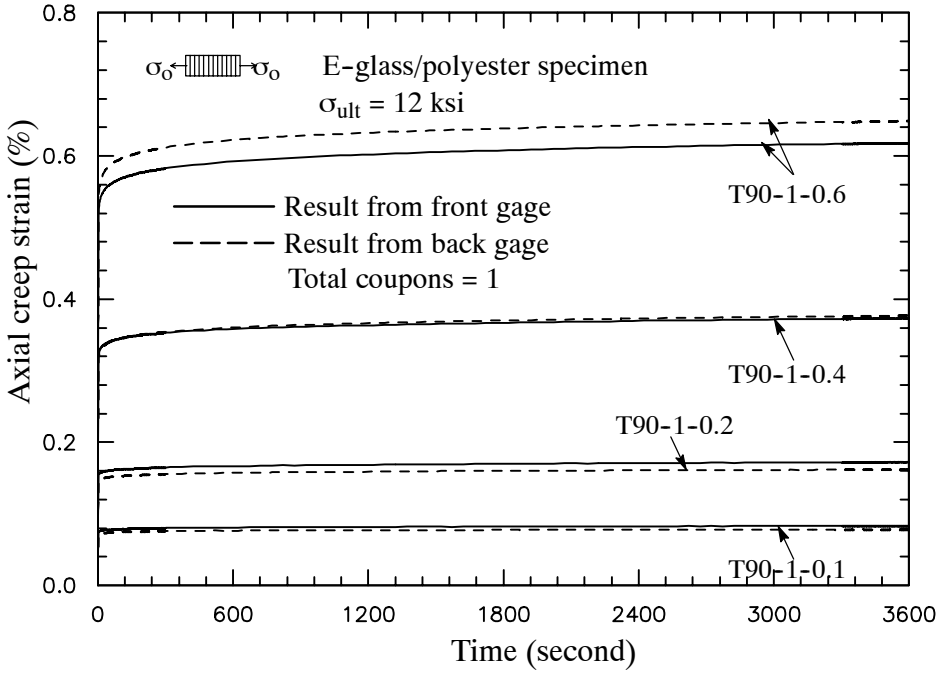

Figure B.20 Axial tension for 90° off-axis coupons.

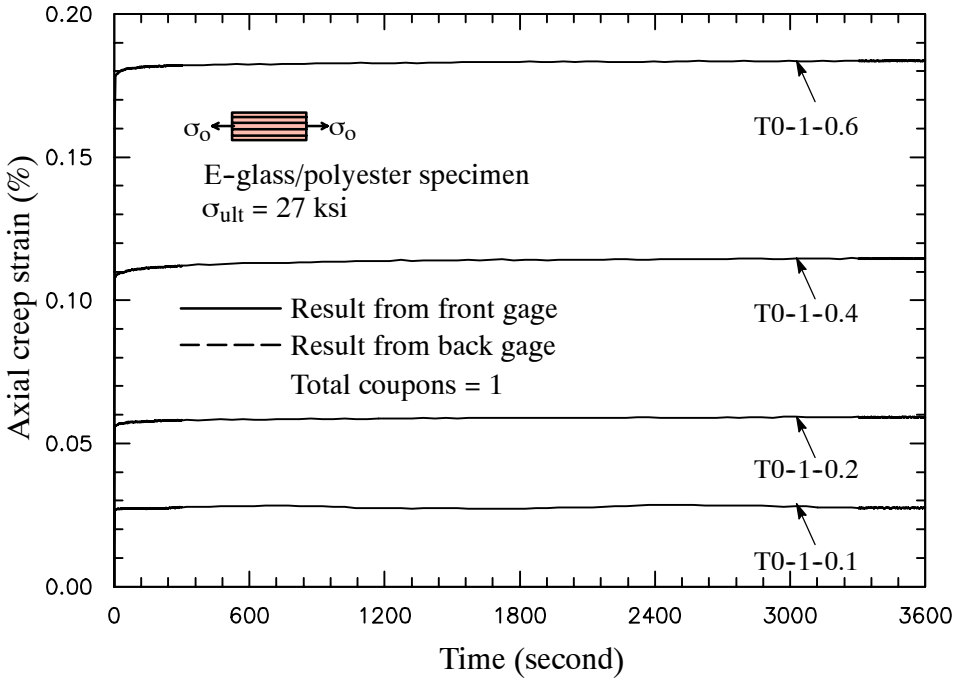

Figure B.21 Transverse tension for uniaxial coupons.

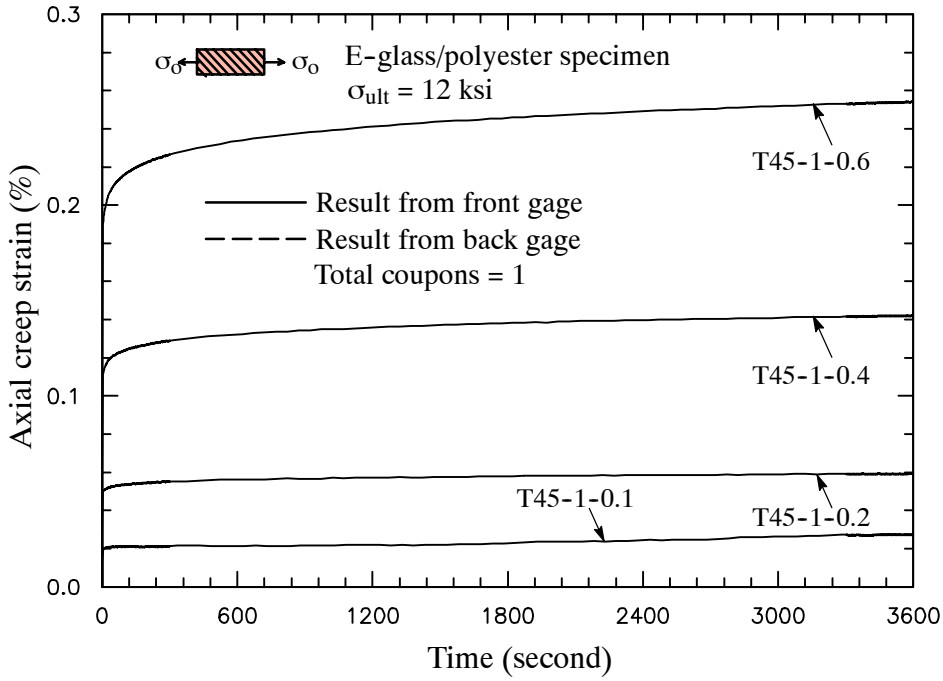

Figure B.22 Transverse tension for 45° off-axis coupons.

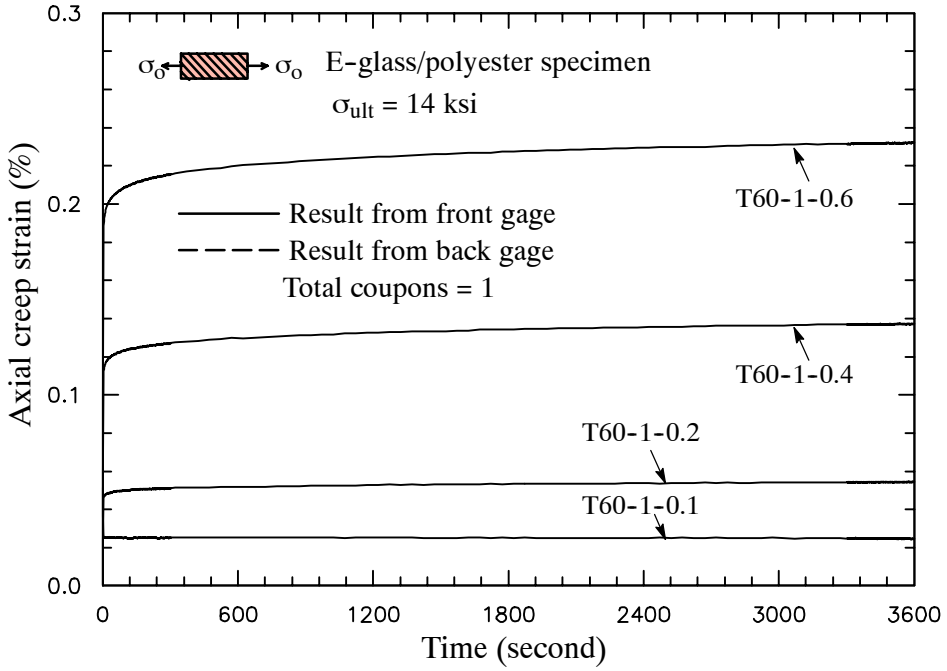

Figure B.23 Transverse tension for 60° off-axis coupons.

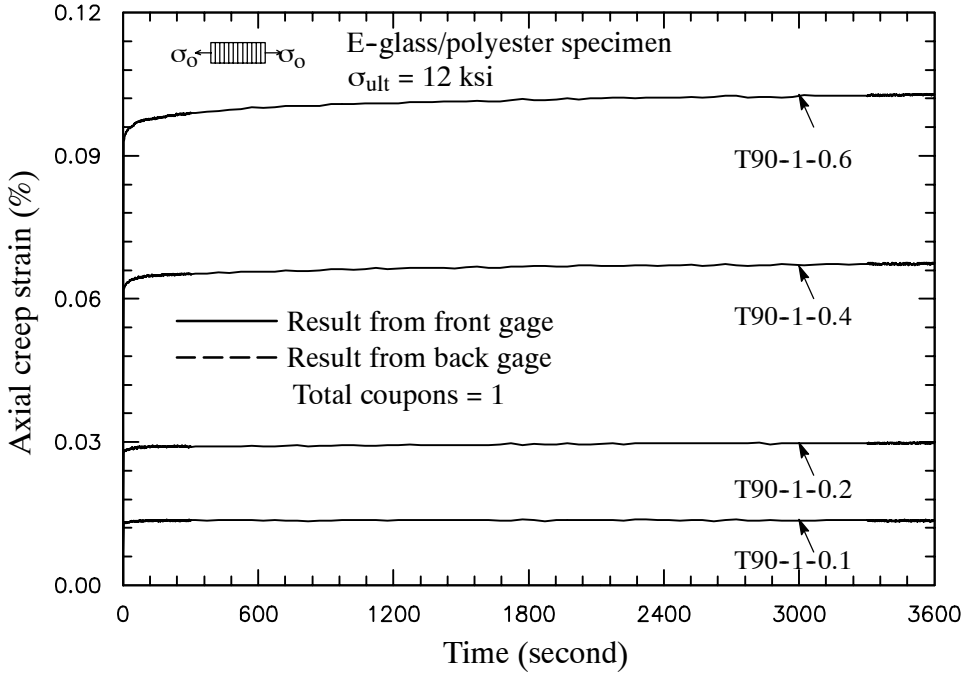

Figure B.24 Transverse tension for 90° off-axis coupons.

B.3 Creep Compression Tests for E-glass/vinylester Off-axis Notched-Coupons

Table B.3 Creep test for notched-plate specimens under compression load.

CS − x − y − z ≡ off-axis angle - coupon number - loading fraction of ultimate

θ	Test	σ_o (ksi)
90°	CS-90°-h1-0.1	1.22
	CS-90°-h1-0.2	2.44
	CS-90°-h1-0.4	4.88
	CS-90°-h1-0.6	7.31
	CS-90°-h2-0.1	1.21
	CS-90°-h2-0.2	2.43
	CS-90°-h2-0.4	4.86
	CS-90°-h2-0.6	7.29
0°	CS-0°-h1-0.1	2.04
	CS-0°-h1-0.2	4.08
	CS-0°-h1-0.4	8.16
	CS-0°-h1-0.6	12.24

θ	Test	σ_o (ksi)
45°	CS-45°-h1-0.1	1.25
	CS-45°-h1-0.2	2.50
	CS-45°-h1-0.4	5.00
	CS-45°-h1-0.6	7.50
	CS-45°-h2-0.1	1.24
	CS-45°-h2-0.2	2.48
	CS-45°-h2-0.4	4.97
	CS-45°-h2-0.6	7.46

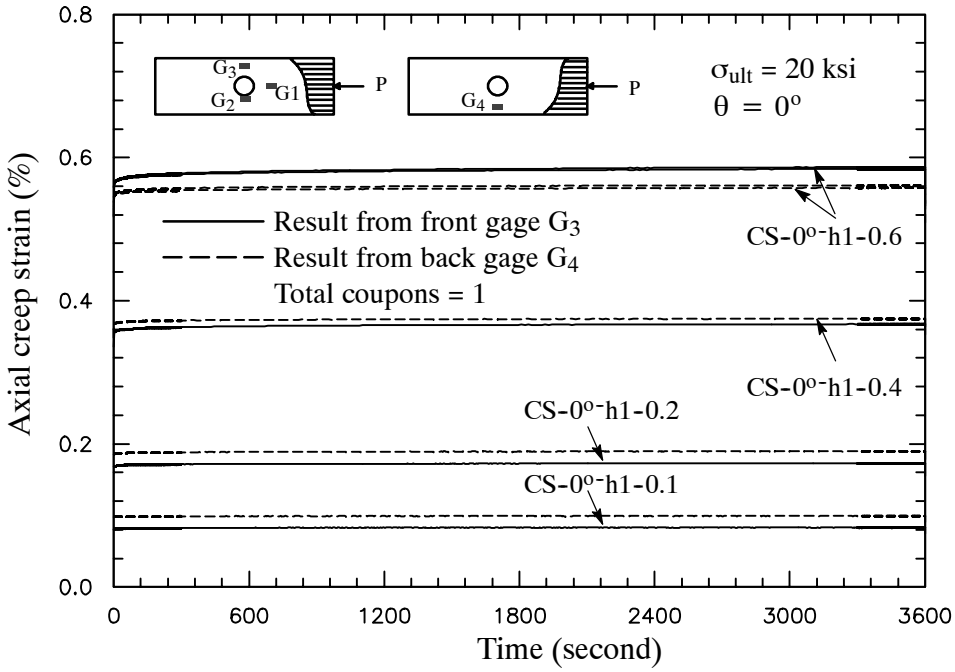

Figure B.25 Axial compression creep strain for uniaxial coupon.

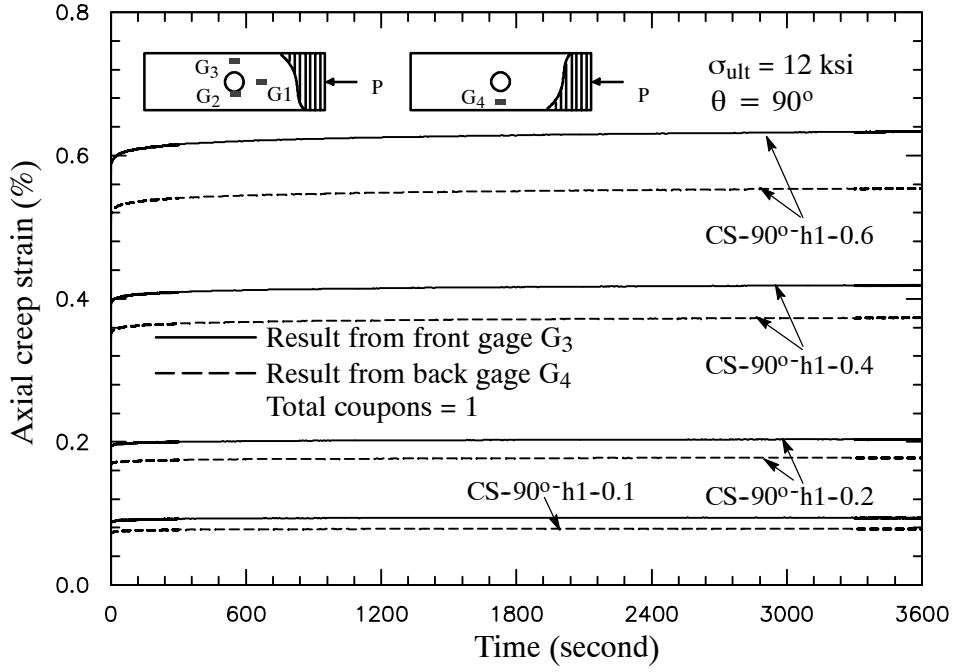

Figure B.26 Axial compression creep strain for transverse coupon.

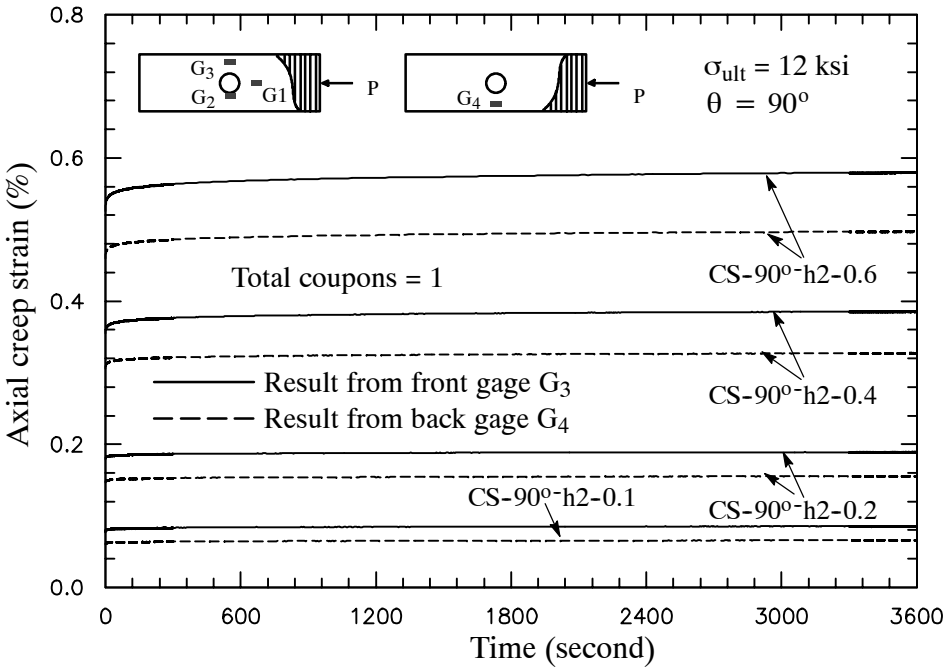

Figure B.27 Axial compression creep strain for transverse coupon.

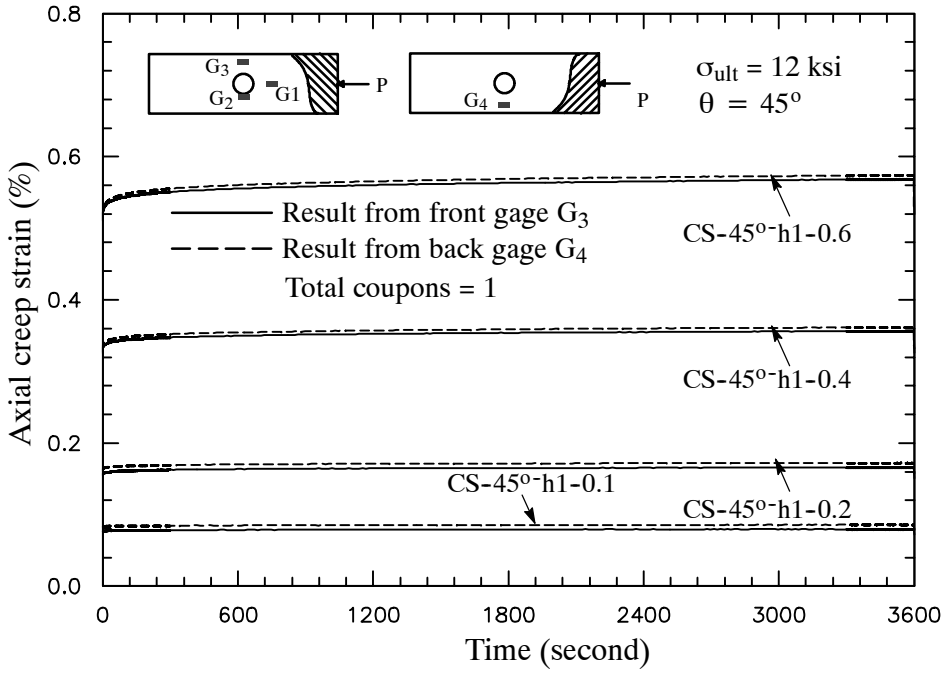

Figure B.28 Axial compression creep strain for 45° off-axis coupon.

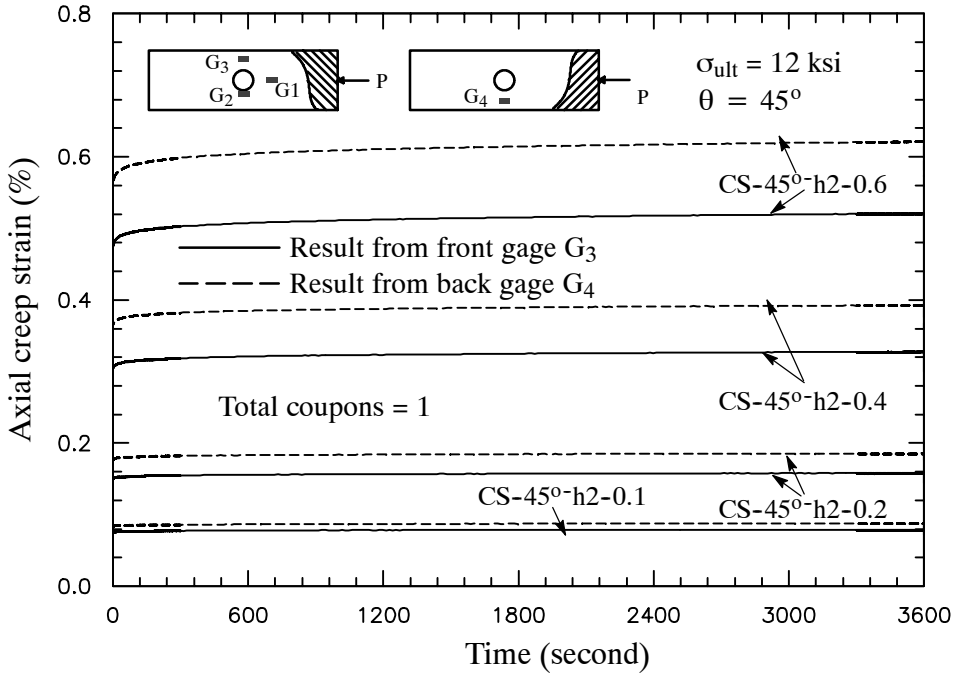

Figure B.29 Axial compression creep strain for 45° off-axis coupon.

REFERENCES

1 ABAQUS, Hibbitt, Karlsson and Sorensen, Inc., (2002) "User's Manual", Version, 6.3.

2 Aboudi, J. (1990), "Micromechanical Characterization of the Non-linear Viscoelastic Behavior of Resin Matrix Composites", Composites Science and Technology, Vol. 38, pp. 371-386.

3 Aboudi, J. (1991), "Mechanics of Composite Materials: A Unified Micromechanical Approach", Elsevier.

4 Aboudi, J. and Cederbaum, G. (1989), "Analysis of Viscoelastic Laminated Composite Plates", Composite Structures, Vol. 12, pp. 243-256.

5 ASTM D3410/D3410M-95, Standard Test Method for Compressive Properties of Polymer Matrix Composite Materials with Unsupported Gauge Section by Shear Loading, American Society of Testing Materials.

6 Bank, L. C. and Mosallam, A. S (1990)., "Creep and Failure of A Fill-Size Fiber Reinforced Plastic Pultruded Frame," Composite Material Technology, pp. 49-56.

7 Bank, L. C. and Yin, J. (1999), "Failure of Web-Flange Junction in Postbuckled Pultruded I-Beams," Journal of Composites for Construction, pp. 177-184.

8 Barbero, E. J. (1991), "Pultruded Structural Shape - from the Constituents to the Structural Behavior, " SAMPE Journal, Vol. 27, pp. 25-30.

9 Barbero, E. J., and Tomblin, J. (1993), "Euler Buckling of Thin-Walled Composite Columns,' Thin-Walled Structures, Vol. 17, pp. 237-258.

10 Barbero, E. J., and Luciano, R. (1995), "Micromechanical Formulas for the Relaxation Tensor of Linear Viscoelastic Composites with Transversely Isotropic Fibers," International Journal of Solids and Strcutures, Vol. 32, No. 13, pp. 1859-1872.

11 Barbero, E. J., Dede, E. K., and Jones, S. (2000), "Experimental Verification of Buckling-mode Interation in Intermediate-length Composite Columns," International Journal of Solids and Strcutures, Vol. 37, pp. 3919-3934.

12 Barpanda, D. and Raju, M. P. (1998), "Effect of hybridization on the Creep and Stress Relaxation Characteristics of Pultruded Composites," Journal of Reinforced Plastics and Composites, Vol. 17, No. 3, pp. 234-249.

13 Benveniste, Y. (1987), "A New Approach to the Application of Mori-Tanaka's Theory in Composite Materials," Mechanics of Materials, Vol. 6, pp. 147-157.

14 Bhalerao, M. S, and Moon, T. J. (1996), "Micromechanis of Local Viscoelastic Buckling in Thick Composites," Composites Part B, 27B, pp. 561-568.

15 Binshan, S. Y., Svenson, A. L., and Bank, L. C. (1995), "Mass and Volume Fraction Properties of Pultruded Glass Fibre-Reinforced Composites," Composites, Vol. 26, pp. 725-731.

16 Biot, M.A. (1954), "Theory of Stress-strain Relations in Anisotropic Viscoelasticity and Relaxation Phenomena," Journal Applied Physics, Vol. 25, pp. 1385.

17 Bradshaw, R. D. and Brinson, L. C. (1999), "A Continuous Test Data Method to Determine a Reference Curve and Shift Rate for Isothermal Physial Aging," Polymer Engineering and Science, Vol. 39, No. 2, pp. 211-235.

18 Bradshaw, R. D. and Brinson, L. C. (1999), "Mechanical Response of Linear Viscoelastic Composite Laminates Incorporating Non-isothermal Physical Aging Effects," Composite Science and Technology, Vol. 59, pp. 1411-1427.

19 Brinson, H. F, Morris, D. H., and Yeow, Y. T. (1978), "A New Experimental Method for the Accelerated Characterization of Composite Materials," Sixth International Conference on Experimental Stress Analysis, Munich.

20 Brinson, H. F (1985), "Viscoelastic Behavior and Lifetime (Durability) Predictions," Proceeding of the European Mechanics Colloquium 182, pp. 3-20.

21 Brionson, L. C. and Gates, T. S. (1995), "Effects of Physical Aging on Long-term Creep of Polymers and Polymer Matrix Composites," International Journal of Solids and Structures, Vol. 32, No. 6/7, pp. 827-846.

22 Brueller, O. S. (1987), "On the Nonlinear Characterization of the Long Term Behavior of Polymeric Materials," Polymer Engineering and Science, Vol. 27, No. 2, pp.144.

23 Cederbaum, G. and Aboudi, J. (1989), “Micro-to-Macro Analysis of Viscoelastic Laminated Plates,” In Composite Structures, Vol. 5, I. H. Marshall. ed., Elsevier, London, pp. 779-793.

24 Christensen, R. M. (1971), “Theory of Viscoelasticity,” Academic Press, New York.

25 Christensen, R. M. (1979), “Mechanics of Composite Materials,” John Wiley & Sons, Inc., New York.

26 Christensen, R. M. and Lo, K. H. (1979), “Solutions for Effective Shear Properties in Three Phase Sphere Cylinder Models,” Journal Mechanics Physics Solids, Vol. 27, pp. 315-330.

27 Coleman, B. D. (1964), “Thermodynamics of Materials with Memory,” Arch. Ratl Mechanics Anal., Vol. 17, pp. 1.

28 Coleman, B. D. and Gurtin, M.E. (1967), “Thermodynamics with Internal State Variables,” Journal Chemical Physics, Vol.47, No.2, pp. 597.

29 Coleman, B. D. and Noll, W. (1961), “Foundation of Linear Viscoelasticity,” Reviews of Modern Physics, 33, pp. 239.

30 Dillard, D. A., Straight, M. R., and Brinson, H. F (1987)., ”The Nonlinear Viscoelastic Characterization of Graphite/Epoxy Composites,” Polymer Engineering and Science, Vol 27, No 2, pp. 116-123.

31 Findley, W. N., Lai, J.S., and Onaran, K (1976), ”Creep and Relaxation of Nonlinear Viscoelastic Materials,” New York, Dover Publication.

32 Fisher, F. T. and Brinson, L. C. (2001), ”Viscoelastic Interphases in Polymer-Matrix Composites: Theoretical Models and Finite Element Analysis,” Composites Science and Technology, Vol. 61, pp. 731-748.

33 Gates, T.S., Veazie, D.R., Brinson, L.C. (1997), ”Creep and Physical Aging in a Polymeric Composite: Comparison of Tension and Compression,” Journal of Composite Materials, Vol. 31, No. 24, pp. 2478-2505.

34 Gibson, R. F (1994)., ”Principles of Composite Material Mechanics,” McGraw-hill, Inc.

35 Gosz, M., Moran, B. and Achenbach, J. D. (1990), “Effect of a Viscoelastic Interface On the Transverse Behavior of Fiber-Reinforced Composites,” National Center for Composite Materials Research, UIUC, Technical Report No. 90-07.

36 Green, A.E. and Rivlin, R. S (1957), ”The Mechanics of Nonlinear Materials with Memory, Part I” Arch. Ratl Mechanics Anal., Vol. 1, pp.1.

37 Ha, K. and Schapery, R. A. (1998), ”A Three-Dimensional Viscoelastic Constitutive Model for Particulate Composites with Growing Damage and Its Experimental Validation,” International Journal Solids Structures, Vol. 35, pp. 3497-3517.

38 Haddad, Y. M. (1988), ”On the Theory of Viscoelastic Solid,” Res Mechanica, Vol. 25, pp. 225.

39 Haj-Ali, R. and El-Hajjar, R. (2003), ”Crack Propagation Analysis of Mode-I Fracture in Pultruded Composites using Micromechanical Constitutive Models,” Mechanics of Material (MOM) Journal, Vol. 35, No. 9, pp. 885-902.

40 Haj-Ali, R. M., and Pecknold, D. A. (1996), ”Hierarchical Material Models with Microstructure for Nonlinear Analysis of Progressive Damage in Laminated Composite Structures,” Structural Research Series No. 611, UILU-ENG-96-2007, Department of Civil Engineering, University of Illinois at Urbana-Champaign.

41 Haj-Ali, R. M., Kilic, M. H., and Zureick, A. H. (2001), ”Three-Dimensional Micromechanics-Based Constitutive Framework for Analysis of Pultruded Structures,” Journal of Engineering Mechanics, Vol. 127, No. 7, pp.653-660.

42 Haj-Ali, R. M., Kilic, M. H. (2002), ”Nonlinear Behavior of Pultruded FRP Composites,” Composites: Part B, Vol. 33, pp. 173.

43 Haj-Ali, R. M., Kilic, M. H. (2003), ”Nonlinear Constitutive Models for Pultruded FRP Composites,” Mechanics of Material (MOM) Journal, Vol. 35, No. 8, pp. 791-801.

44 Haj-Ali, R. and Muliana, A. H. (2003), “Micromechanical Models for the Nonlinear Viscoelastic Behavior of Pultruded Composite Materials,” Int. J. Solids and Structures, 40, pp. 1037-1057.

45 Haj-Ali, R. M., Muliana, A. H. (2004), "Numerical Finite Element Formulation of the Schapery Nonlinear Viscoelastic Material Model," Int. Journal of Numerical Method in Engineering, Vol. 59, No. 1.

46 Hashin, Z. (1964), "Analysis of Composite Materials-A Survey," ASME Journal Applied Mechanics, Vol. 50, pp. 481-505.

47 Hashin, Z. (1990), "Thermoelastic Properties and Conductivity of Carbon/Carbon Fiber Composites," Mechanics of Materials, Vol. 8, pp. 293-308.

48 Hashin, Z. and Rosen, B. W. (1964), "The Elastic Moduli of Fiber Reinfoced Materials," Journal Applied Mechanics, Vol. 31, pp. 223-232.

49 Henriksen, M. (1984), "Nonlinear Viscoelastic Stress Analysis - A Finite Element Approach," Computer and Structures, Vol. 18, No. 1, pp. 133-139.

50 Herakovich, C. T. and Mirzadeh, F. (1991), "Properties of Pultruded Graphite/Epoxy," Journal of Reinforced Plastics and Composites, Vol. 10, pp. 2-28.

51 Herakovich, C. T. (1998), "Mechanics of Fibrous Composites," John Wiley and Sons, Inc., New York.

52 Hiel, C.C., Brinson, H. F., and Cardon A. H. (1983), "The Nonlinear Viscoelastic Response of Resin Matrix Composites," Composite Structures, Vol. 2, I. H. Marshall. ed., Applied Science, pp. 271-281.

53 Hiel, C.C., Cardon A. H., and Brinson, H. F. (1984), NASA Contract Report, 2772.

54 Hill, R. (1964), "Theory of Mechanical Properties of Fiber-Strengthened Materials: I Elastic Behavior," Journal Mechanics Physics Solids, Vol. 12, pp.192-212.

55 Hilton, H. H. (1952), "Creep Collapse of Viscoelastic Columns with Initial Curvatures," Journal of Aeronautical Sciences, Vol. 19, pp. 844-846.

56 Hilton, H. H. (1961), "On the Nonexistence of Finite Critical Times for Generalized Linear Viscoelastic Columns with Arbitrary Initial Curvatures," Journal of Aeronautical Sciences, Vol. 28, pp. 655-656.

57 Horoschenkoff, A. (1990), "Characterization of the Creep Compliance J_{22} and J_{66} of Orthotropic Composites with PEEK and Epoxy Matrices Using the Nonlinear Viscoelastic Response of the Neat Resin," Journal of Composite Materials, vol. 24, pp. 879-891.

58 Howard, C. M. and Holloway, L. (1987), “The Characterization of the Nonlinear Viscoelastic Properties of a Randomly Oriented Fibre/Matrix Composite,” Composites, Vol. 18, No. 4, pp.317-323.

59 Huang, N. C. (1976), ”Creep Buckling of Imperfect Columns,” Journal of Applied Mechanics Transaction ASME, E43, No. 1, pp. 131-136.

60 Hu, H. and Sun, C. T. (2000), ”The Characterization of Physical Aging in Polymeric Composites,” Composites Science and Technology, Vol. 60, pp.2693-2698.

61 Jones (1999), “Mechanics of Composite Materials,”

62 Katouzian, M., Bruller, O. S., and Horoschenkoff, A. (1995), ”On the Effect of Temperature on the Creep Behavior of Neat anc Carbon Fiber Reinforced PEEK and Epoxy Resin,” Journal of Composite Materials, Vol. 29, No. 3, pp. 372-387.

63 Kempner, J. (1954), “Creep Bending and Buckling of Linearly Viscoelastic Columns,” National Advisory Committee For Aeronautics, Technical Note 3136.

64 Kilic, H. (2001), ”Three-Dimensional Micromechanical Models for the Nonlinear Analysis of Pultruded Composite Structures,” Ph.D Thesis, Georgia Institute of Technology.

65 Kilic, H. and Haj-Ali, R. (2003), ”Elastic-degrading Analysis of Pultruded Composite Structures,” Composites Structures, Vol. 60, No. 1, pp. 43-55.

66 Kilic, H. and Haj-Ali, R. (2003), ”Progressive Damage and Nonlinear Analysis of Pultruded Composite Structures,” Composites part B: Engineering, Vol. 34, No. 3, pp. 235-250.

67 Klasztorny, M. and Wilczynski, A. P. (2000), “Constitutive Equations of Viscoelasticity and Estimation of Viscoelastic Parameters of Unidirectional Fibrous Polymeric Composites,” Journal of Composite Material, Vol. 34, No. 19, pp. 1624-1639.

68 Knight, N. F., Jr. and Starnes, J. H., Jr., ”Postbuckling Behavior of Axially Compressed Graphite-Epoxy Cylindrical Panels with Circular Holes,” ASME J. Pressure Vessels Technology, Vol. 107, pp. 394-402, 1985.

69 Lai, J.S., and Findley, W.N. (1973), ”Creep of Polyurethane unde Varying Temperature for Nonlinear Uniaxial Stress,” Transactions of The Society of Rheology, 17, 1, pp. 63-87.

70 Lai, J., Baker, A. (1996), "3-D Schapery Representation for Nonlinear Viscoelasticity and Finite Element Implementation," Computational Mechanics, 18, pp. 182-191.

71 Lemaitre, J. and Chaboche, J. L. (1990), "Mechanics of Solid Materials," Cambridge University Press.

72 Li, R. (1997), "Nonlinear Viscoelastic Stress and Fracture Analyses of Laminated Composites," PhD Dissertation, University of Washington.

73 Lou, Y. C., Schapery, R. A. (1971), "Viscoelastic Characterization of a Nonlinear Fiber-Reinforced Plastic," Journal of Composite Materials, Vol. 5, pp. 208-234.

74 Lubliner, J. (1969), "On Fading Memory in Materials of Evolutionary Type," Acta Mechanica, Vol. 8, pp. 75.

75 Lubliner, J. (1972), "On the Thermodynamic Foundations of Non-linear Solid Mechanics," Int. Jour. Non-Linear Mechanics, Vol. 7, pp. 237.

76 Luciano, R. and Barbero, E. J. (1994), "Formulae for the Stiffness of Composites with Periodic Microstructures," International Journal of Solids and Structures, Vol. 31, No. 21, pp. 2933-2944.

77 Martirosyan, M. M. (1965), "Transient Creep of Glass-Reinforced Plastic," Mekhanika Polimerov, vol. 1, no. 2, pp. 47-54.

78 Mohan, M. and Adams, D. F. (1985), "Nonlinear Creep-Recovery Response of Polymer Matrix and its Composites," Experimental Mechanics, pp. 262-271.

79 Mori, T. and Tanaka, K. (1973), "Average Stress in Matrix and Average Elastic Energy of Materials with Misfitting Inclusions," Acta Metallurgical, Vol. 21, pp. 571-574.

80 Muliana, A. H., Haj-Ali, R. M, Coates, C. W., and Armanios, E. A. (2001), "Failure Prediction of Co-cured Composite Single Lap Joints with Modified Interface," Proceedings of the ASC 16th Technical Conference, Blacksburg, VA, September 10-12.

81 Nemat-Nasser, S. and Hori, M. (1999), "Micromechanics : overall properties of heterogeneous materials," 2nd Ed., Elsevier.

82 Pasricha, A., Tuttle, M. E., and Emery, A. F. (1995), "Time-Dependent Response of IM7/5260 Composites Subjected to Cyclic Thermo-Mechanical Loading," Composite Science and Technology Vol. 55, pp. 49-56.

83 Pasricha, A., Dillard, D. A., and Tuttle, M. E. (1997), "Effect of Physical Aging and Variable Stress History on the Strain Response of Polymeric Composites," Composite Science and Technology Vol. 57, pp. 1271-1279.

84 Pecknold, D. A. and Haj-Ali, R. (1993), "Integrated Micromechanical/Structural Analysis of Laminated Composites," Mechanics of Composite Materials-Nonlinear Effects AMD Vol. 159, pp. 197-206.

85 Peretz, D. and Weitsman, Y. (1983), "The Non-linear Thermo-viscoelastic Characterization of FM-73 Adhesives," Journal Rheology 26, pp. 245-261.

86 Poon, H. and Ahmad, F. (1998), "A Finite Element Constitutive Update Scheme for Anisotropic, Viscoelastic Solids Exhibiting Non-linearity of The Schapery Type," International Journal of Numerical Method in Engineering, Vol. 46, pp. 2027-2041.

87 Roy, S. and Reddy, J. N. (1988), "A Finite Element Analysis of Adhesively Bonded Composite Joints with Moisture Diffusion and Delayed Failure," Computers and Structures Vol 29., No. 6, pp. 1011-1031.

88 Sadkin, Y. and Aboudi, J. (1989), "Viscoelastic Behavior of Thermo-rheologically Complex Resin Matrix Composites," Composites Science and Technology Vol. 36, pp. 351-365.

89 Schaffer, B. G. and Adams, D. F. (1981), "Nonlinear Viscoelastic Analysis of a Unidirectional Composite Material," Journal of Applied Mechanics, Vol. 48, pp. 859.

90 Schapery, R. A. (1964), "Application of Thermodynamics to Thermomechanical, Fracture, and Birefringent Phenomena in Viscoelastic Media," Journal Applied Physics, Vol. 35, pp. 1451.

91 Schapery, R. A. (1967), "Stress Analysis of Viscoelastic Composite Materials," Journal Composite Materials, Vol. 1, pp. 228-267.

92 Schapery, R. A. (1969), "On the Characterization of Nonlinear Viscoelastic Materials," Polymer Engineering and Science, Vol. 9, No. 4, pp. 295-310.

93 Schapery, R. A. (1981), "On Viscoelastic Deformation and Failure Behavior of Composite Materials with Distributed Flaws," Wang and Renton eds., Advanced in Aerospace Structures and Materials, ASME-AD-01, ASME, pp. 5-20.

94 Schapery, R. A. (1997), ”Nonlinear Viscoelastic and Viscoplastic Constitutive Equations Based on Thermodynamics,” Mechanics of Time-Dependent Materials, Vol. 1, pp. 209.

95 Scott, D. W., Lai, J., and Zureick, A. H. (1995), “Creep Behavior of Fiber-Reinforced Polymeric Composites: a Review of the Technical Literature,” Journal Reinforced Plastics and Composites, Vol. 14, pp. 588-617.

96 Scott, D. W. and Zureick, A. H. (1998), “Compression Creep of a Pultruded E-glass/Vinylester Composite,” Composites Science and Technology, Vol. 58, pp. 1361-1369.

97 Skrypnyk, I. D., Spoormaker, J. L., and Kandachar, P (2000)., “A Constitutive Model for Long-Term Behavior of Polymers,” Time Dependent and Nonlinear Effects in Polymers and Composites, ASTM STP 1357, R.A. Schapery and C.T. Sun, Eds., American Society for Testing and Materials, West Conshohocken, PA, pp. 70-82.

98 Smith, S. J., Parsons, I. D., and Hjelmstad, K. D. (1998), “An Experimental Study of the Behavior of Connections for Pultruded GFRP I-beams and Rectangular Tubes,” Composite Structures, Vol. 42, pp. 281-290.

99 Smith, S. J., Parsons, I. D., and Hjelmstad, K. D. (1999), “Finite Element and Simplified Models of GFRP Connections,” Journal of Structural Engineering, pp. 749-756.

100 Sonti, S. S. and Barbero, E. (1996), “Material Characterization of Pultruded Laminates and Shapes,” Journal of Reinforced Plastics and Composites, Vol. 15, pp. 701-717.

101 Southwell, R. V. (1932), “On the Analysis of Experimental Observations in Problems of Elastic Stability,” Proceedings of Royal Society, London (A), Vol. 135, pp. 601-616.

102 Spence, B. R. (1990), ”Compressive Viscoelastic Effects (Creep) of A Unidirectional Glass/Epoxy Composite Material,” 35th International SAMPE Symposium, pp. 1490-1493, April 2-5.

103 Struik, L. C. E. (1978), ”Physical Aging In Amorphous Polymers and Other Materials,” New York, Elsevier Scientific Publishing Company.

104 Taylor, R.L., Pister, K.S., and Goudreau, G.L. (1970), ”Thermomechanical Analysis of Viscoelastic Solids,” International Journal for Numerical Methods in Engineering, Vol. 2, pp. 45-59.

105 Touati, D. and Cederbaum, G. (1997), "On the Prediction of Stress Relaxation From Known Creep of Nonlinear Materials," Journal of Eng. Matr. and Tech., vol 119, pp. 121-124.

106 Touati, D. and Cederbaum, G. (1998), "Post Buckling of Nonlinear Viscoelastic Imperfect Laminated Plates Part I: Material Considerations," Composite Structures, 42, pp. 33-41.

107 Touati, D. and Cederbaum, G. (1998), "Post Buckling of Nonlinear Viscoelastic Imperfect Laminated Plates Part II: Structural Analysis," Composite Structures, Vol. 42, pp. 43-51.

108 Touati, D. and Cederbaum, G. (1998), "Effects of Compressibility on the Postbuckling Behavior of Imperfect Viscoelastic Columns," Composite Structures, Vol. 68, pp. 561-566.

109 Tsai, S. W. and Pagano, N. J. (1968), "Invariant Properties of Composite Materials," Composite Materials Workshop, Technomic Publishing Co.

110 Tuttle, M. E. and Brinson, H. F. (1986), "Prediction of the Long-Term Creep Compliance of General Composite Laminates," Experimental Mechanics, pp. 89-102.

111 Tuttle, M. E., Pasricha, A., and Emery, A. F. (1995), "The Nonlinear Viscoelastic-Viscoplastic Behavior of IM7/5260 Composites Subjected to Cyclic Loading," Journal of Composite Materials, vol. 29, no. 15, pp. 2025-2046.

112 Vakanier, A.R, Zureick, A. and Will, K. M. (1991), "Predictions of Local Flange Buckling in Pultruded Shapes by Finite Element Analysis," Proc. Spec. Conf. Advance Composite Materials in Civ. Engr. Struc., ASCE Matrl. Engr. Division, S. L. Iyer and R. Sen eds., NY, pp. 302-312.

113 Vinogradov, A. M. (1985), "Nonlinear Effects in Creep Buckling Analysis of Columns," Journal of Engineering Mechanics, Vol. 111, No. 6, pp. 757-767.

114 Wang, Y. and Zureick, A. (1994), "Characterization of Longitudinal Tensile Behavior of Pultruded I-shaped Structural Members using Coupons Specimens, Composite Structures, Vol. 29, pp. 463-472.

115 Wilson, D. W., and Vinson, J. R. (1984), "Viscoelastic Analysis of Laminated Plate Buckling," AIAA Journal, Vol. 22, No. 7, pp. 982-988.

116 Yancey, R. N., Pindera, M. J. (1990), "Micromechanical Analysis of the Creep Response of Unidirectional Composites," Journal of Engineering Material and Technology, Vol. 112, pp. 157-163.

117 Yeow, Y.T., Morris, D. H., and Brinson, H. F. (1979), "Time-Temperature Behavior of a Unidirectional Graphite/Epoxy Composite," Composite Material: Testing and Design (Fifth Conference), ASTM STP 674. Tsai Ed., ASTM, pp. 263-281.

118 Yi, S., Hilton, H. H, and Ahmad, M. F. (1996), "Nonlinear Thermo-Viscoelastic Analysis of Interlaminar Stresses in Laminated Composites," Journal Applied Mechanics, Vol. 63, pp. 218-224.

119 Yi, S. (1997), "Finite Element Analysis of Free Edge Stresses in Nonlinear Viscoelastic Composites Under Uniaxial Extension, Bending, and Twisting Loadings," International Journal for Numerical Methods in Engineering, Vol. 40, pp. 4225-4238.

120 Yi, S., Ahmad, M. F., and Hilton, H. H. (1998), "Nonlinear Viscoelastic Stress Singularities Near Free Edges of Unsymmetrically Laminated Composites," International Journal Solids Structures, Vol. 35, No. 24, pp. 3221-3237.

121 Zureick, A., Kahn, L.F., and Bandy, B.J. (1995), "Test on Deep I-shape Pultruded Beams," Journal Reinforced Plastic and Composites, Vol. 14, pp. 378-389.

122 Zureick, A. and Scott, D. (1997), "Short-term Behavior and Design of Fiber Reinforced Polymeric Slender Members under Axial Compression,"Journal of Composites for Construction, ASCE, Vol. 1, No. 1, pp. 140-149.